CHEMICAL APPLICATIONS OF PULSED AND STEADY-STATE NUCLEAR MAGNETIC RESONANCE

by

Keith N. Shaw, B.Sc.

A THESIS SUBMITTED IN PARTIAL FULFILLMENT OF
THE REQUIREMENTS FOR THE DEGREE OF
DOCTOR OF PHILOSOPHY

in the Department
of
Chemistry

We accept this thesis as conforming to the
required standard

THE UNIVERSITY OF BRITISH COLUMBIA

In presenting this thesis in partial fulfilment of the requirements for an advanced degree at the University of British Columbia, I agree that the Library shall make it freely available for reference and study. I further agree that permission for extensive copying of this thesis for scholarly purposes may be granted by the Head of my Department or by his representatives. It is understood that copying or publication of this thesis for financial gain shall not be allowed without my written permission.

Department of CHEMISTRY

The University of British Columbia
Vancouver 8, Canada

Date Nov. 9th, 1971

ABSTRACT

A general matrix formulation for the effects of chemical exchange processes in high resolution nuclear magnetic resonance (NMR) has been developed which allows a concise description and efficient numerical calculation of exchange modified lineshapes for an arbitrary number of spin-sites. A complete description of all rate processes is contained in a single matrix, and both first- and second-order spin systems (as described in terms of a spin density matrix) are accommodated through specific forms for a spin-site frequency matrix.

The hindered rotation about the N-C bond in substituted amides has been studied on a comparative basis using free energies of activation derived from first-order rate constants obtained by complete analyses of digital lineshape data. A versatile FORTRAN computer program has been used for routine iterative lineshape fitting and it has been shown that, even with the precision now attainable using this technique, the most reliable kinetic parameter is the free energy of activation. Huckel Π-MO and semi-empirical SCF-LCAO-MO calculations have been used in a description of the electronic factors determining the barriers to hindered rotation and the charge distributions in the amides studied experimentally.

Application of the Fourier transform in high resolution NMR has also been considered in detail, with particular emphasis upon quantitative lineshape studies using the data available from simple pulsed NMR experiments. The advantages of the pulse method with digital data acquisition have been examined, and the numerical computations and

corrective factors involved have been incorporated into a general and efficient computer program.

TABLE OF CONTENTS

LIST OF TABLES

LIST OF FIGURES

ACKNOWLEDGEMENTS

Sincere thanks are due to Dr. L. W. Reeves under whose supervision this work was accomplished.

Thanks are also due to R. Hobson, E. Allan and R. C. Shaddick for their cooperation during the course of this work. Assistance from the Chemistry Department technical staff and the Computing Centre personnel is also gratefully acknowledged.

CHAPTER I.

INTRODUCTION

In general, the lineshapes and widths of nuclear magnetic resonance (NMR) spectral lines are particularly sensitive to time-dependent processes occurring within a nuclear spin system. Thus, for over a decade NMR has been applied, to varying levels of sophistication, to the study of chemical rate processes. This experimental method allows the determination of precise rate constants and associated activation parameters for molecular processes such as hindered internal rotation, molecular isomerism and chemical exchange which may be described by well defined first order rate constants. A quantitative study leads directly to the evaluation of possible mechanisms for these molecular processes and also may lead indirectly to fundamental information on the electronic structures of the molecular systems and transition states involved.

The significance of the NMR method in chemical kinetic studies lies in its inherent ability to provide data for relatively fast processes from measurements on chemical systems at equilibrium, this information being unattainable through the application of conventional chemical methods. Two fundamental characteristics of NMR allow such measurements:

(i) the characteristic time scales in magnetic resonance are relatively slow for microscopic processes. It is well known that molecular motions give rise to generalized relaxation effects in a nuclear spin system. Fluctuating magnetic fields

associated with lattice motions having frequency components corresponding to the resonant spin precessional frequencies may induce transitions between the nuclear energy levels leading to spin-lattice relaxation processes and observable spectral effects. When molecular systems are studied as non-viscous solutions, these random lattice field fluctuations show only as small time-average effects and the interaction of the nuclear spins with their lattice environment may be considered to be correspondingly weak. Under this condition, the time-dependent interaction of the nuclear spins with fluctuating local magnetic fields becomes dominant. These local fields may be considered to be associated with the molecular electronic chemical shielding and indirect spin-spin coupling mechanisms, in the absence of nuclear electric quadrupolar interactions. Again, if these fluctuations are sufficiently rapid, a time-average magnetic field acts on each nuclear spin resulting in a single resonance spectral line. Very slow fluctuations, however, allow each spin to precess at a frequency characteristic of its chemical environment resulting in a spectrum of resonance multiplets. In the intermediate region (for a diamagnetic spin system) the local magnetic field fluctuations determine the lineshape and width of the resonance spectral lines. Thus it is seen that the overall form of an observed NMR spectrum is critically dependent upon the frequencies associated with local magnetic field fluctuations as compared with the difference

in precessional frequencies of nuclear spins in specific environmental local magnetic fields. Since the environmental field differences are often very small, relatively slow molecular motions give rise to observable spectral effects in NMR spectroscopy and hence rate processes having first-order rate constants in the range 10^{-5} to 10^{-1} sec^{-1} may be studied.

(ii) in the application of NMR it is possible to control the motion of the effective nuclear magnetic dipole moments through the magnitude and form of the impressed rf magnetic field and, thereby, also the mode of observation for a given nuclear spin system. In this manner, both steady-state and pulsed NMR methods may be used to extend the range and accuracy of chemical rate process studies. Moreover, by using a specific type of magnetic resonance detection, all phase information relating to the nuclear motion under consideration is retained. This feature allows detailed correlation time analysis of the nuclear and molecular motions for a spin system and leads, under normal experimental conditions, to a direct correspondence between the steady-state and pulsed mode responses of a resonant spin system through Fourier transform analysis.

The study of chemical rate processes is concerned with the transfer of resonant nuclear spins between different magnetic environments such that a given spin is under the action of an effective fluctuating local magnetic field. Such a transfer process may be described in terms of a generalized transverse spin relaxation mechanism, the transverse component of the effective nuclear magnetization giving rise to the resonance sig-

nal observed under normal NMR experimental conditions. Although the basic concept of transverse spin relaxation in terms of phase relationships between individual nuclear spins (or spin isochromats) is physically simple, an exact theoretical analysis is often subtle and complicated. Analytical formulations for steady-state NMR lineshapes modified by nuclear spin transfer effects are necessarily complicated, even in the simplest cases, and the literature in this field has become quite extensive. The importance of spin relaxation effects was recognized in the original NMR work of Bloembergen et al.[1], who considered magnetic moments under the action of random fluctuating magnetic fields; and concurrently by Bloch[2], in the introduction of his phenomenological equations of motion for a nuclear spin system incorporating a transverse spin relaxation time, T_2. In 1953, Gutowsky et al.[3,4] presented the first formulation for a magnetic resonance lineshape in the presence of transfer processes within a first-order (weakly coupled) nuclear spin system. This semi-classical treatment was based upon the Bloch equations, and the only spectral effect, in addition to those due to natural relaxation processes, is considered due to random modulation of the nuclear spin precessional frequencies. A similar description for such a nuclear spin system, as suggested by Hahn and Maxwell[5], was introduced by McConnell[6]. This formulation allows a simplified introduction of spin transfer probabilities directly into the phenomenological equations, as proposed by Bloch, through terms analogous to those describing transverse spin relaxation. These terms, involving a characteristic correlation time, are an inherent part of a general stochastic theory of magnetic resonance lineshapes as exemplified by the more

sophisticated theories of Markoffian random modulation developed by Anderson[7] and Kubo[8,9]. The introduction of transfer effects in this manner is also consistent with the basic concept, implicit in the phenomenological Bloch equations, that nuclear magnetic dipolar motion associated with generalized relaxation effects may be superimposed on that of an isolated nuclear spin in an applied magnetic field. For a simple uncoupled nuclear spin system, it is possible to avoid an explicit quantum mechanical description of spin transfer effects since the complete spin Hamiltonian, in the absence of a perturbing rf magnetic field, contains only secular terms representing nuclear energy level separations. Furthermore, in certain cases spin-spin coupling may be included through an additional secular term in accordance with normal first order perturbation theory. For a general coupled nuclear spin system, however, magnetic relaxation processes can be rigorously described only in terms of non-equilibrium quantum statistical mechanics in the density matrix formalism[10-13]. The basic complication in a coupled spin system (in a non-viscous liquid) is due to the non-secular term describing indirect spin-spin coupling. This term may be considered to represent a mixing of basis eigen-states in the spin system so that fluctuating magnetic fields associated with the spin-spin mechanism may be effective in inducing transitions between nuclear energy levels. A general quantum mechanical formulation of spin transfer effects in NMR has been developed by Kaplan[14,15] and extended by Alexander[16-19]. Through the definition of a spin transfer operator, this work shows that the description of spin transfer effects is consistent with a generalized spin relaxation theory developed by Bloch[20-22]

and takes a form completely analogous to that used in the stochastic theories. More recently, Johnson[23,24] and Binsch[25] have proposed alternative quantum mechanical formulations for intra-molecular transfer processes in which the time dependence of the average density matrix for all possible molecular spin configurations is described by a Liouville operator[11,26].

Pulsed mode NMR differs from the steady-state mode in that a large pulsed rf magnetic field is applied to a resonant nuclear spin system to rotate the thermal equilibrium resultant nuclear magnetization into a plane perpendicular to the static applied magnetic field. Following the pulse, nuclear spin isochromats precess in the transverse plane and dephase due to magnetic field inhomogeneity and general transverse relaxation processes, the transverse component of the nuclear magnetization giving rise to the observed NMR free induction decay signal. Thus the form of this decay is also strongly dependent upon nuclear spin transfer effects. In 1961, Woessner[27] considered the response of the nuclear magnetization during and following a pulsed magnetic field for an uncoupled spin system in terms of the modified Bloch equations[6] previously mentioned. The form of the predicted free induction decay as modified by spin transfer effects was then qualitatively verified experimentally by Reeves and Wells[28]. However, a single pulse experiment can only give information equivalent to that obtained in steady-state studies of chemical rate processes. On the other hand, pulsed mode NMR becomes a versatile and independent method when multi-pulse sequences are used to produce corresponding spin echo trains[29]. Such pulse sequences effectively remove the influence of magnetic field inhomogeneity, which normally limits the range of rates

that may be measured by NMR techniques. Carr and Purcell[30] and Meiboom and Gill[31] have developed specific multi-pulse sequences to reduce systematic errors in the determination of transverse relaxation times with contributions from spin transfer processes. In 1963, Luz and Meiboom[32] first reported the measurement of spin transfer rates using such a pulse sequence. Analytical formulations for the decay of Carr-Purcell spin echo amplitudes have been developed by Bloom, Reeves and Wells[33] and Powles and Strange[34] for simple uncoupled spin systems in accordance with a stochastic theory based upon a classical statistical averaging of the accumulated phases of spin isochromats. Similar results were obtained by Allerhand and Gutowsky[35,36] using the modified Bloch equations. The analysis has been extended to include coupled spin systems using Alexander's formalism[37,38]. About the same time, Gutowsky, Vold and Wells[39] developed a matrix formulation based upon the Anderson-Weiss[40] and Banwell-Primas[41] treatments of general spin systems.

In the study of chemical rate processes, a fundamental advantage of the pulsed NMR method is an extension to the measurement of rate constants considerably higher than those normally accessible to quantitative steady-state methods. The pulse method, however, shows an inherent lack of selectivity for the various homonuclear spin transitions usually observed in the steady-state high-resolution NMR spectrum of liquids. Due to the wide frequency distribution associated with an intense pulsed rf magnetic field, this field interacts with all nuclei of a given species in a molecular system. Although it is possible to obtain selectivity in a very simple spin system[42] using conventional spin echo techniques, general studies of

transverse relaxation properties of individual nuclear spin transitions are most readily measured using the phenomenon of rotary spin echoes[43-45]. Comparable studies in the steady-state mode use double resonance techniques[46-48]. In addition, these double resonance techniques allow quantitative studies of much slower rate processes than those normally accessible to NMR methods.

Hindered internal rotation in molecular systems such as amides, nitrites and nitrosamines is a process of considerable chemical interest in that the magnitude and form of the potential barrier to rotation is expected to be directly related to the detailed electronic structure of the system. This rotation may be considered in terms of an intramolecular nuclear spin transfer process, described by a first-order rate constant. The NMR methods outlined above are ideally suited to studies of such molecular rate processes, usually inaccessible to chemical kinetic techniques. Of particular interest is the hindered rotation about the N-C bond of amides as originally postulated by Pauling[49], being of importance in the theories of the structure of proteins[50] and many other molecules of biological significance containing the common peptide functional group. Although the IR spectrum of N-methylacetamide had been interpreted[51] in terms of such a rotation, the analysis of the NMR spectrum of N,N-dimethylformamide by Phillips[52] in 1955 demonstrated unequivocally the existence of hindered rotation in such a system. As described in the reviews available[53-57], the determination of hindered internal rotation rates and the corresponding potential barriers, in accordance with first-order absolute rate theory[58], in substituted amides has become one of the major topics of NMR kinetic

studies. To date, however, very few reliable kinetic measurements exist for these systems. Moreover, a comprehensive study of a series of chemically related compounds has not yet been reported. This is due in part to the necessity of optimum instrumental operating conditions and in part to the lack of detailed analysis of the results obtained. In addition, the systematic errors inherent in the different NMR methods applied must be carefully considered. Only very recently has sufficient experimental care been exercised in and sophisticated analysis been applied to the determination of quantitative kinetic data[47,59-63]. Even though the systematic errors involved have been considered in some detail[64], the results obtained using steady-state and pulsed mode NMR are seldom consistent. Nonetheless, the validity of such kinetic data is exemplified by the consistent results obtained (by the fitting of total NMR lineshapes) by independent research groups[59,61] for N,N-dimethylformamide. Of necessity, in the initial development of NMR methods for kinetic studies, molecular systems were chosen for simplicity of analysis rather than chemical significance. Furthermore, approximate methods have been applied without due consideration of their validity in particular studies.

Chemists are basically interested in the electronic structures of and inter-relationships between a series of related molecular systems, for example, the substituted amides. For this reason, the purpose of the present thesis is to develop consistent and versatile theoretical and experimental techniques for effecient analysis of NMR kinetic data in a systematic study of hindered internal rotation in substituted amides. With the advent of field-frequency locked

steady-state spectrometers and digital data acquisition systems, it is now possible to obtain reliable spectral data that may be rapidly processed to give the parameters of chemical interest. General equations are developed, consistent with a prescribed physical model for a given rate process, and the resultant NMR spectra are numerically computed and plotted using a high speed computer. Experimental lineshapes in digital form can then be compared directly with theoretical spectra. The well known uncoupled AB spin system, and the related ABX spin system, is considered in detail to allow the development of a more general model applicable to steady-state and pulsed mode analyses and a comparison of different theoretical treatments.

Under normal experimental conditions, the steady-state and pulsed mode responses of a nuclear spin system are related by a Fourier transformation[66-68]. To date, Fourier transform techniques have not been applied to any extent in high-resolution NMR spectroscopy[69,70] and the emphasis has been upon the enhancement of signal-to-noise ratio[71]. In view of increased interest in lineshape studies, a theoretical analysis has been made to ascertain the possible advantage of such a transformation in the analysis of pulsed mode NMR data. Towards this end, the necessary computer programs for rapid numerical computations have been developed. A spectrometer system for Fourier transform studies has also been developed and the operational characteristics of the critical circuitry involved has been considered in detail. With the availability of digital data acquisition systems, accurate data may be accumulated very rapidly in a most convenient form and it is shown that this general method is extremely versatile

and does not include many of the inherent disadvantages of the corresponding normal steady-state methods. The extension of digital techniques to multi-pulse NMR procedures also has obvious advantages and may lead to a significant reduction in the large systematic errors associated with this method at the present time.

In this thesis, the barriers to internal rotation in a series of substituted amides have been considered using routine total lineshape fitting based upon the physical models, theoretical expressions and computer programs developed. This data has been correlated with that previously available. In addition, molecular orbital calculations applying the Huckel [72-74] and complete neglect of differential overlap (CNDO) [75-77] approximations have been used to interpret the measured kinetic parameters in terms of molecular electronic structure. In particular, the potential barrier to hindered rotation and other (spectral) properties of the parent compound formamide have been considered in detail for comparison, where possible, with alternative molecular orbital calculations. The electronic structure of carbamyl fluoride and the related compounds acetyl fluoride and acetaldehyde have also been studied to obtain information on the general applicability of the aforementioned approximate MO methods.

CHAPTER 2.

THEORY

2.1 Bloch Equations.

To allow a consistent development of the theory of nuclear magnetic resonance effects due to nuclear spin transfer, a classical vector model will be considered to describe the dynamics of a general nuclear spin system. As the Bloch equations for such a system are fundamental to all following discussions, the basis for these equations will be briefly formulated.

The motion of an isolated nuclear magnetic dipole, $\underline{\mu}$, in a time independent uniform magnetic field, $\underline{H}_o$, is described in a fixed frame of reference Oxyz by

$$\frac{d\underline{\mu}}{dt} = \underline{\mu} \times \gamma \underline{H}_o \qquad (2.1.1)$$

where γ is the nuclear gyromagnetic ratio. Assuming the magnetic field to be directed along the z-axis so that $\underline{H}_o = \underline{k}H_o$, (2.1.1) becomes

$$\frac{d}{dt}\underline{\mu} = \omega_o \cdot \underline{\mu} \times \underline{k} \quad , \quad \omega_o = \gamma H_o \qquad (2.1.2)$$

where $\underline{k}$ is the unit vector in the z-direction and ω_o is the Larmor frequency (rads. sec^{-1}). This equation of motion is consistent with quantum mechanical concepts in that it is readily shown[78] that $\underline{\mu}$ may be replaced by the expectation value $\langle\underline{\mu}\rangle$.

The effect of a circularly polarized magnetic field, $\underline{H}(t)$, defined by

$$H_x(t) = H_1\cos\omega t,\ H_y(t) = -H_1\sin\omega t,\ \omega > 0 \qquad (2.1.3)$$

on a nuclear dipole may be represented in terms of a vector model as shown in Fig. 2.1a. That is, for the particular geometrical configuration shown, the nuclear dipole tends to precess about the magnetic field vectors $\underline{H}_o$ and $\underline{H}_1$ with angular frequencies ω_o and ω_1, respectively. In accordance with the general equation (2.1.2),

$$\omega_1 = \gamma H_1. \qquad (2.1.4)$$

Under normal experimental conditions, $\underline{H}_1$ is associated with a linearly polarized magnetic field, $\underline{H}(t)$, defined by:

$$H_x(t) = 2H_1\cos\omega t,\ H_y(t) = 0, \qquad (2.1.5)$$

as produced in a simple coil. A field of this form, however,may be considered in terms of two component circularly polarized fields[79], one of which is equivalent to that described by Eq. (2.1.3).

The complicated overall magnetic dipolar motion due to the independent magnetic fields, $\underline{H}_o$ and $\underline{H}_1$, is simplified by considering the system in a rotating reference frame[80], Ouvz, to eliminate effectively the time dependence associated with $\underline{H}_1$. If the time dependence of $\underline{\mu}$ in the rotating frame of reference is defined by $(d\underline{\mu}/dt)_r$, it follows that

$$\frac{d\underline{\mu}}{dt} = \left(\frac{d\underline{\mu}}{dt}\right)_r + \underline{\omega}_r \times \underline{\mu}\ ,\quad \underline{\omega}_r = -\omega_r \underline{k} \qquad (2.1.6)$$

where $\omega_r(>0)$ is the angular frequency of the rotating frame. Therefore, from Eqs. (2.1.2) and (2.1.6) it is shown that

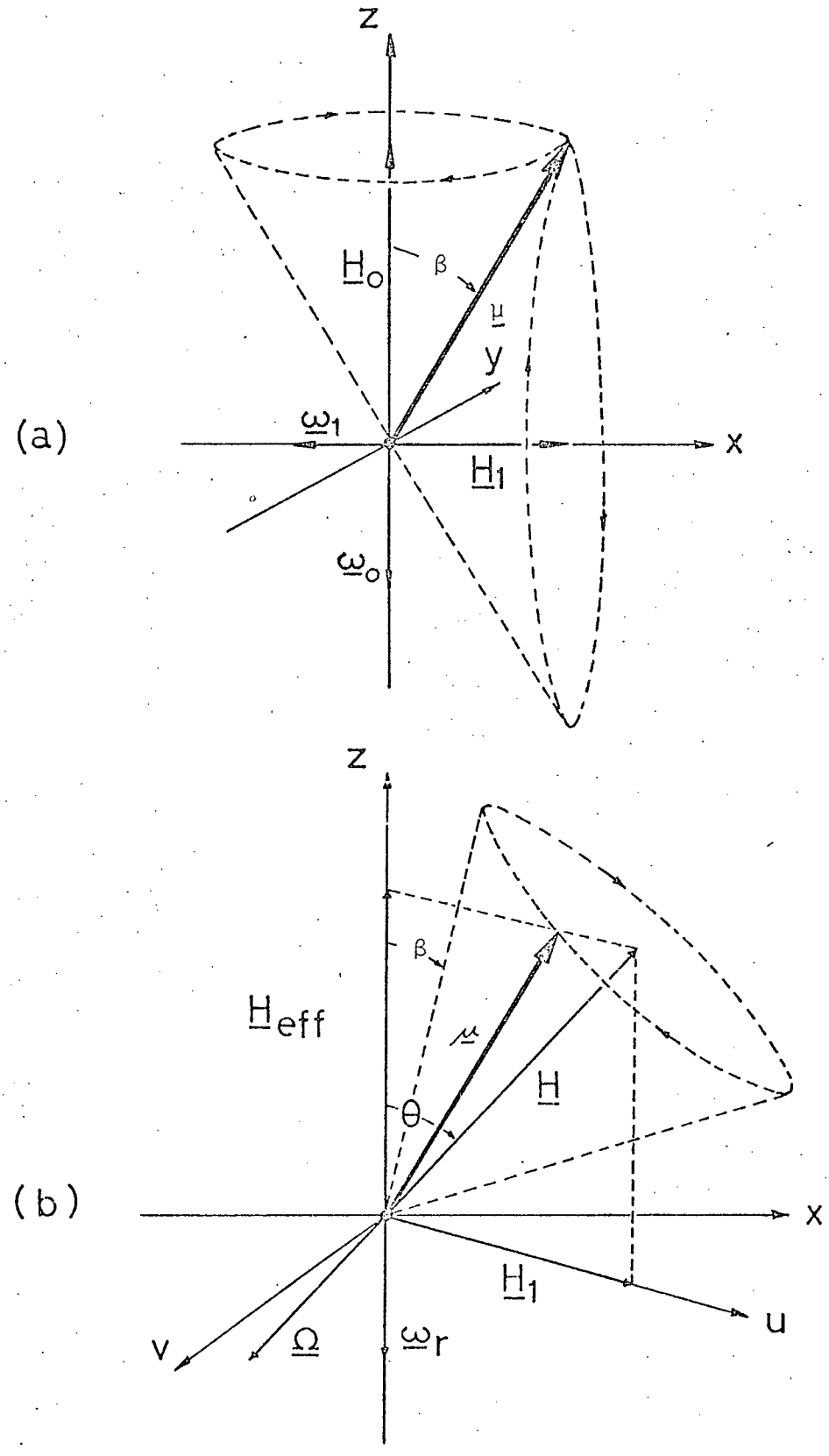

Fig. 2.1 Motion of an isolated nuclear magnetic dipole

$$\left(\frac{d\underline{\mu}}{dt}\right)_r = \underline{\mu} \times (\omega_o - \omega_r)\underline{k} \quad , \tag{2.1.7}$$

and this equation of motion may be expressed in the form

$$\left(\frac{d\underline{\mu}}{dt}\right)_r = \underline{\mu} \times \gamma \underline{H}_{eff} \tag{2.1.8}$$

where $\underline{H}_{eff}$ is an effective magnetic field in the z-direction and $\gamma H_{eff} = \omega_o - \omega_r$. It may be assumed that the magnetic field vector $\underline{H}_1$ is along the u-axis of the rotating frame and that $\omega_r \equiv \omega$, cf. Eq. (2.1.3). Under these conditions, the nuclear magnetic dipole precesses about a resultant time-independent magnetic field $\underline{H}$:

$$\underline{H} = H_1\underline{i} + H_{eff}\underline{k}, \tag{2.1.9}$$

as shown in Fig. 2.1b, with an angular frequency Ω given by

$$\Omega = \left[(\omega - \omega_o)^2 + \omega_1^2\right]^{\frac{1}{2}} \tag{2.1.10}$$

The nuclear magnetic resonance condition may now be defined as that corresponding to a maximum time-independent perturbation of the nuclear dipolar motion by the applied magnetic field, $\underline{H}(t)$, this condition being defined by

$$\omega_r \equiv \omega = \omega_o \ . \tag{2.1.11}$$

Thus, ω_o may be referred to as the resonance (Larmor) frequency for an isolated nuclear spin. Also, in accordance with Eqs. (2.1.8, 10, 11):

$$\left(\frac{d\underline{\mu}}{dt}\right)_r = 0 \quad , \quad \Omega = \omega_1 \quad , \quad \theta = \frac{\pi}{2}$$

and thus the condition on ω defining resonance also determines the

steady-state condition for the nuclear system in the rotating frame of reference. That is, under this condition, an initially in-phase relationship between $\underline{\mu}$ and $\underline{H}_1$, corresponding to maximum interaction, is time-independent. At exact resonance, the resultant magnetic field in the rotating reference frame is simply $\underline{H}_1$ and hence the magnetic dipole precesses about the u-axis at the frequency ω_1. In the fixed reference frame, this resonance precessional motion appears as a slow nutation superimposed upon the Larmor precessional motion with a corresponding change in dipole orientation, as defined by the angle β in Fig. 2.1b.

Under steady-state nuclear magnetic resonance conditions, a spectral line of finite width is observed. The effects of contributing magnetic fields at the site of a specific nuclear spin within a given spin system, in the absence of an applied oscillatory magnetic field, may be considered in terms of:

(i) static field inhomogeneity,

(ii) spin-spin relaxation, and

(iii) spin-lattice relaxation.

A local static magnetic field for a given nuclear spin is determined by the molecular electronic environment, giving rise to a basic chemical shift effect, and by the smaller inhomogeneity associated with the applied magnetic field, $\underline{H}_0$. These fields give rise to a resonance frequency distribution and an associated spectral line broadening. The exact form of the inhomogeneity broadening is difficult to define explicitly, but a common assumption made is that the resonance frequency distribution may be described by a Lorentzian lineshape function, $f(\omega)$, of the

general form

$$f(\omega) = A\left[1 + \zeta^2(\omega-\omega_o)^2\right]^{-1} \qquad (2.1.12)$$

where ω is the independent frequency variable and ω_o is the mean resonance frequency for a given spectral line; A is a normalization constant and ζ is a line-width parameter. The characteristic line-width at half-maximum, A/2, is then given simply as $2/\zeta$. An alternative lineshape function is that corresponding to a Gaussian frequency distribution as described by the lineshape function

$$f(\omega) = A\exp\left[-\tfrac{1}{2}\zeta^2(\omega-\omega_o)^2\right] \qquad (2.1.13)$$

with a corresponding line-width $2(2\ell n2)^{1/2}/\zeta$.

The lifetime within a nuclear Zeeman energy level may be considered to be limited due to simultaneous mutually induced transitions between adjacent resonant nuclear spins, these transitions being induced through a time-dependent magnetic dipolar interaction. In accordance with the quantum mechanical uncertainty principle, such a process leads to an effective broadening of the Zeeman energy corresponding to a finite width for the spectral line associated with the induced transitions, this lifetime broadening being described by a Lorentzian lineshape function. A characteristic spin-spin relaxation time, T_{2o}, may then be defined to describe this line-width in accordance with Eq. (2.1.12), with $\zeta = T_{2o}$. T_{2o} is normally referred to as the natural transverse spin relaxation time. It should be noted that, in more general terms, a characteristic time defined in this manner effectively describes the time-dependent phase relationships

between precessing resonant nuclear spins within a given spin system. Thus the concept of a generalized transverse spin relaxation time is a versatile means of describing many relaxation processes giving rise to spin dephasing effects. In contrast to spin-spin relaxation processes showing a conservation of energy within a spin system, spin-lattice relaxation processes involve a net transfer of energy between the spin system and its lattice environment to maintain thermal equilibrium conditions for the complete spin-lattice system. Also, due to the interaction between the spin system and its lattice environment, fluctuating environmental magnetic fields may induce transitions between nuclear Zeeman energy levels leading to an additional spectral line broadening which may be described by a spin-lattice relaxation time, T_1.

Under the assumption that the complete resonance spectral lineshape is described by a Lorentzian function, a total transverse spin relaxation time, T_2, may be defined by

$$\frac{1}{T_2} = \frac{1}{T_{20}} + \frac{1}{T_2^*} + \frac{1}{T_1} + \frac{1}{\zeta} \qquad (2.1.14)$$

where T_2^* and ζ are relaxation times describing $\underline{H}_0$ field inhomogeneities and additional transverse spin relaxation processes, respectively. In the study of liquid systems, motional averaging determines a general condition:

$$\frac{1}{T_1} \approx \frac{1}{T_{20}} \qquad (2.1.15)$$

in the absence of spin-lattice relaxation mechanisms due to paramagnetic species and nuclear quadrupolar interactions.

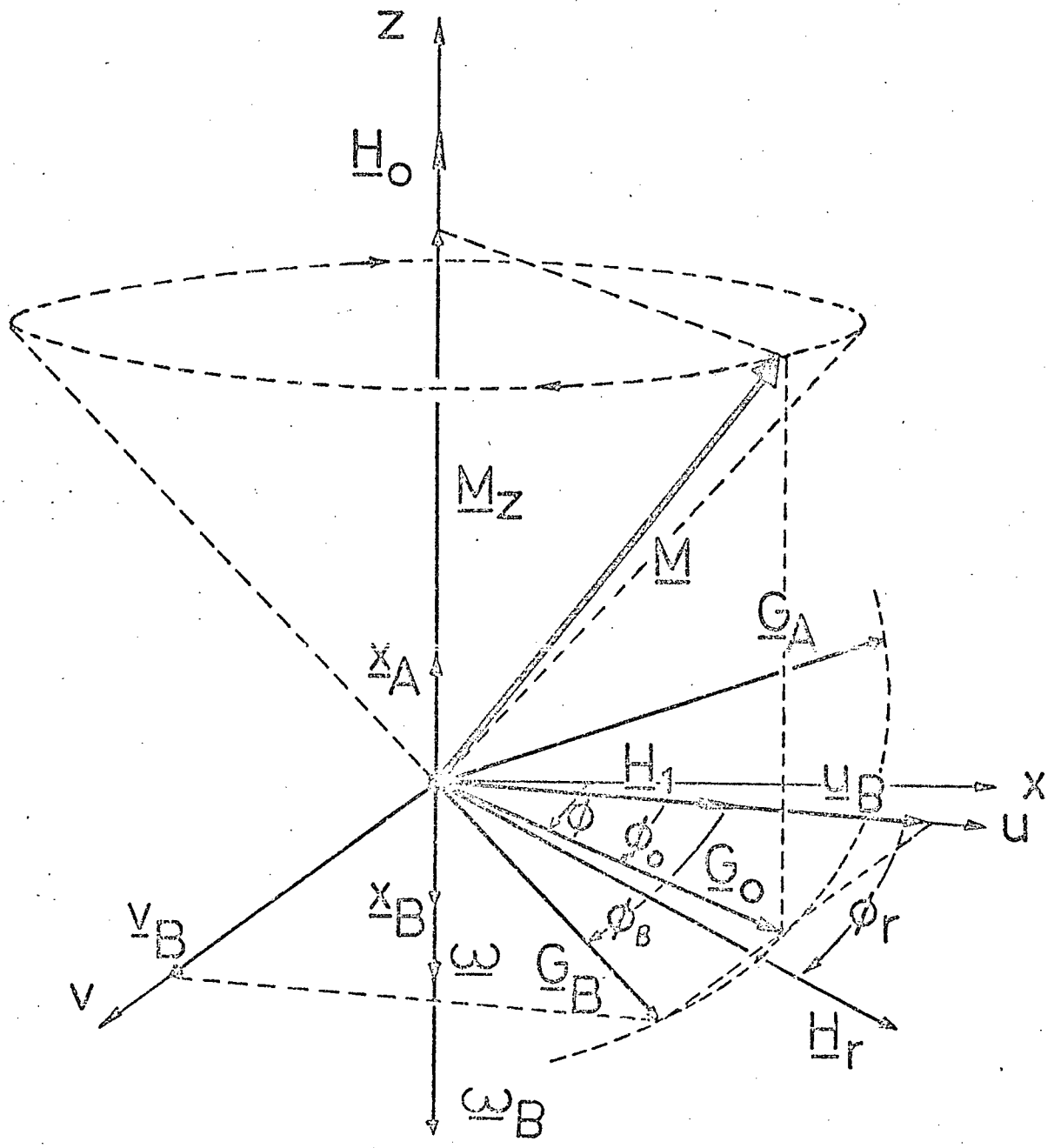

Fig. 2.2 Nuclear spin isochromats in the rotating frame of reference with $\omega_A < \omega_0 < \omega < \omega_B$

To allow a direct application of the semi-classical concepts outlined above, it is now considered that a macroscopic nuclear spin isochromat[2,29], $\underline{M}(\omega_o, \phi)$, may be defined as the resultant magnetization due to all spins having a resonance frequency ω_o and an associated time-dependent phase angle ϕ. In this manner, the resonance frequency distribution for a given spectral line is simply related to the properties of a macroscopic nuclear spin system. The equation of motion for such an isochromat in the rotating frame of reference with an angular frequency ω (corresponding to that of the applied oscillatory magnetic field $\underline{H}(t)$) is given in accordance with Eqs. (2.1.8) and (2.1.9) as

$$\frac{d}{dt}\underline{M}(x,\phi) = \gamma\left[\underline{M}(x,\phi) \times \underline{H}\right] - \frac{1}{T_2}u\,\underline{i} - \frac{1}{T_2}V\,\underline{j} - \frac{1}{T_1}(M_z - M_o)\,\underline{k} \qquad (2.1.16)$$

where u, V, M_z have been defined as the Cartesian components of the isochromat $\underline{M}(x, \phi)$, as shown in Fig. 2.2, and x is now the independent variable defined as $x = \omega - \omega_o$, while M_o is the thermal equilibrium value of M_z. The total effective magnetic field $\underline{H}$ appearing in this equation is $\underline{H} = H_1\underline{i} + (x/\gamma)\underline{k}$, cf. Eq. (2.1.9). It should be noted that the variable x has been defined on the interval $-\infty < x < \infty$ such that $x > 0$ corresponds to $\omega > \omega_o$. From Eq. (2.1.16), the component equations of motion are given as

$$\begin{aligned}
\frac{du}{dt} + \frac{1}{T_2}u - xV &= 0 \\
\frac{dV}{dt} - xu + \frac{1}{T_2}V &= -\omega_1 M_z \\
\frac{dM_z}{dt} - \omega_1 M_z &= -\frac{1}{T_1}(M_z - M_o)
\end{aligned} \qquad (2.1.17)$$

where $\omega_1 = \gamma H_1$, cf. Eq. (2.1.4). These equations form the basis for the formulation of nuclear spin transfer effects in the following section.

2.2 Modified Bloch Equations.

Nuclear spin transfer effects in an uncoupled AB spin system will be considered initially in terms of stochastic principles to develop a simple physical model for such effects. The steady-state NMR spectrum for this spin system may be represented as shown below:

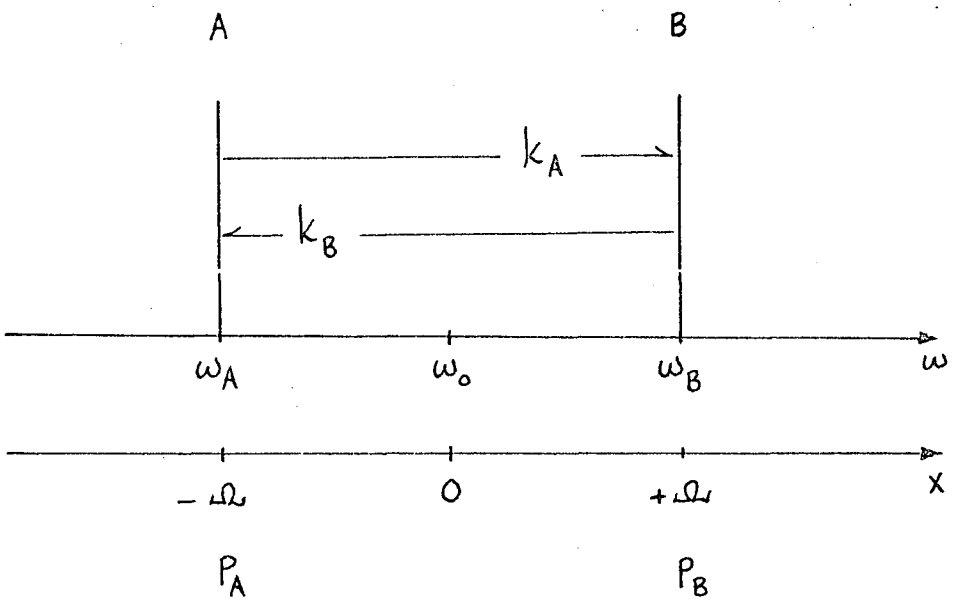

Site-A, associated with a distinct electronic magnetic environment and chemical shift, may be considered in terms of a mean spin isochromat, $\underline{M}_A$, with a resonance frequency $x_A = -\Omega$ relative to the average frequency ω_o:

$$\omega_o = \tfrac{1}{2}(\omega_A + \omega_B) \quad , \quad \omega_A = \omega_o - \Omega, \tag{2.2.1}$$

in the normal rotating frame of reference. At any given time, the fractional population of nuclear spins associated with site-A, p_A, defines the magnitude of the spin isochromat $\underline{M}_A$. In the absence of spin transfer effects, $\underline{M}_A$ and $\underline{M}_B$ precess independently in the applied magnetic field $\underline{H}_o$.

Due to a reversible molecular process (such as a hindered rotation) described by first-order rate constants k_A and k_B, a resonant nuclear spin may be considered to be transferred between the sites A and B in a random statistical manner. The basic assumptions made in describing this transfer process are as follows:

(i) all spins remain in site-A with a mean lifetime τ_A until an instantaneous transfer takes place into site-B. Precessional effects in the transfer interval are neglected and as transfer into a site of the same type has no observable effect on the spin system, only transfer into a different site is considered;

(ii) for any spin in site-A, there is a constant probability k_A per unit time for transfer into site-B, this probability being inversely proportional to the fractional population p_A;

(iii) the lifetime τ_A is independent of the associated spin relaxation times T_{1A} and T_{2A};

(iv) nuclear spin isochromats relax independently except for spin transfer effects.

Under these assumptions, the site lifetime τ_A and the corresponding rate constant k_A are simply related by

$$k_A = \tau_A^{-1}, \tag{2.2.2}$$

and in accordance with the principle of detailed balance[81]

$$p_A k_A = p_B k_B \tag{2.2.3}$$

with

$$p_A + p_B = 1.$$

As the observed NMR signal is due to the transverse component of the nuclear magnetization (and for analytic simplicity) a complex transverse magnetization for site-A, G_A, is defined in the rotating frame of reference by

$$G_A = |u_A + iV_A|, \tag{2.2.4}$$

as shown in Fig. 2.2. The Bloch equations for the spin isochromat M_A may now be expressed in complex form in accordance with Eqs. (2.1.16) and (2.1.17) as

$$\begin{aligned} \frac{d}{dt} G_A + (\epsilon_A + i\omega) G_A &= -i\omega_1 M_{zA} \\ \frac{d}{dt} M_{zA} - i\omega_1 V_A &= -\frac{1}{T_1}(M_{zA} - M_{oA}) \end{aligned} \tag{2.2.5}$$

where $\epsilon_A = \frac{1}{T_{2A}} - i\omega_A$ and $\omega_A = \omega_o - \Omega$. Assuming negligible saturation and quasi-steady-state conditions: $\omega_1 \to 0$, $M_{zA} \to M_{oA}$, and Eq. (2.2.5) reduces to

$$\frac{d}{dt} G_A + (\epsilon_A + i\omega) G_A = -i\omega_1 p_A M_o \tag{2.2.6}$$

with $M_{oA} = p_A M_o$, and M_o the thermal equilibrium z-component magnetization for the complete nuclear spin system. A similar equation applies to the site-B magnetization, so that for the complete spin system:

$$G = G_A + G_B. \tag{2.2.7}$$

Following McConnell[6], the time-dependence of the transverse magnetization $\underline{G}_A$ due to nuclear spin transfer processes may now be described by:

$$\frac{d}{dt}G_A = -k_A G_A + k_B G_B \qquad (2.2.8)$$

such that $-k_A G_A$ defines the rate of transfer of transverse magnetization from site-A and k_A is the first-order rate constant for this transfer. The time-dependence is incorporated into the normal Bloch equations, Eqs. (2.2.6), to give a modified equation of motion for site-A magnetization:

$$\frac{d}{dt}G_A + (\alpha_A + i\omega)G_A - k_B G_B = -i\omega_1 M_o P_A \quad ,$$

and a coupled equation for site-B magnetization

$$\frac{d}{dt}G_B + (\alpha_B + i\omega)G_B - k_A G_A = -i\omega_1 M_o P_B \quad , \qquad (2.2.9)$$

with $\alpha_A = \frac{1}{T_{2A}} + k_A - i\omega_A$, cf. Eq. (2.2.5). Assuming the total transverse relaxation time, T_2, as defined in the absence of spin transfer processes, to be site independent, it follows that

$$\alpha_A + i\omega \equiv r_A + i(x + \Omega), \quad x = \omega - \omega_o \qquad (2.2.10)$$

with $r_A = \frac{1}{T_2} + k_A$. These modified Bloch equations may now be expressed in the matrix form

$$-\frac{d}{dt}\underline{G} = \underline{\underline{R}}.\underline{G} + i\omega_1 M_o \underline{P} \qquad (2.2.11)$$

The term $i\omega_1 M_o \underline{P}$ may be referred to as a driving term, as in the absence of an applied oscillatory magnetic field: $\omega_1 = 0$. Under steady-state conditions, $(d\underline{G}/dt) = 0$, and it follows from Eq. (2.2.11) that

$$\underline{\underline{R}}\cdot\underline{G} = -i\omega_1 M_o \underline{P}, \qquad (2.2.12)$$

or explicitly,

$$\begin{bmatrix} r_A + i(x+\Delta\Omega) & -k_B \\ -k_A & r_B + i(x-\Delta\Omega) \end{bmatrix} \begin{bmatrix} G_A \\ G_B \end{bmatrix} = -i\omega_1 M_o \begin{bmatrix} P_A \\ P_B \end{bmatrix}$$

The total complex transverse magnetization may now be derived from Eq. (2.2.12) as a function of the independent variable x:

$$G(x) = -i\omega_1 M_o \left\{ \frac{\left(\frac{1}{T_2}+k\right) + i\left(x + [1-2P_A]\Delta\Omega\right)}{B+iC} \right\}$$

where

$$B = \frac{1}{T_2}\left(\frac{1}{T_2}+2k\right) + \Delta\Omega^2 - x^2$$

$$C = 2\left[x\left(\frac{1}{T_2}+k\right) - (1-2P_A)k\Delta\Omega\right]$$

and

$$k = \frac{1}{2}(k_A+k_B) \quad , \quad x = \omega - \omega_o \qquad (2.2.13)$$

The NMR absorption mode corresponds to the component transverse nuclear magnetization in quadrature phase with the applied oscillatory magnetic field vector, $\underline{H}_1$, as shown in Fig. 2.2. Thus the absorption mode lineshape, V(x), is given in accordance with Eq. (2.2.13) as the imaginary part of G(x), viz.,

$$V(x) = -\omega_1 M_o \left\{ \frac{\left(\frac{1}{T_2}+2k\right).B + \left(x + [1-2P_A]\Delta\Omega\right).C}{B^2+C^2} \right\} \qquad (2.2.14)$$

This lineshape function applies to a general-population two-site uncoupled AB nuclear spin transfer system under normal steady-state NMR conditions. The term $\omega_1 M_o$ expresses the linear dependence of signal

amplitude upon the magnitude of $\underline{H}_1$, in the absence of saturation effects, and may be considered as a normalization factor.

The two-site equal population system ($p_A = p_B = 0.5$) is of considerable chemical interest, and in accordance with Eq. (2.2.14), the lineshape function V(x) takes the simplified form

$$V(x) = A\left\{\frac{(\frac{1}{T_2}+2k).B + x.C}{B^2+C^2}\right\} \qquad (2.2.15)$$

where

$$B = \frac{1}{T_2}\left(\frac{1}{T_2}+2k\right) + \Omega^2 - x^2$$

$$C = 2x\left(\frac{1}{T_2}+k\right)$$

and A is the normalization constant. From Eq. (2.2.15), the positions of the function V(x) maxima are determined as

$$x' = \pm(\Omega^2 - 2k^2)^{\frac{1}{2}} \qquad \text{rad. sec.}^{-1} \qquad (2.2.16)$$

For $k << \Omega$, $x' = \pm \Omega$, and in this limit of very slow spin transfer, the NMR spectrum consists of two spectral lines separated by the chemical shift 2Ω. As the rate of spin transfer increases, x' decreases and thus a condition for spectral line coalescence may be defined as

$$x' = 0 \text{ and } \sqrt{2}\ k = \Omega. \qquad (2.2.17)$$

It is now convenient to consider general nuclear spin transfer effects in terms of

(i) slow spin transfer: $k < 0.2\ \Omega$,

(ii) intermediate spin transfer: $k \simeq \Omega$,

(iii) fast spin transfer: $k > 5\ \Omega$.

The exchange lineshapes for a representative equal population system,

as given in accordance with Eq. (2.2.15), are shown in Fig. 2.3 for a range of values of the characteristic parameter k/Ω. For clarity, these lineshapes have been normalized, through the constant A, to an arbitrary maximum independent of k. It is important to note that the chemical shift between sites in the absence of exchange, 2Ω, defines the overall range of the rate constant k that may be determined from NMR lineshape analyses. Also, the general population absorption mode lineshape derived for the two-site exchange system, Eq. (2.2.14), is consistent with that given by Gutowsky and Holm[82].

The validity of the phenomenological Bloch equations has been considered in detail[20] and, under the assumptions outlined above, modified Bloch equations may be extended to describe nuclear spin transfer effects in a general first-order NMR exchange system. A matrix formulation for an n-site system, based upon the equations of motion derived above for the simple two-site exchange system, allows a concise description of general transfer effects and also leads to expressions which are readily adapted to efficient computer calculations.

Initially, it is assumed that exchange processes modulate all frequency differences, $|\omega_i - \omega_j|$, associated with n distinct sites of differing Larmor frequency, ω_i. Again following McConnell[6], a transfer of nuclear magnetization may be described for the ξ-mode in the form

$$\frac{d}{dt}\varrho_i = \sum_{\substack{j=1 \\ j\neq i}}^{n} \left[k_{ji}\varrho_j - k_{ij}\varrho_i \right] \qquad (2.2.18)$$

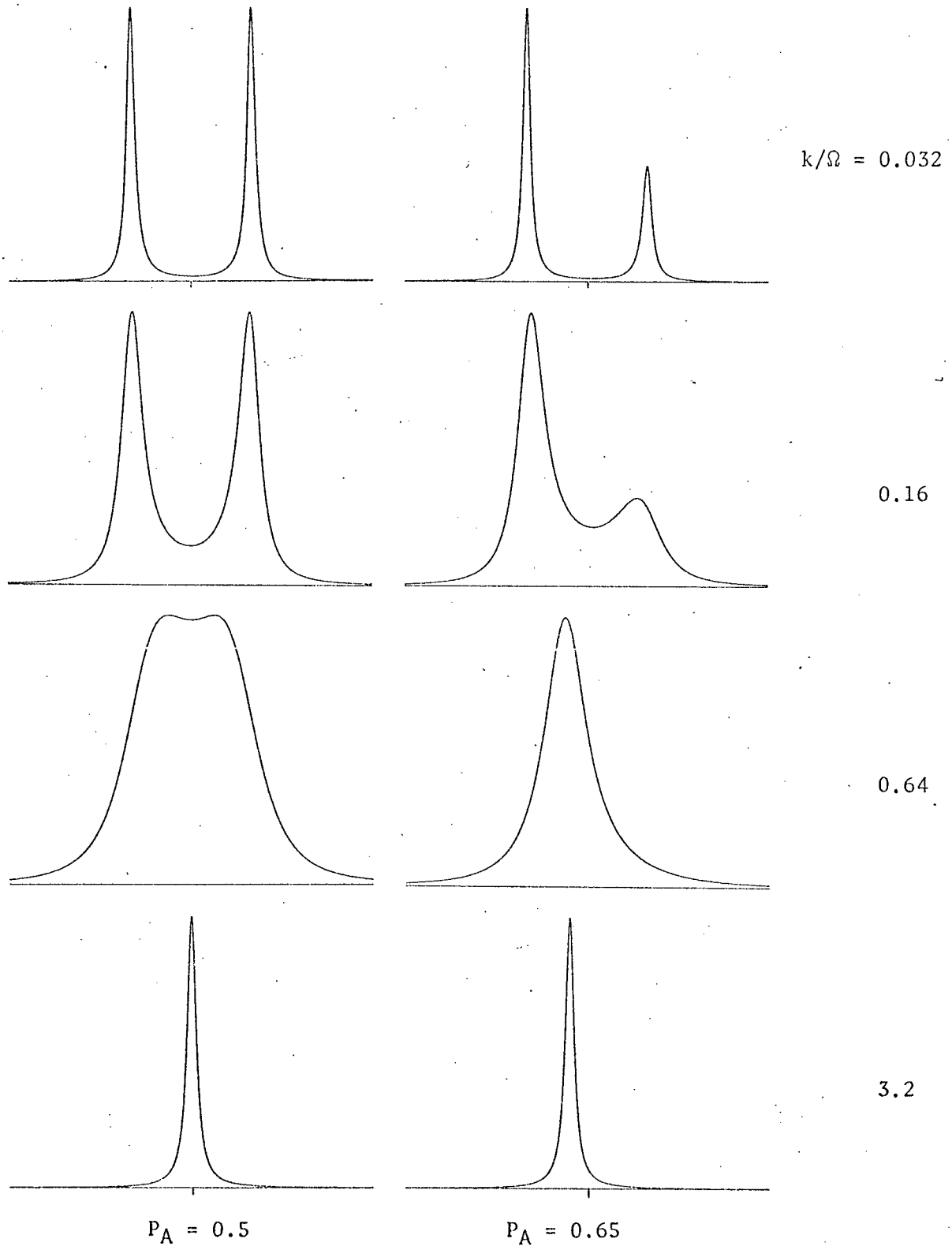

Figure 2.3 Two-site exchange absorption mode lineshapes

cf. Eq. (2.2.8). The indices refer to site and the double indices refer to first order transfer rate constants between sites such that $k_{ij}\xi_i$ represents the rate of transfer of ξ-mode magnetization <u>from</u> site i <u>to</u> site j. This form of notation is important in defining matrix elements for a multi-site exchange process. The time-dependence of the u-mode magnetization associated with site-i may now be expressed in the Bloch form

$$\frac{d}{dt}u_i = -\left[\frac{1}{T_{2i}} - \sum_{j\neq i} k_{ij}\right]u_i + \sum_{j\neq i} k_{ji}u_j + w_i v_i \qquad (2.2.19)$$

with $w_i = \omega - \omega_i$. As usual, ω is the angular frequency of the oscillatory radio frequency field defining the normal rotating frame of reference; ω_i is defined as the site-i resonance frequency, and T_{2i} is the corresponding spin-spin relaxation time including a contribution from magnetic field inhomogeneity. The total u-mode magnetization for the system is then given by $u = \Sigma u_i$, the site magnetization isochromats being independent except for transfer effects. Considering this magnetization as a column vector, $\underline{u}$, Eq. (2.2.19) may be expressed in matrix form to include all sites, viz.,

$$\frac{d}{dt}\underline{u} + \underline{\underline{R}}_2 \cdot \underline{u} - \underline{\underline{w}} \cdot \underline{v} = 0 \quad , \qquad (2.2.20)$$

with $\underline{\underline{R}}_2 = \underline{\underline{T}}_2 + \underline{\underline{K}}$, where $\underline{\underline{T}}_2$ is a diagonal n x n matrix with general element T_{2i} and $\underline{\underline{K}}$ is the transfer rate matrix, n x n, with elements

$$K_{ii} = \sum_{j\neq i} k_{ij} \quad \text{and} \quad K_{ij} = -k_{ji}\,, \; j\neq i \qquad (2.2.21)$$

Similarly, $\underline{\underline{w}}$ is a diagonal frequency deviation matrix, n x n with elements w_i and $\underline{V}$ is the v-mode magnetization vector with elements V_i. The off-diagonal elements of the rate matrix $\underline{\underline{K}}$ are individual first order rate constants for each pair of sites, and the diagonal elements are the sums of rate constants from each site-i. Thus, the diagonal elements represent the overall rate processes for n sites. Also, any column has a zero sum, consistent with detailed balance of rate processes,

$$K_{ii} + \sum_{j \neq i} K_{ji} = 0$$

Similar matrix equations can be written for the v- and z-mode magnetization transfers involved in a chemical exchange process:

$$\frac{d}{dt}\underline{V} + \underline{\underline{R}}_2 \cdot \underline{V} + \underline{\underline{w}} \cdot \underline{u} = -\omega_1 \underline{M}_z$$

$$\frac{d}{dt}\underline{M}_z + \underline{\underline{R}}_1 \cdot \underline{M}_z - \omega_1 \underline{V} = M_o \underline{\underline{T}}_1 \cdot \underline{P}$$

(2.2.22)

where $\omega_1 = \gamma H_1$, $\underline{\underline{R}}_1 = \underline{\underline{T}}_1 + \underline{\underline{K}}$ with $\underline{\underline{T}}_1$ a diagonal spin-lattice relaxation matrix, n x n with elements T_{1i}, T_{1i} being the spin-lattice relaxation time for site-i; $\underline{P}$ is a column vector of the fractional population for each site such that $\sum_{i=1}^{n} p_i = 1$ and $M_{oi} = M_o p_i$ where M_o is the thermal equilibrium value for the z-mode magnetization in site-i. Solving the coupled matrix equations (2.2.20), (2.2.22), the steady-state V-mode magnetization is given explicitly by

$$\underline{V} = -\omega_1 M_o \, \underline{\underline{C}}^{-1} \cdot \underline{\underline{\varepsilon}}_2 \cdot \underline{\underline{\varepsilon}}_1 \cdot \underline{\underline{T}}_1 \cdot \underline{P} \qquad (2.2.23)$$

with

$$\underline{\underline{C}} = \underline{\underline{I}} + \omega_1^2 \underline{\underline{\varepsilon}}_2 \cdot \underline{\underline{\varepsilon}}_1 + \underline{\underline{\varepsilon}}_2 \cdot \underline{\underline{W}} \cdot \underline{\underline{\varepsilon}}_2 \cdot \underline{\underline{W}}$$

Here $\underline{\underline{I}}$ is the unit n x n matrix and $\underline{\underline{\varepsilon}}_1$ and $\underline{\underline{\varepsilon}}_2$ are the inverse matrices corresponding to $\underline{\underline{R}}_1$ and $\underline{\underline{R}}_2$, respectively.

For an arbitrary reference frequency ω_o, the independent frequency variable x may be defined as $x = \omega - \omega_o$ such that for site i

$$\begin{aligned} w_i &= x - \Omega_i \\ \Omega_i &= \omega_i - \omega_o \end{aligned} \qquad (2.2.24)$$

where Ω_i is the chemical shift with respect to ω_o. The vector $\underline{V}$ now defines the steady-state NMR absorption mode spectrum as a function of x, viz.,

$$V(x) = \sum_{i=1}^{n} V_i(x) = \underline{I} \cdot \underline{V} \qquad (2.2.25)$$

The elements of the matrix $\underline{\underline{W}}$ in Eq. (2.2.23) are now defined by Eq. (2.2.24) and $\underline{I}$ is the row vector with each of n elements equal to unity.

The corresponding matrix equations for the steady-state u- and z-mode magnetizations are now given in terms of $\underline{V}$ as

$$\begin{aligned} \underline{U} &= \underline{\underline{\varepsilon}}_2 \cdot \underline{\underline{W}} \cdot \underline{V} \\ \underline{M}_z &= M_o \underline{\underline{\varepsilon}}_1 \cdot \underline{\underline{T}}_1 \cdot \underline{P} + \omega_1 \underline{\underline{\varepsilon}}_1 \cdot \underline{V} \end{aligned} \qquad (2.2.26)$$

This formulation allows a compact and versatile description of general nuclear magnetization transfer effects in a first-order NMR spectrum, including those associated with spin-lattice relaxation[46,48] and nuclear spin transfer saturation.

2.3 Saturation Effects.

Under normal steady-state conditions, a saturation factor S' may be defined for a given NMR spectral line in the form

$$S' = \frac{1}{1 + \omega_1^2 T_1 T_2} \quad , \quad 0 < S' \leq 1$$

Now, since in the presence of chemical exchange saturation effects are described through the matrix C in Eq. (2.2.23) and, in particular, are contained in that part defined as

$$\underline{\underline{S}}' = \underline{\underline{I}} + \omega_1^2 \, \underline{\underline{\varepsilon}}_2 \cdot \underline{\underline{\varepsilon}}_1 \quad , \qquad (2.3.1)$$

it is convenient to replace ω_1^2 by an equivalent parameter β defined in terms of an average saturation factor S' as

$$\beta = \frac{(1 - S')}{S'} \left\langle \frac{1}{T_1 T_2} \right\rangle$$

where the part defined in terms of the relaxation times T_1 and T_2 is an average value for all sites. In this way, Eq. (2.3.1) is written in the form

$$\underline{\underline{S}}' = \underline{\underline{I}} + \beta \, \underline{\underline{\varepsilon}}_2 \cdot \underline{\underline{\varepsilon}}_1 \quad . \qquad (2.3.2)$$

A complete analysis of saturation effects would include the interrelationship with the deviation from steady-state conditions[83]. Under normal experimental conditions, however, locked-field spectrometers allow a very good approximation to the required slow passage conditions and the above formulation is adequate.

The effects of saturation on the NMR absorption mode lineshape have been studied for a particular two-site (A- and B-sites) chemical exchange system described by the spectral parameters: $p_A = 0.5$, $2\Omega = |\Omega_A - \Omega_B| = 10.0$ Hz and $T_{2A} = T_{2B} = 0.64$ sec. Also, as is usual for liquid systems, it is assumed that $T_{1A} = T_{2A}$. The spin-spin relaxation time, T_{2A}, chosen corresponds to a Lorentzian full width at half-maximum of 0.5 Hz and 2Ω is the chemical shift between sites in the absence of exchange, cf. Eq. (2.2.24). By means of an iterative numerical analysis, using Eqs. (2.2.23) and (2.2.25), values of the saturation parameters β and S' were determined corresponding to a prescribed mean deviation of the lineshape function, $V(x)$, from that for the reference limit of zero saturation ($\beta = 0$). A mean percentage deviation, ΔV, was defined for N data points as

$$\Delta V = \frac{1}{N} \sum_{i=1}^{N} \left[\left(V_i^r(x) - V_i(x) \right) / V_i^r(x) \right] . 100$$

in which $V_i^r(x)$ and $V_i(x)$ are the reference and saturated lineshape function values, respectively, corresponding to the frequency value x_i. The results of such an analysis are shown in Fig. 2.4 for $\Delta V = 2\%$ and 5% as plots of β and S' as a function of $\log_{10}(k/2\Omega)$.

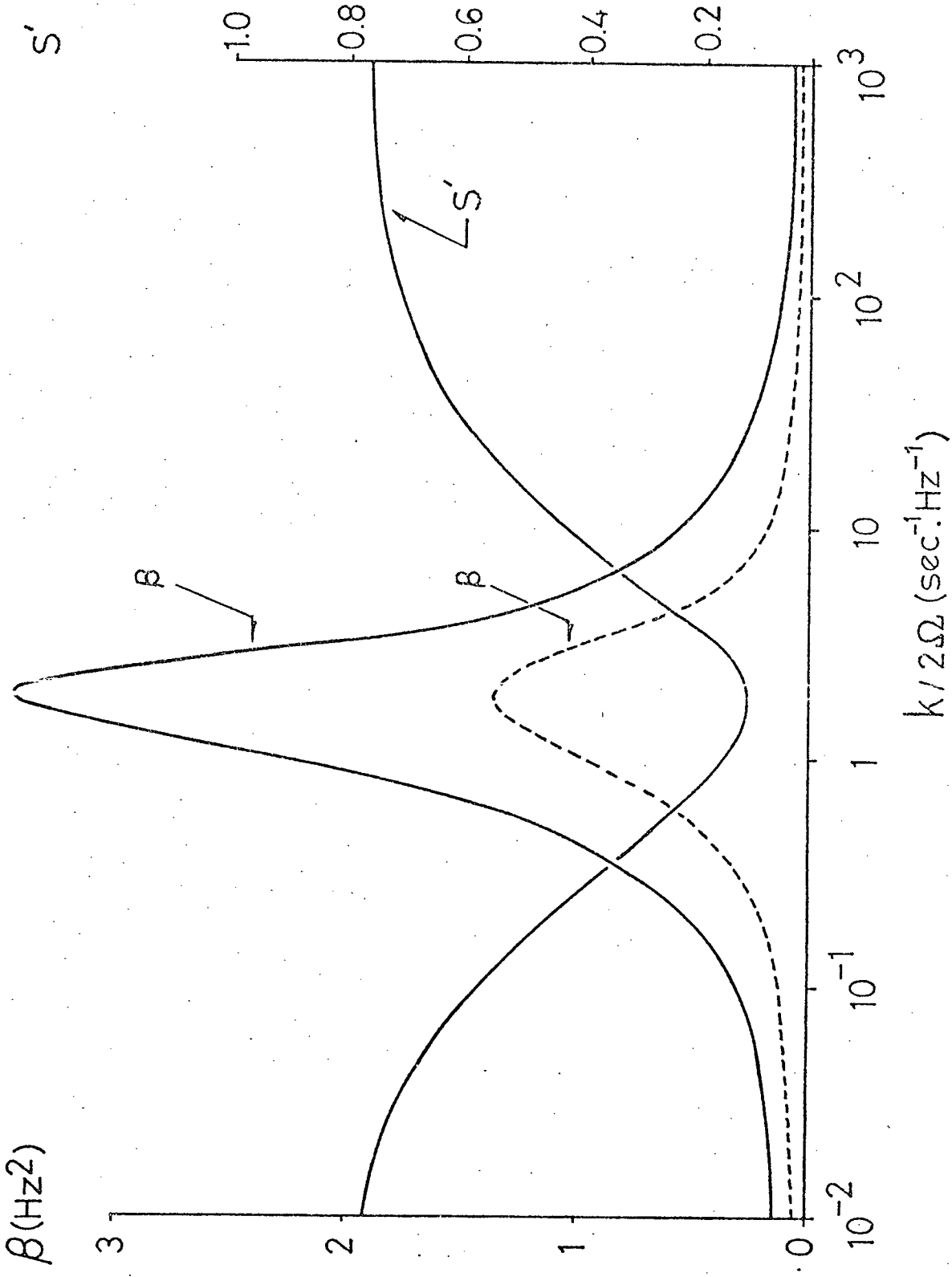

Figure 2.4 Saturation parameters for two-site chemical exchange system.

It is seen that saturation effects for a fixed magnitude of the irradiation rf magnetic field, $2H_1$, are most severe in the limits of very slow ($k << \Omega$) and very fast ($k >> \Omega$) exchange corresponding to spectral lines of minimal width (0.5 Hz). For a mean deviation $\Delta V = 5\%$ the values of H_1 for $k/2\Omega = 0.01$ and 1.0 are computed for ^1H NMR ($\gamma_H = 2.7 \times 10^4$ rads sec^{-1} $gauss^{-1}$) to be 0.56×10^{-2} and 9.4×10^{-2} mgauss, respectively. These fields correspond to a spectral frequency distribution of only 0.002 and 0.04 Hz. However, Grunwald et al.[84] have shown experimentally that H_1 fields an order of magnitude greater than those calculated above give negligible distortion due to saturation for chemical exchange systems. This implies that, in actual fact a complicated combination of steady-state passage conditions and rf power levels (H_1) determine observed saturation effects. As H_1 is increased, saturation gives rise to a general broadening of spectral lines and leads to an increased apparent first-order rate constant, k. A 5% deviation as considered above may lead to an error in a fitted k value of 5-10%. However, an irradiation field in the intermediate exchange region ($k \simeq \Omega$) with a magnitude approximately twenty times greater than that causing distortion in the slow exchange region ($k << \Omega$) is still acceptable (see Fig. 2.4). In the intermediate exchange region, the spectral lines are of maximal width ($\simeq \Omega$ rad. $sec.^{-1}$) and hence minimal intensity. Strictly, a spectral line intensity is linearly proportional to H_1 only in the absence of saturation effects, but it is seen that the intensity and hence signal-to-noise ratio of a recorded lineshape may be increased to levels acceptable for the measurement of reliable

data for lineshape fitting without adverse distortion due to saturation, by increasing H_1 following an experimental linearity check for negligible saturation in the slow exchange limit. Relative H_1 field strengths corresponding to negligible saturation distortion may then be estimated over a complete range of the characteristic parameter $k/2\Omega$ from Fig. 2.4, and hence reliable spectra for complete lineshape fitting may be obtained, in effect, in the limit of zero saturation.

2.4 Zero Saturation Limit.

For a general first-order NMR n-site exchange system, the zero saturation limit may be defined by $\omega_1 \to 0$ ($\omega_1 = \gamma H_1$) and thus the modified Bloch equation describing the steady-state z-mode magnetization is given in matrix form in accordance with Eq. (2.2.22) as

$$\underline{M}_z = M_o \underline{\underline{\varepsilon}}_1 . \underline{\underline{T}}_1 . \underline{P}$$

with $\underline{\underline{\varepsilon}}_1$ the inverse of the matrix $\underline{\underline{R}}_1$. In the absence of chemical exchange, $\underline{\underline{R}}_1 = \underline{\underline{T}}_1$, and hence $\underline{M}_z = M_o \underline{P}$. That is, the z-mode magnetization in each site is directly proportional to the site fractional population, p_j, and is independent of spin-lattice relaxation effects. This condition is shown to be valid also in the presence of chemical exchange for all exchange rates and is considered in detail for a general two-site system at a later point.

The modified Bloch equations describing chemical exchange in the limit of zero saturation reduce to two coupled matrix equations given in accordance with Eqs. (2.2.20) and (2.2.22) :

$$\frac{d}{dt}\underline{u} + \underline{\underline{R}}_2 \cdot \underline{u} - \underline{\underline{W}} \cdot \underline{V} = 0$$

$$\frac{d}{dt}\underline{V} + \underline{\underline{R}}_2 \cdot \underline{V} + \underline{\underline{W}} \cdot \underline{u} = -\omega_1 M_0 \underline{P} \qquad (2.4.1)$$

from which the steady-state v-mode magnetization is given explicitly by

$$\underline{V} = -\omega_1 M_0 \underline{\underline{C}}^{-1} \cdot \underline{P} \qquad (2.4.2)$$

with

$$\underline{\underline{C}} = \underline{\underline{R}}_2 + \underline{\underline{W}} \cdot \underline{\underline{\varepsilon}}_2 \cdot \underline{\underline{W}}$$

Again, the steady-state NMR absorption mode spectrum is determined by V(x) as defined in Eq. (2.2.25). In the limit of zero saturation, Eq. (2.4.2) shows that the NMR absorption intensity is linearly related to the effective magnitude of the irradiating rf magnetic field, H_1, and is independent of spin-lattice relaxation effects for all chemical exchange rates. Within the limits discussed in the preceding section, this is the expression defining the lineshape function V(x) normally used in the analysis of steady-state NMR data.

Although the absorption mode lineshape function, V(x), is given explicitly by Eq. (2.4.2) in terms of the real matrix $\underline{\underline{C}}$, the independent variable x is contained in the frequency deviation matrix $\underline{\underline{W}}$ and hence an evaluation of V(x) over a specified frequency range requires an inversion of the matrix $\underline{\underline{C}}$ for each value of x. An alternative formulation in the limit of zero saturation based upon Eq. (2.4.1) allows a much simplified calculation of V(x). A complex transverse magnetization, $\underline{G}$, may be defined for an n-site exchange system in

vector form as

$$\underline{G} = \underline{u} + i\underline{V} \ , \tag{2.4.3}$$

where the component V_j describes the v-mode magnetization associated with the j-site. From Eq. (2.4.1), the steady-state transverse magnetization is now given by

$$\underline{\underline{G}} = -i\omega_1 M_0 \left[\underline{\underline{R}}_2 + i\underline{\underline{W}} \right]^{-1} \cdot \underline{P}$$

and the corresponding complex lineshape function G(x) follows as

$$G(x) = -i\omega_1 M_0 \, \underline{I} \cdot \left[\underline{\underline{R}}_2 + i\underline{\underline{W}} \right]^{-1} \cdot \underline{P} \tag{2.4.4}$$

where $\underline{I}$ is as defined previously, cf. Eq. (2.2.25). The absorption mode lineshape function, V(x), is simply the imaginary part of G(x). The independent variable x appears now only in the diagonal matrix $\underline{\underline{W}}$, and thus it is possible to transform the matrix $[\underline{\underline{R}}_2 + i\underline{\underline{W}}]$ into a completely diagonal form hence allowing a ready evaluation of G(x) following a single matrix diagonalization. Now consider the matrix $\underline{\underline{R}}$ defined by

$$\underline{\underline{R}} \equiv \underline{\underline{T}}_2 + \underline{\underline{K}} - i\underline{\underline{\Omega}} \tag{2.4.5}$$

and related to $\underline{\underline{R}}_2$ by $[\underline{\underline{R}}_2 + i\underline{\underline{W}}] = \underline{\underline{R}} + ix\underline{I}$. In these equations, $\underline{\underline{\Omega}}$ is a n x n diagonal matrix with elements Ω_j, the chemical shift for the j-site, Eq. (2.2.24), and $\underline{I}$ is the unit n x n matrix. In terms of the diagonalized matrix $\underline{\underline{\Lambda}}$ corresponding to $\underline{\underline{R}}$, Eq. (2.4.4) may be expressed in the form

$$G(x) = -i\omega_1 M_0 \, \underline{I} \cdot \underline{\underline{S}} \cdot \left[\underline{\underline{\Lambda}} + ix\underline{I} \right]^{-1} \cdot \underline{\underline{S}}^{-1} \cdot \underline{P} \tag{2.4.6}$$

where $\underline{\underline{S}}$ is the matrix which diagonalizes $\underline{\underline{R}}$, viz.,

$$\underline{\underline{\Lambda}} = \underline{\underline{S}}^{-1} \cdot \underline{\underline{R}} \cdot \underline{\underline{S}} \tag{2.4.7}$$

Following this transformation, the evaluation of inverse matrix elements is reduced to the determination of reciprocal diagonal elements of the matrix $\underline{\underline{\Lambda}} + ix\underline{\underline{I}}$, and the complex function G(x) is defined in component form by

$$G(x) = -i\omega_1 M_0 \sum_{j=1}^{n} I_j \sum_{k=1}^{n} \sum_{l=1}^{n} S_{jl} (S^{-1})_{lk} P_k / (\lambda_l + ix) \tag{2.4.8}$$

where λ_l is the l-th diagonal element of the matrix $\underline{\underline{\Lambda}}$. S_{jl} and $(S^{-1})_{jl}$ are the jl-th elements of the transformation matrices $\underline{\underline{S}}$ and $\underline{\underline{S}}^{-1}$, respectively. As the matrix elements involved are all complex, the computation of each spectral data point defined by G(x) requires a number of operations in complex arithmetic on a digital computer. These operations are relatively slow and hence the absorption mode lineshape function, V(x), is finally given in terms of operations in real arithmetic only by defining a matrix $\underline{\underline{B}}$ as the real part of the matrix $\underline{\underline{S}} \cdot \left[\underline{\underline{\Lambda}} + ix\underline{\underline{I}}\right]^{-1} \cdot \underline{\underline{S}}^{-1}$. That is, in accordance with Eq. (2.4.6),

$$V(x) = A\ \underline{I} \cdot \underline{\underline{B}} \cdot \underline{P},$$

in which A is a normalization constant, and the matrix elements B_{jk} are given by

$$B_{jk} = \sum_{l=1}^{n} \left\{ a_{jkl} \lambda_l^R + b_{jkl} \left[\lambda_l^I + ix \right] \right\} / d_l$$

where a_{jkl} and b_{jkl} (and λ_l^R and λ_l^I) are the real and imaginary parts

of $S_j \cdot (S^{-1})_k$ (and λ), respectively; d is defined in terms of the independent variable x as

$$d_\ell = (\lambda_\ell^R)^2 + (\lambda_\ell^I + x)^2$$

Analogous to Eq. (2.4.8), V(x) is now given as

$$V(x) = A \sum_{j=1}^{n} I_j \sum_{k=1}^{n} B_{jk} p_k \quad . \tag{2.4.9}$$

A computer program based upon Eqs. (2.4.7) and (2.4.9) has been developed and has been shown to give reliable and efficient iterative total lineshape analyses for multi-site exchange systems.

Although specific details will be discussed in a following chapter dealing with experimental applications, one aspect of a general iterative lineshape fitting procedure should be outlined at this point. In the $(m + 1)^{th}$ iteration, the refined rate constant for any two sites i and j is determined as

$$k_{ij}^{m+1} = k_{ij}^{m} + \Delta k_{ij}$$

and thus in accordance with Eq. (2.4.5),

$$\underline{\underline{R}}^{m+1} = \underline{\underline{T}}_2 + (\underline{\underline{K}}^m + \underline{\underline{\Delta K}}) - i\underline{\underline{\Omega}}$$

$$= \underline{\underline{T}}_2 + \underline{\underline{K}}^{m+1} - i\underline{\underline{\Omega}}$$

where the elements of the matrix $\underline{\underline{\Delta K}}$ are defined in terms of the incremental rate constants Δk_{ij}, cf. Eq. (2.2.21). Now, in the m^{th} iteration, transformation matrices have been determined in accordance with Eq. (2.4.7) such that

$$\underline{\underline{\Lambda}}^m = (\underline{\underline{S}}^{-1})^m \cdot \underline{\underline{R}}^m \cdot \underline{\underline{S}}^m \quad .$$

Thus in the $(m+1)^{th}$ iteration, it follows that a matrix $\underline{\underline{\Lambda}}'$ determined by

$$\underline{\underline{\Lambda}}' = (\underline{\underline{S}}^{-1})^{m} \cdot \underline{\underline{R}}^{m+1} \cdot \underline{\underline{S}}$$

is approximately diagonal. The matrix $\underline{\underline{\Lambda}}'$ may now be diagonalized exactly with considerable reduction in computation time. The $(m+1)^{th}$ iteration transformation matrices, $\underline{\underline{S}}^{m+1}$ and $(\underline{\underline{S}}^{-1})^{m+1}$ are readily obtained as

$$\underline{\underline{\Lambda}}^{m+1} = \underline{\underline{T}}^{-1} \cdot \underline{\underline{\Lambda}}' \cdot \underline{\underline{T}}$$

$$= (\underline{\underline{S}}^{-1})^{m+1} \cdot \underline{\underline{R}}^{m+1} \cdot \underline{\underline{S}}^{m+1}$$

with $\underline{\underline{S}}^{m+1} = \underline{\underline{S}}^{m} \cdot \underline{\underline{T}}$ and $(\underline{\underline{S}}^{-1})^{m+1} = \underline{\underline{T}}^{-1} \cdot (\underline{\underline{S}}^{-1})^{m}$. Having defined the complex matrices $\underline{\underline{\Lambda}}^{m+1}$, $\underline{\underline{S}}^{m+1}$ and $(\underline{\underline{S}}^{-1})^{m+1}$ in this manner, the computation of the lineshape for the rate constants k_{ij}^{m+1} reduces to an application of Eq. (2.4.9).

The complex matrix formulation of chemical exchange processes is most readily illustrated by an analysis of the simple two-site system in the limit of zero saturation. Such a system may be considered with exchange sites A and B defined by relative chemical shifts (rads. sec^{-1}) $\Omega_A = -\Omega$ and $\Omega_B = \Omega$ in terms of the independent frequency variable x with $\omega_o = (\omega_A + \omega_B)$, cf. Eq. 2.2.24), and fractional site populations p_A and p_B. The relaxation, rate and chemical shift matrices are then determined as:

$$\underline{\underline{T}}_1 = \begin{bmatrix} \frac{1}{T_{1A}} & 0 \\ 0 & \frac{1}{T_{1B}} \end{bmatrix} \quad , \quad \underline{\underline{T}}_2 = \begin{bmatrix} \frac{1}{T_{2A}} & 0 \\ 0 & \frac{1}{T_{2B}} \end{bmatrix}$$

$$\underline{\underline{K}} = \begin{bmatrix} k_A & -k_B \\ -k_A & k_B \end{bmatrix}, \qquad \underline{\underline{\Omega}} = \begin{bmatrix} -\omega & 0 \\ 0 & \omega \end{bmatrix}$$

In the limit of zero saturation, the z-mode magnetization is given by Eq. (2.2.22) as

$$\underline{M}_z = M_o \, \underline{\underline{\varepsilon}}_1 \cdot \underline{\underline{T}}_1 \cdot \underline{P}$$

with

$$\underline{\underline{\varepsilon}}_1 = (\underline{\underline{R}}_1)^{-1} = \frac{1}{D} \begin{bmatrix} \frac{1}{T_{1B}} + k_B & k_B \\ k_A & \frac{1}{T_{1A}} + k_A \end{bmatrix}$$

and

$$D = \frac{1}{T_{1A} T_{1B}} + \frac{k_A}{T_{1B}} + \frac{k_B}{T_{1A}}$$

Using Eq. 2.2.3), it is readily shown that the matrix product $\underline{\underline{\varepsilon}}_1 \cdot \underline{\underline{T}}_1 \cdot \underline{P}$ reduces to $\underline{P}$ in this limit, thus showing the validity of the modified Bloch equations as expressed in Eq. (2.4.1). For analytic simplicity it will now be assumed that the spin-spin relaxation times for the two sites are the same so that the matrix $\underline{\underline{T}}_2$ becomes a scalar matrix, viz., $\frac{1}{T_2} \underline{\underline{I}}$ where $\underline{\underline{I}}$ is the 2 x 2 unit matrix. The exchange matrix $\underline{\underline{R}}$, defined by Eq. (2.4.5), may now be expressed in the form

$$\underline{\underline{R}} = \frac{1}{T_2} \underline{\underline{I}} + \left[\underline{\underline{K}} - i\underline{\underline{\Omega}} \right], \qquad (2.4.10)$$

and the diagonal matrix $\underline{\underline{\Lambda}}$ corresponding to $\left[\underline{\underline{K}} - i\underline{\underline{\Omega}}\right]$ is now defined by $\underline{\underline{\Lambda}} = \underline{\underline{S}}^{-1} \cdot \left[\underline{\underline{K}} - i\underline{\underline{\Omega}}\right] \cdot \underline{\underline{S}}$.

If, initially, an equal population system is considered, the diagonal elements of the matrix $\underline{\underline{\Lambda}}$ above are given by

$$\lambda = k \pm \alpha , \quad \alpha = \left[k^2 - \Omega^2\right]^{\frac{1}{2}} , \tag{2.4.11}$$

with $k = k_A = k_B$. The associated transformation matrices are given as

$$\underline{\underline{S}} = \begin{bmatrix} 1 & 1 \\ -\beta_- & \beta_+ \end{bmatrix} , \quad \underline{\underline{S}}^{-1} = \begin{bmatrix} \beta_+ & 1 \\ \beta_- & 1 \end{bmatrix} , \tag{2.4.12}$$

where $\beta_\pm = (\alpha \pm i\Omega)/k$. As the matrix $\left[\underline{\underline{K}} - i\underline{\underline{\Omega}}\right]$, or $\underline{\underline{R}}$, is non-Hermitean, the matrix elements λ are in general complex and the column vectors defining the transformation matrix $\underline{\underline{S}}$ are complex and non-orthogonal. These vectors are normalized in accordance with the condition

$$S^*_{jj} S_{jj} + S^*_{\ell j} S_{\ell j} = 1$$

for $j, \ell = 1, 2$ and S^*_{jj} the complex conjugate of S_{jj}. It should also be noted that all normalization constants have been combined in the factor $k/2\alpha$ in Eq. (2.4.12). The complex lineshape function, G(x), in accordance with Eq. (2.4.6) now takes the form

$$G(x) = -i\omega_1 M_0 \underline{\underline{I}} \cdot \underline{\underline{S}} \cdot \left[\underline{\underline{\Lambda}} + \left(\frac{1}{T_2} + ix\right)\underline{\underline{I}}\right]^{-1} \cdot \underline{\underline{S}}^{-1} \cdot \underline{P} \tag{2.4.13}$$

The parameter α, as defined in Eq. (2.4.11), is real or pure imaginary for $k > \Omega$ and $k < \Omega$, respectively. Thus, from Eq. (2.4.13), the complex

lineshape function for rate constants in the range $0 \leq k \leq \Omega$ is expressed in terms of a real parameter ε as

$$G(x) = iA\left\{\frac{(1+ik/\varepsilon)}{r+i(x+\varepsilon)} + \frac{(1-ik/\varepsilon)}{r+i(x-\varepsilon)}\right\} \qquad (2.4.14)$$

with $A = -\omega_1 M_o$, $r = \frac{1}{T_2} + k$ and $\varepsilon = \left[\Omega^2 - k^2\right]^{\frac{1}{2}}$. The associated lineshape function for rate constants in the range $\Omega \leq k < \infty$ is

$$G(x) = iA\left\{\frac{(1-k/\alpha)}{(r+\alpha)+ix} + \frac{(1+k/\alpha)}{(r-\alpha)+ix}\right\} \qquad (2.4.15)$$

Eqs. (2.4.14) and (2.4.15) allow a lucid and concise description of the NMR absorption lineshape function V(x) for the equal population two-site chemical exchange system. In general, the diagonal matrix elements λ_ℓ determine the positions and line-widths of the component spectral lines and the matrix $\underline{\underline{S}}$ determines the intensities of these lines. Thus, for $0 \leq k \leq \Omega$, Eq. (2.4.14) defines absorption mode components corresponding to modified Lorentzian lines described by the lineshape function

$$V(x) = A\left\{\frac{(r+k)+\frac{k}{\varepsilon}x}{r^2+(x+\varepsilon)^2} + \frac{(r+k)-\frac{k}{\varepsilon}x}{r^2+(x-\varepsilon)^2}\right\} \qquad (2.4.16)$$

In the absence of exchange, $k = 0$ ($r = \frac{1}{T_2}$, $\varepsilon = \Omega$), it is shown that the spectrum consists of pure Lorentzian lines centered at $x = \pm\Omega$ with full widths at half maximum of $2/T_2$, consistent with the normal definitions of 2Ω as the chemical shift between sites and T_2 as the parameter describing spectral line-width in the absence of exchange effects[82]. In the presence of exchange, the spectral components may

be considered in terms of a superposition of pure Lorentzian absorption and associated dispersion functions, the degree of mixing being determined by the factor k/ε in Eq. (2.4.16). For example, for the component centred at $x = \varepsilon$, $V_+(x)$ is given by

$$V_+(x) = A\left\{\frac{r}{r^2+(x-\varepsilon)^2} - \frac{k}{\varepsilon}\left[\frac{(x-\varepsilon)}{r^2+(x-\varepsilon)^2}\right]\right\} \qquad (2.4.17)$$

Thus it is shown that the Lorentzian type component has a full linewidth at half-maximum of $2(\frac{1}{T_2} + k)$, linearly increasing with k, and a position $\varepsilon < \Omega$ such that the component separation, 2ε, decreases with increasing k. A similar function $V_-(x)$ is obtained for the component centred at $x = -\varepsilon$. These basic lineshape characteristics are illustrated in Fig. 2.5 for values of the parameter $k/\Omega < 1$. In Fig. 2.5a, the modified Lorentzian component spectral lines, $V_+(x)$ and $V_-(x)$, are shown as dashed lines; and the resultant lineshape function, $V(x)$, is shown as a full line, cf. Fig. 2.3. In Fig. 2.5b, the combined absorption and dispersion functions, with contributions from the component line at $x = \varepsilon$ being given by the first and second terms, respectively, in Eq. (2.4.17), are shown as the dashed lines. Again, the computed lineshapes have been normalized, through the factor A, to an arbitrary maximum independent of k.

Experimentally, use of an rf phase-sensitive detector allows the observation of an NMR signal proportional to a specific component of the transverse nuclear magnetization, $G(x)$, as an oscillatory linearly polarized component at the irradiation frequency ω in the fixed laboratory frame of reference. The direction of a specific component

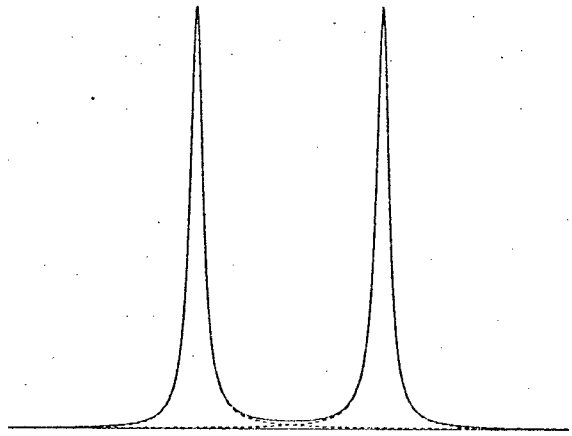

$k/\Omega = 0.032$

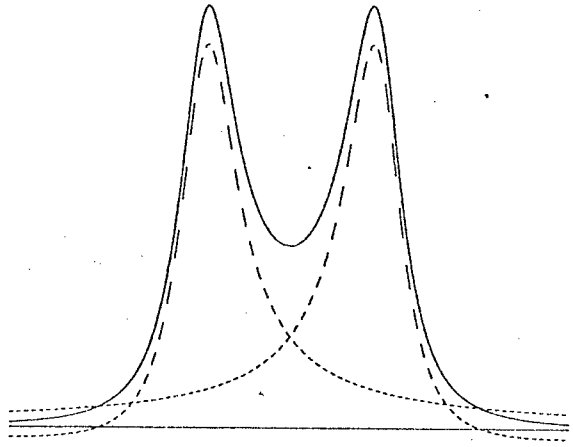

0.32

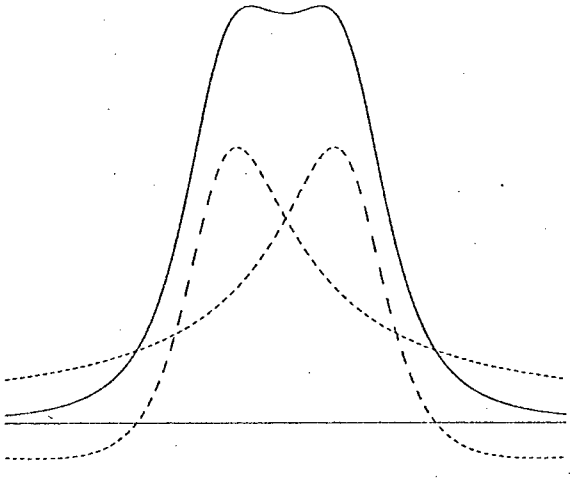

$k/\Omega = 0.64$

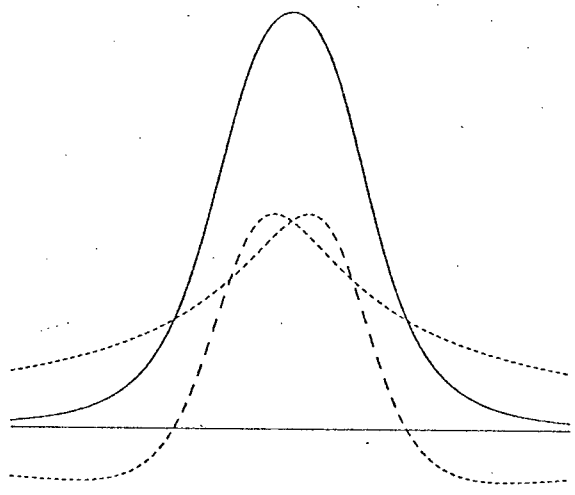

0.80

Figure 2.5(a) Modified Lorentzian component spectral lines and resultant absorption mode exchange lineshapes.

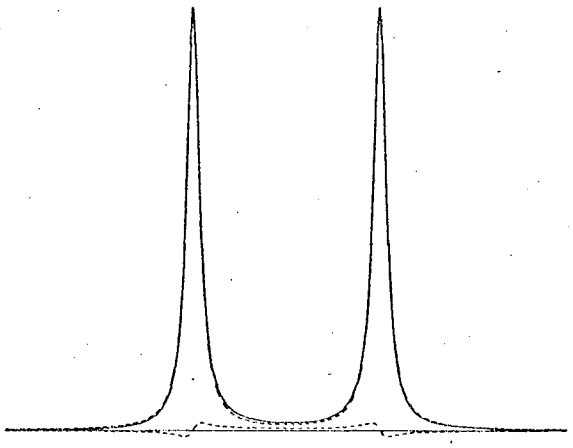

$k/\Omega = 0.032$

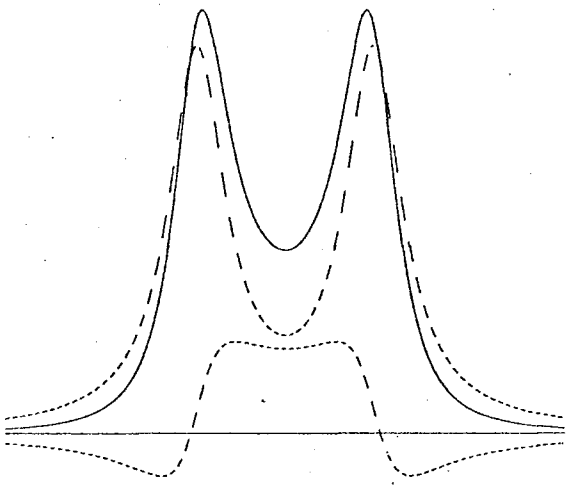

0.32

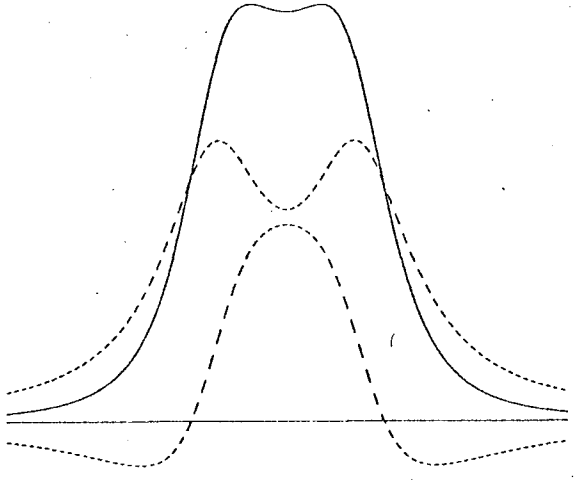

$k/\Omega = 0.64$

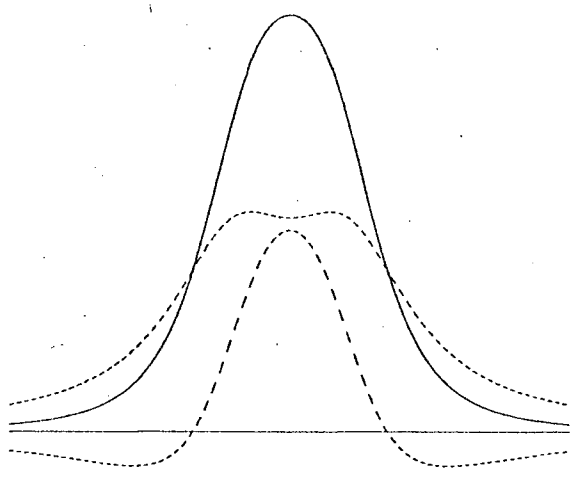

0.80

Figure 2.5(b) Combined absorption and dispersion functions and resultant absorption mode exchange lineshapes.

of transverse magnetization is defined by the relative phase angle ϕ_r between the detector reference rf field vector $\underline{H}_r$ and the rf irradiation field vector $\underline{H}_1$ defining the u-axis of the normal rotating frame of reference, cf. Fig. 2.2. Thus in the absence of exchange efffects, by setting $\phi_r = 90$ the specific component corresponding to the v-mode magnetization vector $\underline{V}$ is observed. The absorption mode spectrum consists of pure Lorentzian lines (assuming a simple $1/T_2$-type spin-spin relaxation mechanism) centred at $x = \pm\Omega$ or, $\omega = \omega_o \pm \Omega$. The general dispersion mode spectrum is described by a lineshape function u(x) given in accordance with Eq. (2.4.16) as

$$u(x) = -A\left\{\frac{(x+\varepsilon) - \frac{k}{\varepsilon}r}{r^2 + (x+\varepsilon)^2} + \frac{(x-\varepsilon) + \frac{k}{\varepsilon}r}{r^2 + (x-\varepsilon)^2}\right\} \qquad (2.4.18)$$

where $u_+(x)$, analogous to $V_+(x)$ in Eq. (2.4.17), is

$$u_+(x) = -A\left\{\frac{(x-\varepsilon)}{r^2+(x-\varepsilon)^2} + \frac{k}{\varepsilon}\left[\frac{r}{r^2+(x-\varepsilon)^2}\right]\right\} \qquad (2.4.19)$$

This form of spectrum is observed by setting $\phi_r = 0$. The first term in Eq.(2.4.19) describes the dispersion mode line centred at $x = +\Omega$ in the limit of no exchange. In the presence of chemical exchange for $k < \Omega$, the mixing of normal absorption and dispersion mode NMR signals associated with the v- and u-mode components, respectively, of the transverse magnetization in the rotating frame of reference may now be considered qualitatively in terms of the behaviour of the transverse components of the individual nuclear spin isochromats, $\underline{M}(x, \phi)$. In the absence of chemical exchange, T_2 is the relaxation time describing the isochromat dephasing and consequential spectral

line-width due to local magnetic field inhomogeneity giving rise to distributions of Larmor frequencies centred at the A- and B-site resonance frequencies, $x = \pm\Omega$. This type of isochromat dephasing is a coherent effect. In the presence of chemical exchange, however, the individual spin isochromats are involved in a transfer between sites corresponding to distinct local magnetic fields (chemical shifts) at random times. Conversely, it may be considered that each spin isochromat experiences a randomly fluctuating local magnetic field with a fundamental frequency component in the associated frequency distribution of k rads. $sec.^{-1}$. This random process alters the form of isochromat dephasing, which may now be described in terms of a probability function[33,85] for the isochromat relative phase distribution, and the time average effect for all isochromats is observed as an effective mixing of the normal u- and v-mode transverse magnetizations as described by Eqs. (2.4.16) and (2.4.18). It should be emphasized that the function V(x) by definition describes the spectrum as observed in the presence of exchange processes for the phase sensitive detector relative phase $\phi_r = 90$, and this will always be referred to as the absorption mode signal. Now, if the fundamental frequency associated with the fluctuating local magnetic field due to a chemical exchange process becomes comparable to the frequency difference between exchange sites, 2Ω, the modification of the basic T_2 isochromat dephasing is expected to be most significant. This is actually observed in the form of maximal broadening and coalescence of the component spectral lines for rate constants $k \simeq \Omega$. For rate constants $k \simeq \Omega$, it follows from Eq. (2.4.16) that

$$V(x) = A \left\{ r\left[\frac{1}{r^2+(x+\varepsilon)^2} + \frac{1}{r^2+(x-\varepsilon)^2}\right] + \frac{k}{\varepsilon}\left[\frac{(x+\varepsilon)}{r^2+(x+\varepsilon)^2} + \frac{(x-\varepsilon)}{r^2+(x-\varepsilon)^2}\right]\right\} \qquad (2.4.20)$$

Thus it is seen that the lineshape characteristics are strongly dependent upon the second term, in addition to the broadening described by the parameter r, due to the factor $k/\varepsilon \to \infty$. It is this factor that describes the well known sensitivity of the observed absorption mode lineshape to rate constant for a particular chemical shift difference between exchange sites in the region about component line coalescence. For $k = \Omega$ ($\varepsilon = 0$) the second term in Eq. (2.4.20) now makes no effective contribution to the lineshape function V(x) and thus the spectrum consists of a single Lorentzian line centred at $x = 0$ with full width at half-maximum of $2r = 2\left[\frac{1}{T_2} + \Omega\right]$ and intensity factor $2Ar$. Qualitatively, this is consistent with the simple isochromat model for exchange effects previously discussed. As the rate of isochromat transfer between exchange sites increases, or conversely, as the fundamental frequency associated with the fluctuating local magnetic field for any isochromat increases, the time average contribution from the normal dispersive u-mode magnetization is maximized and then effectively cancelled out for the particular condition $k = \Omega$. This cancellation coincides with an exact averaging of the component line separation, 2ε, to zero. Also, for all rate constants $k > \Omega$ there is no effective contribution to the lineshape from a dispersive type function.

For rate constants $k > \Omega$, the absorption mode lineshape function is given in accordance with Eq. (2.4.15) as

$$V(x) = A\left\{(1+\tfrac{k}{\alpha})\frac{r-\alpha}{(r-\alpha)^2+x^2} + (1-\tfrac{k}{\alpha})\frac{r+\alpha}{(r+\alpha)^2+x^2}\right\} \qquad (2.4.21)$$

with $r = \frac{1}{T_2} + k$, $\alpha = (k^2 - \Omega^2)^{\frac{1}{2}}$. That is, the spectrum consists of a modified Lorentzian line centred at $x = 0$ which may be described as the superposition of two Lorentzian components, that giving a positive contribution to $V(x)$ being defined as

$$V_+(x) = A(1+\tfrac{k}{\alpha})\frac{r-\alpha}{(r-\alpha)^2+x^2}$$

with a full width at half-maximum of $2(r - \alpha)$ and an intensity factor $A(1 + k/\alpha)$. The parameters r and α determine a linewidth which decreases with increasing k and a maximum value for the intensity factor of $2A$. The other component defined in Eq. (2.4.21) gives a negative contribution and is a Lorentzian function with line-width $2(r + \alpha)$, increasing linearly with k, and intensity factor $A(1 - k/\alpha)$. Again, for $k \simeq \Omega$ the lineshape is strongly dependent upon the factor k/α (as $\alpha \to 0$) and the observed lineshape is particularly sensitive to the rate constant k in this region. In the limit of very fast exchange ($k >> \Omega$) the component $V_+(x)$ becomes dominant and the absorption mode spectrum consists of a single Lorentzian line with line-width $2/T_2$ and an intensity factor $2A$, consistent with the fact that the intensities associated with the component lines at $x = \pm\Omega$ in the limit of slow exchange have now combined in the single line centred at the mean Larmor frequency. These lineshape characteristics are shown in Fig. 2.6 for two values of $k/\Omega > 1$ where again the computed

(a)

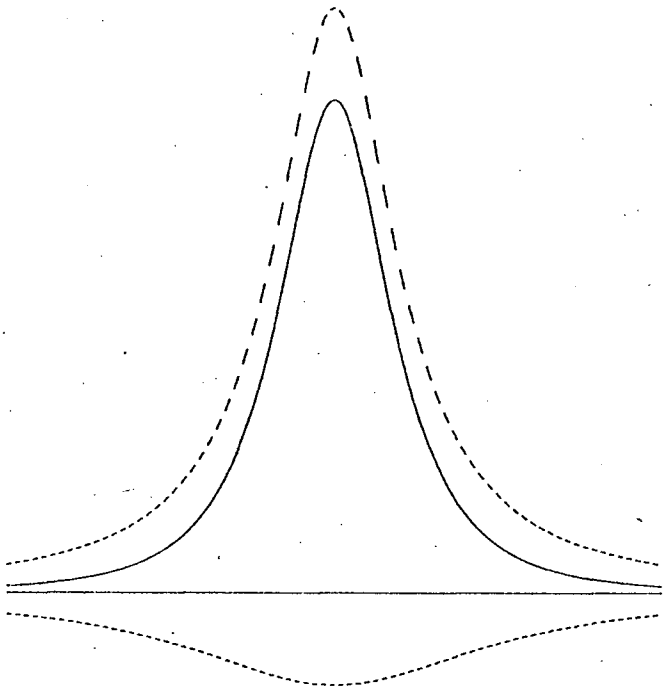

$k/\Omega = 1.10$

(b)

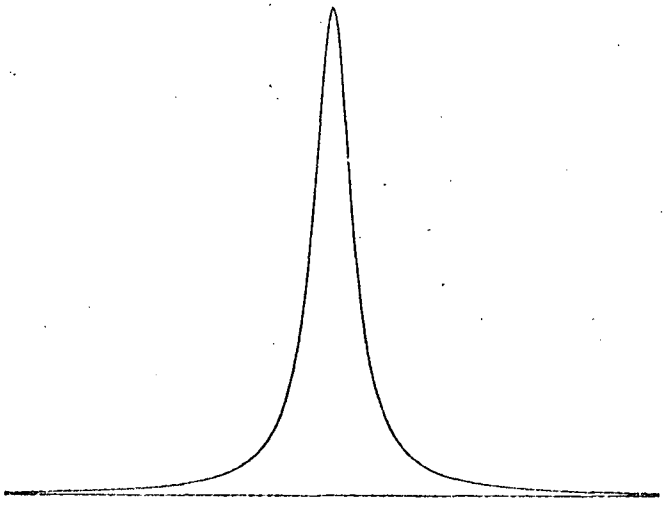

$k/\Omega = 3.2$

Figure 2.6 Modified Lorentzian component functions and resultant absorption mode exchange lineshapes.

lineshapes have been normalized to an arbitrary maximum independent of k. In Fig. 2.6a, the component Lorentzian functions $V_+(x)$ and $V_-(x)$ are shown as dashed lines; and the resultant lineshape function $V(x)$ is shown as a full line. In Fig. 2.6b, the functions $V_+(x)$ and $V(x)$ are shown to be very nearly equivalent.

A similar matrix treatment for the more general unequal population, $p_A \neq p_B$, two-site exchange system using Eqs. (2.4.10) and (2.4.13) leads to complex lineshape functions for $0 \leq k \leq \Omega$:

$$G(x) = iA\left\{\frac{(1+i\frac{k}{\varepsilon})-(1-2p_A)\frac{\Omega}{\varepsilon}}{r+i(x+\varepsilon)} + \frac{(1-i\frac{k}{\varepsilon})+(1-2p_A)\frac{\Omega}{\varepsilon}}{r+i(x-\varepsilon)}\right\} \qquad (2.4.22)$$

and for $\Omega \leq k < \infty$:

$$G(x) = iA\left\{\frac{(1-\frac{k}{\alpha})-i(1-2p_A)\frac{\Omega}{\alpha}}{(r+\alpha)+ix} + \frac{(1+\frac{k}{\alpha})+i(1-2p_A)\frac{\Omega}{\alpha}}{(r-\alpha)+ix}\right\} \qquad (2.4.23)$$

where the characteristic parameters are defined by

$$\varepsilon = \left[\Omega^2 - k^2 - 2i(1-2p_A)k\Omega\right]^{\frac{1}{2}}$$

$$\alpha = \left[k^2 - \Omega^2 + 2i(1-2p_A)k\Omega\right]^{\frac{1}{2}}$$

$$r = \frac{1}{T_2} + k$$

with $k = \frac{1}{2}(k_A + k_B)$, $2\Omega = \omega_B - \omega_A = \Omega_B - \Omega_A$, and $\omega_o = \frac{1}{2}(\omega_A + \omega_B)$. In this case the parameters ε and α remain complex, but they may be compared directly with the analogous parameters used in the analysis of the equal population system. It is interesting to note that these parameters now determine both component line position (imaginary part)

and line-width (real part) for all rate constants k, whereas in the equal population case the real parameters ϵ and α determined only line position or line-width, respectively. In the limit of slow exchange, for a general population two-site exchange system analogous to that already discussed, it is shown from Eq. (2.4.22) that the absorption mode lineshape function simplifies to the form

$$V(x) = A\left\{ p_A \frac{r}{r^2 + (x+\Omega)^2} + (1-2p_A)\frac{r}{r^2+(x-\Omega)^2}\right\} \quad (2.4.24)$$

Thus, in the absence of exchange (k = 0), the spectrum consists of pure Lorentzian lines centred at $x = -\Omega$ and $x = +\Omega$ with intensity factors p_A and $(1 - p_A) = p_B$, respectively, and full widths at half-maximum of $2/T_2$. In the limit of very fast exchange the second term in Eq. (2.2.23) becomes dominant and the absorption mode spectrum consists of a single Lorentzian line

$$V(x) = 2A\left\{ \frac{1/T_2}{(1/T_2)^2 + (x-(1-2p_A)\Omega)^2}\right\}$$

centred at $x = (1 - 2p_A)\Omega$ with a line-width $2/T_2$. That is, for the unequal population exchange system the spectral line in this limit is positioned away from the mean frequency $x = \frac{1}{2}(\Omega_A + \Omega_B) = 0$ towards the resonance frequency corresponding to the larger population exchange site. A reformulation of the imaginary parts of Eqs. (2.4.22) and (2.4.23) shows that these general equations are equivalent to the expression previously derived, cf. Eq. (2.2.14), for a two-site exchange system.

2.5 First-Order J-Coupling.

In previous sections, a multi-site nuclear spin exchange system has been considered in terms of distinct sites of differing Larmor frequency ω_i, an implicit assumption being that each site is associated with a particular molecular electronic environment and corresponding relative chemical shift Ω_i. The effect of chemical exchange on spin-spin multiplets in NMR spectra was recognized in the original work of Gutowsky and co-workers[3,4], and various approximate analytical expressions have been developed to derive kinetic data for specific cases[61, 84, 86,87]. J-coupling in a general first-order NMR exchange system, however, is readily included in a matrix formulation of exchange processes based upon a simple stochastic model as already developed.

A general spin Hamiltonian for a system of N-spins in the absence of exchange processes may be considered in the form

$$\mathcal{H} = \mathcal{H}_o + \mathcal{H}_{L\Omega} + \mathcal{H}_J^{(1)} + \mathcal{H}_J^{(2)} \qquad (2.5.1)$$

where it is assumed that all terms in this Hamiltonian are expressed in energy units $h = h/2\pi$, h being Planck's constant. A term describing the interaction of the observing rf magnetic field with the nuclear spin system is not necessary in the following analysis. $\mathcal{H}_o$ is a generalized Zeeman term

$$\mathcal{H}_o = -\omega_o \sum_{i=1}^{N} I_{zi} \qquad (2.5.2)$$

with a reference Larmor frequency ω_o rad. $sec.^{-1}$ defined as

$$\omega_o = \gamma H_o - \Delta, \qquad \Delta > 0. \tag{2.5.3}$$

As usual, I_{zi} is the z-component spin angular momentum operator for the i^{th}-spin and H_o is the magnitude of the static magnetic field applied in the positive z-direction of the Cartesian rotating and fixed reference frames. In Eq. (2.5.3), γ is the nuclear gyromagnetic ratio for the resonant spins in a general hetero-nuclear system and Δ is a frequency shift parameter, defined to be positive, determining the origin for the independent frequency variable x, cf. Eq. (2.2.24). This form of frequency variable allows an arbitrary choice of frequency origin and a simplified analysis of general NMR spectra, while being directly related to the experimental irradiating frequency ω. $\mathcal{H}_\Omega$ is the chemical shift term

$$\mathcal{H}_\Omega = -\sum_{i=1}^{N} \Omega_i I_{zi} \tag{2.5.4}$$

in which Ω_i is the chemical shift for the i^{th}-spin, or site-i, relative to the reference Larmor frequency ω_o, cf. Eq. (2.2.24). In this manner, Ω_i may be considered as the site-i Larmor frequency in terms of the independent variable x. The definition of $\mathcal{H}_\Omega$ in terms of the observable Ω_i may be related to the concept of a positive electronic shielding parameter[88] σ_i, describing the local time-independent magnetic field in the z-direction: $H_i = (1 - \sigma_i)H_o$, such that $\mathcal{H}_\Omega = \gamma H_o \sum_{i=1}^{N} \sigma_i I_{zi}$. Increased shielding of the i^{th}-spin, as described by an increased σ_i value, thus corresponds to a decrease in the Larmor frequency ω_i at constant magnetic field H_o. In the particular case for which $\Delta = 0$ ($\omega_o = \gamma H_o$), all site Larmor

frequencies are such that $\omega_i \leq \omega_o$ and hence all relative chemical shifts are negative.

The partial Hamiltonian $\mathcal{H}_J^{(1)}$ may be referred to as a first-order coupling term and is given as

$$\mathcal{H}_J^{(1)} = \sum_{i=1}^{N} \sum_{j>i} J_{ij} I_{zi} I_{zj} \qquad (2.5.5)$$

where J_{ij} is the indirect (scalar) spin-spin coupling constant between the i^{th}- and j^{th}-spins. Thus, $\mathcal{H}_J^{(2)}$ is a second-order coupling term of the form

$$\mathcal{H}_J^{(2)} = \frac{1}{2} \sum_{i=1}^{N} \sum_{j>i} J_{ij} \left[I_i^+ I_j^- + I_i^- I_j^+ \right] \qquad (2.5.6)$$

In the I_z-representation, with basis functions as simple products of eigen-functions of the spin operator I_z, the term $\mathcal{H}_J^{(2)}$ corresponds to off-diagonal elements in the spin Hamiltonian matrix $\underline{\underline{\mathcal{H}}}$. A first-order NMR spectrum may be defined by the condition $J_{ij} \ll |\Omega_i - \Omega_j|$ and, as the matrix $\underline{\underline{\mathcal{H}}}$ is diagonal in Ω_i all off-diagonal matrix elements may be neglected in a first-order determination of spectral transition frequencies and intensities. The Hamiltonian term $\mathcal{H}_J^{(2)}$, however, has been shown to give rise to a spin-spin relaxation mechanism which may be described by Bloch type equations for weakly coupled nuclear spin systems[89]. The effect of such a relaxation mechanism in addition to chemical exchange processes is not included at this point.

In the I_z-representation, the effective spin Hamiltonian for a weakly coupled (first-order) spin system,

$$\mathcal{H}' = \mathcal{H}_o + \mathcal{H}_\Omega + \mathcal{H}_J^{(1)} \qquad (2.5.7)$$

is diagonal and all terms correspond to secular energies defining first-order spin transitions. The energy E_ℓ associated with the basis function (also an eigen-function of $\mathcal{H}'$) ϕ_ℓ is now given as

$$E_\ell = -\omega_o \sum_{i=1}^{N} m_{\ell i} - \sum_{i=1}^{N} \Omega_i m_{\ell i} + \sum_{i=1}^{N} \sum_{j>i} J_{ij} m_{\ell i} m_{\ell j} , \qquad (2.5.8)$$

where $I_{zi}\phi_\ell = m_{\ell i}\phi_\ell$, and $\phi_\ell = \prod_{i=1}^{N} \xi_{\ell i}$. I_{zi} is the spin operator corresponding to the i^{th}-part, $\xi_{\ell i}$, of the product function ϕ_ℓ. Thus, for spin $I = \frac{1}{2}$, $m_{\ell i} = +\frac{1}{2}, -\frac{1}{2}$ for $\xi_{\ell i} = \alpha, \beta$, where α and β are the spin eigen-functions defined by $I_{zi}|\alpha\rangle = +\frac{1}{2}|\alpha\rangle$, $I_{zi}|\beta\rangle = -\frac{1}{2}|\beta\rangle$.

Spin systems commonly occurring in studies of multi-site exchange processes, especially hindered internal rotation, may be analyzed as first-order ABX and ABX_3 $I = \frac{1}{2}$ systems with $J_{AB} = 0$. As the simple ABX system includes all the salient features of a general analysis, this particular system will now be considered in some detail. The first-order spin Hamiltonian for an ABX ($J_{AB} = 0$) spin system may be expressed in accordance with Eq. (2.5.7) as

$$\mathcal{H}' = -\omega_o\left[I_{zA} + I_{zB} + I_{zX}\right] + \Omega\left[I_{zA} - I_{zB}\right] + \Omega_X I_{zX} + J_{AX} I_{zA} I_{zX} + J_{BX} I_{zB} I_{zX}, \qquad (2.5.9)$$

with chemical shifts defined as: $\omega_A = \omega_o - \Omega$, $\omega_B = \omega_o + \Omega$ and $\omega_X = \omega_o - \Omega_X$ where $\omega_o = \frac{1}{2}(\omega_A + \omega_B)$ and hence $\Delta = \gamma H_o - \frac{1}{2}(\omega_A + \omega_B)$, cf. Eq. (2.5.3). Simple product basis functions, ϕ_ℓ, in the I_z-representation for this 3-spin ($I = \frac{1}{2}$) system are given in Table 2.1, where in general $\phi_\ell = \xi_{\ell A}\xi_{\ell B}\xi_{\ell X}$; by definition, these functions are also eigen-functions of the spin Hamiltonian $\mathcal{H}'$. The corresponding energy levels, as derived from Eq. (2.5.8), are also given in Table 2.1.

TABLE 2.1

BASIS (EIGEN) FUNCTIONS FOR ABX ($J_{AB} = 0$) SPIN SYSTEM, $I = \frac{1}{2}$ NUCLEI, AND CORRESPONDING ENERGY LEVELS

ℓ	Basis function, ϕ_ℓ	Energy level, E_ℓ
1	$\alpha\alpha\alpha$	$-\frac{3}{2}\omega_o + \frac{1}{2}\Omega_X + \frac{1}{2}J_+$ [a]
2	$\alpha\beta\alpha$	$-\frac{1}{2}\omega_o + \frac{1}{2}\Omega_X + \Omega - \frac{1}{2}J_-$
3	$\beta\alpha\alpha$	$-\frac{1}{2}\omega_o + \frac{1}{2}\Omega_X - \Omega + \frac{1}{2}J_-$
4	$\beta\beta\alpha$	$\frac{1}{2}\omega_o + \frac{1}{2}\Omega_X - \frac{1}{2}J_+$
5	$\alpha\alpha\beta$	$-\frac{1}{2}\omega_o - \frac{1}{2}\Omega_X - \frac{1}{2}J_+$
6	$\alpha\beta\beta$	$\frac{1}{2}\omega_o - \frac{1}{2}\Omega_X + \Omega + \frac{1}{2}J_-$
7	$\beta\alpha\beta$	$\frac{1}{2}\omega_o - \frac{1}{2}\Omega_X - \Omega - \frac{1}{2}J_-$
8	$\beta\beta\beta$	$\frac{3}{2}\omega_o - \frac{1}{2}\Omega_X + \frac{1}{2}J_+$

a $J_\pm = \frac{1}{2}(J_{BX} \pm J_{AX})$; $J_{AX}, J_{BX} > 0$

TABLE 2.2

TRANSITION FREQUENCIES FOR ABX ($J_{AB} = 0$) SPIN SYSTEM

Transition Number [a]	Transition Type	Energy levels [b]	Frequency x
1	A	(1,3), (2,4)	$-\Omega - \frac{1}{2} J_{AX}$
2	A	(5,7), (6,8)	$-\Omega + \frac{1}{2} J_{AX}$
3	B	(1,2), (3,4)	$\Omega - \frac{1}{2} J_{BX}$
4	B	(5,6), (7,8)	$\Omega + \frac{1}{2} J_{BX}$
1	X	(1,5)	$-\Omega_X - J_+$ [c]
2	X	(3,7)	$-\Omega_X - J_-$
3	X	(2,6)	$-\Omega_X + J_-$
4	X	(4,8)	$-\Omega_X + J_+$

a These transition numbers correspond to those used in Figs. 2.7 and 2.9.

b The bracket (ℓ,m) refers to energy levels E_ℓ and E_m, and corresponding eigen-functions ϕ_ℓ and ϕ_m, given in Table 1.

c $J_\pm = \frac{1}{2} (J_{BX} \pm J_{AX})$; $J_{BX}, J_{AX} > 0$

The allowed transition frequencies, in terms of the independent variable x, are listed in Table 2.2. The eigen functions ϕ_ℓ and ϕ_m corresponding to the energy levels determining these spectral transitions are indicated by the brackets (ℓ, m). By definition $\Omega_B > 0 > \Omega_A > \Omega_X$, and it is assumed initially that $J_{BX} > J_{AX} > 0$ such that $J_\pm = \frac{1}{2}(J_{BX} \pm J_{AX}) > 0$. In the absence of exchange, for a molecular system without a preferred conformation, all transition intensities in the AB-part of the NMR spectrum are equal, as are those in the X-part. In a more general case, these intensities may be determined by the fractional populations of a number of possible conformations.

The AB-part of the ABX spectrum consists of the four transitions 1 - 4 (each of which is doubly degenerate as $J_{AB} = 0$) as shown in Fig. 2.7. Thus the J-coupling due to the X-spin determines four effective Larmor frequencies $x = -\Omega \pm \frac{1}{2}J_{AX}$ and $x = \Omega \pm \frac{1}{2}J_{BX}$, which may in turn be considered to define four distinct exchange sites. Such sites are analogous to the two environmental sites with Larmor frequencies $x = \pm \Omega$ in the absence of J-coupling. In a general description of exchange effects, a basic environmental (chemical shift) site with an associated X-spin state may now be referred to as <u>spin site</u> -j with Larmor frequency x_j, cf. Eq. (2.2.24). In this manner x_j may be considered as an effective chemical shift. Thus for the J-couplings defined above, spin site-1 corresponds to a basic A-site associated with an α X-spin state, as shown by the eigen-functions corresponding to the energy levels defining the Larmor (transition) frequency $x_1 = -\Omega - \frac{1}{2}J_{AX}$: $(\alpha\alpha\alpha, \beta\alpha\alpha)$ and $(\alpha\beta\alpha, \beta\beta\alpha)$, cf. Tables 2.1 and 2.2. Thus it is seen that J-coupling in a first-order NMR spectrum for a spin system with chemical

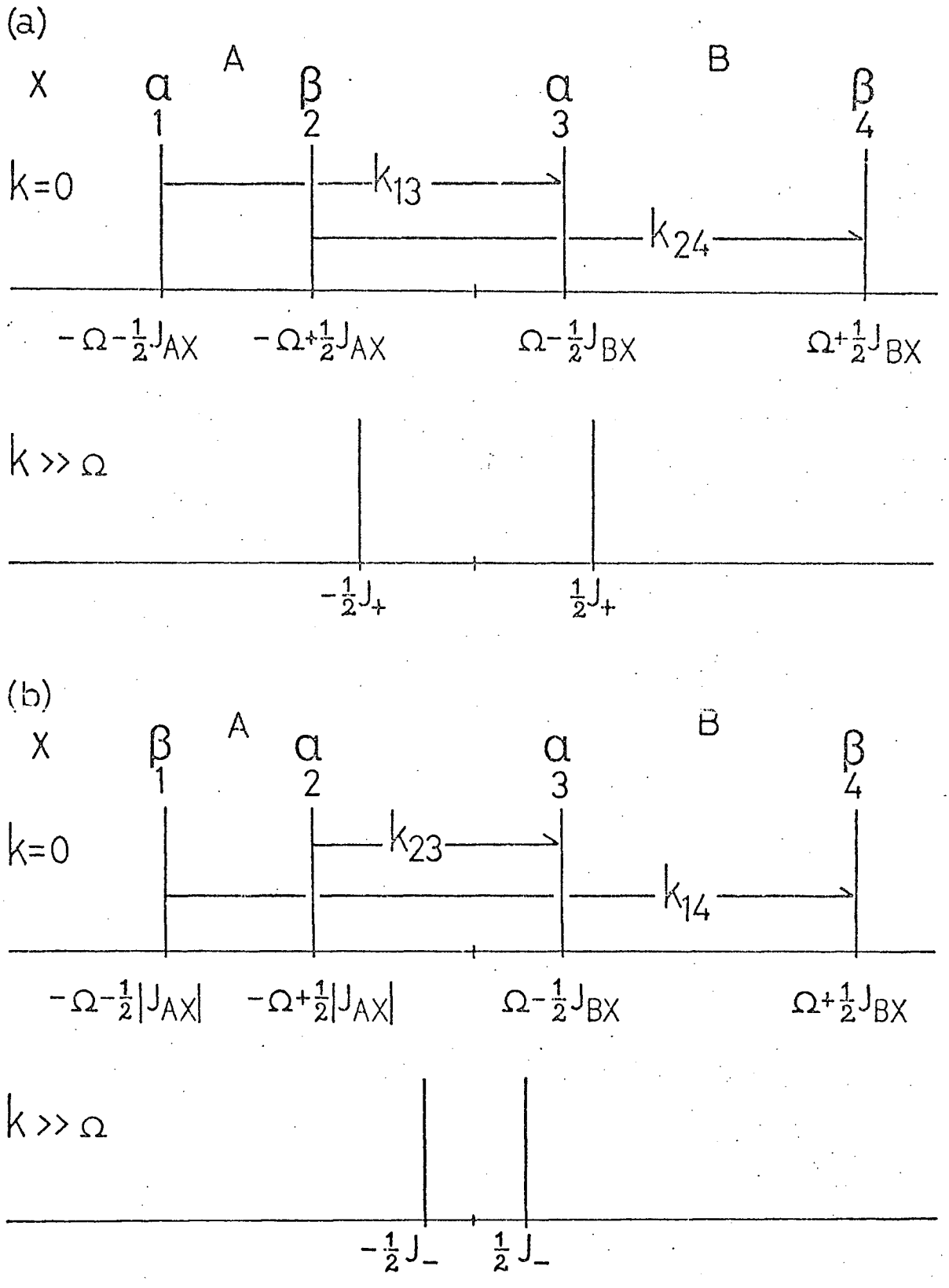

Figure 2.7 AB-part of first-order ABX spectrum

exchange processes, simply increases the number of possible exchange sites to be considered in a description of the system by modified Bloch equations.

Consistent with the semi-classical vector model previously discussed, the nuclear magnetization associated with a general spin site-j may be considered in terms of a spin isochromat $\underline{M}(x_j, \phi_j)$ with a characteristic Larmor frequency x_j and a relative phase (with respect to the u-axis of the normal rotating frame of reference uvz) ϕ_j, cf. Fig. 2.2. The fractional population of spin site-j, p_j, determines the magnitude of $\underline{M}(x_j, \phi_j)$. In the presence of a chemical exchange process defined in terms of a first-order rate constant k sec.$^{-1}$, the spin isochromat is involved in a random transfer between spin site-j and spin site-i described by a rate constant k_{ji}, cf. Eq. (2.2.18). Conversely, it may be considered that this isochromat experiences a randomly fluctuating local magnetic field with a fundamental frequency component in the associated frequency distribution of k rad. sec.$^{-1}$. The basic assumption for a stochastic description of such an exchange process in a first-order nuclear spin system may be summarized as follows:

(i) the isochromat $\underline{M}(x_j, \phi_j)$ remains in spin site-j with a mean lifetime τ_j until a random instantaneous transfer to a different site takes place, such that precessional effects in the transfer interval may be neglected;

(ii) the site lifetime τ_j is independent of the associated spin-spin and spin-lattice relaxation times, T_{2j} and T_{1j}, respectively;

(iii) individual spin isochromats relax independently except for site transfer effects; and

(iv) for the spin isochromat $\underline{M}(x_j, \phi_j)$ in spin site-j there is a constant probability per unit time, k_{ji}, for transfer <u>into</u> site-i, this probability being inversely proportional to the fractional site population p_j.

Under these assumptions, a site lifetime τ_j and associated rate constants, k_{ji}, are simply related as

$$\Sigma\, k_{ji} = \tau_j^{-1}, \tag{2.5.10}$$

where i ($i \neq j$) includes all allowed transfer sites connected with site-j. Also in accordance with the principle of detailed balance[82] for the rate processes, site population and rate constants for any two spin sites satisfy

$$p_i k_{ij} = p_j k_{ji} \tag{2.5.11}$$

These generalized relationships may be compared with those for the simple two-site exchange system initially discussed, cf. Eqs. (2.2.2) and (2.2.3).

Exchange effects in a first-order ABX ($J_{AB} = 0$) NMR spectrum may now be described in terms of this stochastic model. Only general <u>intramolecular</u> exchange processes (for example, hindered internal rotation) will be discussed explicitly. The basic exchange process is assumed to be a transfer of nuclear magnetization between spin-sites distinguished by chemical shifts for the A- and B-spins, $-\Omega$ and $+\Omega$, respectively, cf. Eq. (2.5.9). This process is defined in terms of a single first-order rate constant, k sec.$^{-1}$, which is necessarily defined as a reduced rate constant for a general exchange system. The

AB-part of the ABX spectrum is shown in Fig. 2.7a for the spin system in the absence of exchange (k = 0) with coupling constants $J_{BX} > J_{AX} > 0$. In Fig. 2.7a, the basic A and B environmental sites are indicated along with the X-spin state corresponding to each AB-exchange spin-site. All possible transfers between the four AB spin-sites may be represented by:

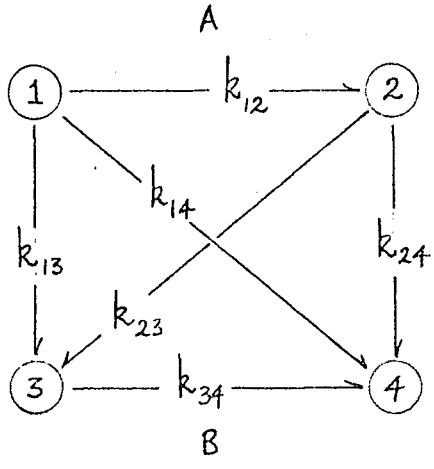

(2.5.12)

the forward transfers only, of the pairs defined by Eq. (2.5.11) being shown for clarity. Consistent with assumption (i) above, it is to be assumed that the X-spin state is unchanged in a site transfer interval and hence the allowed transfers are 1 - 3 and 2 - 4 as defined by the rate constants k_{13} (k_{31}) and k_{24} (k_{42}). This is readily seen from a comparison of the spin eigen-functions, cf. Table 2.1 associated with the doubly degenerate transitions 1 and 3:

1	3
$\xi_A\xi_B\xi_X$	$\xi_A\xi_B\xi_X$
ααα	ααα
βαα	αβα
αβα	βαα
ββα	ββα

(2.5.13)

where 1 is a first-order A-spin transition as defined by the usual spin transition operator I_A^+: $I_A^+|\beta\alpha\alpha\rangle = |\alpha\alpha\alpha\rangle$ and $I_A^+|\beta\beta\alpha\rangle = |\alpha\beta\alpha\rangle$. Similarly, 3 is a B-spin transition and thus the transfer as defined is between basic A and B environmental sites as required. Also, all product eigen-functions concerned have an α X-spin part. This type of site transfer is to be compared with the transfers 1 - 2 and 2 - 4 involving a change in X-spin state.

The simple stochastic model considered above is consistent with a quantum mechanical treatment of exchange processes. It may be assumed that the molecular system following a nuclear spin-site transfer has a spin Hamiltonian of the same form as it had initially, and that this Hamiltonian differs only in that the non-equivalent A- and B-spins have interchanged magnetic properties. An operator may now be defined[15,16] to describe the change of total nuclear spin state, under exchange, as determined by spin eigen-functions within the limits of separability of a wave-function for the complete molecular-spin system[20]. For an intramolecular exchange process, the nuclear spin state of an individual molecule following a spin-site transfer is determined completely by the original state. This is actually the fundamental difference between such a process and an intermolecular chemical exchange process in which the state of an individual molecule following site transfer depends upon the original state of this molecule and also upon the state of the interacting molecule involved[17]. For an intramolecular AB spin-site transfer in the first-order ABX system, an exchange operator, P, may be defined by $P|\alpha\alpha\xi_x\rangle = |\alpha\alpha\xi_x\rangle$ and $P|\alpha\beta\xi_x\rangle = |\beta\alpha\xi_x\rangle$. Thus, it is seen that this operator defines

exactly the transitions involved in the allowed site transfer, as defined in terms of the stochastic model above and represented in Eq. (2.5.13) for the eigen-functions having an α X-part.

Spin-sites 1 and 2 differ only in the X-spin state, the eigen-functions associated with transition 2 being (ααβ, βαβ) and (αββ, βββ), Table I. Thus the transfer 1 - 2 does not contribute to NMR spectral characteristics specifically associated with the stochastic exchange basic A- and B-spin sites. Such site transfers, however, correspond to transitions induced by the interaction of a randomly fluctuating magnetic field with the X-spin of the ABX spin system leading to X-spin lifetime limiting as described by a correlation time τ_c^{90}. In addition, if the X-spin has a quadrupole moment ($I \geqslant 1$), the interaction of a randomly fluctuating electric field gradient may lead to a similar relaxation mechanism with a different correlation time, τ_Q. For the similar transfers 1 - 2 and 2 - 3, the correlation time τ_c may be considered to define rate constants: $k_{12} = k_{34} = \tau_c^{-1}$. Also, such a mechanism may lead to effective transfers 1 - 4 and 2 -3, and in this case the rate constants k_{14} and k_{23} would be defined as a sum of contributions from exchange and X-spin transition processes. The overall effect of these additional spin relaxation processes on NMR spectral characteristics would be expected to depend upon the parameters $(\tau_c J_{AX})^{-1}$ and $(\tau_c J_{BX})^{-1}$.

In accordance with Eq. (2.4.6), a complex lineshape function G(x) determining the steady-state NMR spectrum associated with n spin-sites is expressed in the form

$$G(x) = A\, \underline{I}\cdot\underline{\underline{S}}\cdot\left[\underline{\underline{A}} + (1/T_2 + ix)\underline{\underline{I}}\right]^{-1}\cdot\underline{\underline{S}}^{-1}\cdot\underline{P} \qquad (2.5.14)$$

in which $\underline{\underline{\Lambda}}$ is the diagonal matrix corresponding to an n x n matrix $\underline{\underline{K}} - i\underline{\underline{\Omega}}$, the diagonal matrix $\underline{\underline{\Omega}}$ being defined by the spin-site Larmor frequencies x_j in terms of the independent frequency variable x. It has been implicitly assumed that the spin-spin relaxation time is the same for all spin-sites in defining the relaxation matrix $\underline{\underline{T}}_2$ as a scalar matrix $(1/T_2)\underline{\underline{I}}$, with $\underline{\underline{I}}$ the n x n unit matrix. This simplification is allowed by assuming that the spin-spin relaxation time T_2 is independent of spin-site and that all non-secular relaxation processes[91], as described by off-diagonal elements in $\underline{\underline{T}}_2$, are negligible. Although additional relaxation processes associated with the J-coupled X-spin and considered above as contributing to spin-site transfer are not further considered at this point, these processes are equivalently described by off-diagonal elements in the relaxation matrix $\underline{\underline{T}}_2$. Lineshape characteristics for the AB-part of the ABX ($J_{AB} = 0$) spectrum in the presence of exchange are concisely described through a 4 x 4 rate matrix $\underline{\underline{K}}$ defined by Eq. (2.2.21) with $k_{ji} = 0$ for any transfer not allowed in terms of the stochastic exchange model. It is to be noted that the diagonal matrix element k_{jj} corresponds to the inverse site-lifetime τ_j^{-1}, cf. Eq. (2.5.10). Thus the $\underline{\underline{K}}$ and $\underline{\underline{\Omega}}$ matrices for an equal population exchange system with coupling constants $J_{BX} > J_{AX} > 0$, and spin-sites as ordered in Fig. 2.7a are given explicitly as

$$\underline{\underline{K}} = \begin{bmatrix} k & 0 & -k & 0 \\ 0 & k & 0 & -k \\ -k & 0 & k & 0 \\ 0 & -k & 0 & k \end{bmatrix}$$

and

$$\underline{\underline{\iota\Omega}} = \begin{bmatrix} -\iota\Omega - \tfrac{1}{2}J_{AX} & 0 & 0 & 0 \\ 0 & -\iota\Omega + \tfrac{1}{2}J_{AX} & 0 & 0 \\ 0 & 0 & \iota\Omega - \tfrac{1}{2}J_{BX} & 0 \\ 0 & 0 & 0 & \iota\Omega + \tfrac{1}{2}J_{BX} \end{bmatrix} \tag{2.5.15}$$

The vectors $\underline{P}$ and $\underline{I}$ in Eq. (2.5.14) are defined by four equal elements 0.25 and 1.0, respectively. The extension to a more general unequal population system only requires the evaluation of $\underline{\underline{K}}$ matrix elements in accordance with Eqs. (2.2.21) and (2.5.11), consistent with the site-population vector, $\underline{P}$, elements. Equation (2.5.14) allows a very efficient numerical analysis of the NMR absorption mode lineshape function, V(x), given as the real part of G(x), and the development of computer programs for rapid iterative fittings of this theoretical function to experimental data. Absorption mode lineshapes have been calculated for the AB-part of an ABX spectrum defined by the arbitrary parameters Ω = 4.0 Hz, J_{AB} = 0, J_{AX} = +2.0, J_{BX} = +5.0 Hz, T_2 = 0.64 sec. (0.5 Hz full-width at half-maximum) and are shown in Fig. 2.8a for rate constants in the range $0 \leqslant k \leqslant 200$ sec.$^{-1}$. The lineshape functions have been normalized to a maximum intensity independent of k. It is seen that in the limit of fast exchange ($k >> \Omega$, this part of the spectrum reduces to a doublet. This feature is characteristic of an A_2X spin system and is consistent with the expectation that in this exchange limit basic A and B environmental sites become equivalent. As shown in Fig. 2.7a, for J_{AX} and J_{BX} of the same sign, the resultant lines are centred at $x = \pm\frac{1}{2}J_+$ with $J_+ = \frac{1}{2}(J_{BX} + J_{AX})$. These positions

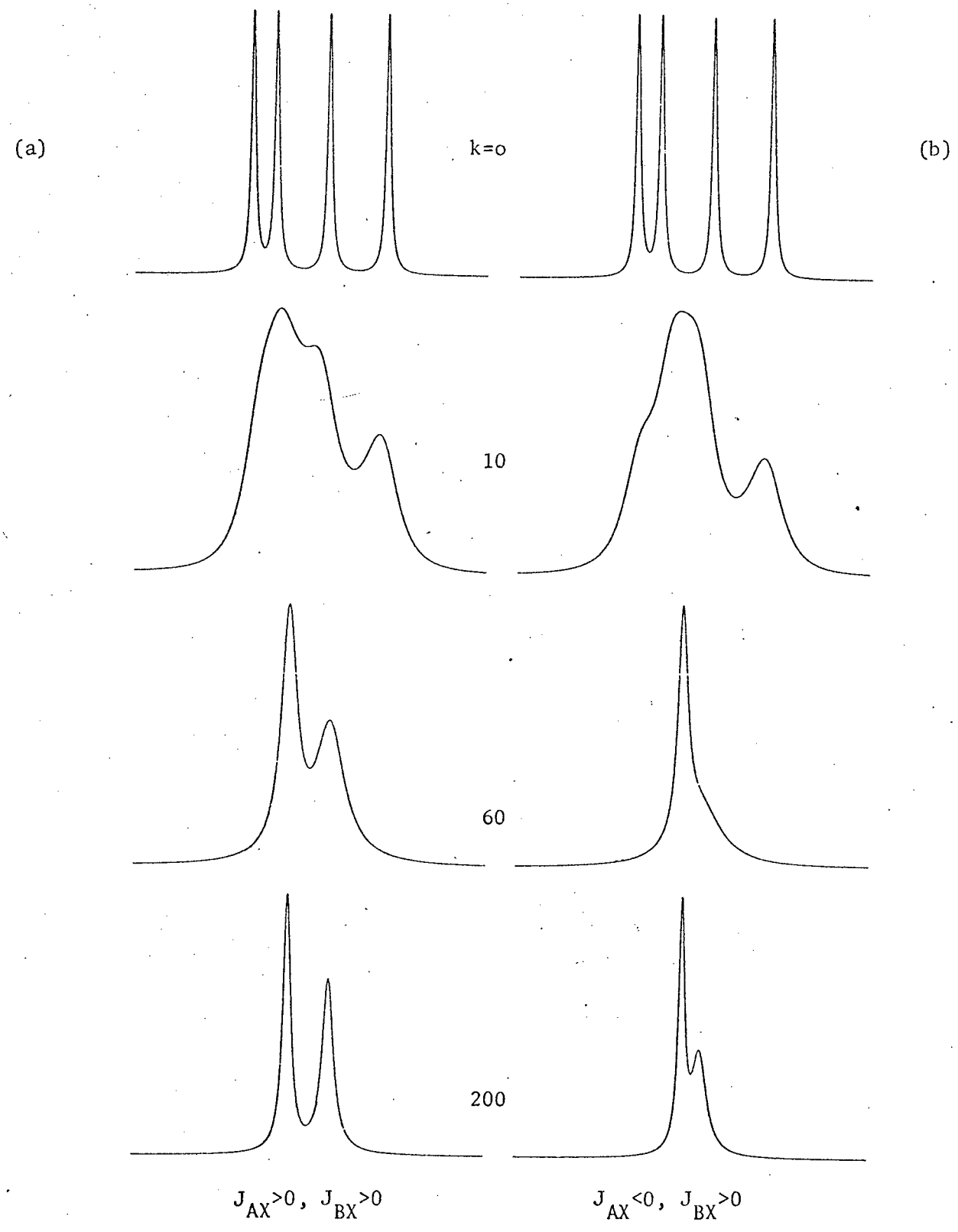

Figure 2.8 Intramolecular exchange lineshapes for the AB-part of a first-order ABX spin system.

may be modified, however, by temperature dependent chemical shifts, ω_A and ω_B.

Now for an ABX ($J_{AB} = 0$) spin system with J_{AX} and J_{BX} of different sign, the first-order spin Hamiltonian may be expressed in accordance with Eq. (2.5.9) as

$$\mathcal{H}' = -\omega_o\left[I_{zA} + I_{zB} + I_{zX}\right] + \Omega\left[I_{zA} - I_{zB}\right] + \Omega_X I_{zX}$$
$$- |J_{AX}| I_{zA} I_{zX} + J_{BX} I_{zB} I_{zX} \qquad (2.5.16)$$

where it is assumed that $J_{AX} < 0$ and $J_{BX} > 0$. Thus the corresponding energy levels, as determined using Eq. (2.5.8) are given by substituting $-|J_{AX}|$ for J_{AX} in Table I; the allowed transitions are similarly derived from those listed in Table 2. The AB-part of the spectrum for this spin system is shown in Fig. 2.7b, in which the ordered transitions 1 and 2 now correspond to β and α X-spin states, respectively. Therefore, in this case, the intramolecular AB exchange process is described by the rate constants designated as k_{14} and k_{23}; moreover, the rate matrix $\underline{\underline{K}}$ for an equal population system is given explicitly as

$$\underline{\underline{K}} = \begin{bmatrix} k & 0 & 0 & -k \\ 0 & k & -k & 0 \\ 0 & -k & k & 0 \\ -k & 0 & 0 & k \end{bmatrix} \qquad (2.5.17)$$

This matrix defines the absorption mode lineshapes shown in Fig. 2.8b for $J_{AX} = -2.0$ Hz and $J_{BX} = +5.0$ Hz. In the region of coalescence ($k \simeq \Omega$) and in the fast exchange limit, for a given rate constant k

describing the intramolecular exchange process, these lineshapes are distinctly different from those previously discussed, cf. Fig. 2.8a. Hence the relative signs of the coupling constants J_{AX} and J_{BX} may be determined directly from lineshape fitting of an exchange modified spectrum; in general, this additional information is readily available through a simple study of the temperature dependence of a first-order NMR spectrum (or part of) for a spin system undergoing chemical exchange. Of course, such information is equivalent (or complementary) to that obtained using the well-known double resonance techniques. This lineshape method, however, may allow the determination of relative signs of coupling constants for systems to which double resonance techniques are inapplicable or only applied with great difficulty. A further consequence of the different relative signs of J_{AX} and J_{BX} is that the resultant lines in the fast exchange limit spectrum are now centred at $x = \pm \frac{1}{2}J_{-}$, where $J_{-} = \frac{1}{2}(J_{BX} - |J_{AX}|)$, as shown in Fig. 2.7b.

Exchange effects in the X-part of an ABX ($J_{AB} = 0$) spectrum are also described by 4 x 4 matrices $\underline{\underline{K}}$ and $\underline{\underline{\Omega}}$, completely analogous to those given in Eqs. (2.5.15) and (2.5.17). A general X-part spectrum for $J_{BX} > J_{AX} > 0$ may be represented as shown in Fig. 2.9a in the absence of exchange ($k = 0$) and in the fast exchange limit ($k >> J_{-}$), with $J_{-} = \frac{1}{2}(J_{BX} - J_{AX})$; the corresponding absorption mode lineshapes for the arbitrary ABX spectral parameters defined above ($\Omega = 4.0$ Hz, $J_{AX} = 2.0$ Hz) are shown in Fig. 2.10a. For an equal population system, it is to be noted that the exchange process is defined in terms of the single matrix element $K_{32} = -k_{23} = -k$, as shown in Fig. 2.9a with the spin-sites involved corresponding to the AB spin

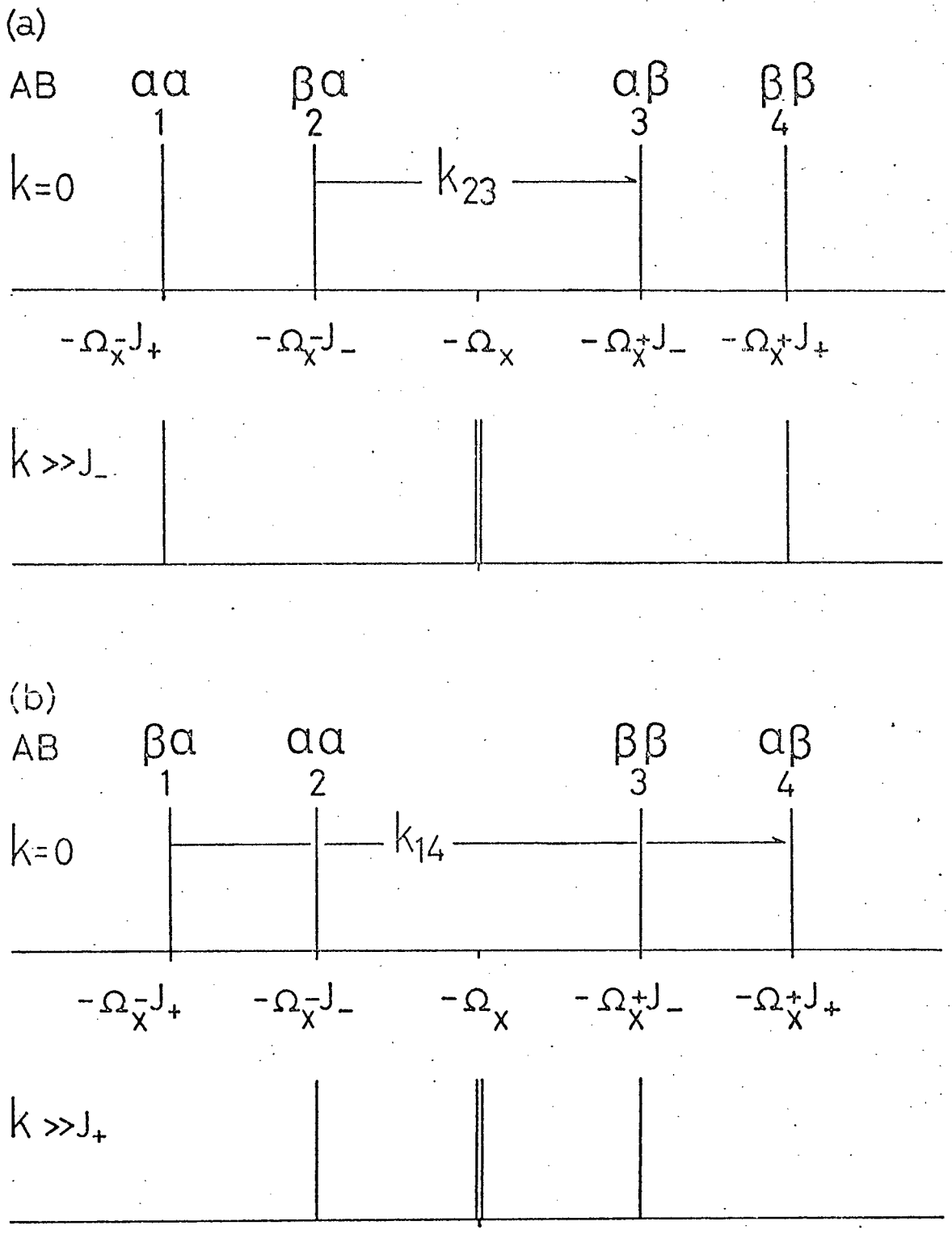

Figure 2.9 X-part of first-order ABX spectrum

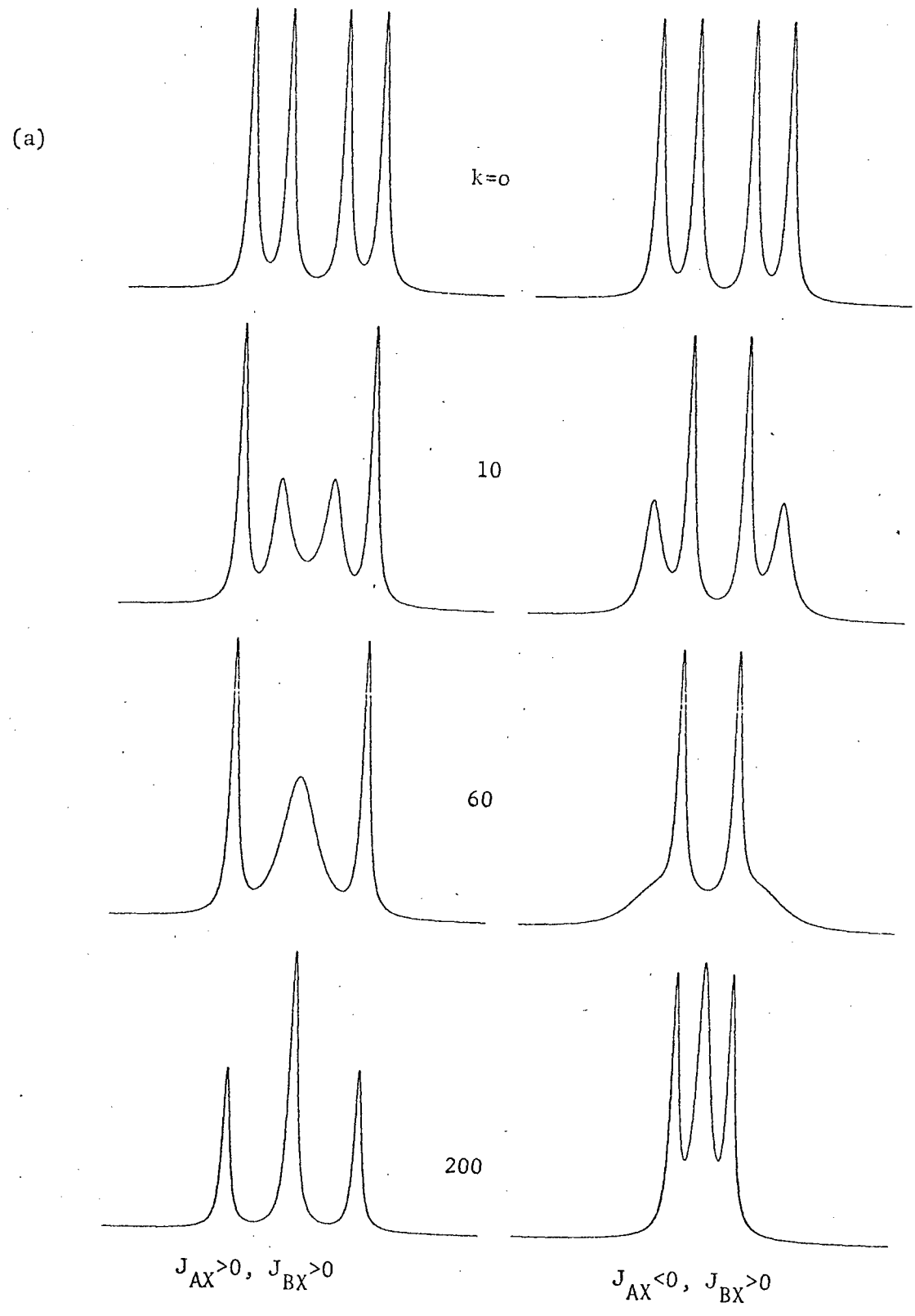

Figure 2.10 Intramolecular exchange lineshapes for the X-part of a first-order ABX spectrum

states αβ and βα. Similarly, Fig. 2.9b shows the general X-part spectrum for $J_{AX} < 0$ and $J_{BX} > 0$. In this case the fast exchange limit may be defined by $k >> J_+$, with $J_+ = \frac{1}{2}(J_{BX} + |J_{AX}|)$. The corresponding ($\Omega$ = 4.0 Hz, J_{AX} = - 2.0 Hz) absorption mode lineshapes are shown in Fig. 2.10b, and again, the relative signs of the coupling constants J_{AX} and J_{BX} give rise to marked differences in these lineshapes allowing a simple sign determination from experimental spectra.

A lineshape analysis of both the AB- and X-parts of an experimental ABX spectrum allows a check on the internal consistency of the fitting procedure used to obtain rate constants. Also, the coalescence condition for the AB-part of the spectrum is defined by the chemical shift difference 2Ω, whereas the corresponding condition for the X-part is defined by the parameters $J_- = \frac{1}{2}(J_{BX} - J_{AX})$ and $J_+ = \frac{1}{2}(J_{BX} + |J_{AX}|)$ for the same and different relative signs of J_{AX} and J_{BX}, respectively. Thus, if J_- (or J_+) and Ω differ significantly, a lineshape analysis of both parts of the spectrum allows an accurate determination of rate constants over an extended temperature range leading to more reliable activation parameters for the intramolecular exchange process involved.

2.6 Second-Order J-Coupling.

In a general nuclear spin system, the non-secular part of the spin Hamiltonian describing indirect spin-spin coupling may be considered to represent a mixing of basic spin eigen-states. As mixed states are most conveniently described by a density matrix[11,92], spin transfer effects in a second-order (tightly-coupled) spin system can be rigorously described only in terms of quantum-statistical mechanics[10] using

the spin density matrix formalism[14, 16, 23]. An intramolecular chemical exchange process will be considered in terms of a density matrix for an ABX spin system to develop a more general model for exchange and to show a correlation with the semi-classical modified Bloch equations already presented for a first-order ($J_{AB} = 0$) ABX spin system.

The spin Hamiltonian for a general ABX spin system in a fixed frame of reference may be expressed in the form

$$\begin{aligned}\mathcal{H} &= \mathcal{H}_o + \mathcal{H}_{\Omega} + \mathcal{H}_J^{(1)} + \mathcal{H}_J^{(2)} \\ &= -\omega_o\left[I_{zA} + I_{zB} + I_{zX}\right] + \Omega\left[I_{zA} - I_{zB}\right] + \Omega_X I_{zX} \\ &\quad + JI_{zA}I_{zB} + J_{AX}I_{zA}I_{zX} + J_{BX}I_{zB}I_{zX} + \tfrac{1}{2}J(I_A^+I_B^- + I_A^-I_B^+) \qquad (2.6.1)\end{aligned}$$

where J is the AB indirect spin-spin coupling constant and all other parameters have been previously defined, cf. Eqs. (2.5.1) and (2.5.9). For simplicity, the relative chemical shifts for the A- and B-spins have been defined as $\Omega_A = -\Omega$ and $\Omega_B = +\Omega$, cf. Eq. (2.5.4). In a more general formulation, the Zeeman and chemical shift terms in Eq. (2.6.1) would be expressed as

$$\mathcal{H}_o + \mathcal{H}_{\Omega} = -(\omega_o - \bar{\Omega})\left[I_{zA} + I_{zB} + I_{zX}\right] - \left[\Omega_A I_{zA} + \Omega_B I_{zB} + \Omega_X I_{zX}\right] \qquad (2.6.2)$$

with $\bar{\Omega} = \tfrac{1}{2}(\Omega_A + \Omega_B)$.

In the Schrödinger representation with basis functions ϕ_ℓ, an N-spin system is described by the wave function

$$\psi(t) = \sum_{\ell=1}^{N} c_\ell(t)\phi_\ell, \qquad (2.6.3)$$

and the time-dependent expansion coefficients define an ensemble-average spin density matrix[11], $\underline{\rho}$, with elements

$$\rho_{j\ell}(t) = \langle\phi_j|\rho|\phi_\ell\rangle = c_j(t)c_\ell^*(t). \qquad (2.6.4)$$

A simplified Schrödinger equation of motion[92] for this density matrix is now obtained as

$$\frac{d}{dt}\underline{\rho} = i\left[\underline{\rho}, \underline{\mathcal{H}}\right] - \frac{1}{T_1}(\underline{\rho} - \underline{\rho}^\circ) - \frac{1}{T_2}\underline{\rho} \qquad (2.6.5)$$

by adding phenomenological terms[21] to define spin-spin and spin-lattice relaxation, such that $\underline{\rho}^\circ$ is the ensemble thermal equilibrium density matrix. The Hamiltonian $\mathcal{H}$ is given in Eq. (2.6.5) in matrix form for the chosen basis $\{\phi_\ell\}$. A random intramolecular spin transfer, as defined by a correlation time τ, may be described by an additional term in the density matrix equation of motion[14-16]

$$\frac{d}{dt}\underline{\rho} = \left[\mathrm{E}\,\underline{\rho}\,\mathrm{E} - \underline{\rho}\right]\tau^{-1} \qquad (2.6.6)$$

where E is a spin operator defined under the assumptions that following spin transfer the spin Hamiltonian has the same form and that non-equivalent spins have simply interchanged magnetic properties. In Eq. (2.6.6), τ may be considered as the average time between spin transfers and hence a first-order rate constant for the transfer process may be defined as $k = \tau^{-1}$.

Under the action of an observing rf field, $\underline{H}_1$, the spin system is most conveniently considered in an interaction representation corresponding to the classical rotating reference frame previously discussed. The equation of motion for the density matrix in such a

representation, and in the limit of zero saturation such that the spin system shows a minimal deviation from thermal equilibrium conditions, is given in accordance with Eqs. (2.6.1), (2.6.5) and (2.6.6) in component form as

$$\frac{d}{dt}\rho_{jl} = ix\langle\phi_j|\left[\rho, I_{zA}+I_{zB}+I_{zX}\right]|\phi_l\rangle + i\omega\langle\phi_j|\left[\rho, I_{zA}-I_{zB}\right]|\phi_l\rangle$$

$$+ i\omega_X\langle\phi_j|\left[\rho, I_{zX}\right]|\phi_l\rangle + iJ\langle\phi_j|\left[\rho, I_{zA}I_{zB}+\tfrac{1}{2}(I_A^+I_B^- + I_A^-I_B^+)\right]|\phi_l\rangle$$

$$+ iJ_{AX}\langle\phi_j|\left[\rho, I_{zA}I_{zX}\right]|\phi_l\rangle + iJ_{BX}\langle\phi_j|\left[\rho, I_{zB}I_{zX}\right]|\phi_l\rangle$$

$$+ k\langle\phi_j|E\rho E|\phi_l\rangle - k\rho_{jl} - \frac{1}{T_2}\rho_{jl}$$

$$+ i\omega_1\langle\phi_j|\left[\rho, I_{xA}+I_{xB}+I_{xX}\right]|\phi_l\rangle \quad , \tag{2.6.7}$$

where $\omega_1 = \gamma H_1$ and x is the independent frequency variable (rad. sec.$^{-1}$) defined as $x = \omega - \omega_o$, cf. Eq. (2.2.24). In the high temperature approximation[16], an evaluation of the matrix element describing the interaction of the spin system with the irradiating rf field in Eq. (2.6.7) is simplified by defining a real constant C such that

$$i\omega_1\langle\phi_j|\left[\rho, I_{xA}+I_{xB}+I_{xX}\right]|\phi_l\rangle = -iC(M_j-M_l) \tag{2.6.8}$$

where $C = \omega_o\omega_1/2kT$, k in this instance being the Boltzmann constant.

The component quantum number M_ℓ is given by $M_\ell = \sum_{i=1}^{N} m_{\ell i}$, cf. Eq. (2.5.8); that is, for the basis function ϕ_ℓ: $\left[I_{zA} + I_{zB} + I_{zX} \right] \phi_\ell = M_\ell \phi_\ell$.

The expectation value of the complex transverse nuclear magnetization, $\underline{G}$, as defined in Eq. (2.4.3) and shown in Fig. 2.2, is now given directly in terms of the spin system transition operator I^+ and the frequency variable x as

$$G(x) = A\langle I^+ \rangle = Tr\{\underline{\underline{\rho}} \cdot \underline{\underline{I}}^+\} \qquad (2.6.9)$$

where A may be treated as a normalization constant and Tr{...} denotes the trace of the matrix product $\underline{\underline{\rho}} \cdot \underline{\underline{I}}^+$ over the spin states. The matrix elements $\rho_{j\ell}$ are in general complex[11] and show an implicit x dependence through Eq. (2.6.7). The transition operator I^+ defines the non-zero elements of the matrix $\underline{\underline{I}}^+$ in the basis $\{\phi_\ell\}$ and hence effectively determines the density matrix elements defining G(x) in Eq. (2.6.9). Consistent with the normal selection rule for magnetic dipolar transitions, the total ABX spin system (I = ½ spins) operator may be defined as $I^+ = I_A^+ + I_B^+ + I_X^+$, such that $I^+ \phi_j = \delta_{M_\ell, M_j + 1} \phi_\ell$, cf. Eq. (2.6.8). The basis functions connected by this operator differ in only one part $\xi_{\ell i}$ of the product function ϕ_ℓ, cf. Eq. (2.5.8), corresponding to the component operator I_i^+. In this manner, it is possible to assign transitions to a specific spin within a given spin system in the first-order J-coupling limit. It should be noted at this point, however, that the operator defined above does not determine the combination transitions of finite intensity normally associated with a tightly coupled nuclear spin system. These combination transitions may be determined only by generalizing the operator I^+ to connect <u>all</u>

basis function ϕ_j and ϕ_ℓ with $M_\ell - M_j = +1$. The product basis functions ϕ_ℓ for an ABX ($I = \frac{1}{2}$) spin system and the corresponding upper diagonal $\underline{\underline{I}}^+$ matrix are shown in Table 2.3, the elements determining combination transitions being in parentheses. For the basis functions ordered as shown in Table 2.3 the matrix elements I^+_{13} and I^+_{24} define A-spin transitions in the first-order limit as already described for an ABX ($J_{AB} = 0$) spin system, cf. Table 2.2. The corresponding B-spin transitions are defined by the matrix elements I^+_{12} and I^+_{34}; in accordance with Eq. (2.6.9), the density matrix elements ρ_{21}, ρ_{31}, ρ_{42} and ρ_{43} describe an AB-part of a general ABX spectrum. Thus the $\underline{\underline{I}}^+$ matrix in the factored form indicated in Table 2.3 shows that the ABX transitions may be considered in terms of sets of density matrix elements

$$G^*(x) = A\left\{ (\rho_{12} + \rho_{13} + \rho_{24} + \rho_{34}) + (\rho_{56} + \rho_{57} + \rho_{68} + \rho_{78}) + (\rho_{15} + \rho_{26} + \rho_{27} + \rho_{36} + \rho_{37} + \rho_{48}) \right\} \qquad (2.6.10)$$

where $\rho_{j\ell} = \rho^*_{\ell j}$ for the Hermitean density matrix[11] $\underline{\underline{\rho}}$. The density matrix elements within each of these sets are now defined by coupled equations of motion of the form given in Eq. (2.6.7).

A basic intramolecular exchange process may now be considered to correspond to a transfer of nuclear magnetization between spin-sites distinguished by chemical shifts for the coupled inequivalent A- and B-spins, $-\Omega$ and Ω, respectively. An example of such a process is the hindered rotation in a molecular system having two possible conformations giving rise to the AB-spin inequivalence, this rotation being defined in terms of a single first-order rate constant, k sec.$^{-1}$. For the chosen product basis functions ϕ_ℓ, the operator E given in Eq. (2.6.6) and

Table 2.3

Basis Functions for ABX Spin Systems

$I = \frac{1}{2}$ Nuclear Spins

ℓ	1	2	3	4	5	6	7	8
ϕ_ℓ	$\alpha\alpha\alpha$	$\alpha\beta\alpha$	$\beta\alpha\alpha$	$\beta\beta\alpha$	$\alpha\alpha\beta$	$\alpha\beta\beta$	$\beta\alpha\beta$	$\beta\beta\beta$
M_ℓ	$\frac{3}{2}$	$\frac{1}{2}$	$\frac{1}{2}$	$\frac{1}{2}$	$\frac{1}{2}$	$\frac{1}{2}$	$\frac{1}{2}$	$\frac{3}{2}$

Spin Transition Operator $\underline{\underline{I}}^+$ Matrix in Basis $\{\phi_\ell\}$.

	1	2	3	4	5	6	7	8
1	0	1	1	0	1	0	0	0
2		0	0	1	0	1	(1)	0
3			0	1	0	(1)	1	0
4				0	(1)	0	0	1
5					0	1	1	0
6						0	0	1
7							0	1
8								0

describing the above exchange process for an equal population system may be defined by

$$E|\alpha\alpha\xi_x\rangle = |\alpha\alpha\xi_x\rangle, \qquad E|\alpha\beta\xi_x\rangle = |\beta\alpha\xi_x\rangle \tag{2.6.11}$$

Application of this exchange operator in Eq. (2.6.7) shown that under steady-state conditions ($\frac{d}{dt}\underline{\underline{\rho}} = 0$) the density matrix elements describing an AB-part of the ABX spectrum in the presence of exchange are given by sets of coupled equations which may be expressed in the general matrix form:

$$\underline{\underline{R}}'\cdot\underline{G}' = -i\underline{C}\underline{P}' \tag{2.6.12}$$

such that

$$\begin{bmatrix} r+i\left[x+\omega+\frac{1}{2}(J+J_{AX})\right] & -i\frac{J}{2}-k \\ -i\frac{J}{2}-k & r+i\left[x-\omega+\frac{1}{2}(J+J_{BX})\right] \end{bmatrix} \begin{bmatrix} \rho_{13} \\ \rho_{12} \end{bmatrix} = -iC \begin{bmatrix} 1 \\ 1 \end{bmatrix}$$

and

$$\begin{bmatrix} r+i\left[x+\omega-\frac{1}{2}(J-J_{AX})\right] & i\frac{J}{2}-k \\ i\frac{J}{2}-k & r+i\left[x-\omega-\frac{1}{2}(J-J_{BX})\right] \end{bmatrix} \begin{bmatrix} \rho_{24} \\ \rho_{34} \end{bmatrix} = -iC \begin{bmatrix} 1 \\ 1 \end{bmatrix}$$

(2.6.13)

where $r = \frac{1}{T_2} + k$. It is assumed that spin-spin relaxation effects in the absence of exchange are defined by the single relaxation time T_2, cf. Eq. (2.6.5). The above matrix equation is equivalent to those previously derived in terms of semi-classical modified Bloch equations for the simple two-site exchange system, cf. Eq. (2.2.12), and a multi-site exchange system in the first order J-coupling limit, (cf. Eq. 2.4.4). In the tightly coupled ($J_{AB} \neq 0$) ABX spin system, linear combinations of the vector elements G'_j may be considered to define transverse spin-site magnetizations analogous to those associated with the isochromats $\underline{M}(x_j, \phi_j)$ in the first-order limit, cf. Fig. 2.2. That is, a spin-site magnetization vector $\underline{G}$ is defined by

$$\underline{\underline{D}} \cdot \underline{G} = -iC\underline{Q} \qquad (2.6.14)$$

where $\underline{\underline{D}}$ is the diagonal matrix corresponding to $\underline{\underline{R}}'$. In this manner, the elements of the matrix $\underline{\underline{D}}$ determine the positions and general lineshape characteristics for specific spin-sites and the elements of the vector $\underline{Q}$ determine the overall spectral intensities associated with these sites. It should be noted that, through the definition of the general spin density matrix element in Eq. (2.6.4), this diagonal matrix is equivalent to that obtained in a basis $\{\psi_\ell\}$ consisting of eigen-functions ψ_ℓ of the spin Hamiltonian defined in Eq. (2.6.1). The above diagonalization procedure is also directly related to that already used in the simplified first-order limit, cf. Eq. (2.4.6). The detailed form of the AB-part spectrum associated with the vector elements designated as $G'_1 = \rho_{13}$ and $G'_3 = \rho_{12}$ may now be determined in terms of the vector elements G_1 and G_3 (defining spin-sites 1 and 3) corresponding to the

diagonal matrix elements D_1 and D_3 given from Eq. (2.6.13) as

$$D_1 = r + i\,x + \tfrac{1}{2}(J + J_+) + D_- \quad ,$$

$$D_3 = r + i\,x + \tfrac{1}{2}(J + J_+) - D_-$$

with $D_- = \tfrac{1}{2}\,4(\Omega^2 - k^2) + J(J - 4ik) + J_-(J_- - 4\Omega)^{\frac{1}{2}}$ and $J_\pm = \tfrac{1}{2}(J_{BX} \pm J_{AX})$. In accordance with Eq. (2.6.14), a partial lineshape function may now be expressed in the form

$$G_1(x) + G_3(x) = iA\left\{\frac{a+id}{\mathcal{D}_1} + \frac{b+ie}{\mathcal{D}_2}\right\} \qquad (2.6.15)$$

where the normalization constant A includes C and the complex $\underline{Q}$ vector elements corresponding to G_1 and G_3 have been defined as $Q_1 = a + id$ and $Q_3 = b + ie$. These intensity vector elements are now determined by equating Eqs. (2.6.13) and (2.6.15), that is

$$(r + k) + i\,x + J + \tfrac{1}{2}J_+ = (a + id)\{r + i[x + \tfrac{1}{2}(J + J_+) - D_-]\} +$$
$$+ (b + ie)\{r + i[x + \tfrac{1}{2}(J + J_+) + D_-]\}.$$

Thus the partial lineshape corresponding to spin-sites 1 and 3 is given in terms of $G_1(x)$ and $G_3(x)$, where

$$G_1(x) = i\frac{A}{2}\,\frac{1 - \beta_-}{r + i[x + \tfrac{1}{2}(J+J_+) + D_-]}$$

$$G_3(x) = i\frac{A}{2}\,\frac{1 + \beta_-}{r + i[x + \tfrac{1}{2}(J+J_+) - D_-]} \qquad (2.6.16)$$

with $\beta_- = (\tfrac{1}{2}J - ik)/D_-$. As usual, the absorption mode spectrum is described by the imaginary parts of $G_1(x)$ and $G_3(x)$. In the absence of

exchange (k = 0), Eq. (2.6.16) shows that $G_1(x)$ defines a Lorentzian absorption mode line with a full-width at half-maximum of $2/T_2$ rad. $sec.^{-1}$ centred at $x_1 = -\frac{1}{2}(J + J_+) - D_-$ with a relative intensity of $1 - J/2D_-$. This component line is represented as spin site-1 in Fig. 2.11 showing the complete AB-part of the ABX spectrum, where it has been assumed that $J_{BX} > J_{AX} > J > 0$. As the independent frequency variable x and the common relaxation time T_2 form part of the diagonal elements of the matrix $\underline{\underline{R}}'$ in Eq. (2.6.12), this matrix may be reformulated to give

$$\left[\underline{\underline{R}} + \left(\frac{1}{T_2} + ix\right)\underline{\underline{I}}\right]\underline{G}' = -iC\underline{P}' \ , \qquad (2.6.17)$$

where $\underline{\underline{I}}$ is the unit matrix. Spectral characteristics associated with exchange are now defined in terms of a diagonal matrix $\underline{\underline{\Lambda}}$ corresponding to $\underline{\underline{R}}$, where in accordance with Eq. (2.6.14)

$$\left[\underline{\underline{\Lambda}} + \left(\frac{1}{T_2} + ix\right)\underline{\underline{I}}\right]\underline{G} = -iC\underline{Q}. \qquad (2.6.18)$$

The elements of the matrix $\underline{\underline{\Lambda}}$, λ_j, and the corresponding intensity factors Q_j are given in Table 2.4 for all spin sites-j in the AB-part of an ABX spectrum. Thus it is seen that in the absence of exchange, the density matrix elements ρ_{12}, ρ_{13}, ρ_{24} and ρ_{34} determine the spectral characteristics for the spin sites 1 - 4, this part of the spectrum consisting of a typical AB quartet. It is interesting to note the correlation between these particular density matrix elements and the energy levels defining the degenerate AB spin sites for a first-order ($J_{AB} = 0$) ABX spin system as listed in Table 2.2.

For the type of intramolecular exchange process under consideration for an ABX spin system, the exchange operator E determines

Table 2.4

AB-Part of an ABX Spectrum

Spin Site-j	Matrix Element λ_j	Intensity Factor Q_j
1	$\frac{1}{2}(J + J_+) + D_-$	$1 - \beta_-$
2	$-\frac{1}{2}(J - J_+) + D_+$	$1 + \beta_+$
3	$\frac{1}{2}(J + J_+) - D_-$	$1 + \beta_-$
4	$-\frac{1}{2}(J - J_+) - D_+$	$1 - \beta_+$
5	$\frac{1}{2}(J - J_+) + E_-$	$1 - \gamma_-$
6	$-\frac{1}{2}(J + J_+) + E_+$	$1 + \gamma_+$
7	$\frac{1}{2}(J - J_+) - E_-$	$1 + \gamma_-$
8	$-\frac{1}{2}(J + J_+) - E_+$	$1 - \gamma_+$

$$D_\pm = \tfrac{1}{2}\left[4(\Omega^2 - k^2) + J(J \pm 4ik) + J_-(J_- - 4\Omega)\right]^{\frac{1}{2}}$$

$$E_\pm = \tfrac{1}{2}\left[4(\Omega^2 - k^2) + J(J \pm 4ik) + J_-(J_- + 4\Omega)\right]^{\frac{1}{2}}$$

$$\beta_\pm = \left[\tfrac{1}{2}J \pm ik\right]/D_\pm \ , \quad \gamma_\pm = \left[\tfrac{1}{2}J \pm ik\right]/E_\pm$$

$$J_\pm = \tfrac{1}{2}(J_{BX} \pm J_{AX})$$

the independence of the two quartets forming the AB-part of the spectrum. Thus the form of the matrices in Eq. (2.6.13), as defined by the spin transition operator I^+ (and E) allows a relatively simple analytical formulation of the absorption mode lineshape for a component AB quartet. From Eq. (2.6.16) and similar expressions for $G_2(x)$ and $G_4(x)$, this lineshape is obtained for an equal population exchange system as

$$V(w) = A\left\{\frac{(r+k)A_+ + (w+J)B_+}{A_+^2 + B_+^2} + \frac{(r+k)A_- + (w-J)B_-}{A_-^2 + B_-^2}\right\} \quad (2.6.19)$$

where

$$A_\pm = \frac{1}{T_2}\left(\frac{1}{T_2} + 2k\right) + \omega^2 - \left(w \pm \frac{J}{2}\right)^2 + \frac{J^2}{4}$$

$$B_\pm = 2w\left(\frac{1}{T_2} + k\right) \pm \frac{1}{T_2}J$$

The independent frequency variable w has been defined, to simplify the above expression, as $w = x + \frac{1}{2}J_+$ for the AB quartet centred on $x = -\frac{1}{2}J_+$, cf. Table 2.4. Also, in this manner Eq. (2.6.19) may be applied in general for a similar intramolecular exchange process in an arbitrary AB spin system. Such an analytical expression for the absorption mode lineshape allows a very efficient iterative comparison with experimental data. Also, it is readily seen that Eq. (2.6.19) reduces to the lineshape equation previously derived for the simple two site uncoupled AB spin system, cf. Eq. (2.2.15) with $x = w$, from semi-classical modified Bloch equations. Using Eq. (2.6.19) and a similar expression for the AB quartet centred at $x = \frac{1}{2}J_+$, lineshapes have been calculated for a range of the parameter k/Ω and are shown in Fig. 2.11. These absorption

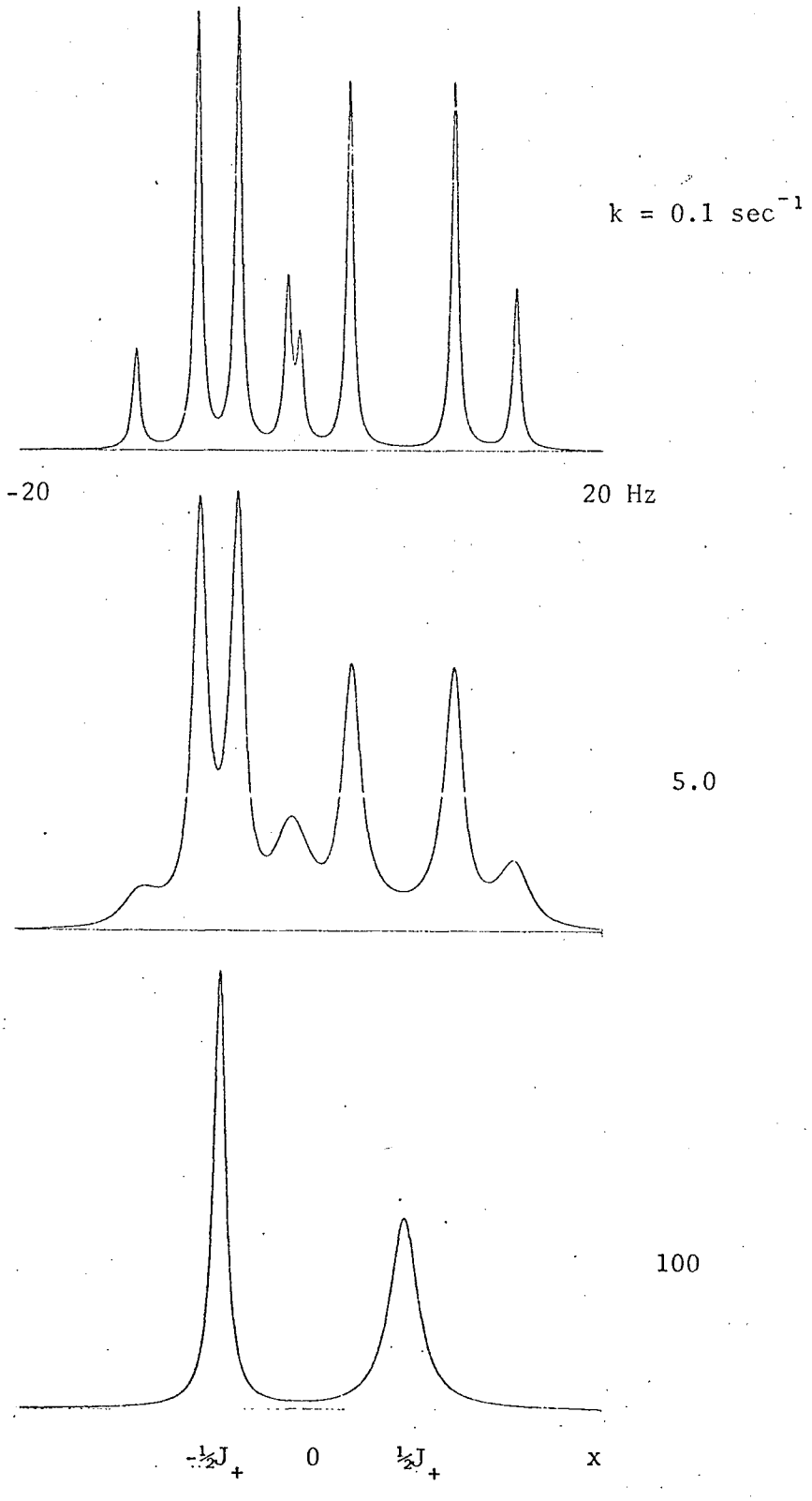

Fig. 2.11 AB-part of a general ABX spectrum.

mode lineshapes are defined by the parameters Ω = 4.0 Hz, J = 4.2 Hz, J_{AX} = 10.0 Hz, J_{BX} = 15.0 Hz and T_2 = 0.64 sec. (0.5 Hz full-width at half-maximum), and may be compared with those for the first-order ABX spin system shown in Fig. 2.8a.

A basic intramolecular exchange process has been considered in terms of a transfer of nuclear magnetization between spin-sites distinguished by distinct chemical shifts for the coupled inequivalent A- and B-spins. The operator describing this process, cf. Eq. (2.6.6), may be generalized to include an unequal population exchange system. An example of this more general exchange process is the hindered rotation in a molecular system having two possible conformations, one of which is preferred. The exchange terms in the component equation of motion for the density matrix, Eq. (2.6.7), may be considered in the form $k_A\langle\phi_j|E\rho E|\phi_\ell\rangle - k_B\rho_{j\ell}$, where k_A is the probability for a transfer from a basic A-spin site with a fractional population p_A. In terms of a matrix equation of the general form given in Eq. (2.6.12), the density matrix elements ρ_{12} and ρ_{13} are now defined by

$$\begin{bmatrix} r_A + i\left[\chi + \omega + \tfrac{1}{2}(J + J_{AX})\right] & -i\frac{J}{2} - k_B \\ -i\frac{J}{2} - k_A & r_B + i\left[\chi - \omega + \tfrac{1}{2}(J + J_{BX})\right] \end{bmatrix} \begin{bmatrix} \rho_{13} \\ \rho_{12} \end{bmatrix} = -iC \begin{bmatrix} p_A \\ p_B \end{bmatrix} \quad (2.6.20)$$

where $r_A = \frac{1}{T_2} + k_A$ with $p_A + p_B = 1$ and $p_A k_A = p_B k_B$. This matrix formulation for an unequal population system allows a much simpler calculation of lineshapes, for the particular exchange process under consideration, than an alternative procedure proposed by Johnson[23].

The partial lineshape associated with the above density matrix elements is given by $G_1(x)$ and $G_3(x)$ in Eq. (2.6.16) where the parameters D_- and β_- are now defined as

$$\mathcal{D}_- = \tfrac{1}{2}\left[4(\omega^2-k^2) + J(J-4ik) + J_-(J_--4\omega) - 4ik(\Delta J + 2i\Delta k\omega)\right]^{\frac{1}{2}}$$

and

$$\beta_- = \left[\tfrac{J}{2} - ik - \Delta J - \Delta p\omega \right] / \mathcal{D}_-$$

with $\Delta J = J_+ - (p_A J_{BX} + p_B J_{AX})$, $2k = k_A + k_B$ and $\Delta p = p_A - p_B$. The complete AB-part spectrum may now be defined in terms of the matrix elements λ_j and corresponding intensity factors Q_j, cf. Eq. (2.6.18), as given in Table 2.4 with modified parameters:

$$\mathcal{D}_\pm = \tfrac{1}{2}\left[4(\omega^2-k^2) + J(J\pm 4ik) + J_-(J_--4\omega) - 4ik(\Delta J + 2i\Delta k\omega)\right]^{\frac{1}{2}}$$

$$E_\pm = \tfrac{1}{2}\left[4(\omega^2-k^2) + J(J\pm 4ik) + J_-(J_-+4\omega) + 4ik(\Delta J - 2i\Delta k\omega)\right]^{\frac{1}{2}}$$

$$\beta_\pm = \left[\tfrac{J}{2} \pm ik - \Delta J - \Delta p\omega \right] / \mathcal{D}_\pm$$

$$\gamma_\pm = \left[\tfrac{J}{2} \pm ik + \Delta J - \Delta p\omega \right] / E_\pm \qquad (2.6.21)$$

It has been assumed that all J-coupling constants in the ABX spin system have the same sign. For the particular exchange process considered, the form of the AB-part spectrum may be critically dependent upon the relative signs of these coupling constants due to terms such as $\pm 4ikJ$ and $\pm 4J_-\Omega$ in the characteristic parameters $D_\pm$ and $E_\pm$. Thus the relative signs of J_{AX} and J_{BX} with respect to the AB coupling constant J determine the form of the AB-part spectrum in a manner similar to that for a first-order ABX system as illustrated in Fig.

2.8, and a complete lineshape fit to experimental data may allow a simple determination of the relative signs of all coupling constants for a general ABX spin system.

The X-part of an ABX spectrum has been shown to be determined by the six spin density matrix elements ρ_{15}, ρ_{26}, ρ_{27}, ρ_{36}, ρ_{37} and ρ_{48}, cf. Eq. (2.6.10). The elements ρ_{27} and ρ_{36} are associated with combination transitions, and comparison with the energy levels determining the X-part of a first-order ABX spectrum, cf. Table 2 shows that (2, 7) and (3,6) are not included in this limit. The chosen basis functions ϕ_1, ϕ_5, ϕ_4 and ϕ_8 are invariant under the exchange operator E as defined in Eqs. (2.6.6) and (2.6.11), and hence ρ_{15} and ρ_{48} are directly related, through Eq. (2.6.14), to the transverse magnetization associated with spin-sites 1 and 6 as shown in Fig. 2.12. In the presence of exchange, these spin-sites correspond to simple Lorentzian lines determined from Eqs. (2.6.7) and (2.6.14) as

$$G_1(x) = iA \frac{\frac{1}{T_2}}{\frac{1}{T_2} + i(x + \omega_x + J_+)}$$

$$G_6(x) = iA \frac{\frac{1}{T_2}}{\frac{1}{T_2} + i(x + \omega_x - J_+)} \qquad (2.6.22)$$

The remaining spin-site magnetizations are determined by a 4 x 4 matrix $\underline{R}$ in Eq. (2.6.16), that is

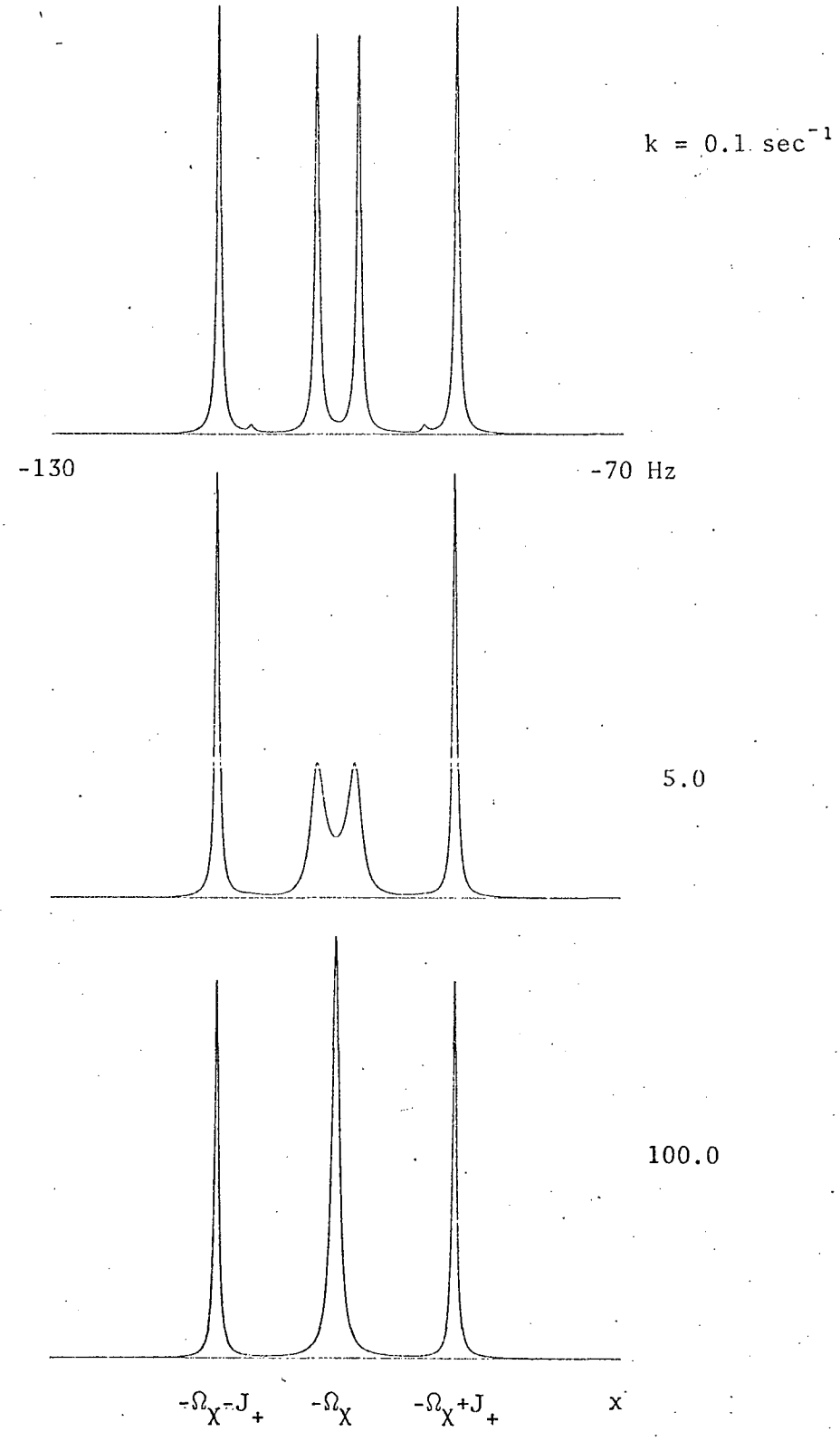

Fig. 2.12 X-part of a general ABX spectrum.

$$\underline{\underline{R}} = \begin{bmatrix} k+iJ_- & -i\frac{J}{2} & i\frac{J}{2} & -k \\ -i\frac{J}{2} & k+2i\omega & -k & i\frac{J}{2} \\ i\frac{J}{2} & -k & k-2i\omega & -i\frac{J}{2} \\ -k & i\frac{J}{2} & -i\frac{J}{2} & k-iJ_- \end{bmatrix}, \quad \underline{G}' = \begin{bmatrix} \rho_{26} \\ \rho_{27} \\ \rho_{36} \\ \rho_{37} \end{bmatrix}, \quad \underline{P}' = \begin{bmatrix} 1 \\ 0 \\ 0 \\ 1 \end{bmatrix} \qquad (2.6.23)$$

where $[\underline{\underline{R}} + \{\frac{1}{T_2} + i(x + \Omega_x)\}\underline{\underline{I}}]\underline{G}' = -iC\underline{P}'$. The elements of the vector $\underline{P}'$ corresponding to combination transitions (2 and 5 in Fig. 2.12) are set equal to zero to allow a consistent application of the generalized I^+ operator in the evaluation of the general spin density matrix equation of motion term given in Eq. (2.6.8). The lineshape function G(x) describing this portion of the ABX spectrum is most readily evaluated by considering the above equation in the general forms given in Eqs. (2.6.16) and (2.6.17). That is, a diagonal matrix $\underline{\underline{\Lambda}}$ is derived from the matrix $\underline{\underline{R}}$ through a similarity transformation as described in detail for the first-order ABX spin system, cf. Eq. (2.5.14). For a tightly coupled spin system, however, the vector $\underline{I}$ in Eq. (2.5.14) must take the same form as $\underline{P}$ to allow for the effect of combination transitions on the overall lineshape. Computed lineshapes for the X-part of an equal population ABX spin system are shown in Fig. 2.12 for the parameters chosen to define the AB-part spectrum, cf. Fig. 2.11. Again, these lineshapes may be compared with those for the first-order ABX system, cf. Fig. 2.10a. It is to be noted that for particular cases, for example, when J_{BX}, $J_{AX} >> J$ in a heteronuclear system, it is possible

to treat the X-part spectrum as that in the first-order limit. In this approximation, the overall lineshape is simply obtained in terms of $G_1(x)$ and $G_6(x)$ given in Eq. (2.6.22) and a lineshape for an effective two-site exchange system with spin-site frequencies defined in Table 2 as $x_3 = -\Omega_x - J_-$ and $x_4 = -\Omega_x + J_-$, cf. Eq. (2.2.15) with $\Omega = J_-$. The basic condition for this approximation, of course, corresponds to a complete neglect of the off-diagonal elements in J in the matrix $\underline{\underline{R}}$. In general, the effect of different relative signs of J_{AX} and J_{BX} is very similar to that illustrated for the first-order case in Fig. 2.10b.

A detailed analysis of a general ABX spin system has allowed a consistent development of the physical model and matrix formulation required for a description of intramolecular exchange effects in a tightly coupled spin system. Although analytical lineshape equations may be derived in part for more complicated spin systems, a formulation of exchange effects applicable to the numerical computation of the lineshape functions G(x) and V(x) for a general tightly coupled N-spin system may now be described in terms of the properties of the density matrix model considered above. In general, having determined the density matrix elements required in the description of an NMR spectrum (or part of one) through the generalized transition operator I^+ in Eq. (2.6.9), these elements must be evaluated in accordance with the component equation of motion, Eq. (2.6.7). In the chosen basis $\{\phi_\ell\}$, the equation of motion term involving the independent frequency variable in an interaction representation is simply

$$ix\langle\phi_j|[\rho, \sum_{i=1}^{N} I_{zi}]|\phi_\ell\rangle = -ix\rho_{j\ell} \qquad (2.6.24)$$

The effective spin Hamiltonian in this representation may now be considered in the form $\mathcal{H}_\Omega + \mathcal{H}_J^{(1)} + \mathcal{H}_J^{(2)}$, analogous to that defined in Eq. (2.6.1). The part $\mathcal{H}_\Omega + \mathcal{H}_J^{(1)}$ is diagonal in the basis $\{\phi_\ell\}$ and hence it follows that

$$\langle\phi_j|[\rho, \mathcal{H}_\Omega + \mathcal{H}_J^{(1)}]|\phi_\ell\rangle = (\mathcal{H}'_{\ell\ell} - \mathcal{H}'_{jj})\rho_{j\ell} , \qquad (2.6.25)$$

with the Hamiltonian matrix element $\mathcal{H}'_{\ell\ell}$ defined by

$$\mathcal{H}_{\ell\ell} = -\sum_{i=1}^{N} \omega_i m_{\ell i} + \sum_{i=1}^{N}\sum_{j>i} J_{ij} m_{\ell i} m_{\ell j} \qquad (2.6.26)$$

where $I_{zi}\phi_\ell = m_{\ell i}\phi_\ell$, cf. Eq. (2.5.8). It is to be noted that the term $\mathcal{H}'_{\ell\ell} - \mathcal{H}'_{jj}$ defines a first-order transition energy and hence the spin density matrix element defines directly a spin-site in this limit, as previously considered for particular spin systems. Such a relationship is defined in general through the definition of a Liouville operator[92], such that the elements of the density matrix $\underline{\underline{\rho}}$ may be considered as components of a vector in a suitably defined vector space. The derivation super-operator used by Banwell and Primas[41] in a direct calculation" of NMR spectra is in fact identical to the Liouville operator defined by Fano[92]. As the second-order coupling Hamiltonian term, $\mathcal{H}_J^{(2)}$, mixes functions in the basis $\{\phi_\ell\}$ and corresponds to the off-diagonal part of the complete spin Hamiltonian, this term leads to a mixing of spin density matrix elements. Thus it follows that

$$\langle\phi_j|[\rho, \mathcal{H}_J^{(2)}]|\phi_\ell\rangle = \mathcal{H}^{(2)}_{Jj\ell'}\rho_{j\ell'} - \mathcal{H}^{(2)}_{Jj'\ell}\rho_{j'\ell} \qquad (2.6.27)$$

where $\mathcal{H}_J^{(2)}\phi_\ell = \phi_{\ell'}$ and $\mathcal{H}_J^{(2)}\phi_j = \phi_{j'}$. Similarly, the term defining exchange effects is evaluated as

$$k\langle\phi_j|E\rho E|\phi_\ell\rangle = k\rho_{j''\ell''}, \qquad (2.6.28)$$

where $E\phi_\ell = \phi_{\ell''}$. Construction of a vector $\underline{G}'$ with elements $\rho_{j\ell}$ as determined by the transition operator I^+ and also indexing vectors associated with the effective density matrix subscript contraction, specific spin Hamiltonian matrix elements and the basis functions connected by the exchange operator E allows the matrix $\underline{\underline{R}}$ in Eq.(2.6.14) to be efficiently assembled on a computer. All elements of this matrix are numerically evaluated in terms of the normal spin Hamiltonian elements defined for a specific spin system in the basis $\{\phi_\ell\}$, by making use of Eqs. (2.6.24) - (2.6.28). The computation of the absorption mode lineshape function V(x) then reduces to applications of the basic equations given in Eq. (2.4.6) and (2.4.9). The overall dimensionality of the matrix $\underline{\underline{R}}$ for an intramolecular exchange process is determined by the number of density matrix elements defined by I^+ in Eq. (2.6.9), that is, the number of allowed and combination transitions for a given spin system. As the diagonalization of the complex matrix $\underline{\underline{R}}$ and the inversion of the associated complex transformation matrix $\underline{\underline{S}}$ are the time determining computational procedures, all factorizations of these matrices as defined by the form of the Hamiltonian for a specific spin system should be taken into account. A computer program GENLIN has been developed on the basis of the simplified density matrix formulation outlined above, and will be described in more detail as related to the analysis of a particular 4-spin system in an experimental section of this thesis.

It is to be noted that, during the course of the work described here, Binsch [93] independently proposed a similar method of numerical analysis for tightly coupled spin systems based upon a more formal theory in the Liouville representation.

CHAPTER 3

INSTRUMENTATION

3.1 FT-1064 Computer Interface

Complete lineshape analyses of chemical exchange processes using NMR involve sets of data points defining the experimentally recorded steady-state spectra, a set of discrete data points being fitted to a theoretical lineshape equation to obtain a specific rate constant. The tedious manual conversion of the recorded data to digital frequency and corresponding amplitude values may be eliminated by using an electronic signal sampling device and an analog-to-digital (A-D) converter linked to a small computer with a magnetic memory core to store the digital information. Of course, the computer must scan its memory locations (channels) in synchronization with the spectrometer frequency (or field) sweep so that the signal amplitude data point in any given memory location may be accurately assigned a frequency value derived from two calibration frequencies. The digital information may be transferred to a full-scale digital computer, to allow an efficient iterative lineshape fit, via an incremental magnetic tape or a direct line if this is available. The FABRITEK FT-1064 computer has been used, in conjunction with the spectrometer-computer interface unit described below, to give an automatic digitization and fitting of NMR lineshape data.

The interface unit has been designed to allow a general appli-

cation of the FT-1064 computer with only simple modifications of spectrometer circuitry. Initially it will be assumed that the NMR signal-to-noise ratio is such that a single scan of the steady-state spectrum is sufficient to obtain data of a quality warranting a complete lineshape analysis. A block diagram showing the basic units of the interface is given in Fig. 3.1, and the associated timing control sequence may be represented as shown in Fig. 3.2. In the single scan mode, the spectrometer sweep mechanism is used under normal operating conditions and the NMR signal at the output of the spectrometer recorder amplifier is fed continuously to a high impedance input differential amplifier, A, and then to the sampling A-D converter, SW/1, of the FT-1064 computer. This differential amplifier acts as a buffer between the sampling device and the spectrometer and also allows a versatile gain and dc level control independent of the normal spectrometer controls. At time t_o the control bistable multivibrator, B, changes to its active state under the action of the manual sweep trigger, T. This multivibrator is used as a master control and as a trigger buffer, the multivibrator state at any time being shown by the indicator I. At this time, t_o, a trigger pulse from the control bistable initiates the FT-1064 channel sweep and simultaneously a positive pulse is ac-coupled to the input of the spectrometer recorder amplifier. The emitter follower F1 acts as a buffer between the control bistable and the FT-1064 sweep unit which has a relatively low input impedance. The monostable multivibrator M supplies a 5 msec pulse of an amplitude sufficient to give a well-defined vertical marker on the recorder chart, this marker accurately determining the position of the initial

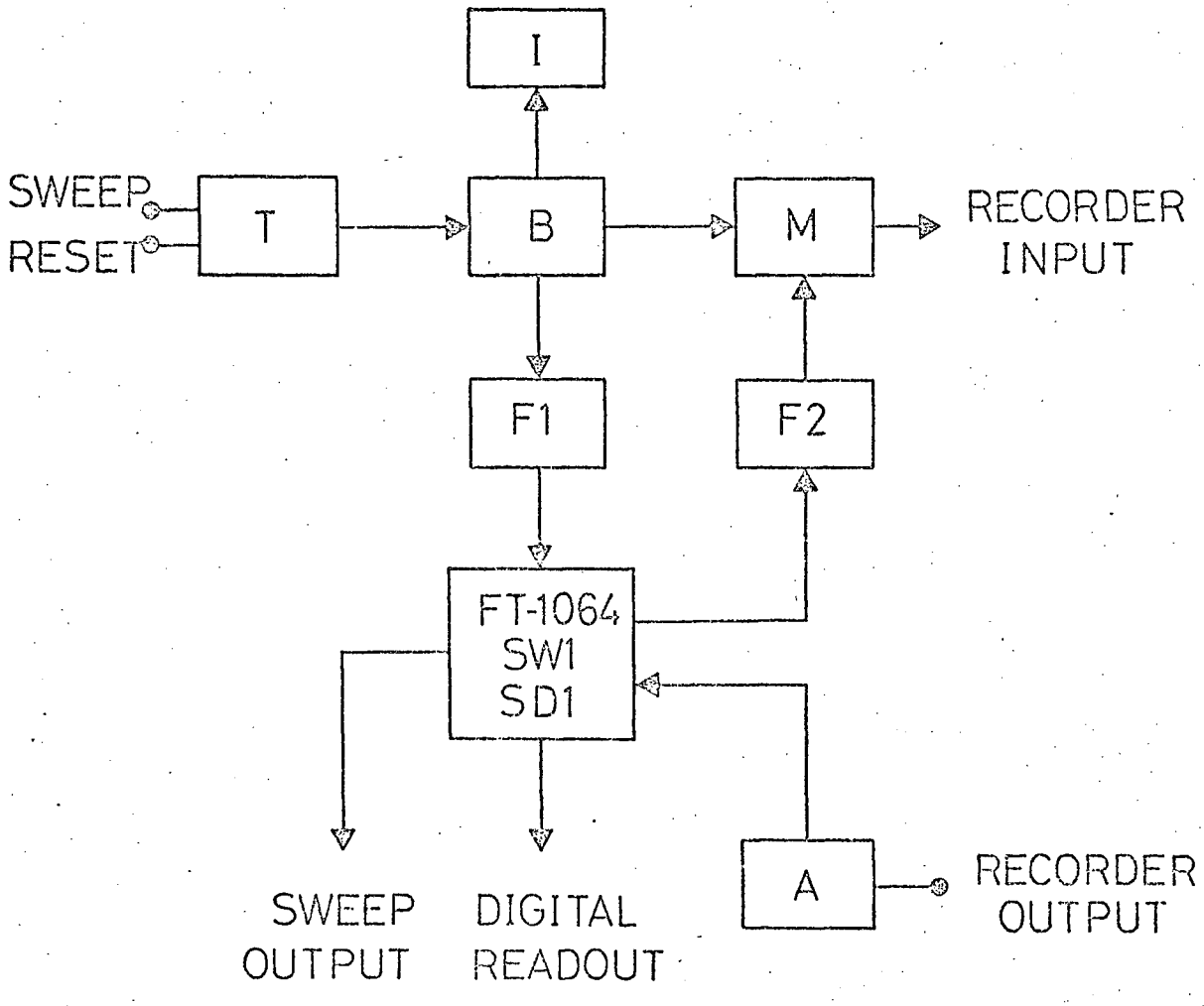

Fig. 3.1 FT-1064 computer sweep control

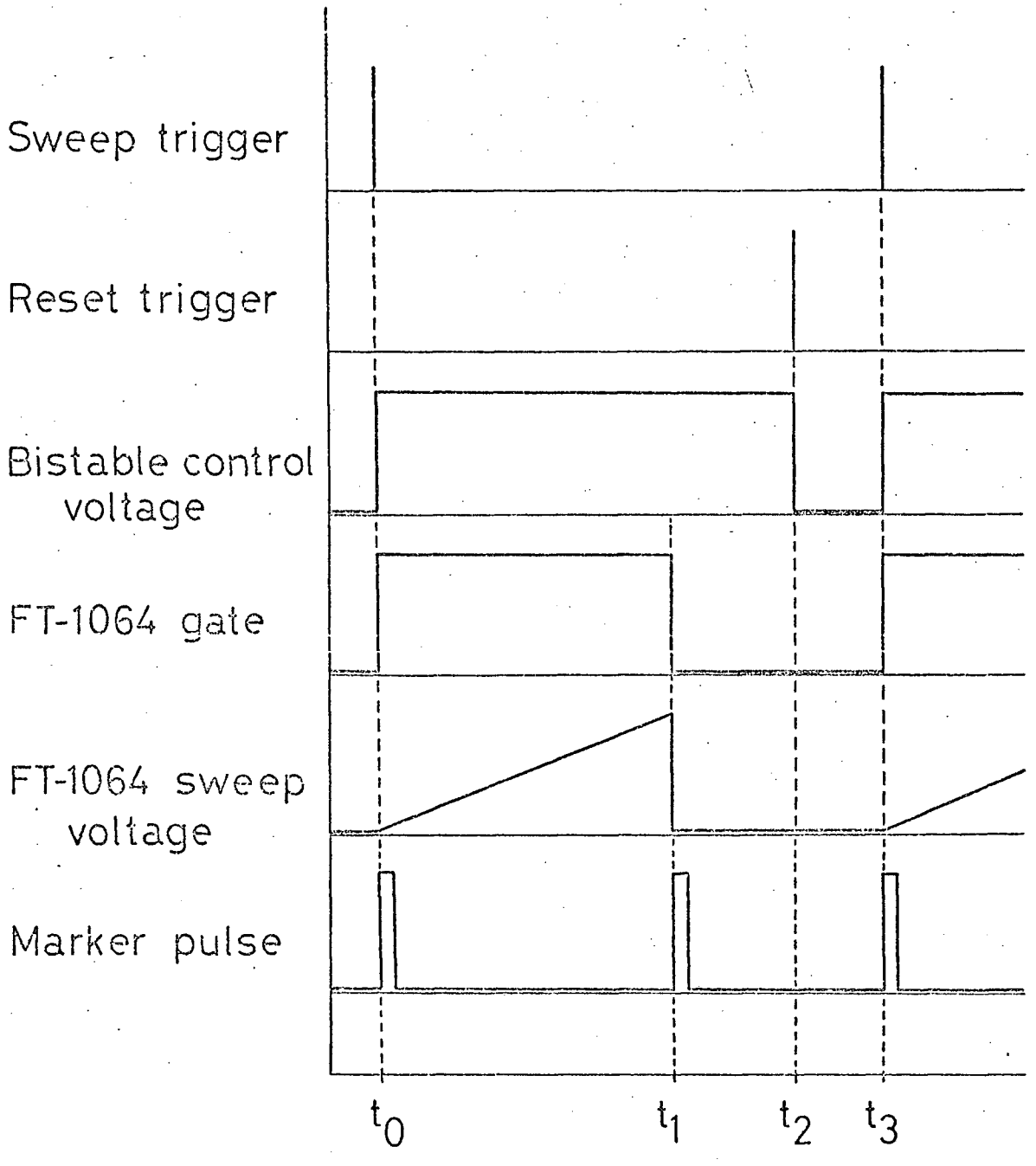

Fig. 3.2 FT-1064 control sequence

digitized data point as the sweep times used correspond to 50 msec - 2 sec per channel. A 5 msec pulse has been found to give a fast rising marker within the normal response time limit of the recorder system. In the time interval t_o to t_1 the control bistable remains in the active state, the FT-1064 gate voltage is positive and the linear channel sweep voltage changes as shown in Fig. 3.2. The analog NMR signal is sampled and digitized and also recorded on the spectrometer chart over this time interval, the digital signal amplitude data being continuously stored in the computer magnetic core memory. At time t_1, the FT-1064 channel sweep is complete and a positive pulse derived from the trailing edge of the gate, in the inversion and differentiation unit F2, triggers the monostable multivibrator, M, to give a second marker which determines the position of the final digitized data point. The calibration frequencies corresponding to the initial and final digitized data points are now obtained by direct measurement of the observing frequency relative to the NMR field locking frequency by matching the recorder pen position with the chart markers. In this manner these frequencies are readily determined to an accuracy of ± 0.1 Hz, which requires a counter gate time of at least 10 secs and in turn prevents an accurate frequency measurement during a spectrum scan, and are also shown to be reproducible within these limits. For an N-channel sweep, the frequency associated with channel n and signal amplitude V_n is simply given by $\omega_n = \omega_o + n.\ \Delta\omega$, with the frequency increment $\Delta\omega$ defined as $\Delta\omega = (\omega_1 - \omega_o)/(N-1)$ where ω_o and ω_1 are the calibration frequencies corresponding to the markers set at times t_o and t_1, respectively. The control bistable in its active state prevents an inadvertant computer

sweep, and preceding a new sweep this bistable state must be changed under the action of the manual reset trigger T at a time t_2, as shown in Fig.3.2. The spectrometer recorder may now be repositioned for another single scan and the FT-1064 channel sweep is initiated again by the manual sweep trigger, T, at time t_3. In this way the spectrometer may be swept in an arbitrary direction and digitized data may be stored in independent sections of the computer memory core.

The detailed circuit diagram for the interface unit is given in Fig. 3.3, and the pertinent control waveforms and voltages are included on this diagram. The manual trigger circuits centred on the 2N3646 high speed NPN silicon switching transistors T1 and T2 are particularly simple and have been shown to be completely reliable in operation. With switch S1 open, T1 is biased into conduction and the collector voltage is held at +0.4V while the base capacitor C_1 is charged to +4.5V. When the switch S1 is closed, the capacitor C_1 is discharged and T1 is cut-off as the base voltage falls to near 0V. The collector voltage rises and the positive going output trigger pulse following differentiation has an amplitude of $\sim$ 2V with a rise time of 0.1 μsec. When S1 is reopened, C_1 recharges with a time constant R_1C_1 and a spurious trigger waveform (normally associated with switch bounce) is eliminated. The emitter-coupled control bistable multivibrator, T3 and T4, is of conventional design and uses a single MC-715 MRTL dual triple-input gate with a switching threshold of +0.7V and switching times of the order of 0.1 μsec. The quiescent and active states of the control bistable correspond to T4 collector voltages of +0.2 amd +4.2V, respectively. A similar MRTL circuit, T7-T9, is used for the monostable

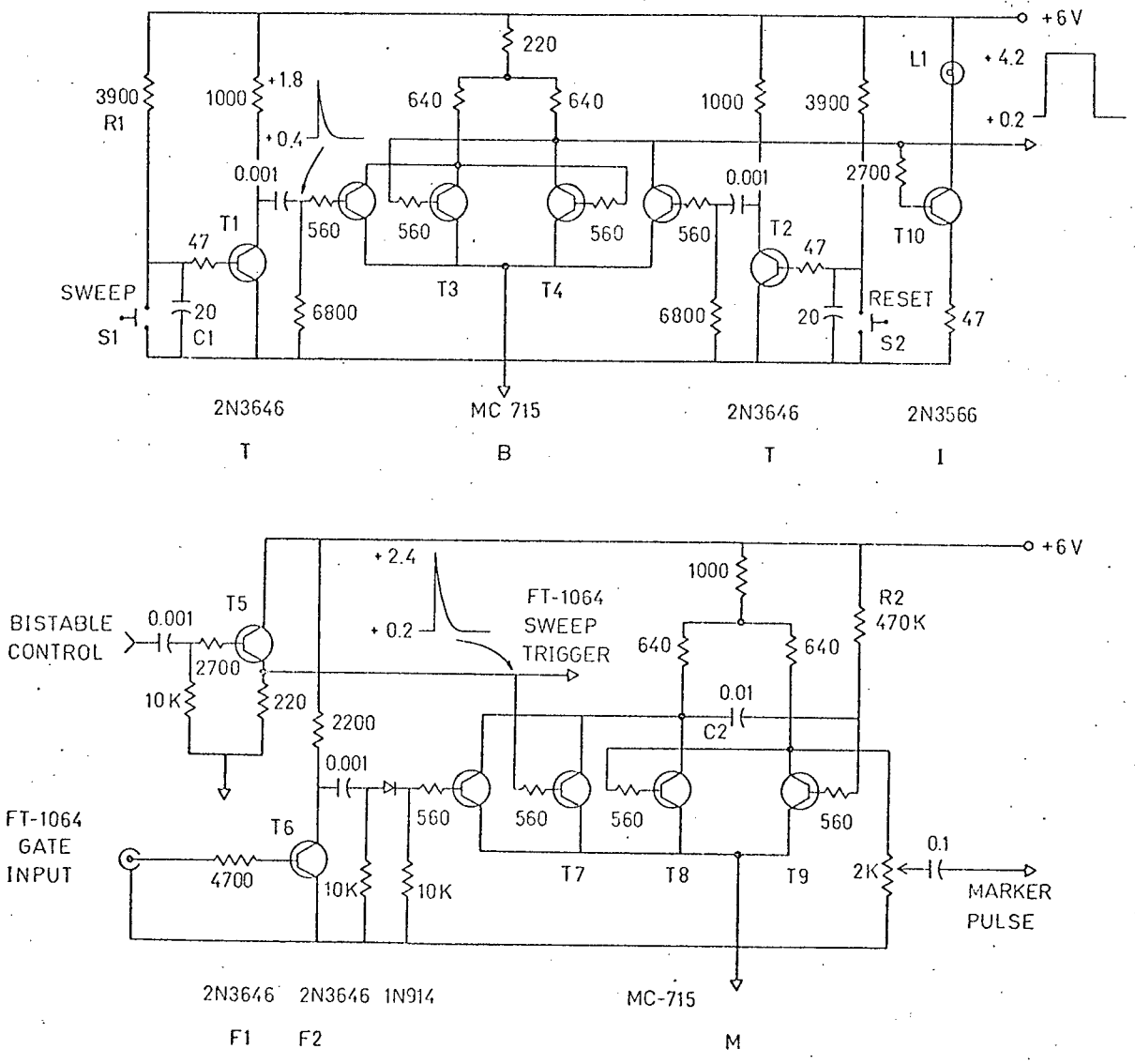

Fig. 3.3 Spectrometer-computer interface unit

multivibrator,the output pulse width being determined by the time constant R_2C_2. The indicator circuit consists of a series connected lamp, L1, and single transistor, T10, such that this transistor is biased into conduction and the lamp is on when the control bistable is in its active state.

The circuitry for the differential amplifier, A in Fig. 3.1, is shown in Fig. 3.4 and is based upon Philbrick operational amplifiers, types 1009 and 1301. The 1009 is a general purpose low-noise unit which features an FET input stage to provide an input impedance of 20M for the unity gain configuration used. This allows essentially complete isolation of the computer sampling unit from the spectrometer system, even though dc-coupling is retained to provide an undistorted low frequency signal response. The high input impedance also allows a simple dc zero level control through a voltage summing at one input of the differential amplifier. The 1301 operational amplifier is used as a variable gain inverting dc amplifier with a maximum gain of 10 with switch S1 in position 1. The overall linearity of the amplifier was checked over the output voltage range -5 to +5V and was found to be better than 0.4%. The output of this amplifier may be fed directly to the FT-1064 SD/1 sampling A-D converter with an input impedance of 5K.

An oscilloscope display of the computer memory contents over 1024 channels is available and the digital data pertaining to a particular memory location is indicated on the analog signal display by an intensified spot. This digital display allows a most convenient method of selecting a smaller number of data points to be fitted to a theoretical lineshape, the associated frequency

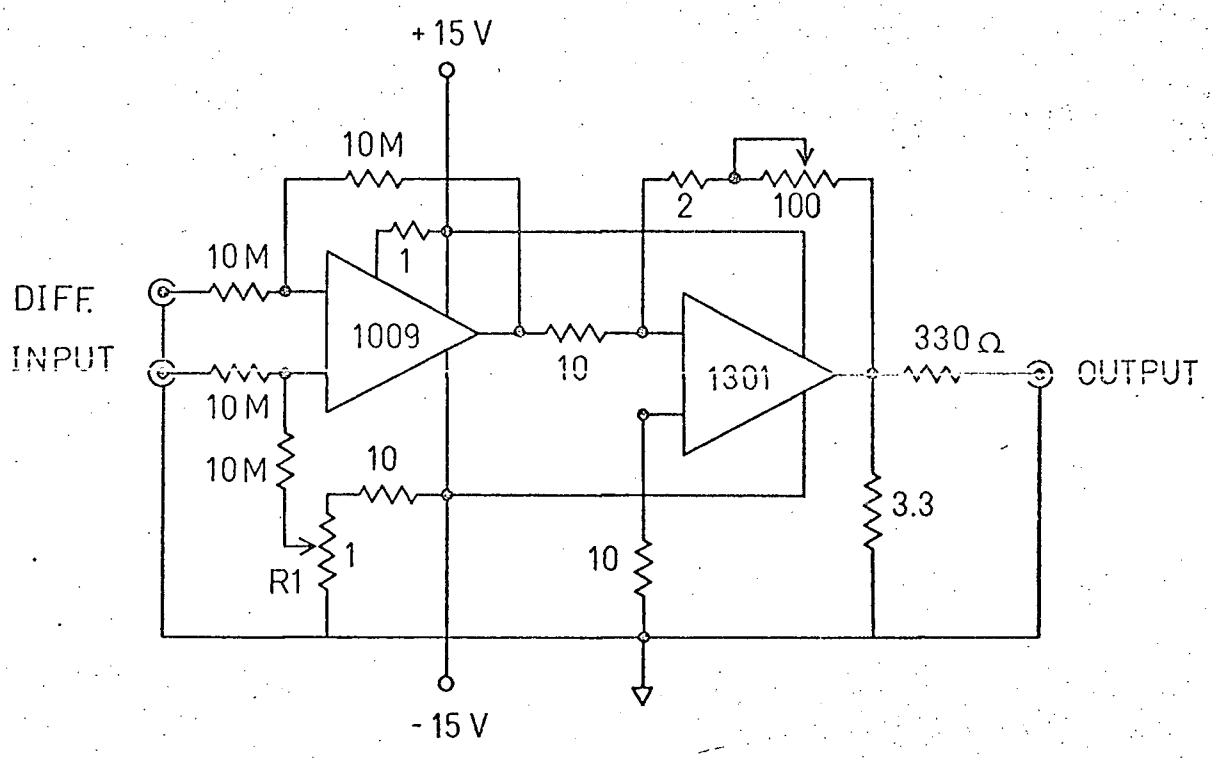

Fig. 3.4 Differential amplifier circuit

being directly related to the channel (memory location) number as previously described. In general, the digital data is transfered from the memory core to an incremental magnetic tape using a FABRITEK FT-282 control unit with a KENNEDY Model 1400 tape recorder. A digitized signal amplitude value is stored and read out as a word consisting of two bytes, each byte being six binary bits. This digital word form, however, is only compatible with IBM 360 arithmetic following a conversion to the standard 18 bits for this system. Thus a mixed FORTRAN-IV/SYMBOLIC program GET was developed to allow the efficient reading of the magnetic tape in the form of independent ordered bytes, the unpacking of selected two byte words and the setting up of an array of equivalent three byte words for the iterative lineshape fitting. Although 1024 data points were available from the FT-1064 computer, an optimum minimal number of data points were actually used for the lineshape fitting. For two- and four-site exchange spectra, it was found that the accuracy of the fitting was not increased above 64 or 128 data points. Thus these data points were selected at optimized intervals over the frequency range of the digitized data by the program GET and the total CPU time required for a completely automatic lineshape fit to the taped digital data was of the order of 10 secs per spectrum using the IBM 360/67 system. The complete interface unit described above has been used with most satisfactory results with both a JEOLCO C-60 and a VARIAN HA-100 spectrometer, only the addition of the two recorder inter-connections shown in Fig. 3.1 being required to link the spectrometer to the FT-1064 computer.

If the signal-to-noise ratio for a single scan spectrum is insufficient to allow a reliable lineshape analysis, it is necessary to operate the computer-spectrometer system in a multi-scan accumulative mode. In this case the internal sweep frequency oscillator of the NMR spectrometer is replaced by an external voltage controlled oscillator driven in synchronization with the FT-1064 channel sweep by the dc voltage available, as shown in Fig. 3.2. Thus the normal recorder sweep mechanism is disabled, but the internal field lock is retained. Once the required signal-to-noise ratio is attained the digital data is used as previously described, and a permanent chart recording is obtained by feeding the computer memory analog output to the spectrometer recorder operating in its normal linear sweep mode using the above interface unit to trigger the analog read-out and to place the frequency calibration markers.

3.2 Rf-pulse gate

An ideal pulsed NMR spectrometer would consist of a transmitter supplying a high intensity rf pulse over a very short time interval, as compared with the nuclear relaxation times involved, to rotate the nuclear magnetization through a well-defined angle β, cf. Fig. 2.1; and a receiver that would instantly record the free induction decay signal following the pulse without distortion or the addition of noise. In practice, it is difficult to produce a large constant amplitude rf magnetic field associated with an accurately timed pulse having a closely controlled width and minimal rise and fall times. Also, it is only possible to have a low noise (so that overall sensitivity is limited by the thermal noise in the sample coil) linear receiver with a minimal time for recovery from overload following the rf pulse. In addition, an rf phase coherent system is required to retain the nuclear spin isochromat [29] phase information inherent in the detected free induction decay or spin echo, and to be able to accurately determine resonance conditions and the detailed form of the spin isochromat motion under the action of specific types of rf pulses in a general multi-pulse sequence. An rf phase sensitive detection scheme has also been shown to provide accurately linear detection of weak signals and to allow full usage of post-detection integration[120,121]. In high resolution NMR applications, the overall stability of the spectrometer system is critical. Following the original pulsed NMR experiments of Hahn [29] and Carr and Purcell [30], a number of spectrometer systems have been described in the literature [110-119]. However, Fourier transform applications and the study of

chemical exchange using multi-pulse sequences require particularly sophisticated instrumentation. Indeed, the large systematic errors apparent in the kinetic parameters derived from pulsed mode NMR data may be largely due to the lack of such apparatus.

One of the most critical component units in a pulse spectrometer is the rf-pulse gate. This gate is required to provide pulses of constant width and amplitude with a very high rf suppression in the time interval following each pulse. The ratio of the amplitude of an rf pulse (on-period) to the steady rf feedthrough (off-period) may be referred to as the gate rejection ratio, α. The rf feedthrough may be considered to be negligible as long as the resonance saturation factor S', cf. Eq. (2.3.1), is in the range $0.99 < S' < 1.0$. The factor 0.99 corresponds to a saturation effect distortion of the free induction decay of about 1% over the entire measurement time interval. If the $\pi/2$-pulse width is assumed to be $0.01\ T_2$, where T_2 is the total transverse relaxation time, the restriction on the spin-lattice relaxation time T_1 satisfying the above saturation condition is $T_1 < 4 \times 10^{-6}\ \alpha\ T_2$ [1, 116]. In liquids $T_1 \simeq T_2$, and this implies that the minimum rejection ratio required is $\alpha \simeq 2 \times 10^5$, or 110 dB. For normal high resolution NMR in liquids $T_2 \sim 0.6$ sec, and hence a pulse width of $0.01\ T_2$ corresponds to 6 msecs. In studying chemical exchange processes, however, the effective transverse relaxation time may be significantly decreased and hence a $\pi/2$-pulse width of the order of micro-seconds is desirable. In Fourier transform applications large phase errors that are difficult to quantitatively correct may arise through the general inability to measure the free induction decay

signal for times $t \rightarrow o$. To minimise these errors it is necessary to use relatively short $\pi/2$-pulses and a receiver with a fast recovery from overload. Thus general specifications for an rf-pulse gate in a pulse spectrometer used for chemical exchange studies and high resolution Fourier transform applications may be given as: $\pi/2$-pulse width = 10-20 μsec, rise and fall time = 0.1 μsec and rejection ratio $\alpha = 10^6$ (120 dB).

The only gate systems in the literature that appear to meet the above specifications are those of Blume [115] and Lowe and Tarr [118]. The Blume gate has been adapted by Clark [116] and Bloom [122] and co-workers. This circuit uses an expensive 7077 planar triode as a grounded-grid rf amplifier so that the very low cathode-to-plate capacitance of 0.01 rf severely restricts rf feedthrough, with careful electronic construction. Lowe and Tarr use a transistorised rf gate with a relatively low rejection ratio followed by a multi-stage gated high power rf amplifier. The gate described here has been developed to avoid the use of special components, an elaborate construction or a gated high power rf amplifier. In addition, it has been designed to be a simple and adaptable unit that may be readily linked with standard NMR and rf instrumentation while meeting the specifications outlined above.

The detailed circuit diagram for the rf pulse gate operating at 10MHz is given in Fig. 3.5(a), and the pertinent voltage levels and waveforms are included on this diagram. The dc supply voltages were chosen to match those available from the stabilized power supply for the TEKTRONIX 160 series pulse generators[125] used to set up general multiple

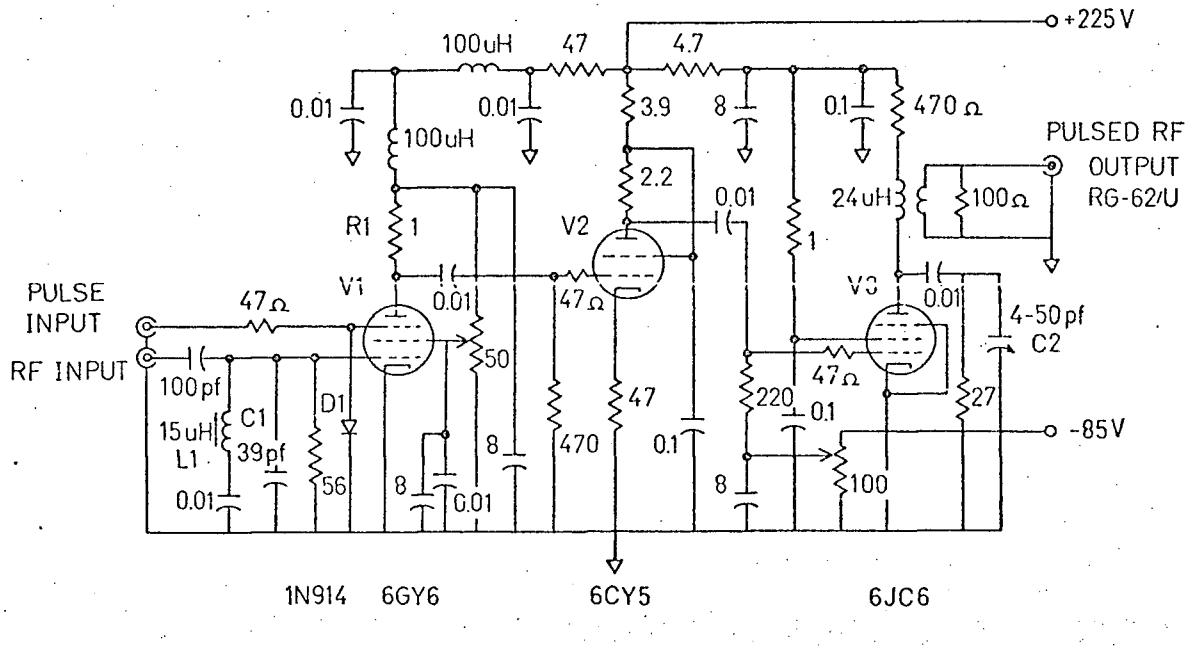

Fig. 3.6 (a) Rf-pulse gate

and/or repetitive pulse sequences. Of course, all power leads are heavily filtered to prevent rf leakage between units of the complete pulse spectrometer. The 6GY6, V1, is operated as a low gain class A gated rf amplifier with a tuned input and an untuned output. This vacuum tube is a sharp cut-off pentode with dual control grids, g_1 and g_3, and low inter-electrode capacitances. The tuned grid circuitry is carefully shielded through the vacuum tube socket, but this is actually the only mechanical rf shielding used. V1 is biased into cut-off in the gate quiescent state (off-period) by a dc bias Vg_3 = -12V, and the rf feedthrough for this stage for the maximum input voltage of 0.8V p-p is less than 15 mV p-p. This feedthrough is due mainly to the grid-to-plate capacitance which has a minimum value of 0.026 pF. When the gate system is driven into the active state (on-period) by a positive control pulse applied to the second control grid, g_3, the voltage Vg_3 is held at near the cathode potential by the limiting diode D1 and the 6GY6 acts as an amplifier with Vg_1 = -0.4V. This amplifier gives a maximum output of 12V p-p and hence the rejection ratio for this first stage of the gate system is of the order of 10^3 (60 dB). It should be noted here that as the capacitance between the two control grids is less than 1 pF, excellent rf isolation of the control pulse circuitry is very simply attained. The low plate load resistance, R1, and plate-to-cathode capacitance of 6pF determine the rise and fall times for the rf pulse and associated pedestal in the stage output circuit as less than 0.2 μsec. The 6CY5, V2, acts as a pulse inverter

to give an undistorted gating waveform for the 6JC6, V3, output amplifier. This tetrode has a low grid-to-plate capacitance (0.03 pF) and rf feedthrough is minimised in this stage by using the particular configuration shown in Fig. 3.5(a). As this stage is untuned, the rf gain is less than unity which further reduces feedthrough in the quiescent stage and also determines the 6JC6 input voltage of 4V p-p (maximum) in the active state. The 6JC6 is operated as a high gain class C amplifier and the control grid bias is adjusted to give a maximum rejection ratio and minimum pulse rise and fall times, which are facilitated by the low-Q plate circuit. Again a low grid-to-plate capacitance of 0.02 pF leads to a stage rejection ratio of 4×10^3 (72 dB). The rf gate output is obtained through an inductive link, the output impedance being approx. 100 Ω. The output pulse characteristics are illustrated in Fig. 3.6 and may be summarised as follows: output voltage $\lesssim$ 20V p-p, rf feedthrough < 15 μV p-p, rise-time < 0.4 μsec and fall time < 0.1 μsec. The feedthrough voltage was measured using a high gain linear rf amplifier with an input impedance of 75 Ω at 10MHz and a detection threshold of 2μV p-p, and hence the overall rejection ratio for the gate circuit may be considered to be accurately determined as greater than 120 dB. The operating frequency of the rf gate described above is readily changed to any frequency up to 20 MHz by varying only C1 and C2, and the output pulse characteristics are shown to be within the 10MHz limits given above.

The rf gate control monostable multivibrator circuit is given in Fig. 3.5(b). This pulse generator was developed as an integral

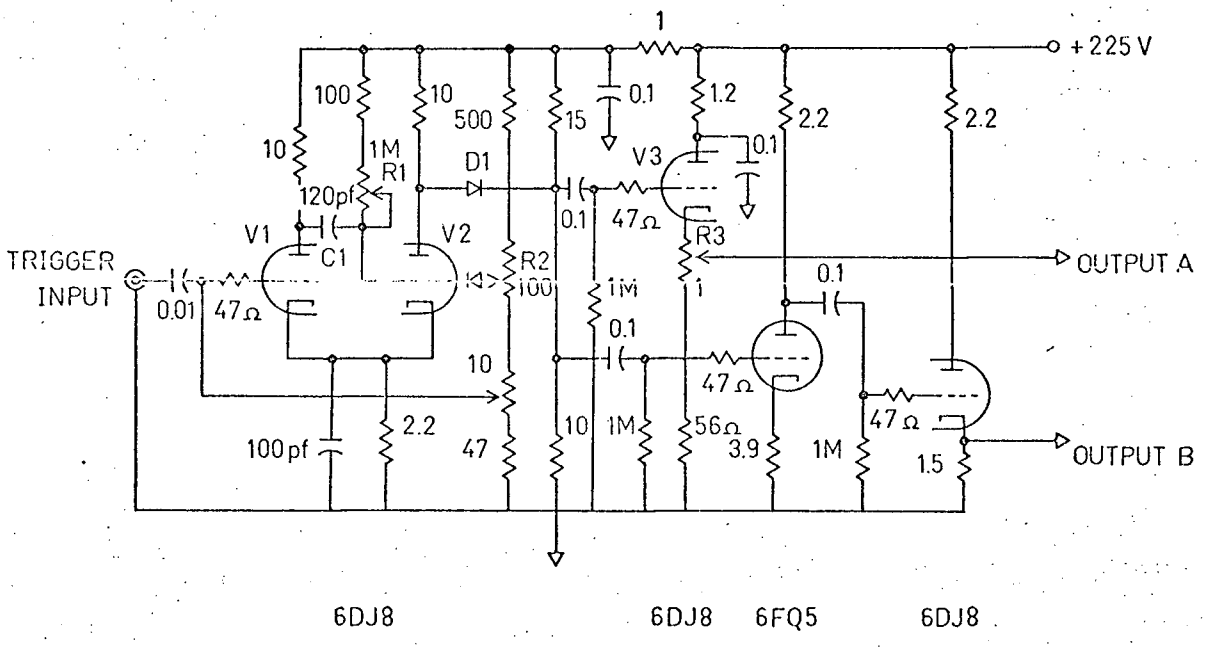

Fig. 3.6 (b) Control dc-pulse generator

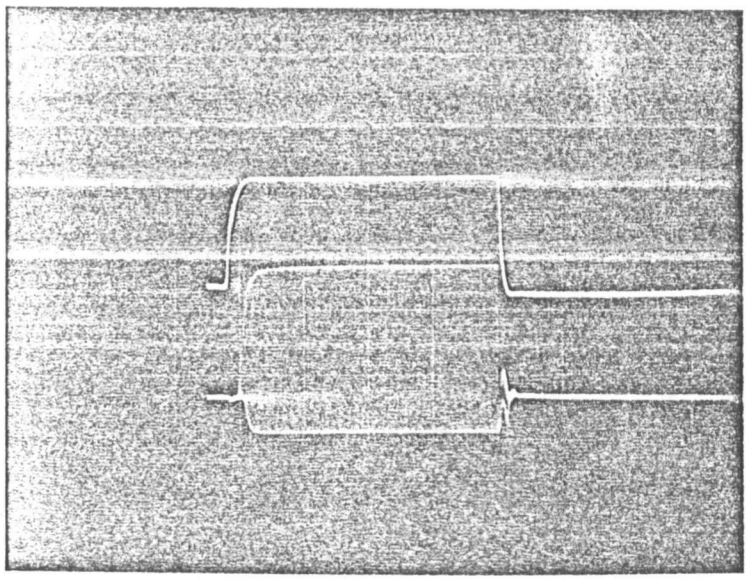

Gate control waveform and output rf pulse.

(0.5 μsec/cm)

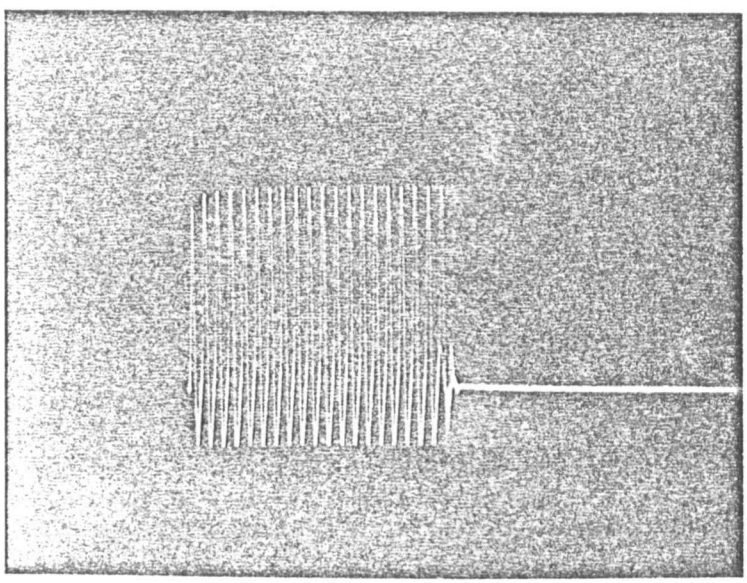

Output rf pulse (0.5 μsec/cm, 5V/cm)

Fig. 3.6 Rf-pulse gate operational characteristics.

part of the rf gate system to attain the rf pulse rise and fall times previously specified, a TEKTRONIX 161 pulse generator being inadequate in this respect, and to simplify the rf isolation of this control circuitry. The cathode-coupled multivibrator using the 6DJ8 double triode, V1 and V2, was designed following well known principles [123,124], the critical gating pulse fall time being minimised through a careful study of the multivibrator characteristics, the use of the plate-catching diode D1 and isolation of the multivibrator circuitry by a cathode follower, V3. This follower configuration reduces the effective capacitance at the output plate (V2) of the multivibrator, this capacitance being the major factor defining the output pulse fall time. The pulse-width, t_w, is governed by the time constant R_1C_1 and the grid bias for V1, and hence a versatile width control is obtained through the variation of both of these parameters by R1 and R2. For the component values shown, t_w may be varied from 5 to 100 μsecs and may be readily adjusted to within 1% of a specified value. The inherent pulse-width jitter is measured as less than 0.05% of the pulse-width. The output pulse amplitude may be varied, through R3, between 1 and 30V. The gate control pulse is shown in Fig. 3.6, and the dc pulse rise and fall times are measured under normal rf gate operating conditions as 0.1 and 0.05 μsec, respectively. These switching times allow an rf pulse to be defined in terms of an integral number of rf cycles, and also allow the development of a completely coherent pulse system. In such a system, the pulse gate waveform is locked to the rf waveform and hence a sequence of rf pulses with an identical phase may be generated. The control pulse generator is triggered by a 6V positive

pulse at the control grid of V1. All additional timing triggers are derived from the low impedance pulse outputs A and B in Fig. 3.6(b).

In the complete pulse spectrometer, the pulse from the rf gate is used as the input to a conventional high power rf amplifier using push-push frequency doublers (to give a final operating frequency of 10, 20 or 40 MHz) and push-pull class C amplifiers. Rf pulse shape distortion is minimised by using only low-Q tuned circuits. With a stabilized high voltage power supply for the final rf amplifier, up to 1.6 kW (400 V p-p into a 100 Ω resistive load) is available in a pulse sequence with a minimum pulse interval of 60 μsecs. A typical π/2-pulse width for ^{1}H NMR (γ_H = 2.7 x 10^4 rad. sec^{-1} $gauss^{-1}$) is 10 μsecs, and this corresponds to an H_1 magnetic field of 5.8 gauss over the sample volume. It should be noted that, for the Varian V-4300 crossed-coil probe used, the transmitter coil is 25 mm in diameter while the sample tube is normally 5 mm with a corresponding 8 mm receiver coil. Although the crossed-coil system attenuates the available rf power in a pulse, it does give a high homogeneity H_1 field over the sample volume which is usually more important in high resolution applications. In addition, when this coil system is used in conjunction with a modified LEL linear rf amplifier [125], the time for recovery from over-load following an rf pulse is typically less than 5 μsecs when the probe is correctly balanced. An improved rf phase-sensitive detection scheme uses a HP 10514B broad band mixer, with inputs from the LEL signal amplifier and a simplified reference amplifier [125], followed by a low output impedance dc amplifier which drives all recording devices

including the FABRITEK FT-1064 computer. The overall linearity of the receiver system has been checked over the input range of 10 μV to 10 mV p-p at a gain of 10^4 to be better than 2%.

CHAPTER 4

EXPERIMENTATION AND CALCULATIONS

4.1 Hindered rotation in amides.

4.1.1 N,N-dimethyl carbamyl chloride.

This compound was chosen for an initial study of the hindered rotation about the N-C bond in amides, due to the electron delocalisation in the NCO bond system, using the steady-state NMR methods described in detail in Chapter 2 of this thesis. Although a number of substituted amides have been studied, the parameters derived from the NMR data show a large variance and a semi-quantitative correlation of the data available is not possible. The only example of an N-C rotational barrier that has been studied using complete NMR lineshape analyses in independent laboratories, and for which the kinetic parameters are apparently consistent within the calculated experimental errors, is that for N,N-dimethyl formamide [59,61]. However, this result is fortuitous in view of the fact that one of the models used [61] for this four-site exchange process is incorrect. Thus the kinetic data obtained here for N,N-dimethyl carbamyl chloride (DMCC) is intended for comparison with that available from a recent independent study using a complete lineshape analysis [60] and spin echo studies [35,59] to substantiate the general validity and reliability of the application of NMR methods to the study of hindered rotation.

DMCC was obtained from K & K Laboratories Co. Ltd., and was purified by a double vacuum distillation and stored over molecular

sieves. Experimental and literature physical constants agreed for this compound. As DMCC is a liquid (b.p. = 165°C at 760 mm) this amide was studied neat and in the non-polar solvent carbon tetrachloride (6 mole %). In preparing the NMR samples, 2 mole % of tetramethyl silane (TMS) was added to provide a stable field-frequency lock signal and 2 mole % of dioxane was also added as a reference peak as it is conveniently placed with respect to the DMCC spectrum and has a temperature independent linewidth. The samples were thoroughly degassed by the usual freeze-pump-thaw cycle and were sealed in vacuo in thin-walled NMR tubes of 5 mm o.d..

The NMR spectra were obtained on a JEOLCO JNM-C-60H spectrometer used in the internal lock mode and equipped with the JES-VT-2 variable temperature controller. The temperature is normally monitored by a thermocouple placed near the sample in the temperature control gas stream. As a temperature measurement is critical in quantitative kinetic studies, especially when it is only possible to apply complete lineshape analyses over a relatively small temperature range, the temperature was calibrated with a second thermocouple immersed in the same volume of sample contained in an open non-spinning NMR tube and also by replacing the sample with the ethylene glycol sample supplied by Varian. In addition, the temperature was checked before and after a number of spectra were recorded. Two conclusions were immediately evident. While the use of the non-spinning sample does not give a reliable measurement of the spinning sample temperature, the instrument thermocouple temperature reading can be accurately correlated with that given from the ethylene glycol chemical shift-temperature equation reported by

Van Geet [126]. As the absolute error in the sample temperature measurement was estimated to be ± 0.3°C, it was also shown that the sample temperature was constant within these limits over the recording time for a number of spectra at a given controller temperature setting. Thus, in general, it is possible to use the instrument thermocouple measurements calibrated at four temperatures with the glycol sample to reduce the time involved with continual sample replacement. Sweep rates as low as 0.05 Hz sec^{-1} were used to ensure a good approximation to slow passage conditions and spectra were checked for possible distortion due to saturation, cf. section 2.3. At each temperature, field curvature and homogeneity and rf phase adjustments were made to ensure reproduction of the true spectral lineshape. The resultant linewidth at half-maximum of the reference peak was held within the range 0.3 - 0.5 Hz. Multiple spectra were obtained at each temperature and any spectra that were not precisely reproducible were discarded.

The hindered rotation in DMCC may be considered as an equal population two-site exchange process and hence the steady-state NMR absorption mode lineshape function, V(x), is given by Eq. (2.2.15) in accordance with the stochastic model described in detail in section 2.2. The experimental spectral data is converted to a series of N digital amplitude values, $V'(x_i)$, and associated frequencies, x_i. These frequencies are derived from two calibration frequencies measured directly as the difference between the sweep (observing) frequency and the fixed field lock frequency, to an accuracy of ± 0.1 Hz. A FORTRAN-IV computer program PLONK has been developed to allow an efficient iterative lineshape analysis of the digitized data. The iterative fitting is based upon

a simple but effective search routine which rapidly converges to a best-fit parameter value through a series of optimised parameter increments, the best-fit value corresponding to a minimum in the sum of squares of deviations [127], S, where

$$S = \sum_{i=1}^{N} [V'(x_i) - V(x_i)]^2$$

and $V(x_i)$ is the theoretical lineshape amplitude for $x=x_i$. The lineshape function is normalised to the experimental data, $V'(x_i)$, through the constant A in Eq. (2.2.15). The parameters to be considered in a general lineshape analysis are the chemical shift between exchange sites 2Ω, cf. Eq. (2.2.1), the transverse relaxation time T_2 describing the residual linewidth in the absence of exchange and the first order rate constant k defining the exchange process. T_2 is defined in terms of the linewidth of the reference peak, where it is implicitly assumed that the magnetic field homogeneity is described by a Lorentzian frequency distribution, and is considered to be a fixed parameter. A standard non-linear least squares regression analysis [128] using Ω and k as variable parameters was shown to be unreliable, especially for data obtained above the coalescence temperature, and this is probably due to the unusual forms of the partial derivatives required, $\left(\frac{\partial V}{\partial \Omega}\right)_{x_i}$ and $\left(\frac{\partial V}{\partial k}\right)_{x_i}$. Therefore, the program PLONK takes k as the variable parameter for a specific Ω value, with the option of being able to vary Ω in a well-defined manner to determine the coupled parameter values corresponding to a minimum S value. This appears to be the most satisfactory form of analysis to determine a temperature dependence of the chemical shift,

2Ω. For N = 20-60, the CPU time involved for each k iterative fit is of the order of 4 secs on an IBM 360/67 system, and the setting up of all arrays for control of a CALCOMP plotter takes less than 1 sec. Typical lineshape fits for DMCC (neat) using the computer program described above and a constant chemical shift 2Ω = 6.80 Hz at 60 MHz are shown in Fig. 4.1, and the rate constants obtained by averaging the k values from the fitting of multiple spectra at all temperatures are summarised in Table 4.1. It should be noted that the mean deviation, calculated as

$$\frac{1}{N} \sum_{i=1}^{N} [V'(x_i) - V(x_i)]/V(x_i),$$

for the spectra shown in Fig. 4.1 is 1.5%.

The Arrhenius plot for DMCC (neat) is shown in Fig. 4.2. The activation energy, E_a, for the hindered rotation is determined as 17.64 ± 0.52 kcals. $mole^{-1}$ from a least squares fit to the usual equation [129]

$$k = A \exp(-E_a/RT), \qquad (4.1.1)$$

where T is the absolute temperature, A is the frequency factor for the rate process and R is the universal gas constant (1.986 cal. deg^{-1} $mole^{-1}$). Both E_a and A are assumed to be temperature independent, and the activation energy is defined as the difference between the average energies of the ground state and the activated transition state involved in the hindered rotation. A thermodynamical formulation of reaction rates [130] shows that

TABLE 4.1

Kinetic data for N,N-dimethyl carbamyl chloride

(neat)

Temp.°C	k sec^{-1}
28.7	4.32
29.2	4.52
33.0	6.35
33.2	6.35
35.8	8.16
39.4	11.74
39.4	11.46
40.5	10.55
41.5	13.59
46.8	23.00
48.4	25.99
50.8	32.02

E_a = 17.64 ± 0.52 kcals. $mole^{-1}$

$\Delta H^{\#}$ = 17.05 kcals. $mole^{-1}$ at 25°C

$\Delta S^{\#}$ = 0.8 ± 1.6 cal deg^{-1} $mole^{-1}$

$\Delta G^{\#}$ = 16.82 kcals. $mole^{-1}$

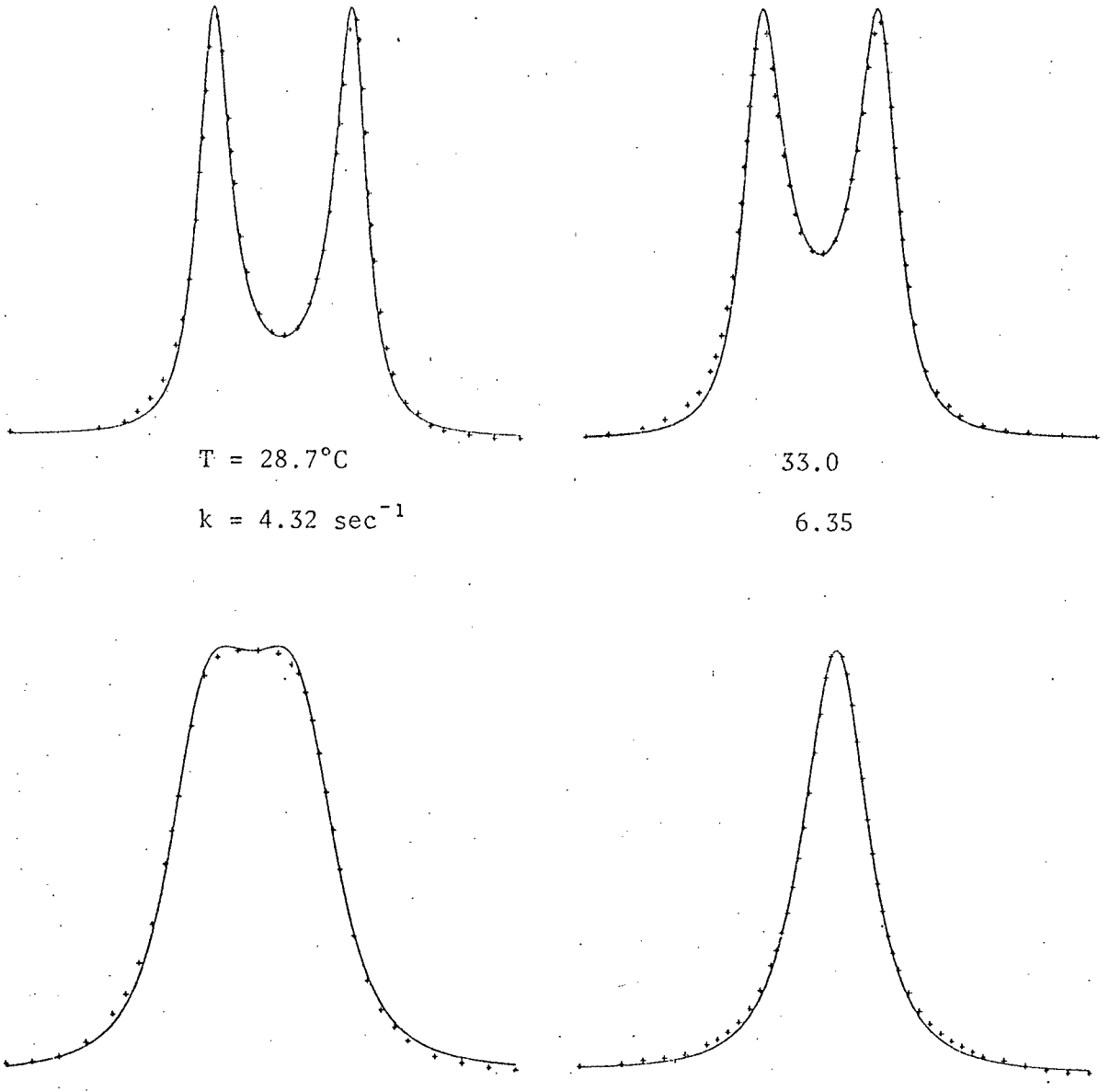

Fig. 4.1 Lineshape fits for N,N-dimethyl carbamyl chloride, two-site equal population exchange system.

$$k = \frac{kT}{h} \exp(-\Delta G^{\#}/RT)$$

$$= \frac{kT}{h} K^{\#} \qquad (4.1.2)$$

where k is the Boltzmann constant, h is Planck's constant and $\Delta G^{\#}$ is the free energy of activation. $K^{\#}$ may be interpreted as an equilibrium constant for the interchange between ground and activated states, and may therefore be defined in terms of the increase in energy in forming the transition state, $\Delta E^{\#}$, by the general relationship

$$\frac{d}{dT} \ln K^{\#} = \frac{\Delta E^{\#}}{RT^2} . \qquad (4.1.3)$$

Thus it follows that

$$E_a = \Delta E^{\#} + RT$$

and the enthalpy of activation, $\Delta H^{\#}$, may now be defined as

$$\Delta H^{\#} = \Delta E^{\#} - P\Delta V^{\#} ,$$

where $\Delta V^{\#}$ is the increase in volume on going into the transition state. For the unimolecular hindered rotation process, $\Delta V^{\#} = 0$ and in this particular case $\Delta H^{\#}$ may be calculated directly from the experimental activation energy at a given temperature as

$$\Delta H^{\#} = E_a - RT . \qquad (4.1.4)$$

Substitution for E_a in Eq. (4.1.1) now allows a determination of the entropy of activation, $\Delta S^{\#}$, in accordance with Eq. (4.1.2) as

$$\Delta S^{\#} = R[\ln \frac{\Lambda h}{kT} - 1], \qquad (4.1.5)$$

with $$\Delta G^{\#} = \Delta H^{\#} - T\Delta S^{\#} \qquad (4.1.6)$$

The activation parameters calculated for DMCC (neat) at 25°C are included in Table 4.1 and are in very good agreement with those obtained by Neuman et al. [60] (E_a = 16.9 ± 0.5 kcals. mole $^{-1}$, $\Delta G^{\#}$ = 16.8 kcals mole $^{-1}$, $\Delta S^{\#}$ = -1.6 cals. deg^{-1} mole $^{-1}$). It has previously been noted [59, 60, 64] that as increasing care is taken in obtaining kinetic data using NMR methods, the values of E_a and A tend to increase while the free energy of activation remains nearly constant. The data presented here exemplify the trends. For hindered rotations in N,N-dimethyl amides the entropy of activations is expected to be relatively small [47, 59]. As this entropy change in liquids is most probably associated with a difference in the solvation structures for the ground and transition states it is predicted that there will be a small increase in entropy on formation of the transition state, in that the dipole moment for this state is normally smaller than that for the planar ground state. Within the error limits given above, and calculated as the statistical 95% confidence limits, this is shown to be the case for DMCC studied as a neat liquid. In comparison, the entropy of activation derived from spin-echo data is ~ -10.5 cals. deg.$^{-1}$ mole^{-1} and the corresponding activation energy for DMCC (neat) is 14.0 ± 0.9 kcals. mole^{-1} [35, 59]. It is to be noted, however, that under the assumption that $\Delta S^{\#}$ = 0. the activation energy may be calculated from the spin-echo data at the coalescence temperature[47]

to be 17.5 kcals $mole^{-1}$, in excellent agreement with the steady-state value presented above. In addition, the free energy of activation is determined as $\Delta G^{\#}$ = 16.6 kcals $mole^{-1}$, cf. 16.8 kcals $mole^{-1}$ Table 4.1.

Solute-solvent interactions for the strongly polar DMCC molecule (μ = 4.08D [147]) may be expected to influence the magnitude of the potential barrier for hindered rotation in this amide. Thus DMCC was also studied as a dilute (6 mole %) solution in the non-polar solvent CCl_4 to minimise such interactions. The kinetic data obtained from total lineshape analyses, using a constant chemical shift 2Ω = 7.1 Hz at 60 MHz are summarised in Table 4.2. The corresponding Arrhenius plot is shown in Fig. 4.2 and the activation energy is determined as 17.05 ± 0.47 kcals $mole^{-1}$. Thus this parameter shows only a small solvent dependence. The entropy of activation is again very small but formally negative, $\Delta S^{\#}$ = -0.6 ± 1.5 cals deg^{-1} $mole^{-1}$. Although the hindered rotation in this particular amide is shown to be nearly independent of solute concentration, the form of the magnetic anisotropy of the carbonyl group [132, 133], which is assumed to be the dominant mechanism giving rise to the chemical shift between the N-methyl groups cis and trans to this functional group, is changed significantly from that in the neat liquid system. This change is presumably due to the break-down of a specific solute-solvent interaction.

In order to consider the inter-relationships between derived activation parameters, all data available for the hindered rotation in DMCC have been correlated in Table 4.3. The $\Delta G^{\#}$, $\Delta H^{\#}$ and $\Delta S^{\#}$ values have been calculated for a fixed temperature of 25°C. The overall

TABLE 4.2

Kinetic data for N,N-dimethyl carbamyl chloride

(6% CCl_4 solution)

Temp. °C	k sec^{-1}
0.5	0.44
5.9	0.52
15.2	1.25
30.5	6.30
34.5	9.45
39.3	13.54
44.0	18.83
44.6	18.85
48.8	31.58
49.5	33.62
54.5	51.05
54.8	55.55
58.0	93.42
63.2	137.10

E_a = 17.05 ± 0.47 kcals. $mole^{-1}$

$\Delta H^{\#}$ = 16.46 kcals. $mole^{-1}$ at 25°C

$\Delta S^{\#}$ = -0.6 ± 1.5 cal. deg^{-1} $mole^{-1}$

$\Delta G^{\#}$ = 16.64 kcals. $mole^{-1}$

TABLE 4.3

N,N-dimethyl carbamyl chloride activation parameters

ref.	E_a	$\Delta G^{\#}$	$\Delta H^{\#}$	$\Delta S^{\#}$
a	17.64 ± 0.52	16.82	17.05 ± 0.52	0.8 ± 1.6
a	17.05 ± 0.47	16.64	16.46 ± 0.47	-0.6 ± 1.5
b	16.9 ± 0.5	16.8	16.3 ± 0.5	-1.6 ± 2.0
b	17.7 ± 0.9	16.3	17.1 ± 0.9	2.6 ± 3.2
c	14.0 ± 0.9	16.6	13.4 ± 0.9	-10.6 ± 2.7
c	9.7 ± 0.5	16.6	9.1 ± 0.5	-25.3 ± 2.8
c	8.6 ± 1.7	16.6	8.0 ± 1.7	-28.9 ± 5.5
d	7.3 ± 0.5	16.4	6.7 ± 0.5	-27.1 ± 2.4
e	6.8 ± 0.2	16.2	6.2 ± 0.2	-33.6 ± 1.0
f	8.65 ± 0.88	16.3	8.06 ± 0.88	-27.5 ± 3.0

a This work

b R.C. Neuman, D.N. Roark and V. Jonas JACS 89, 3412, 1967

c A. Allerhard and H.S. Gutowsky J.Chem.Phys. 41, 2115, 1964

d M.T. Rogers and J.C. Woodbrey J.Phys.Chem. 66, 540, 1962

e J.C. Woodbrey and M.T. Rogers JACS 84, 13, 1962

f E. Krakower, Ph.D. Thesis, UBC, 1967.

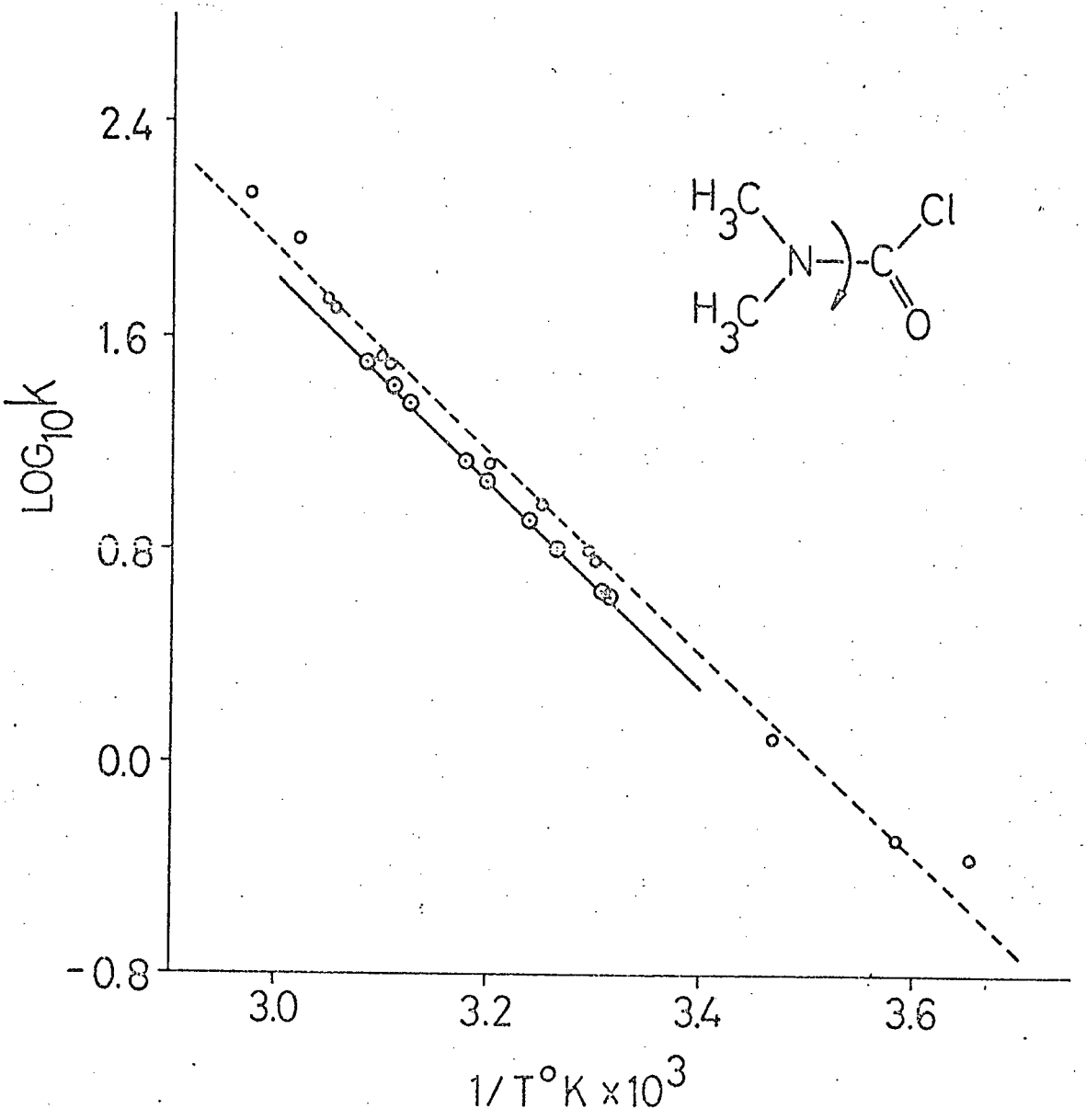

Fig. 4.2 Arrhenius plots for N,N-dimethyl carbamyl chloride.

o 6% CCl_4 solution

⊙ neat liquid

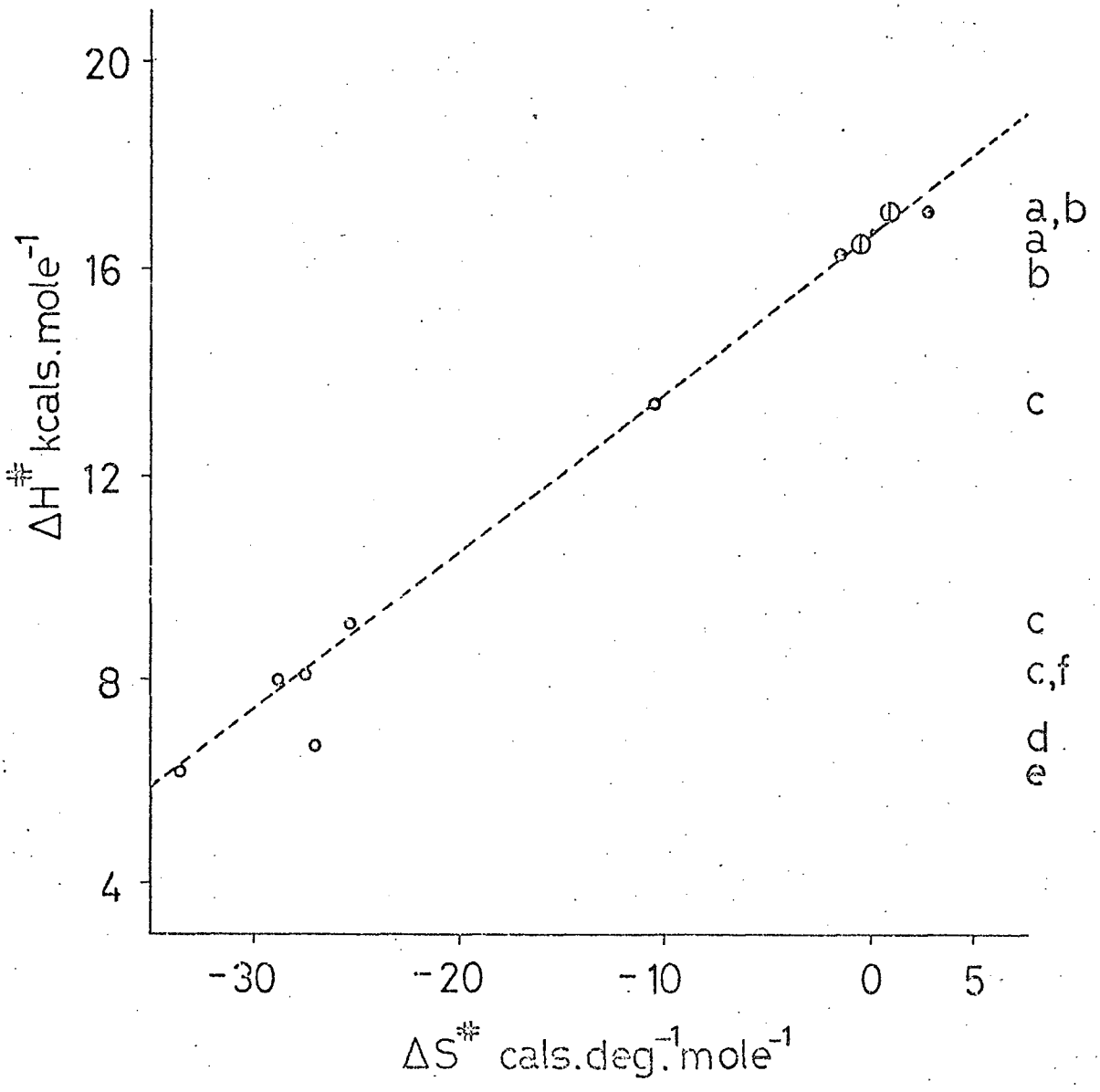

Fig. 4.3 Variation of activation parameters for hindered rotation in N,N-dimethyl carbamyl chloride.

variation in $\Delta H^{\#}$ and $\Delta S^{\#}$, as obtained using different methods of analysis and also different solvents and solute concentrations, is shown graphically in Fig. 4.4. The large variation in these parameters for identical chemical systems is due to relatively small errors in the experimental determination of specific rate constants and/or temperatures. Although these errors may give rise to only a small change in the slope of the corresponding Arrhenius plot over the temperature range for a particular study, this temperature range is usually very small (20-80°C) and hence relatively large variations in the E_a and A values determined from Eq. (4.1.1) soon become evident. This of course leads to corresponding variations in $\Delta H^{\#}$ and $\Delta S^{\#}$ in accordance with Eqs. (4.1.4) and (4.1.5), respectively. In general, as shown in Fig. 4.4, higher E_a ($\Delta H^{\#}$) values are associated with higher A values [47, 64], and vice versa. Except for a single point, however, a linear correlation between $\Delta H^{\#}$ and $\Delta S^{\#}$ is obtained and this implies that the free energy of activation, $\Delta G^{\#}$, is approximately invariant to small systematic errors inherent in the determination of E_a and A, cf. Eq. (4.1.6). Thus it becomes evident that the only significant parameter obtained from NMR data may indeed be the free energy of activation [64].

The activation parameters for DMCC determined by complete lineshape analyses are shown in detail in Fig. 4.5, this method of analysis giving the most reliable and highest precision estimates of these parameters. The data obtained in independent studies are consistent well within the calculated error limits, but it is still not possible to reliably compare the enthalpies of activation determined for the neat amide and the amide in a CCl_4 solution. Again the free

energy of activation becomes the most significant parameter, and is determined for $\Delta S^{\#} = 0$, cf. Eq. (4.1.6) and Fig. 4.4, as $\Delta G^{\#} = 16.65$ kcals mole^{-1}. In this particular case it is interesting to note that the slope of the linear plot shown in Fig. 4.5 defines a characteristic temperature of 258°K, which is to be compared with that of 298°K at which $\Delta H^{\#}$ and $\Delta S^{\#}$ have been calculated. This temperature difference may be considered to indicate a small dependence of $\Delta G^{\#}$ on solvent and thus may be used to semi-quantitatively describe solute-solvent interactions for a series of substituted amides. For the hindered rotation in an amide, a free energy change is expected to be defined primarily by intramolecular effects and hence is much simpler to interpret than the energy of activation which is sensitive to intermolecular effects. Also,there is a general tendency in rate processes in solution for enthalpy and entropy changes to compensate each other [134, 135] so that the effective change in free energy is reduced and becomes less sensitive to external effects. This compensation effect is simply interpreted in terms of a solute-solvent interaction. Any interaction that leads to a stronger binding of solvent molecules to a solute molecule lowers the enthalpy of the system, and also, by restricting the freedom of motion of both solute and solvent molecules this interaction lowers the entropy. This characteristic is shown by the parameters presented in Fig. 4.4. In this particular case, it may be considered that a decrease in entropy for the planar ground state (relative to that for the hindered rotation transition state) of DMCC as a neat liquid, due to a dipolar solute-solute (solvent) interaction, leads to a

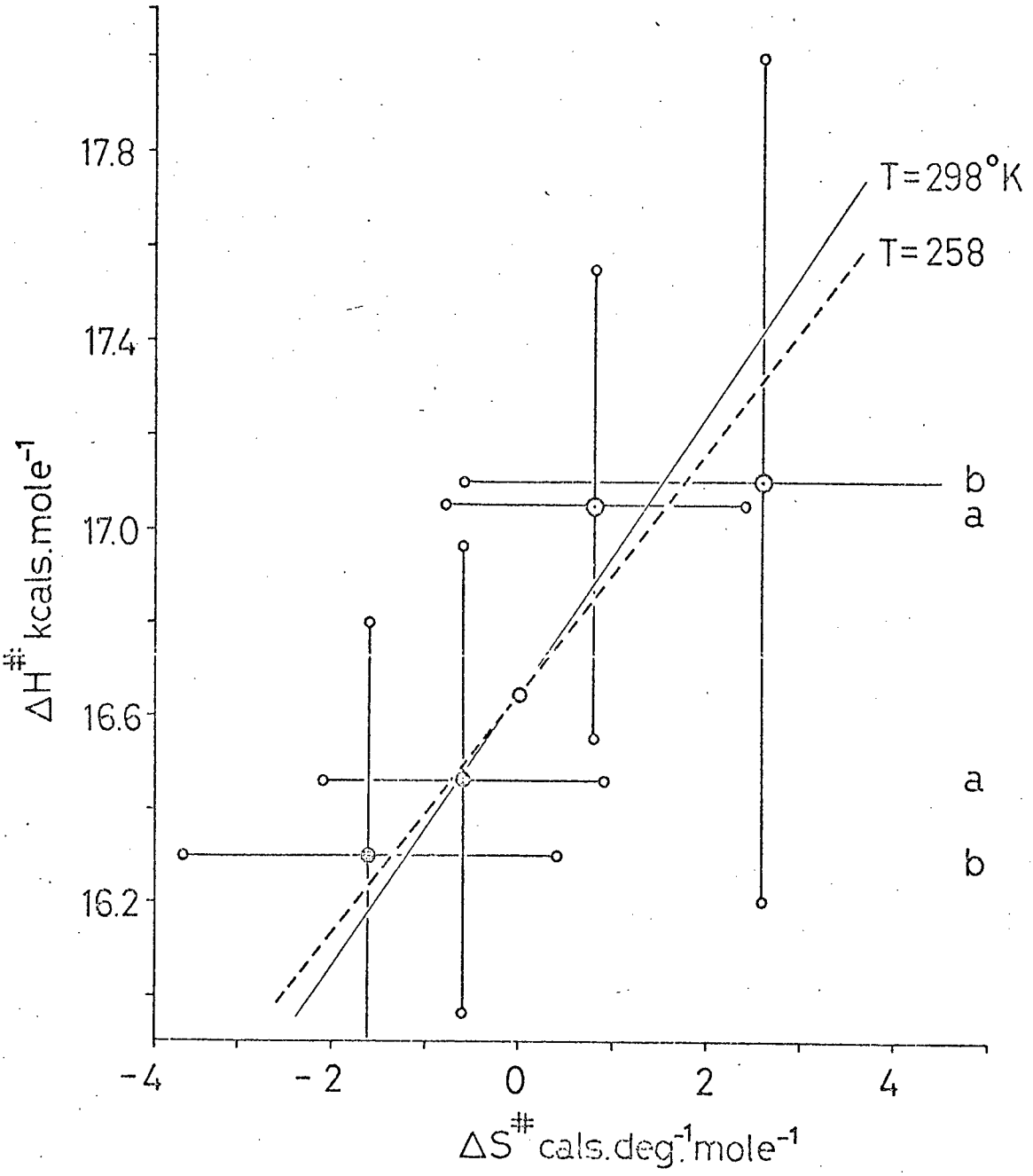

Fig. 4.4 Activation parameters obtained by complete lineshape analysis for N,N-dimethyl carbamylchloride

● 6% CCl_4 solution

o neat liquid

small positive $\Delta S^{\#}$ value as compared with a commensurate negative $\Delta S^{\#}$ value for a dilute CCl_4 solution in which such an interaction is presumably minimised. In general, although different solvents and substituents influence $\Delta H^{\#}$ and $\Delta S^{\#}$ in a complex manner, the partial compensation effect is of such a form that their influence on $\Delta G^{\#}$ is much simpler in form. Until the present steady-state NMR lineshape data is supplemented by spin-echo and double resonance data of comparable precision over an extended temperature range, it appears that the free energy of activation is the only parameter that will allow quantitative correlations for a series of substituted N,N-dimethyl amides.

4.1.2 N,N-dimethyl carbamyl bromide

N,N-dimethyl carbamyl bromide (DMCB) was chosen as a halo-substituted N,N-dimethyl amide in a series to allow a consistent study of substituent effects on the hindered rotation about the amide N-C bond.

DMCB was prepared by saturating ~10 gms of N,N-dimethyl carbamyl chloride (DMCC)[136] by bubbling a mixture of HBr and N_2 gases through the neat liquid chloride kept at 0°C. The N_2 stream removed any HCl or Cl_2 formed and significantly increased the yield of the carbamyl bromide. The bromide was purified by multiple distillations at ~10 mm, the boiling point of the final product being 63°C at this pressure. The product was identified by NMR and was shown to contain ~2% of the carbamyl chloride, this being verified by the elemental analysis:

	C	H	Br	Br + Cl	
Calculated	23.68	3.95	52.63		%
Found	24.54	4.30	-	54.11	%

This liquid amide was studied neat as solute-solvent interactions were shown to have only a small effect on the hindered rotation in the similar DMCC system, and on the activation parameter of interest at this point ($\Delta G^{\#}$), as discussed in the preceding section. The NMR sample was prepared as previously outlined. Complete lineshape analyses for this two-site equal population exchange system, using the iterative fitting program PLONK, gave the results summarised in Table 4.4. Typical lineshape fits are shown in Fig. 4.5. These fits were not improved (within the rate constant error bounds) by considering a temperature dependent chemical shift 2Ω, cf. Eq. (2.2.1), and thus the cis-trans N-methyl chemical shift may be assumed to be 5.4 ± 0.2 Hz at 60 MHz over the temperature range -15°C to 70°C. As this chemical shift is reduced by 20% and 32% from those for DMCC and the parent amide DMF (N,N-dimethyl formamide, $2\Omega = 8.1$ Hz), respectively, considerable magnetic anisotropy associated with the C-Br bonding system is indicated. This anisotropy is of a form that partially compensates that due to the C = O system, and this compensation effect is also shown by the C - Cl bonding system in that this chemical shift for DMCC is reduced by 16% from that for DMF. However, it is to be noted that these chemical shift variations are due in part to intermolecular interactions and electric field effects [133, 137]. The activation parameters calculated for DMCB at 25°C are given in Table 4.4,

TABLE 4.4

Kinetic data for N,N-dimethyl carbamyl bromide

(neat)

Temp. °C	k sec^{-1}
-10.2	0.62
- 2.0	2.06
- 1.0	2.14
7.2	3.60
7.3	3.52
11.5	5.52
15.7	7.35
16.2	7.28
16.4	8.67
19.0	11.2
19.4	14.0
19.7	15.0
24.0	20.9
24.0	21.5
32.5	33.7
36.6	60.2
48.8	125.5
55.0	161.9
58.7	300.3
61.6	464.1

continued/...

TABLE 4.4 continued

E_a = 15.25 ± 0.36 kcals. $mole^{-1}$

$\Delta H^{\#}$ = 14.66 kcals. $mole^{-1}$ at 25°C

$\Delta S^{\#}$ = -3.3 ± 1.2 cals. deg^{-1} $mole^{-1}$

$\Delta G^{\#}$ = 15.66 kcals. $mole^{-1}$

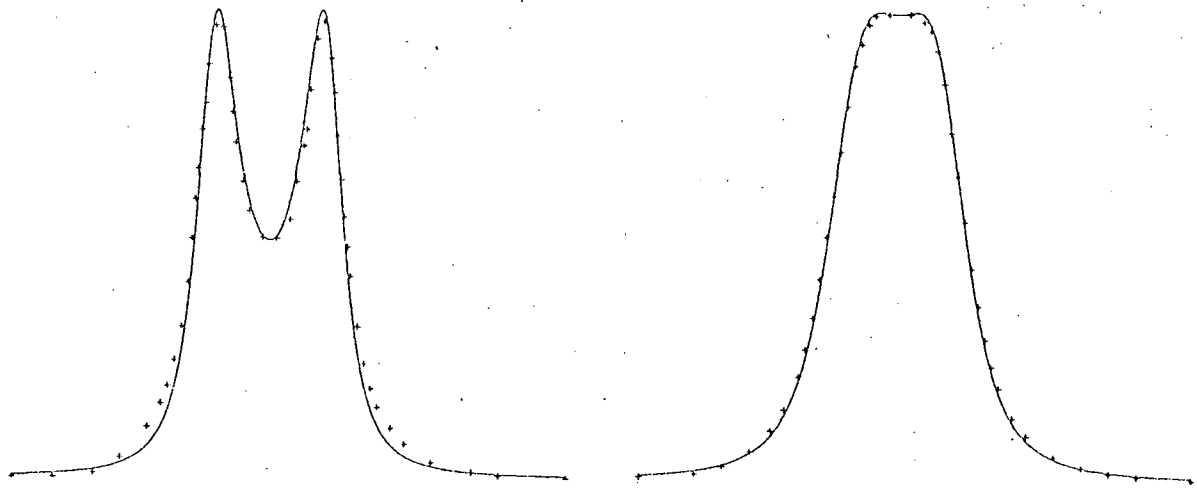

T = 11.5°C

k = 5.52 sec^{-1}

19.4

14.0

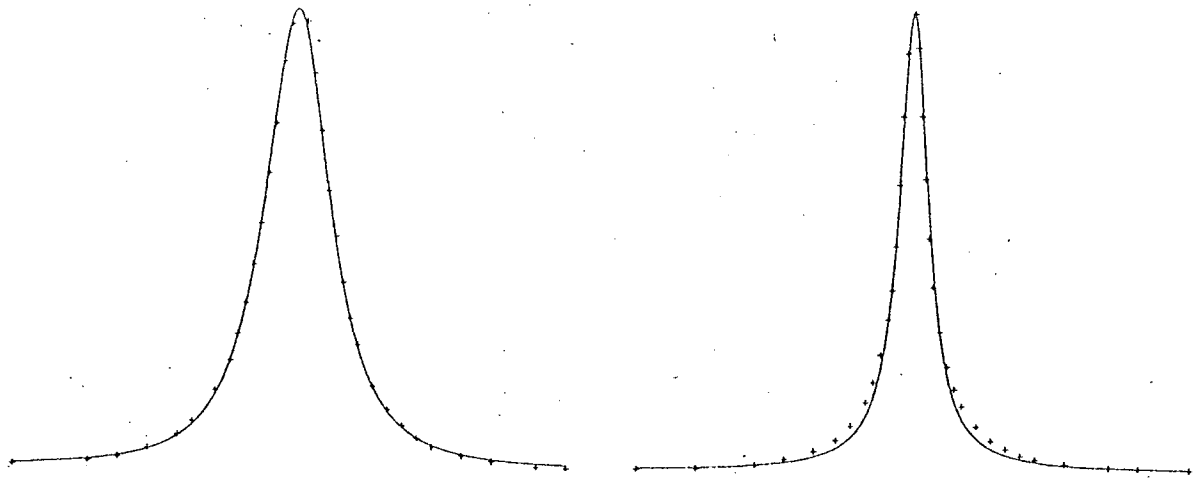

T = 24.0°C

k = 20.9 sec^{-1}

36.6

60.2

Fig. 4.5 Lineshape fits for N,N-dimethyl carbamyl bromide, two-site equal population exchange system.

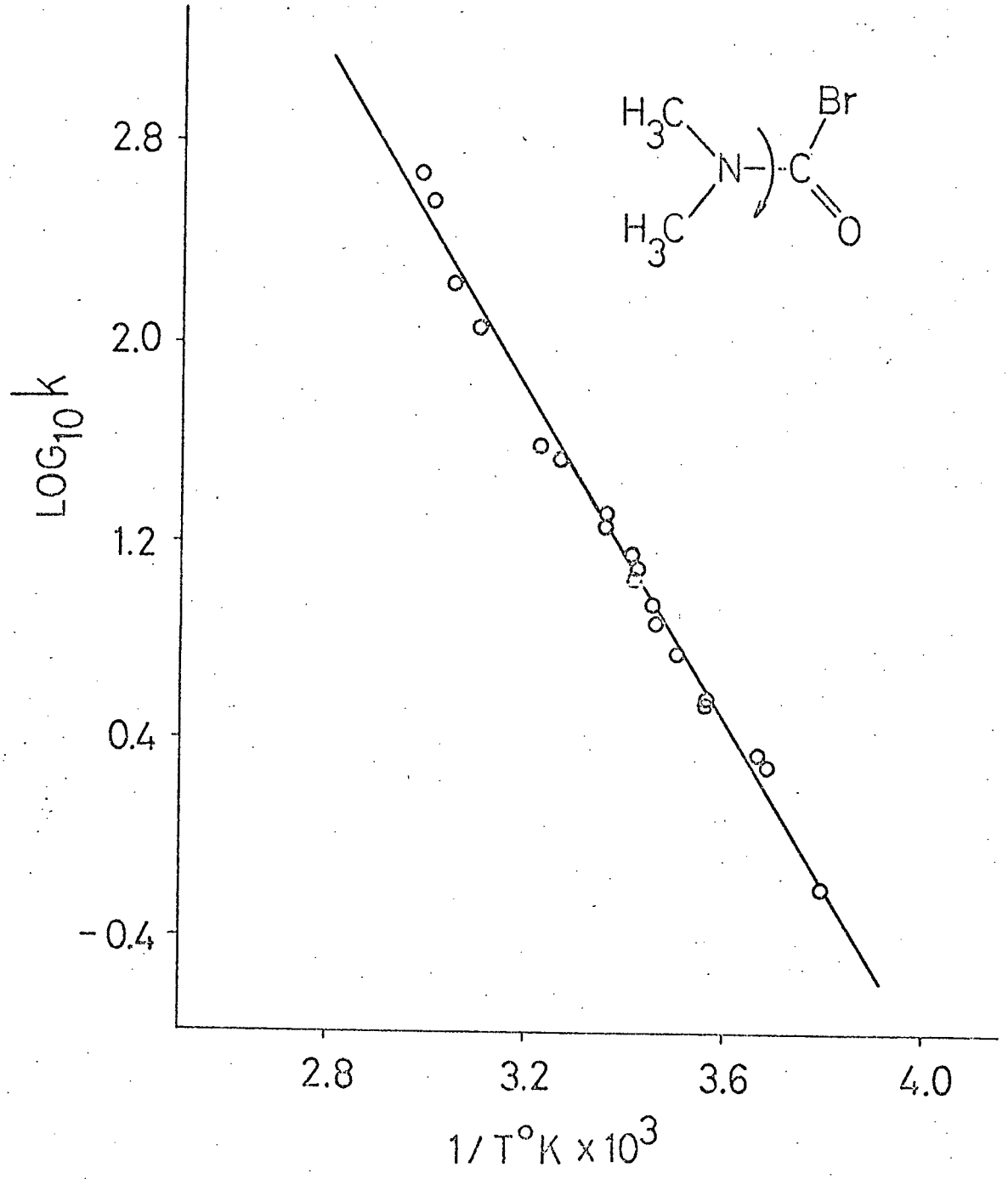

Fig. 4.6 Arrhenius plot for N,N-dimethyl carbamyl bromide

the energy of activation for the hindered rotation being determined from the Arrhenius plot shown in Fig. 4.6 as 15.25 ± 0.36 kcals. $mole^{-1}$. Again the entropy of activation $\Delta S^{\#}$ = -3.3 ± 1.2 cals. $deg.^{-1}$ $mole^{-1}$ is determined to be relatively small, as expected for the type of rate process under consideration.

4.1.3 Methyl N,N-dimethyl carbamate

The methyl ester of N,N-dimethyl carbamic acid, methyl N,N-dimethyl carbamate (DMCO), was studied to allow a comparison of the O-methyl group with halogens and pseudo-halogens as substituents in an amide series.

If hindered rotation about the N-C bond is present in this carbamate, the rate process may be analysed in terms of a simple two-site equal population exchange system as this compound is not expected to have a preferred conformation and the spin-spin coupling between the N-methyl and O-methyl protons will be negligible. However, Drago et al [138] have reported the N-methyl groups in this carbamate to be equivalent in the neat liquid and in a number of solutions at all temperatures down to -46°C, showing that the barrier to rotation about the N-C bond is inherently low, that is less than about 8 kcals. $mole^{-1}$. A later study by Lustig et al [139] showed that this barrier to rotation is increased in chloroform solutions and that a cis-trans N-methyl inequivalence is observed at ~-25°C, the associated chemical shift being dependent upon solute concentration. The increased nitrogen lone pair delocalisation in a $CHCl_3$ solution, leading to an N-C rotation

observable by NMR, is presumably due to a hydrogen-bonding interaction between the carbonyl oxygen lone pair electrons and the solvent molecules which would tend to preferentially stabilize the amide resonance form represented as $N^{+} = C = O^{-}$. Thus DMCO is studied here as a 10 mole % $CHCl_3$ solution to obtain an estimate of the effect of such a solvent interaction on the N - C = 0 bond system and to allow a correlation with a simple molecular orbital model developed in a later section. A 10% solution corresponds to a near maximal N-methyl chemical shift (2Ω) of only 1.8 ± 0.1 Hz at 60 MHz and at -30°C.

DMCO was prepared through the reaction of dimethylamine with methyl chloro-formate as described by Hartman and Brethen[141]. The liquid product was purified by distillations at ~40 mm and stored over molecular sieves, the final product having a boiling point of 58°C at this pressure, cf. lit. value 56.5 - 57°C[141]. The NMR sample was prepared as previously described for DMCC, with Spectrograde deuterochloroform which had been thoroughly dried over molecular sieves.

Owing to the very small chemical shift 2Ω, cf. Eq. (2.2.1), the temperature range for the kinetic study is limited to 25°C. Therefore, to obtain reliable rate constants from complete lineshape analyses, a large number of spectra were fitted at each temperature using the program PLONK, as described in section 4.1.1. The shift 2Ω was shown to be temperature independent (± 0.1 Hz) within the lineshape fitting error limits attainable. The averaged rate constants, k sec^{-1}, are given in Table 4.5 and the corresponding Arrhenius plot is shown in Fig. 4.8. The energy of activation, E_a, is determined as 15.18 ± 0.58 kcals $mole^{-1}$

TABLE 4.5

Kinetic data for N,N-dimethyl carbamate

(10% $CHCl_3$ solution)

Temp. °C	k sec^{-1}
-23.9	0.25
-22.5	0.41
-16.0	0.76
-14.6	1.05
-14.4	1.15
- 9.3	1.36
- 9.3	1.44
- 8.9	1.57
- 8.3	1.68
- 5.4	2.23
- 5.2	2.46
- 2.7	3.18
- 2.2	3.42
- 1.1	4.18
- 1.0	4.43
1.5	5.36

E_a = 15.18 ± 0.58 kcals. $mole^{-1}$

$\Delta H^{\#}$ = 14.54 kcals. $mole^{-1}$ at 25°C

$\Delta S^{\#}$ = -2.0 ± 2.2 cals. deg^{-1} $mole^{-1}$

$\Delta G^{\#}$ = 15.19 kcals. $mole^{-1}$

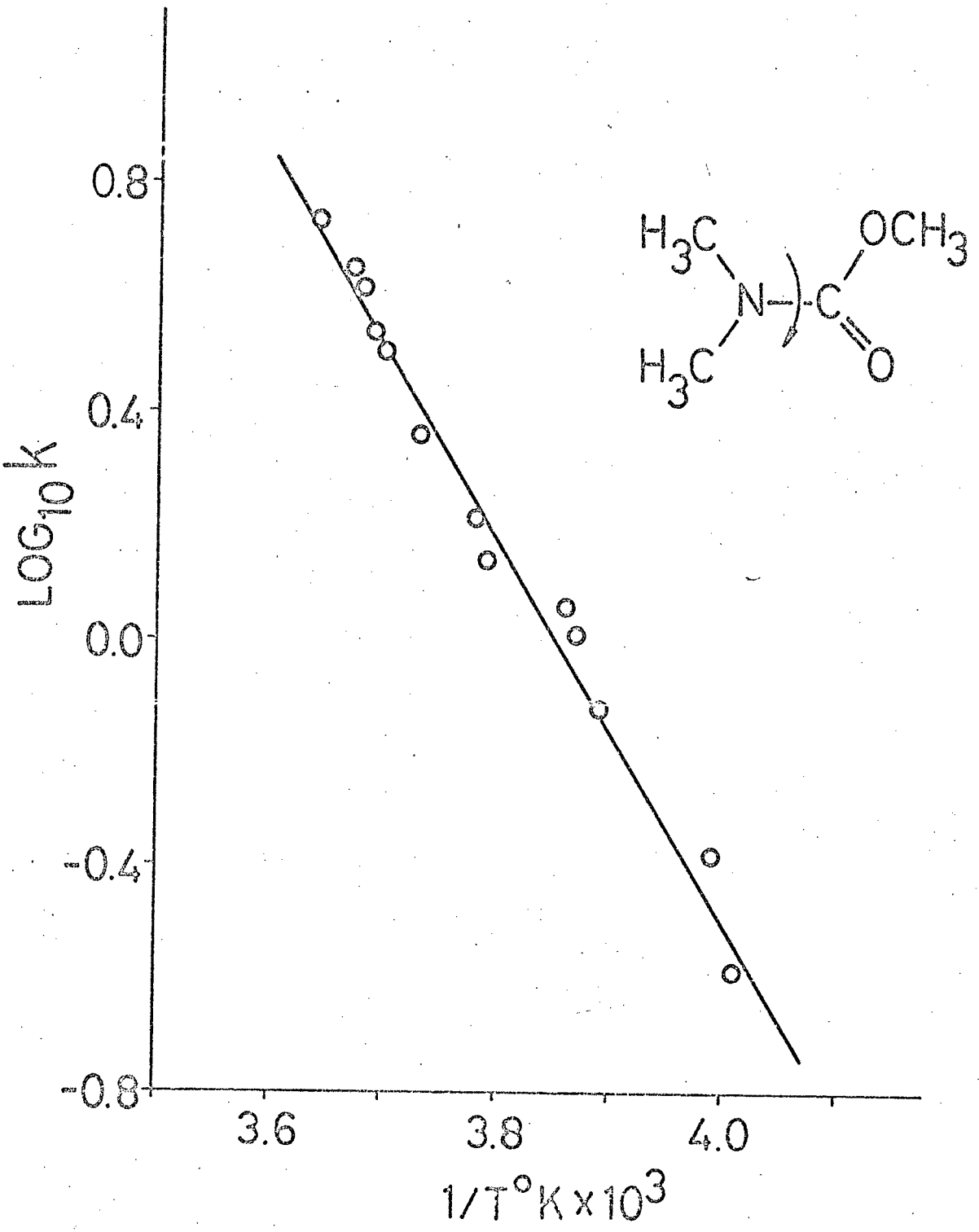

Fig. 4.7 Arrhenius plot for methyl N,N-dimethyl carbamate (10% $CHCl_3$ solution)

and thus it is shown that the carbonyl-$CHCl_3$ interaction increases the barrier to hindered rotation for DMCO by about 8 kcals. $mole^{-1}$. This implies that, in general, the magnitude of E_a (or $\Delta G^{\#}$) for the N - C rotation may be a sensitive measure of intermolecular interactions with an amide C = O group, when these parameters are derived through complete NMR lineshape analyses. The small entropy of activation determined from the above kinetic data for DMCO, $\Delta S^{\#} = -2.0 \pm 2.2$ cals deg^{-1} $mole^{-1}$, implies that the carbonyl - $CHCl_3$ interaction and hence solute-solvent structure is very nearly invariant to the change in overall dipolar character of the amide system in forming the transition state for the rate process under consideration. The magnitude of the chemical shift 2Ω is difficult to interpret as it will depend upon a modification of the form of the C = O magnetic anisotropy due to the $CHCl_3$ hydrogen-bonding and also the magnetic anisotropy associated with the $C-OCH_3$ group, in addition to solvent and electric field effects[137].

4.1.4 N,N-dimethyl carbamyl fluoride

N,N-dimethyl carbamyl fluoride (DMCF) was studied as a further member of a series of halo-substituted N,N-dimethyl amides showing hindered rotation about the N - C bond. Although this compound is well known as a specific enzyme inhibitor[142, 143] very little information is available on its electronic structure as compared with other amides of importance in biochemical systems[144]. A study of this compound allows a direct comparison of the data available from molecular orbital calculations for N,N-dimethyl formamide (DMF) and DMCF and for

the parent compounds formamide and carbamyl fluoride. Carbamyl fluoride is stable only at relatively low temperatures[145] and thus it is not possible to experimentally determine the barrier to hindered rotation for this particular amide.

DMCF was prepared by a simple exchange reaction between N,N-dimethyl carbamyl bromide (DMCB) and AgF, using CH_3CN as a solvent. The yield was low (~ 10%), however, and an improved method of preparation utilizes SbF_3 as a fluorinating agent[146]. The product was purified by vacuum distillations at ~10mm (bp = 35°C), and also by a distillation at 760 mm (bp = 129°C) using a spinning-band column, and gave an elemental analysis:

	C	H	F	
Calculated	39.58	6.59	20.88	%
Found	39.81	6.58	20.68	%

DMCF was studied as a 16 mole % CCl_4 solution to minimise solute-solvent interactions for this highly polar compound (μ = 4.02D[147]). The NMR sample was prepared in the manner previously described and as usual dioxane was used as the reference peak defining the transverse relaxation time, T_2, in the absence of chemical exchange. DMCF gives an A_3B_3X spectrum, the methyl group A_3 being trans to the carbonyl oxygen atom and resonating at a lower field than the B_3 group. This spectral assignment is consistent with the general NMR chemical shift characteristics associated with the magnetic anisotropy of the carbonyl group[132, 133, 148]. In addition, the unequal ^1H - ^{19}F spin-spin coupling constants are determined in the absence of exchange ($\sim$ - 20°C)

as $|J_{AX}| = 0.3 \pm 0.05$ and $|J_{BX}| = 0.8 \pm 0.05$ Hz, consistent with a normal trans coupling (J_{BX}) being greater than a cis coupling[152]. This assignment is similar to that made for N,N-dimethyl formamide[59,61], in which case $J_{AX} = 0.35$ and $J_{BX} = 0.60$ Hz. These couplings may be compared with those for the related acetyl compounds CH_3CFO ($J_{HF} = 7.6$ Hz) and CH_3CHO ($J_{HH} = 2.85$ Hz), showing the effect of the interposed N atom and the N-C double bond character on these indirect spin-spin couplings. The chemical shift between the A and B methyl groups (2Ω) in DMCF is very small, solvent and concentration dependent, and also temperature dependent. For example, the values of 2Ω for the neat amide and a 16 mole % CCl_4 solution at $\sim$-20°C are 1.2 ± 0.1 and 2.20 ± 0.05 Hz, respectively, at 100 MHz. The corresponding shift at 30.5°C for the CCl_4 solution is 1.75 ± 0.05 Hz. This particular shift was also measured at 220 MHz and was shown to be accurately consistent with the overall assignment made for the AB-transitions. The methyl proton chemical shift is predominantly due to the combined effect of the magnetic susceptibility anisotropies of the C-F and C=O bond systems. The relatively small 2Ω value thus indicates that the forms of the susceptibility tensors associated with the electronic charge distributions localised in these two bonds are such that the two methyl shielding regions have very similar characteristics. This in turn may imply that delocalisation of fluorine $2p_\pi$ electrons, as represented by the resonance form $N - \underset{\underset{O^-}{|}}{C} = \overset{+}{F}$, is significant in the ground state of DMCF. Such a charge distribution would lead to an anisotropy of the C-F bond which is not axially symmetric and is comparable to that normally

associated with the C=O system. The temperature dependence of 2Ω may be ascribed to a temperature dependent intermolecular dipole-dipole association which affects the magnetic anisotropies of the C=O and/or C-F groups, and hence it becomes apparent that the reduction of solute-solvent interactions in a CCl_4 solution may increase the probability of solute-solute interactions between the polar DMCF molecules.

Although chemical shifts are generally dependent upon detailed solvent interactions, indirect spin-spin couplings are usually very nearly independent of these intermolecular effects. In the case of an amide such as DMCF, however, such interactions may stabilize the

ground-state resonance form $\overset{+}{N} = C - F$ (with O^-) leading to enhanced couplings

between the methyl protons and the fluorine nuclear spin due to the increased N-C double-bond character. This is actually observed experimentally, in that $|J_{BX}| = 1.1 \pm 0.1$ Hz for neat DMCF. This is an increase of 0.3Hz as compared with the value for the DMCF/CCl_4 solution, showing that the CCl_4 solvent does break down specific solute-solute interactions to some extent. As the four-bond spin-spin coupling J_{HH} between the A_3 and B_3 methyl groups in N,N-dimethyl amides is negligible [151], the ^1H NMR spectrum for the DMCF spin system may be analysed in terms of an AB-part of a first-order ABX ($J_{AB} = 0$) spectrum as described in detail in section 2.5 of this thesis and illustrated in Fig. 2.7. The couplings J_{AX} and J_{BX} are shown to be temperature independent (within experimental error), as the averaged coupling in the limit of very fast

exchange ($k \gg \Omega$) is determined as 0.6 ± 0.1 Hz corresponding to a calculated coupling $J_+ = \frac{1}{2}(J_{AX} + J_{BX}) = 0.55 \pm 0.10$ Hz. The observed lineshapes in the presence of exchange unambiguously lead to the conclusion that the relative signs of these couplings are the same, as implicitly assumed in the above definition of the parameter J_+. The characteristic AB- part of a first-order ABX spectrum is shown in Fig. 2.7 (a) for $J_{BX} > J_{AX} > 0$, where for $k \gg \Omega$ the spectrum reduces to an A_2X form with an effective coupling J_+. In such an analysis for DMCF it has been assumed that the two-bond spin-spin couplings between the methyl protons and the amide ^{14}N nuclear spin are negligible. Although a ^1H - $\{^{14}N\}$ double resonance study[150] of N-substituted amides indicated that these couplings were indeed negligibly small, the data available from further studies using ^{15}N- amides[151,152] leads to calculated ^{14}N coupling constants J_{NA} and J_{NB} of 0.7 and 0.8 Hz, respectively. Nevertheless, it may be assumed that the methyl protons are completely decoupled by quadrupolar ^{14}N nuclear spin-lattice relaxation[153]. It should be noted, however, that the X-part of the complete A_3B_3X spectrum may show effects due to the coupling J_{NX}, this three-bond coupling being enhanced by the N-C partial double bond character. The ^{14}N - ^1H coupling J_{NX} for N,N-dimethyl formamide is calculated as 10.4 Hz[152], and hence the corresponding ^{14}N - ^{19}F coupling may be of the order of 15 Hz. For a scalar coupling of this magnitude, the ^{14}N quadrupolar relaxation mechanism may give only a partial spin-spin decoupling due to the temperature dependence of the molecular reorientation giving rise to the time-dependent electric field gradient

at the ^{14}N nucleus.

The first-order rate constants, k, describing the hindered rotation in DMCF have been determined using total lineshape analyses in terms of the stochastic model for such a multi-site exchange process developed in section 2.5. The absorption mode lineshape function, V(x), is the real part of the complex function G(x) given in Eq. (2.5.14). The diagonal matrix $\underline{\underline{\Lambda}}$ and associated transformation matrices $\underline{\underline{S}}$ and $\underline{\underline{S}}^{-1}$ appearing in this expression are derived from a 4 x 4 matrix $[\underline{\underline{K}} - i\underline{\underline{\Omega}}]$ defining the specific rate process for the equal population DMCF exchange system and the Larmor frequencies for the four spin-sites to be considered (cf. Fig. 2.7). The matrices required for $J_{BX} > J_{AX} > 0$ have been given explicitly in Eq. (2.5.15). A FORTRAN-IV computer program GPLONK was developed to allow a rapid numerical calculation of general multi-site exchange lineshapes based upon the component expressions given as Eqs. (2.4.8) and (2.4.9). Representative intramolecular exchange lineshapes for the AB-part of a first-order ABX spin system, as calculated using GPLONK, are shown in Fig.2.8. The CPU time involved on an IBM 360/67 system for each 600 point spectrum, including the setting-up of control arrays for a CALCOMP plotter, is less than 4 secs which exemplifies the advantages of applying a matrix formulation, and the specific component form previously described in detail, to lineshape calculations. The program GPLONK, in conjunction with a subroutine GFITT, also allows an efficient automatic iterative fitting of a theoretical lineshape to digitized experimental data. The subroutine GFITT is based upon the simple search through optimised parameter increments previously described, cf. section 4.1.1, where the

matrix $\underline{\underline{K}}$ is changed iteratively in accordance with the general procedure outlined in section 2.4 following Eq. (2.4.9).

Multiple spectra were obtained for the DMCF CCl_4 solution at each of nine temperatures over the range -15.2 to 78.2°C using a FABRITEK FT-1064 computer with the spectrometer-computer interface described in section 3.1. A typical sampled and digitized spectrum for DMCF is shown in Fig. 3.5. Because of the very small methyl chemical shift 2Ω for DMCF, and hence NMR lineshape frequency interval, it is difficult to obtain accurately reproducible steady-state spectra even with the overall stability available from a field-frequency locked spectrometer. Some typical lineshape fits are shown in Fig. 4.9 and the average rate constants obtained from multiple fits at each temperature are summarised in Table 4.6. The temperature dependences of the chemical shifts ω_A and ω_B, cf. Eq. (2.2.24), derived from these lineshape fits are shown in Fig. 4.8 along with the mean frequency ω_0 defining the reference zero for the independent variable x. All frequencies are measured with respect to that for TMS at constant field. The variation in methyl chemical shifts is presumably due to a stereospecific intermolecular interaction which may lead to a small change in the form of the anisotropic shielding associated with the C=O and C-F groups in DMCF. Thus the chemical shift 2Ω varies from 2.2 to 1.4 Hz over the temperature range -15.2 to 78.2°C. The coupling constants J_{AX} and J_{BX} were assumed to be temperature independent, and the chemical shifts corresponding to minimum error multiple lineshape fits were found to be consistent to within $\pm$ 0.05 Hz. Thus this lineshape fitting procedure may be used to determine small chemical shifts and/or

TABLE 4.6

Kinetic data for N,N-dimethyl carbamyl fluoride

(16 mole % in CCl_4)

temp., °C	k, sec^{-1}	error
12.2	0.076	4.8
15.6	0.159	4.2
30.2	0.550	3.7
32.5	0.692	4.1
37.6	1.99	2.2
44.9	2.29	1.2
46.5	2.57	1.3
53.8	5.11	1.3
62.7	9.55	3.9
78.2	26.3	4.6

$E_a = 18.3 \pm 0.6$ kcals. $mole^{-1}$

$\log_{10}A = 12.9$

$\Delta H^{\#} = 17.7 \pm 0.6$ kcals. $mole^{-1}$

$\Delta S^{\#} = -1.4 \pm 2.1$ cal.deg^{-1}. $mole^{-1}$

$\Delta G^{\#} = 18.2 \pm 0.6$ kcals. $mole^{-1}$

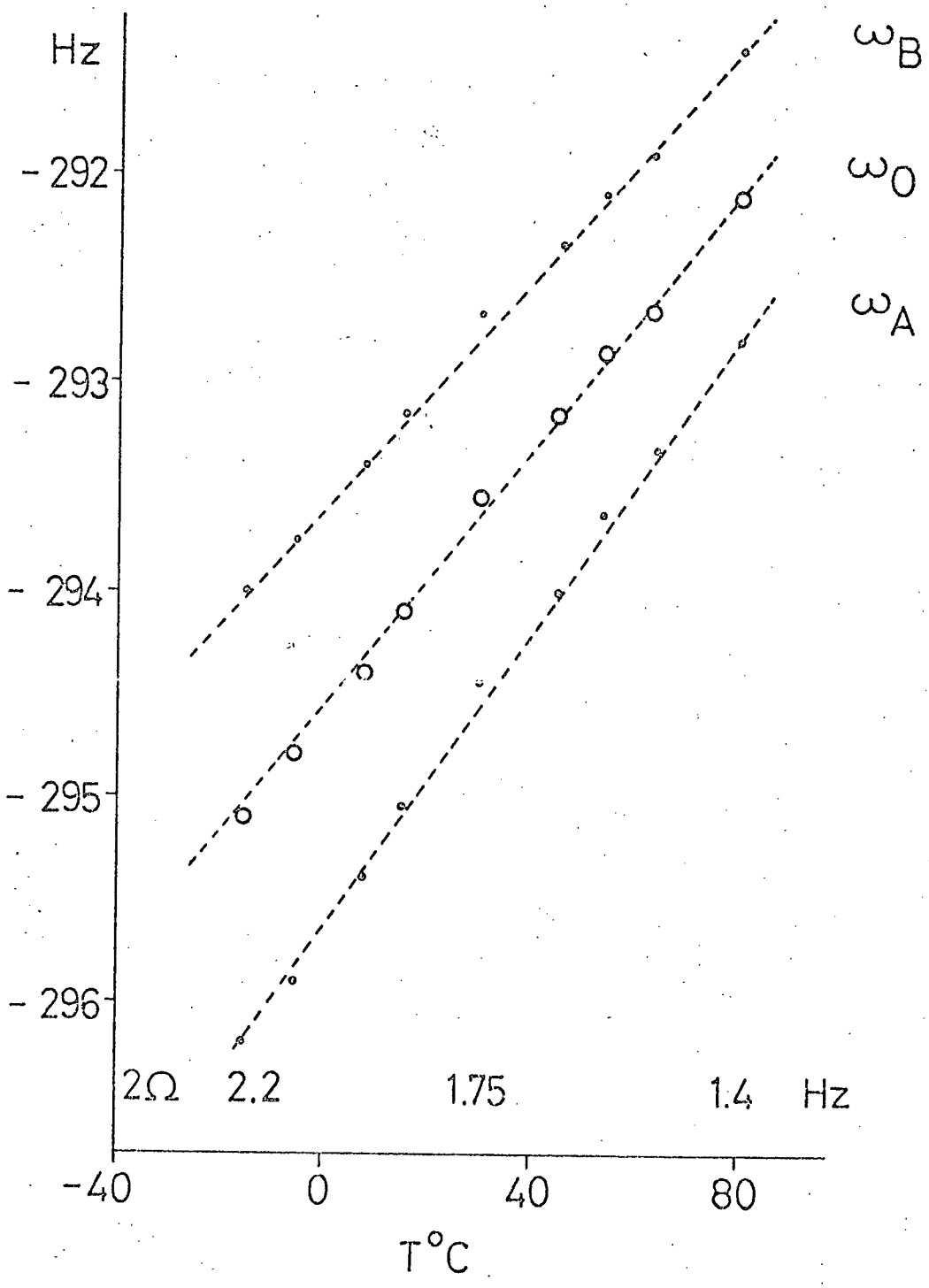

Fig. 4.8 Temperature dependence of chemical shifts for N,N-dimethyl carbamyl fluoride

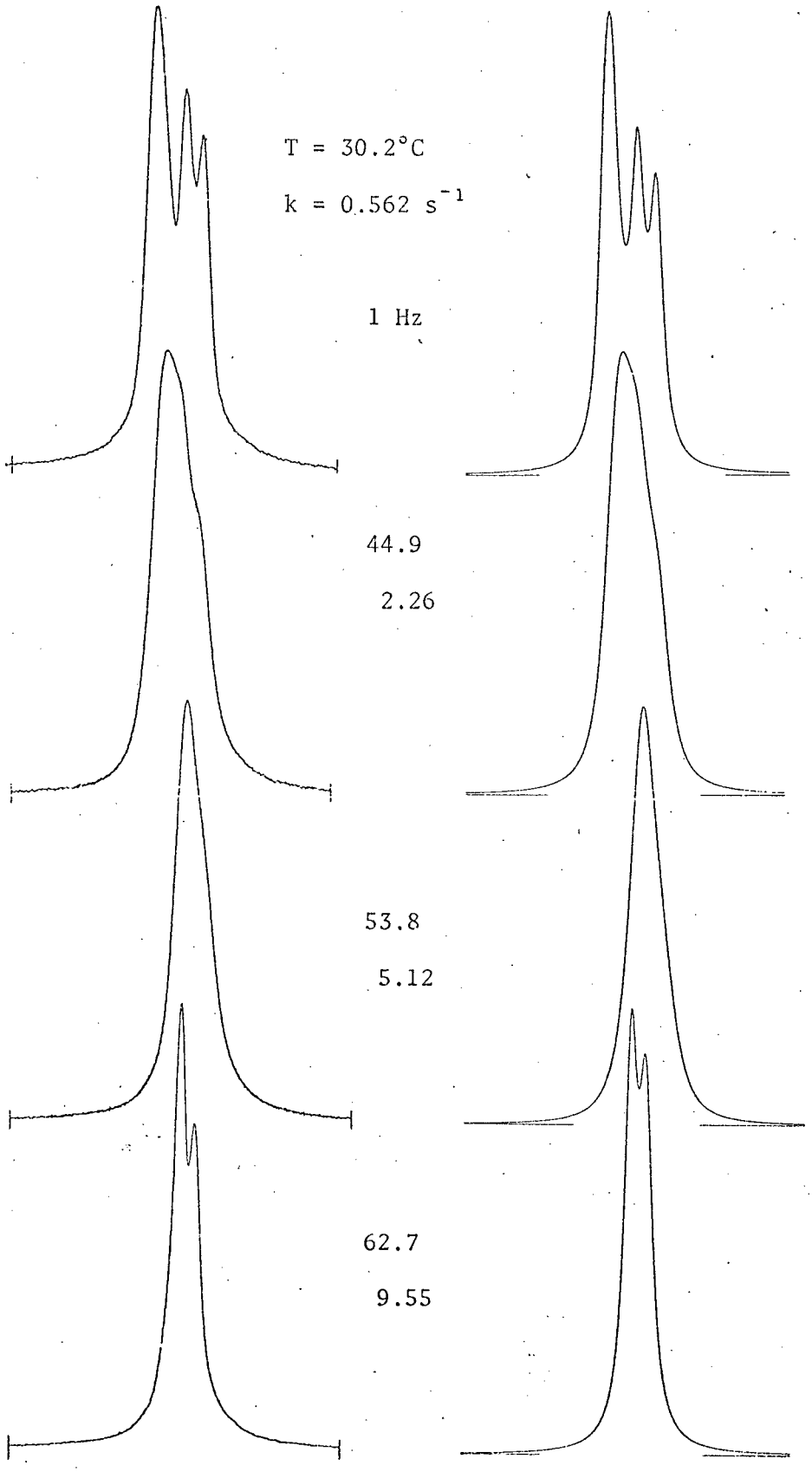

Fig. 4.9 Total lineshape fits for N,N-dimethyl carbamyl fluoride

coupling constants to this precision[154,155], which could not be obtained under normal NMR spectral resolution. It is to be noted that the errors (cf. section 4.1.1) for the DMCF fitted lineshapes are maximal in the limits of very slow and very fast exchange. This may be due to the difficulty in recording the steady-state lineshapes over a frequency range of only 5Hz, but in actual fact these lineshapes were accurately reproducible within the error limits involved. Also, in the very slow exchange limit, the residual linewidths were greater than the reference widths and hence additional transverse relaxation effects may have been observed in this particular amide. Such effects may arise from anisotropic nuclear dipole-dipole, quadrupolar and chemical shift interactions through incomplete averaging by molecular reorientation[156,157]. In addition, enhanced cross-relaxations associated with these anisotropic tensor interactions may give rise to differential linewidths in the absence of hindered rotation in DMCF. Such relaxation processes have not been included in the analysis reported here. The Arrhenius plot for DMCF is most satisfactory, however, and is shown in Fig. 4.10. The activation energy is determined as 18.3 ± 0.6 kcals. $mole^{-1}$. The free energy of activation is then calculated at 25°C as $\Delta G^{\#}$ = 18.2 ± 0.6 kcals. $mole^{-1}$, with an entropy of activation $\Delta S^{\#}$ = -1.4 ± 2.1 cal. $deg^{-1}mole^{-1}$which is of a magnitude typical of the hindered rotations in all of the substituted N,N-dimethyl amides studied here.

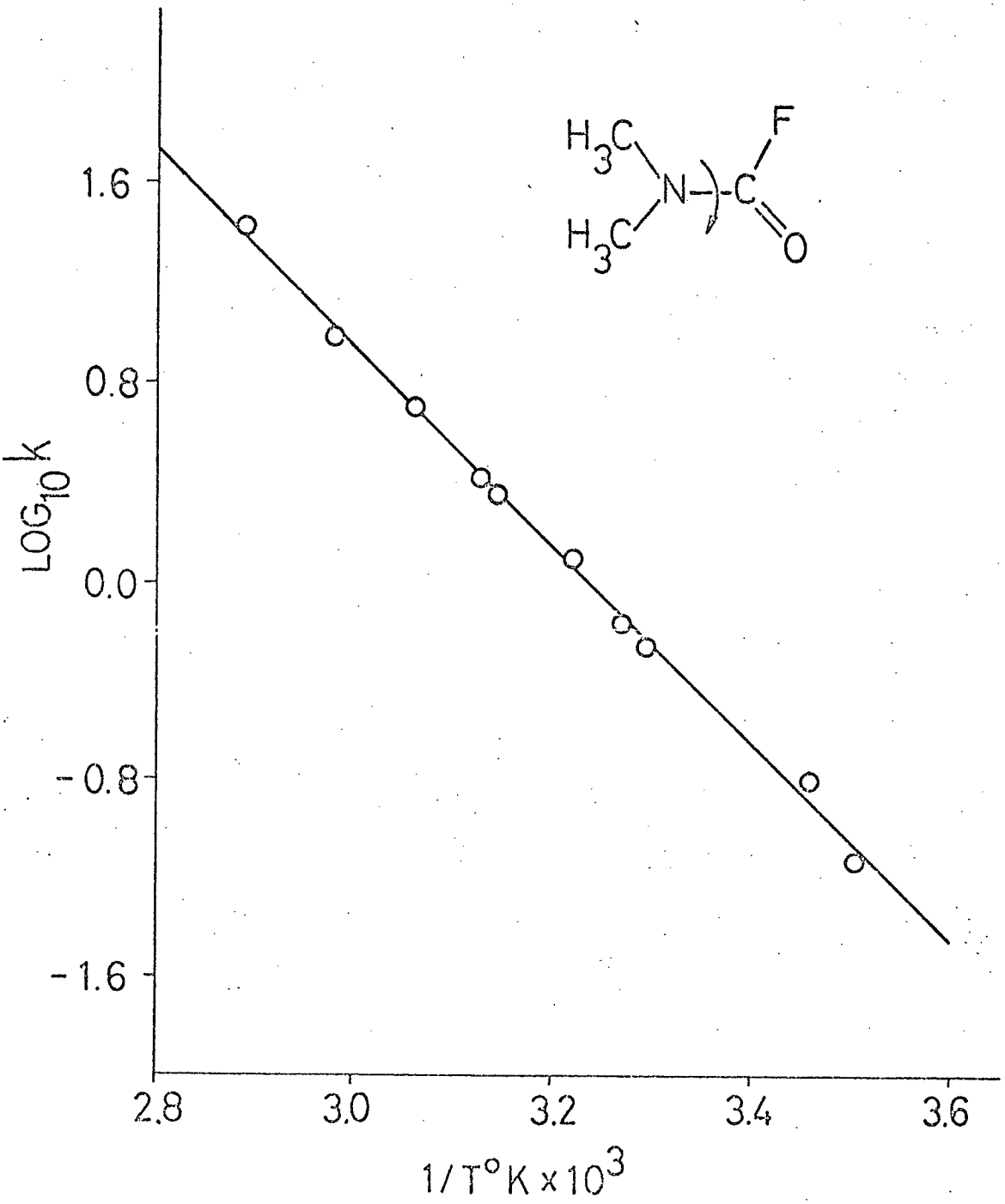

Fig. 4.10 Arrhenius plot for N,N-dimethyl carbamyl fluoride

4.1.5. Formamide

Although some semi-quantitative kinetic data were available for the hindered rotation in formamide[158,159], a total lineshape analysis had not been reported and hence this parent amide was studied to obtain reliable activation parameters for comparison with those for the substituted N,N-dimethyl amide series already discussed. It is also of interest to compare the experimentally determined rotation barriers in formamide and N,N-dimethyl formamide (DMF) to allow a further correlation with the corresponding series of parent amides, which are usually experimentally inaccessible but are certainly more convenient for molecular orbital calculations being the simplest molecular containing the N-C=O bond system. Of course, the barrier in formamide is of fundamental importance as a reference point for all descriptions of substituent effects on the hindered rotation about the N-C bonds in amides and of the bonding characteristics in these compounds. In the course of the work described here, an independent NMR lineshape study was reported[160] and the additional data now available may be used to ascertain the applicability of the general lineshape fitting procedure to a more complicated tightly-coupled nuclear spin system. As already described in detail in section 2.6, the analysis of chemical exchange in a tightly-coupled (second-order) spin system requires a complete spin density matrix treatment.

In contrast to DMF, there are two complicating factors in an NMR study of the hindered rotation in formamide. Firstly, the quadrupolar ^{14}N nucleus leads to very broad resonances for the directly

bonded amino protons eliminating all chemical shift information for these protons[161], and hence it is necessary to use an isotopically enriched ^{15}N-formamide sample[158] or double rf-irradiation[159]. The former simplification is preferable for a quantitative lineshape study as the distortion inherent in spin-spin decoupling is difficult to evaluate. Secondly, the intermolecular exchange of the basic amino protons of formamide gives additional spin transfer effects in the steady-state spectrum and the inclusion of such effects in a lineshape analysis leads to a large increase in the computer core and time required for numerical calculations. In principle it is possible to determine the rates of the intramolecular (hindered rotation) and intermolecular exchange processes simultaneously from lineshape fits, but as the latter process is not of current interest it may be suppressed over the temperature range for an intramolecular exchange study by using acetone as a solvent[158].

^{15}N-enriched (98 atom %) formamide was obtained from Merck Sharp and Dohme and was studied as a 10 mole % acetone (spectro-grade) solution. The commercial formamide was used without further purification and was dried with the solvent over molecular sieves. Hexamethyldisiloxane ($\sim$2%) was added to the NMR sample for field-frequency locking. A separate single line was not required for a reference lineshape standard as the acetone peak is available and a convenient standard is also present in the C-part of the ABCX ^{15}N-formamide ^{1}H spectrum. That is, in the absence of intermolecular exchange there are four lines that have widths that are invariant to exchange effects,

cf. section 2.5, and hence these lines may be used to estimate the linewidth associated with magnetic field inhomogeneity and slow intermolecular exchange which may be present at higher temperatures. The NMR sample was thoroughly degassed by the usual freeze-pump-thaw cycle and was sealed in vacuo in thin walled tubes of 5 mm o.d..

The ^1H NMR spectra were obtained at 100 MHz with a Varian HA-100 spectrometer equipped with a V-6031 variable-temperature probe and temperature controller. The V-6031 controller maintains a preset temperature for the N_2 gas heating or cooling the sample, and the gas temperature is sensed at about 5 cm from the sample volume in the spectrometer receiver coil. Thus the sample temperature was measured before and after recording a spectrum using a standard methanol (or glycol) sample and interpolation of the -OH chemical shifts obtained in HA-mode using the data of Van Geet[126]. The temperature thus determined is estimated to be accurate to ± 0.3°C and was shown to be stable, within these limits, over a period of about 20 mins. The spectra were recorded at sweep rates of 0.02 or 0.05 Hz sec^{-1} to best approximate steady-state conditions, and with a low amplitude rf field (∿ 0.02 mgauss) to minimise lineshape distortion due to saturation effects. At each temperature, to ensure reproducibility, at least four spectra were digitised and stored using a Fabritek FT-1064 computer interfaced with the HA-100 as described in section 3.1. All frequencies were measured, using the V-4315 counter, with reference to HMDS as the internal standard. An optimum H_o field homogeneity was maintained over the temperature range -15 to 83°C corresponding to a 0.4 Hz resolution (T_2 = 0.8 sec.) and a

reference lineshape that best approximated a symmetrical Lorentzian shape. Wilmad PS-505 5 mm thin-walled sample tubes were used to attain reproducible spinning characteristics and field homogeneity control.

The hindered rotation in ^{15}N-formamide may be considered in terms of a mutual spin transfer of the A- and B- spins in an ABCX nuclear spin system, for which the basic equal population chemically shifted sites are predominantly due to the diamagnetic susceptibility anisotropy of the carbonyl group. Consistent with prior studies within this section, the amino B- proton which is cis to the carbonyl oxygen is assigned to high-field of the A-proton, and thus the C- spin is the formyl proton which is to low-field relative to both the A- and B- protons. Owing to the specific interaction of the acetone solvent molecule with the solute molecule, it is to be expected that the amino protons will have chemical shifts showing significant temperature dependences, while spin-spin couplings are usually less sensitive to intermolecular interactions. Therefore, initially, it is necessary to carefully analyse the ABCX spectrum in the absence of exchange effects to determine the form of the temperature dependences, if any, for the spectral parameters. The spectra were analysed using a computer program NMRFIT, which is a much modified version of LAOCOON[162] giving a very efficient iterative fit of spectral parameters to transition frequences, by assigning all 24 lines over the temperature range -12.4 to 30.2°C. The resultant chemical shifts and couplings are given in Table 4.7, along with those obtained from the earlier study of an acetone solution of the same concentration[158]

Table 4.7

Spectral parameters for ^{15}N-formamide

		$^{\dagger}\Omega_A$	Ω_B	Ω_C	J_{AB}	J_{AC}	J_{BC}	J_{AX}	J_{BX}	J_{CX}	ref.
a)	-12.4	-4.9	4.9	-84.6	2.8	1.8	13.5	90.1	87.5	15.1	this work
	-5.0	-5.7	5.7	-90.3	2.8	1.7	13.5	90.2	88.3	15.2	"
	3.0	-7.0	7.0	-97.4	2.8	1.7	13.5	90.0	87.6	15.3	"
	30.2	-10.3	10.3	-118.8	2.8	1.6	13.5	90.0	87.6	15.5	"
a)		-10.7	10.7	-118.8	2.9	1.7	13.5	91.0	88.0	16.4	(158)
b)		-12.1	12.1	-97.0	2.8	1.7	13.4	89.7	86.4	16.4	(152)
c)		-18.5	18.5	-69.8	2.6	1.6	13.5	89.3	87.1	15.6	(160)
d)		-9.9	9.9	-102.5	2.7	1.7	13.5	--	--	--	(159)

a) 10 mole % acetone solution, -12.4 to 30.2°C

b) 35 mole % acetone solution, 30°C

c) 14.1 % diglyme solution, 25°C

d) 22.2% acetone solution

† All chemical shifts refer to 100 MHz NMR.

and those from more recent studies using similar solvents[152,159,160]. Only relatively small variations in the values of the coupling constants are evident for different concentrations of formamide in acetone and diglyme as solvent, and are even smaller over the temperature interval of 42°C for the 10 mole% acetone solution. Thus all coupling constants are assumed to be temperature independent in the following lineshape analysis. As is normal, the trans coupling J_{BC} is much greater than the cis coupling J_{AC}, both being enhanced due to the partial double bond character of the interposed N-C bond. The chemical shifts Ω_A, Ω_B and Ω_C, however, show relatively large variations with solute concentration and temperature. In Table 4.7, the reference frequency ω_0 defining the independent frequency variable x for a lineshape analysis is taken as the average of the shifts ω_A and ω_B, cf. Eq. (2.2.24), and hence $\Omega_C < \Omega_A < 0 < \Omega_B$. The shifts ω_A, ω_B and ω_C are measured relative to hexamethyl-disiloxane and ω_C is shown to be approximately constant while ω_A and ω_B ($\Omega_A = \omega_A - \omega_0$) have relatively strong temperature dependences as illustrated in Fig. 4.11. As the chemical shifts derived using NMRFIT were reproducible to within ± 0.2 Hz and as the variation over the temperature interval -12.4 to 30.2°C was linear, as depicted by the open points in Fig. 4.11, it was assumed that a linear extrapolation could be used to determine the chemical shifts used in a lineshape fit at any temperature up to 85°C. The actual lineshape fits showed that the variations of all chemical shifts over this temperature range are indeed linear, in that the chemical shifts corresponding to the minimum error fits are shown as the closed

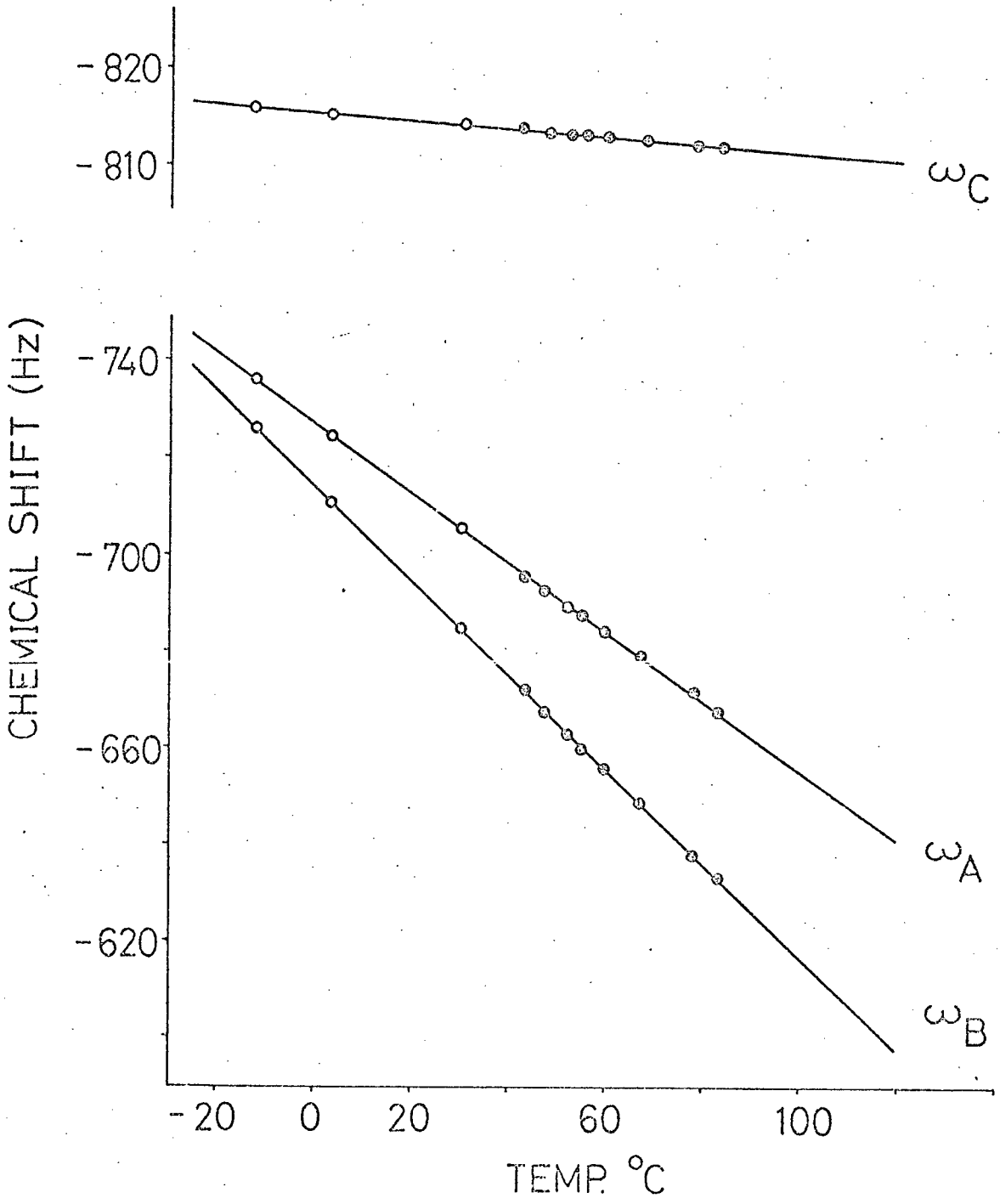

Fig. 4.11 Temperature dependence of the chemical shifts for ^{15}N-formamide, 10% acetone solution

points in Fig. 4.11.

The absorption mode steady-state NMR lineshapes for the ABC-part of the ABCX ^{15}N-formamide system as modified by mutual transfer of the A- and B-spins have been calculated using a FORTRAN-IV computer program GENLIN. The theory for these calculations has been discussed in detail in section 2.6 and the computer program is based upon the matrix equation Eq. (2.6.17), which is derived from the general component equation of motion for the spin density matrix, cf. Eq. (2.6.7). The spin transition operator matrix, $\underline{\underline{I}}^{+}$, in the basis of simple product functions for the four spin system is very similar to that given explicitly for the ABX (or ABC) spin system in Table 2.3. In fact the matrix given in Table 2.3 forms a block diagonal part of the complete ABCX transition matrix which defines 30 transitions, including allowed and "combination" transitions, in the ABC-part of the ABCX spectrum and hence the fundamental matrix $\underline{\underline{R}}'$, cf. Eq. (2.6.12), is a 30 x 30 matrix with complex elements. To simplify the calculation for the large number of numerical spectral data points ($\sim$1000) required in an iterative lineshape fitting procedure for such a complicated spectrum, the matrix $\underline{\underline{R}}'$ is transformed to diagonal form and the frequency dependent part is retained as the scalar matrix $x\underline{\underline{I}}$, $\underline{\underline{I}}$ being the 30 x 30 unit matrix. In comparison with Eq. (2.4.6) giving the complex lineshape function G(x) for a first-order spin system, the diagonal matrix $\underline{\underline{\Omega}}$ is derived from the matrix $\underline{\underline{R}}$ given in Eq. (2.4.5) where $\underline{\underline{\Omega}}$ is now an off-diagonal matrix. The elements of the matrix $\underline{\underline{\Omega}}$ are formally defined by the Liouville Hamiltonian operator[92,93], but

are very simply determined using a simple algorithm based upon Eq. (2.6.27). On diagonalisation, in the absence of exchange effects, this matrix directly determines the second-order transition frequencies and associated complex intensities. It is to be noted that the diagonal elements of the matrix $\underline{\underline{\Omega}}$ are first-order approximations to the transition frequencies, and indeed the only change in going to a second-order analysis of exchange effects using this matrix formulation is in the definition of the spin-site frequency matrix, $\underline{\underline{\Omega}}$, in Eq. (2.4.5). Following the similarity transformation as given in Eq. (2.4.7), the numerical lineshape computation is reduced to simple multiplications in real arithmetic as previously described, cf. Eq. (2.4.8). The computer program GENLIN is complicated by involved indexing and sorting to maximise the computational efficiency and such details need not be discussed at this point. The advantage of using the matrix formulation described as part of this work, however, is exemplified by comparison with the computational methods used in the independent study of ^{15}N-formamide[160]. The CPU time quoted for the computation of a single spectral data point for a 4-spin system using an IBM 360/75 computer is 0.3 second[163], and hence the time involved for a 1000 point spectrum as required for a reliable visual or numerical comparison with experimental data is 5 minutes. The CPU time for the calculation of the same spectrum using the program GENLIN on an IBM 360/75 computer is less than 10 seconds, representing a reduction in time by a factor of about thirty. That is, in approximately 2 minutes it is possible to obtain a completely automatic numerical

iterative lineshape fit over any prescribed frequency range and to a precision of the order of 1% for the first-order rate constant defining the intramolecular exchange. The subroutine GFITT used in conjunction with GENLIN for the iterative fitting has been previously descibed, cf. section 4.1.1.

The average rate constants obtained from multiple lineshape fits to both the AB- and C- parts of the ^{15}N-formamide spectrum over the temperature range 43.3 to 83.0°C are listed in Table 4.8 and the complete lineshapes corresponding to these particular rate constants are shown in Fig. 4.12. These lineshapes may be compared with those obtained at 60 MHz [158, 160]. The effect of the temperature dependent chemical shifts Ω_A and Ω_B is clearly shown in Fig. 4.12. Also, from the form of the minimum error lineshape fits, it is readily determined that the relative signs of the coupling constants J_{AC} and J_{BC} are the same. The lineshapes in Fig. 4.12 may be compared with those calculated for the closely related ABX spin system, Figs. 2.8 and 2.10 showing the effects of the relative signs of the coupling constants J_{AX} and J_{BX}. The effect of the couplings with the same sign is especially obvious in the C-part of the spectrum. This sign determination is consistent with a double resonance study[152]. The upper temperature limit for the study of intramolecular exchange is determined as that at which the additional intermolecular exchange effects become significant. That is, the linewidth associated with the latter process increases to 0.8 Hz at 83°C and this was considered to be the maximum allowable contribution for the overall lineshape fits not to be

TABLE 4.8

Kinetic data for formamide

(10% acetone solution)

Temp°C	k sec^{-1}
43.3	3.63
45.5	4.68
47.5	6.46
49.0	6.76
52.2	9.55
54.6	10.50
55.0	10.00
59.4	15.90
60.0	19.10
67.0	33.90
77.4	69.10
77.6	75.90
78.0	85.10
83.0	120.00

E_a = 19.27 ± 0.37 kcals.$mole^{-1}$

$\Delta H^{\#}$ = 18.68 kcals.$mole^{-1}$ at 25°C

$\Delta S^{\#}$ = 3.0 ± 1.2 cals. deg^{-1} $mole^{-1}$

$\Delta G^{\#}$ = 17.77 kcals.$mole^{-1}$

affected by this approximation within the overall fitting error limits attainable. The four narrow lines in the C-part of the spectrum which may be used to monitor this linewidth contribution are clearly shown in Fig. 4.12. The Arrhenius plot is shown in Fig. 4.13 and the activation energy obtained is 19.3 ± 0.4 kcals. $mole^{-1}$ which is consistent with the earliest estimate for this parameter[158], namely 18 ± 3 kcals. $mole^{-1}$. At 25°C, the free energy of activation is determined as $\Delta G^{\#}$ = 17.8 ± 0.4 kcals. $mole^{-1}$ with a corresponding entropy of activation $\Delta S^{\#}$ = 3.0 ± 1.2 cals. $deg.^{-1}mole^{-1}$. These activation parameters may now be compared with those obtained for a ^{14}N-formamide acetone solution (22.2%)[159]: $\Delta G^{\#}$ = 17.0 ± 1.9 kcals.$mole^{-1}$ and $\Delta S^{\#}$ = -5.4 ± 2.4 cal.$deg.^{-1}$ $mole^{-1}$, and for a ^{15}N-formamide diglyme solution (14.1%)[160]: $\Delta G^{\#}$ = 17.8 ± 0.2 kcals.$mole^{-1}$ and $\Delta S^{\#}$ = 4.0 ± 0.7 cals.deg^{-1}. $mole^{-1}$. Although the entropies of activation are positive and negative for the lineshape and double resonance studies, respectively, they are relatively small as is to be expected for an internal rotation process. A positive entropy corresponds to a more ordered ground state, for the formamide-acetone complex, and as the planar ground state may be expected to have the largest dipole moment this is consistent with an increased solute-solvent electrostatic interaction leading to a more stable complex in solution with reduced degrees of freedom. However, there are two possible pyramidal transition states for the formamide hindered rotation, and while these states have very different dipolar character they have nearly identical energies, as calculated for an isolated molecule. Thus if solvation plays an important role, it may well be that the more dipolar transition state of the two

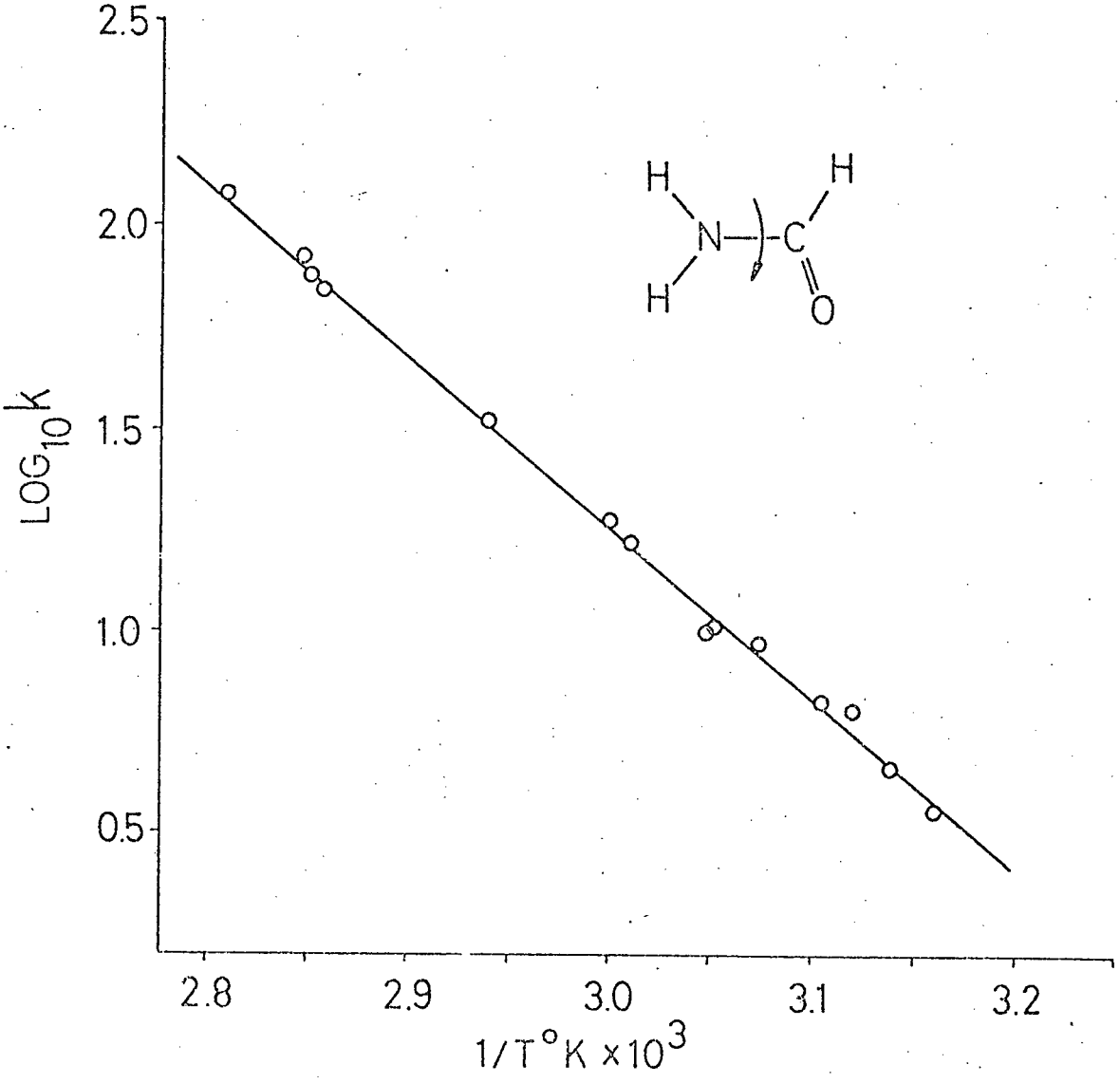

Fig. 4.13 Arrhenius plot for ^{15}N-formamide, 10% acetone solution

possible is stabilised by solvation leading to a decreased entropy and a negative entropy of activation. The different transition states will be further discussed in a following section. In view of the large variations in activation parameters normally associated with independent NMR determinations, cf. Table 4.3, it is gratifying to see the agreement on both the activation energy and free energy of activation for formamide as determined using total lineshape analyses. Of course this is the first comparison of results from complete density matrix lineshape studies and the agreement may be somewhat fortuitous in that different solvents and slightly different solute concentrations were used, although the solvents do have similar characteristics. Nevertheless, in general, it may be expected that more reliable rate constant determinations are possible for more complicated tightly-coupled spin systems. It is well recognised that the most accurate kinetic data are obtained for a simple two-site exchange system in the region of coalescence. As there are a number of analogous regions for a more complicated spin system spanning a larger range of rate constants, it is to be expected that more reliable primary data may be obtained by lineshape analysis over an increased temperature range. Thus with the advent of efficient computer programs, such as GENLIN described in this work, to handle more complicated spin systems in an iterative NMR lineshape fitting procedure, a wider variety of chemical systems of current interest showing kinetic effects may be particularly amenable to study using the NMR technique.

4.2 Hindered rotation in amides, Huckel MO calculations

The systematic experimental study of hindered rotation about the N-C bond in a series of N,N-dimethyl amides of the form N-C(=O)-X with different substituents X, as described in the preceding sections, has shown that the free energy of activation for the rotation process is nearly independent of inter-molecular interactions. Thus this free energy may be considered as the activation parameter characterising the intramolecular rate process. In addition, it is apparent that systematic experimental errors inherent in the determination of specific rate constants using steady-state NMR lead to minimal error in the estimation of this particular activation parameter. In terms of the usual absolute rate theory, the effect of molecular structural or substituent changes on a rate process is reflected by the free energy of activation[129] and hence this thermodynamic parameter may be correlated with the changes in the total molecular energy, as calculated using molecular orbital (MO) theory, corresponding to the structural or substituent changes. The early work of Woodbrey and Rogers [87] shows that the barrier to hindered rotation in amides is strongly influenced by the substituent X. In this work the barriers were determined using only approximate analyses of steady-state NMR data, however, and the activation energies were discussed qualitatively in terms of the effect of a given substituent on the bond-order of the N-C bond. Now that reliable values of the free energies of activation are available, a semi-quantitative correlation with data available from MO calculations is feasible. Thus a simple model may be developed,

within the framework of a linear combination of atomic orbitals (LCAO) MO theory [72], to describe the interactions between the carbonyl group, the nitrogen lone pair electrons and the substituent X in a substituted amide. A calculation of the energy change (electronic only in the simplest model) on rotation about the N-C bond and direct comparison with the experimental data then allows an evaluation of the general validity of the model and possibly a simple semi-quantitative physical description of the hindered rotation and the effects of different substituents on the barrier to rotation. Although a number of calculations based upon simple Huckel molecular orbital (HMO) theory have been reported for amides[164-168], the only calculation of this type for a series of related compounds is that reported by Sandström[169] for a series of substituted N,N-dimethylthioamides. In the latter study, the free energies of activation obtained from NMR spectra show only a crude correlation with N-C π-bond orders calculated using a modified ω-Huckel method[170,171], while a slightly improved correlation is obtained with the corresponding loss in π-electron energy which occurs when the dimethylamino group is rotated with respect to the thiocarbonyl group about the N-C bond. In this section, a simple π-electron HMO model is used to calculate both bond orders and electron delocalisation energies for a series of substituted N,N-dimethyl amides.

The application of quantum-mechanical methods to the calculation of molecular properties for systems of chemical interest at this time still involves a number of approximations, and consequently the emphasis has been placed upon correct numerical agreement with experimental data. In the MO approximation, electrons are assigned to

molecular orbitals which are most conveniently chosen to be one electron wavefunctions expressed as linear combinations of a finite number of atomic orbitals, ϕ_μ. That is, the LCAO-MO ψ_j is given as

$$\psi_j = \sum_\mu C_{j\mu}\phi_\mu \qquad (4.2.1)$$

where the coefficients $C_{j\mu}$ are determined by a variational calculation[172]. Through neglect of all two-electron interactions, the total molecular wave-function may be considered as a simple product of these one-electron molecular orbitals so that the total electronic energy, for a singlet ground state, is given as the sum of the energies for electrons in the occupied molecular orbitals. In the simplest LCAO-MO theory, an electron may be considered to occupy a one-electron MO in a central field due to all other electrons and nuclei in a given molecule. In this manner the energy associated with the MO ψ_j, E_j, is determined by an effective Hamiltonian, H. In accordance with the variational principle, for this Hamiltonian, the eigen-functions ψ_j and eigen-values E_j are given in terms of a set of simultaneous equations[172]:

$$\sum_\nu [H_{\mu\nu} - \delta_{\mu\nu}E_j]\, C_{j\mu} = 0 \quad , \qquad (4.2.2)$$

where $H_{\mu\nu}$ is the Hamiltonian matrix element for the particular basis AO's ϕ_μ and ϕ_ν. It may be assumed that the basis functions form an orthonormal set and that all effects of AO overlap are described by the off-diagonal matrix elements $H_{\mu\nu}(\mu\neq\nu)$, and hence $\delta_{\mu\nu}$ is the Kronecker delta function. Inclusion of overlap[184] leads to a different charge distribution in a molecule but has only a small effect on delocalisation

energies and total π-energies. Thus although it is more rigorous to include overlap, in general no significant improvement occurs in the results from simple Huckel MO calculations. Initially all of the eigenvalues are calculated using the secular determinantal equation:

$$|H_{\mu\nu} - \delta_{\mu\nu}E| = 0 \quad , \qquad (4.2.3)$$

and then the expansion coefficients $C_{j\nu}$ are determined as solutions of the simultaneous equations Eq. (4.2.2) with constant coefficients defined by $H_{\mu\nu}$ and the specific eigenvalue E_j. Given an explicit form for the one-electron effective Hamiltonian operator, the matrix elements $H_{\mu\nu}$ may be calculated in the chosen basis of AO's, $\{\phi_\mu\}$, and similarly the overlap integrals may be evaluated. However, in such a simplified form of LCAO-MO theory there is little point in defining the Hamiltonian operator explicitly and hence the matrix elements are defined only in terms of empirical parameters. The inclusion of orbital overlap as described by the integrals $S_{\mu\nu}$ is not consistent with the complete neglect of all electron-electron and electron-nucleus interactions, and hence it must be assumed that such interactions are included in the estimation of the empirical parameters, which are obtained from comparison of the resultant MO data with specific experimental quantities or by direct comparison with well defined molecular properties. A further simplification may be considered in the study of π-conjugated molecules such as amides, in that to the level of approximation under consideration the π-electrons may be assumed to be independent of the σ-electrons. That is, the σ-electrons are considered to form a localised

bonding system which does not vary significantly in form with structural or substituent changes. This is probably a good approximation for the substituted N,N-dimethyl amides with a single variable substituent X and a structural change corresponding to a simple rotation of the dimethylamino group about the N-C bond. The differential energy, ΔE, corresponding to structural or substituent changes may now be considered in the partitioned form

$$\Delta E = (\Delta E^{\sigma} + \Delta E^{n}) + \Delta E^{\pi} \quad , \qquad (4.2.4)$$

where $\Delta E^{\pi} = \sum_{j} E^{\pi}_{j}$, the summation being over the occupied π- molecular orbital energies, and ΔE^{n} represents any change in the non-bonding interaction energy. Thus in conjugated molecules, for simplicity, the bonding characteristics and energy variations due to structural and substituent changes may now be described in terms of a π-electron only LCAO-MO model. From calculations based upon this model, the bonding characteristics are described in terms of delocalised molecular orbitals defined as linear combinations of $2P_z$ - AO's (π-type), and the differential energy becomes $\Delta E^{\pi} + \Delta E^{n}$ in accordanee with Eq. (4.2.4)

The following simple Huckel calculations are based upon the much simplified π-only LCAO-MO model with the aim of checking the general applicability of such a model to a description of the hindered rotation in substituted amides. Attempts have been made to incorporate electron repulsion into simple Huckel theory[173,174], but at this level of approximation such a procedure is difficult to justify in that a redefinition of the purely empirical parameters is involved. Therefore

a non-iterative Huckel calculation is used in this study with the effective Hamiltonian matrix elements for substituted amides being defined by empirical Coulomb integrals, α_X, and resonance integrals, β_{C-X},[72] where

$$\alpha_X = \alpha^\circ + h_X \beta^\circ$$

and

$$\beta_{C-X} = k_{C-X} \beta^\circ \qquad (4.2.5)$$

As only relative energies are significant, the standard Coulomb integral α° may be taken as the energy reference zero and then the matrix elements α_X and β_{C-X} are defined in terms of the standard resonance integral, $\beta^\circ<o$, which is usually taken as that for the C-C bond in benzene[175]. It is to be noted that the parameter β_{C-X} refers to N-C, C=O and C-X π-type bonds in the substituted amides >N-C(=O)-X, all other off-diagonal Hamiltonian matrix elements being defined to be zero. In describing the energy variation for hindered rotation about the N-C bond, due to delocalisation of the formal lone pair electrons on the sp^2-hybridised N atom, the energy for the planar ground state is given as a sum of π-MO energies. In the rotation transition state, the dimethylamino group is rotated into a plane perpendicular to that of the carbonyl group and hence the conjugation between the amino and :C(=O)-X groups is broken down as the symmetry relationship necessary for π-bonding between these two groups no longer exists. In this case the molecular energy must be considered as a sum of π-MO energies for the C(=O)-X group and a contribution from non-bonding electrons on the N atom, E^n, cf. Eq. (4.2.4). Thus the differential π-energy associated with the

hindered rotation is given as

$$\Delta E_{\pi} = E^{\pi}(\underset{\underset{O}{\|}}{N\text{-}C\text{-}X}) - \{E^{\pi}(\underset{\underset{O}{\|}}{C\text{-}X}) + 2h_N\}, \qquad (4.2.6)$$

where the energies are given in terms of the Hamiltonian matrix:

$$\begin{array}{c|ccc} k_N & k_{C-N} & 0 & 0 \\ \hline k_{C-N} & k_C & k_{C=O} & k_{C-X} \\ 0 & k_{C=O} & k_O & 0 \\ 0 & k_{C-X} & 0 & k_X \end{array} \qquad (4.2.7)$$

in units of β°, cf. Eq. (4.2.5). The only non-bonding energy is that described by h_N in Eq. (4.2.6) as steric interactions are not significant for the substituents under consideration.

In contrast to an ab initio calculation, the values chosen for the empirical parameters h_X and k_{C-X} are of primary importance since they alone may determine the results of a simple Huckel MO calculation and therefore represent the essential characteristics of the simplified model being used here. A Coulomb resonance integral is expected to be directly related to both the ionisation potential and electron affinity for a given atom in a molecule, and hence to the atomic electro-negativity[176-178]. The concept of variable electro-negativity has been introduced by Jaffe and coworkers[179,180], and this allows the rigorous definition of an orbital electro-negativity which may be considered as a measure of the attracting power of an atom, as it exists in a molecule, toward an electron in a specific type of AO, that is for a specific

atomic valence state. Thus the π-orbital electronegativities for sp^2-hybridised N,C and O atoms have been used to fix the h_X parameters as 0.7, 0.0 and 1.4, respectively. These parameters may be compared with "standard" values[181]. The parameter h_N has also been modified to allow for the hyperconjugative effect of the N-methyl groups for the amides under consideration. For the general substituent X in the N,N-dimethyl amides, it has been assumed that all multi-atomic substituent groups may adequately be represented as pseudo-atoms[182,183] and are therefore characterised by a single h_X parameter derived through a linear relationship with the corresponding group electro-negativities. The set of h_X parameters used in the Huckel MO calculations is given in Table 4.9 along with references to the method for calculation of the group electronegativities, namely the use of a variable electronegativity for the central atom in a group and equalisation of electronegativity[179] in all bonds. The resonance integral, and hence the parameter k_{C-X}, characterises the π-bonding between the C atom and the atom or pseudo-atom X and is expected to be directly related to the bond length γ(C-X) [185,186] or the overlap integral between $2P_Z$-AO's[187]. The k_{C-X} values derived through a linear correlation with bond lengths and corresponding overlap integrals[188] for the carbamyl fluoride structure shown in Fig. 4.22 are 0.90(0.90), 0.80(0.86) and 0.60(0.52) for the C=O, N-C and C-F bonds, respectively. As it is difficult to estimate overlap integrals for pseudo-atoms, the similarity of the above sets of parameters indicates that this difficulty may be avoided by using the simpler correlation with bond lengths, and hence the set of k_{C-X} parameters given in Table 4.9 has been determined in this way from the

Table 4.9

Huckel M O data for hindered rotation in substituted N,N-dimethyl amides

X	ε_X	h_X	k_{C-X}	$\Delta E^{\dagger}$	$\Delta G^{\#}$	p_{N-C}	p^{G}_{C-O}	p^{T}_{C-O}	q_N
H	-	-	-	0.759	21.0	0.766	0.516	0.753	1.58
CN [a]	4.17	4.6	0.55	0.737	20.6	0.752	0.511	0.731	1.59
F [a]	3.95	4.0	0.60	0.728	18.2	0.746	0.508	0.723	1.60
Cl [a]	3.00	1.4	0.40	0.715	16.8	0.737	0.502	0.704	1.58
Br [a]	2.80	0.8	0.32	0.710	15.7	0.735	0.500	0.694	1.61
OCH_3 [b]	2.68	0.65	0.50	0.639	(5.8)	0.685	0.473	0.613	1.65
SCN [c]	3.91	3.85	0.39	0.745	(21.4)	0.757	0.512	0.739	1.59
NCS [c]	4.15	4.50	0.54	0.737	(20.2)	0.752	0.511	0.731	1.59
N_3 [c]	4.42	4.90	0.54	0.739	(20.4)	0.753	0.511	0.734	1.59
NCO [a]	3.05	1.55	0.56	0.686	(12.6)	0.717	0.492	0.674	1.63
NH_2 [b]	2.61	0.80	0.60	0.621	(3.0)	0.670	0.465	0.597	1.66
NMe_2 [b]	2.40	0.70	0.60	0.609	(1.0)	0.661	0.460	0.583	1.67

$k_N = 0.7$ $k_{C-N} = 0.8$

$k_C = 0.0$ $k_{C=O} = 0.9$

$k_O = 1.4$

† in units of β <o, see text

a) W. Gordy and W.J.O. Thomas J. Chem. Phys. 24, 439, 1956

b) J.E. Huheey J. Phys. Chem. 69, 3284, 1965

c) J.E. Huheey J. Phys. Chem. 70, 2086, 1966

structures available for amides or the related acetyl compounds $H_3C\text{-}\overset{\overset{O}{\|}}{C}\text{-}X$ and formyl compounds $H\text{-}\overset{\overset{O}{\|}}{C}\text{-}X$.

The differential energies, ΔE_π, for hindered rotation in substituted N,N-dimethyl amides are given in Table 4.9 along with the N-C π-bond orders for the planar ground states and the C-O π-bond orders for the ground and rotation transition states, $p^G_{C=O}$ and $p^T_{C=O}$, respectively. These bond orders are defined in terms of the LCAO-MO expansion coefficients as[190]:

$$p_{\mu\nu} = 2 \sum_j C_{j\mu} C_{j\nu} \quad , \qquad (4.2.8)$$

where ϕ_μ and ϕ_ν are $2P_Z$-AO's on bonded atoms and the summation is over the occupied π molecular orbitals. A corresponding π-charge density is defined as:

$$p_{\mu\mu} = 2 \sum_j C_{j\mu} C_{j\mu} \quad , \qquad (4.2.9)$$

and these densities for the N atom in the amide ground states, q_N, are also listed in Table 4.9.

As the NMR spectrum for N,N-dimethyl urea shows a single sharp peak for the N-methyl protons down to -118°C, the free energy of activation for hindered rotation in this amide may be estimated as 3 kcal. $mole^{-1}$ at 298°K. The correlation diagram for free energy of activation, $\Delta G^\#$, and Huckel MO differential π-energy, ΔE_π, given as Fig. 4.14 includes the estimated energy for $X=NH_2$ as an experimental point and also a preliminary value of $\Delta G^\# = 20.6 \pm 0.8$ kcal.$mole^{-1}$ for N,N-dimethyl carbamyl cyanide (X=CN). The correlation obtained is excellent, which

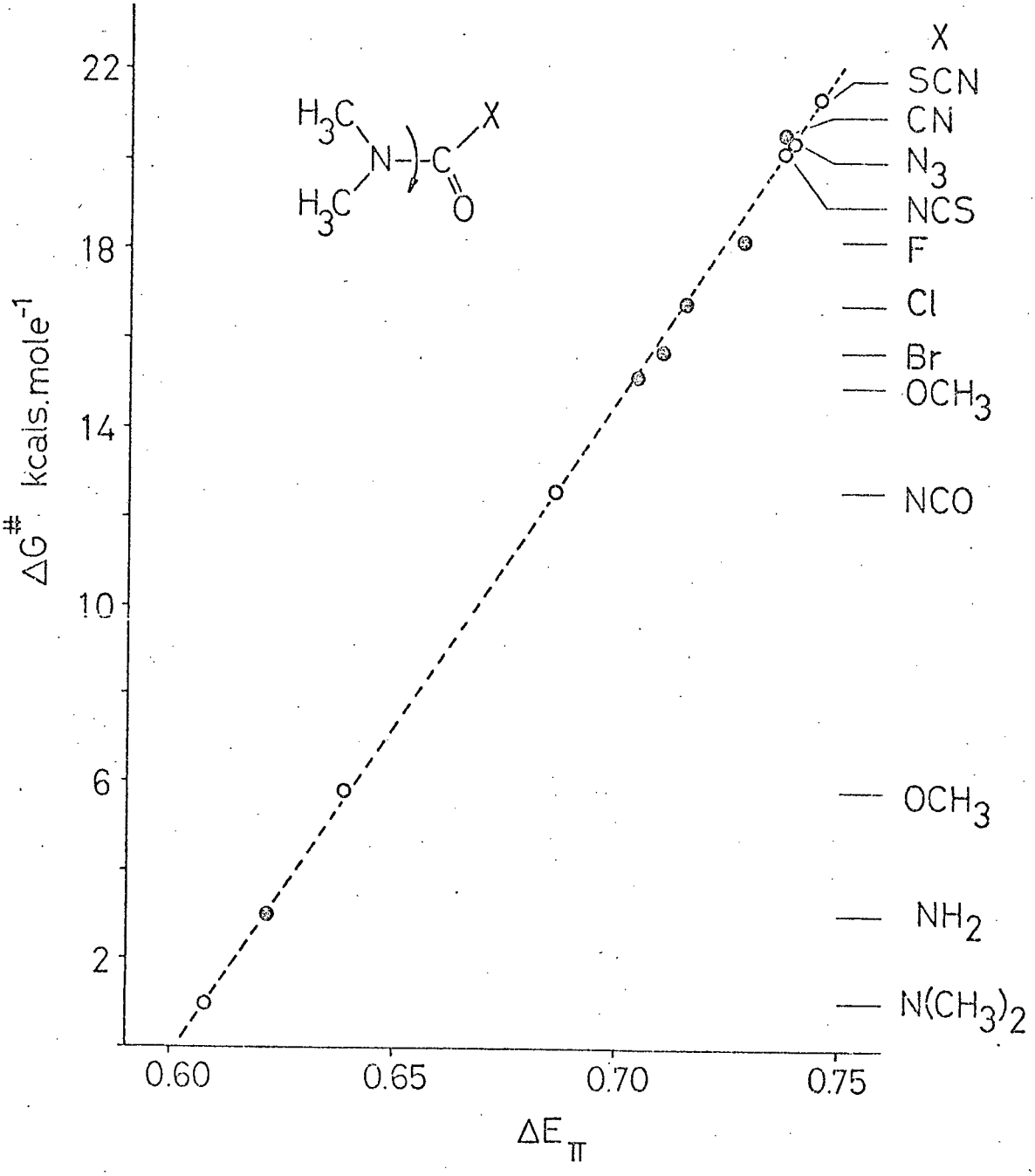

Fig. 4.14 Correlation of free energy of activation for hindered rotation with Huckel MO differential π-energy

shows that the method of parameterisation is consistent for such a series of compounds and also indicates that the change in π-energy on breaking down the conjugation through the N-C bond may be a dominant factor in determining the barrier to hindered rotation about this bond. It is of some interest to consider in more detail the calculated differential π-energy for methyl N,N-dimethyl carbamate ($X=OCH_3$), as experimentally it was found that the barrier to hindered rotation increased by at least 8 kcals. $mole^{-1}$ with chloroform as a solvent, cf. section 4.1.3. With the h_X and k_{C-X} values listed in Table 4.9, $\Delta E_\pi'$ is calculated as 0.639 β° which corresponds to a $\Delta G^\#$ value of 5.8 kcal. $mole^{-1}$, as shown by the open point in Fig. 4.14, which is consistent with the experimental results. Now if it is postulated that the chloroform forms a stereo-specific hydrogen-bond with the carbonyl lone pair σ-electrons, this interaction would modify the Coulomb integral for the carbonyl oxygen atom and hence the Huckel parameter h_0. Such a solute-solvent interaction would be expected to increase the contribution from the resonance form II shown below in the carbamate ground state, and thus this interaction is described by an increase in the magnitude of h_0.

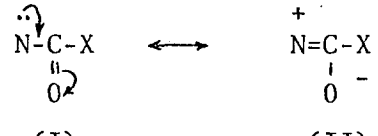

(I) (II) (4.2.10)

The effect of a variable h_0, with all other parameters as listed in Table 4.9, is shown in Fig. 4.15; and it is seen that the h_0 value

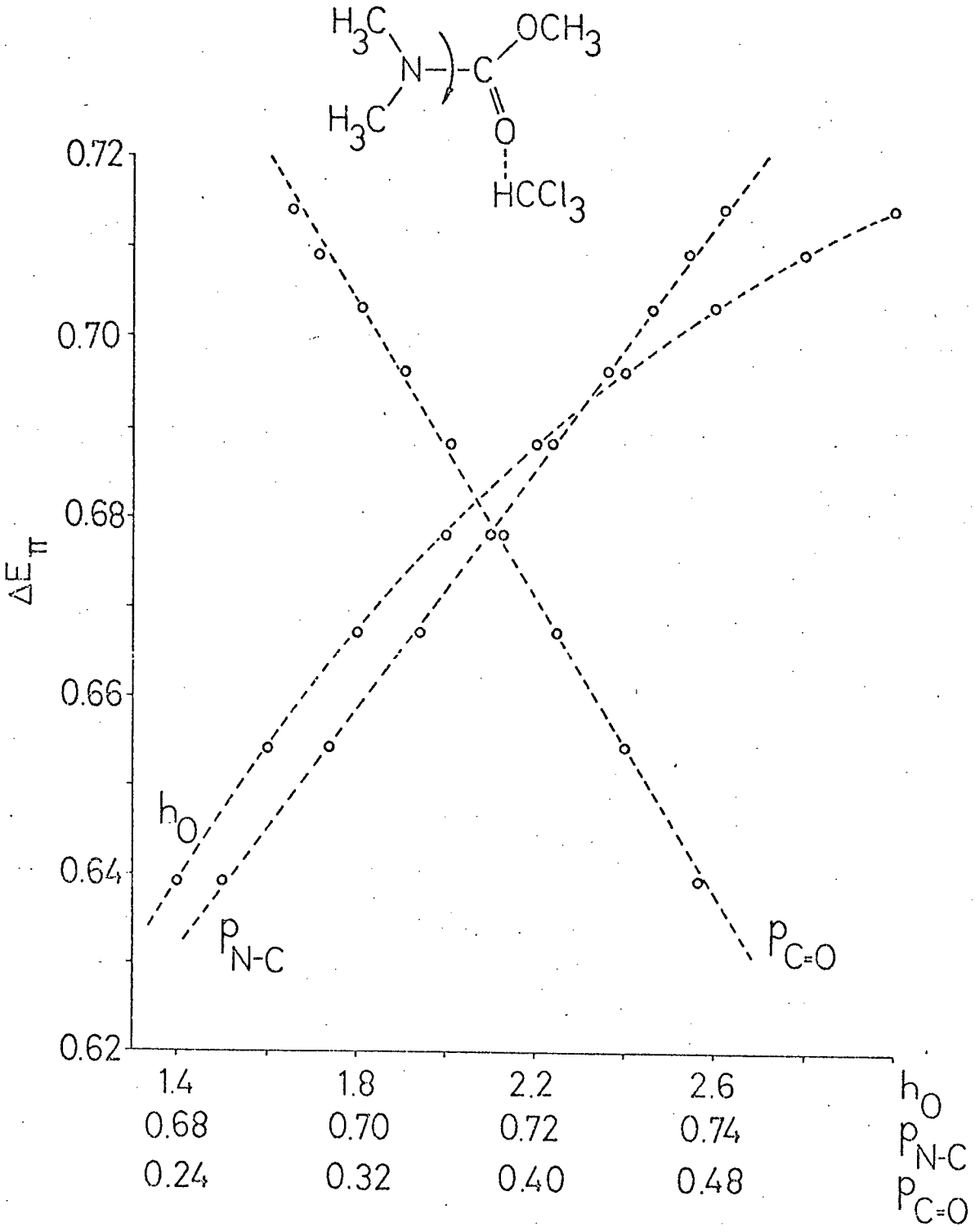

Fig. 4.15 Effects of variable carbonyl oxygen Huckel theory Coulomb integral, h_0, for methyl N,N-dimethyl carbamate calculation

corresponding to $\Delta E_{\pi} = 0.705\ \beta°$ and hence $\Delta G^{\#} = 15.2$ kcal.mole^{-1}, as shown by the closed point for X=OCH$_3$ in Fig. 4.14, must be increased to 2.6. Thus although the simple Huckel π-MO model predicts an increased barrier to rotation for the specific interaction at the carbonyl oxygen, the change in the h_0 parameter required to reproduce the magnitude of the increase in $\Delta G^{\#}$, as determined experimentally in section 4.1.3, is relatively large. It is also possible that the barrier to rotation about the N-C bond may be affected by the chloroform forming a hydrogen bond with the methoxy oxygen lone pair σ-electrons. Such an interaction may lead to an increased contribution from the resonance form III shown below, and is described in terms of the simple Huckel π-MO

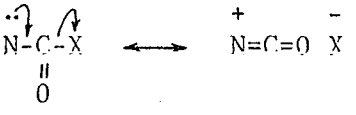

(4.2.11)

(III)

model by an increase in the magnitude of h_X for X=OCH$_3$. Thus ΔE_{π} is calculated as 0.702 β° for h_X= 1.95, as compared with 0.65 in Table 4.9, corresponding to $\Delta G^{\#}$ = 15 kcals. mole^{-1}. An increase in the barrier to rotation is predicted as a consequence of the specific solute-solvent interaction at the methoxy oxygen atom, but again the change in the h_X parameter required is relatively large. In so far that the increment in h_0 required to give a calculated $\Delta E_{\pi} \sim 0.71\ \beta°$ is much less than the corresponding increment in h_X, a specific interaction at the carbonyl atom is predicted to have a more significant effect on the barrier to rotation. This is consistent with the interaction effect being transferred through the carbonyl π-bond, this bond being described by

$k_{C=O}$ = 0.9 as compared with k_{C-OCH_3} = 0.5. Of course, if the interaction between solute molecule and O atom is only described by a relatively large change in h_O, the value of $k_{C=O}$ should also be varied and thus the commensurate change in h_O will be reduced.

From the correlation diagram given in Fig. 4.14 the free energies of activation for hindered rotation in N,N-dimethyl amides with pseudo-halogen substituents X = SCN, NCS, N_3 and NCO, and also in the symmetrical tetramethyl urea (X = $N(CH_3)_2$) may be predicted from the calculated ΔE_π values. These $\Delta G^\#$ values are included in Table 4.9 and are shown as open points in Fig. 4.14. The $\Delta G^\#$ - ΔE_π correlation indicates that as the electro-negativity of the substituent increases, the barrier to hindered rotation also increases. This is consistent with an increased contribution from the resonance form IV shown below corresponding to a decreased barrier, as a delocalisation of π-electrons

(4.2.12)

(IV)

on the atom or pseudo-atom substituent group X is possible for all of the substituents considered here. As shown in Fig. 4.16, however, there is no simple correlation between the free energies of activation $\Delta G^\#$, as measured or predicted in accordance with the Huckel π-MO model, with the atomic or group electro-negativities ε_X. Thus the use of even a simplified LCAO-MO model for the description of hindered rotations in amides is justified if a semi-quantitative correlation is to be attempted using reliable experimental data. The self-consistency of the

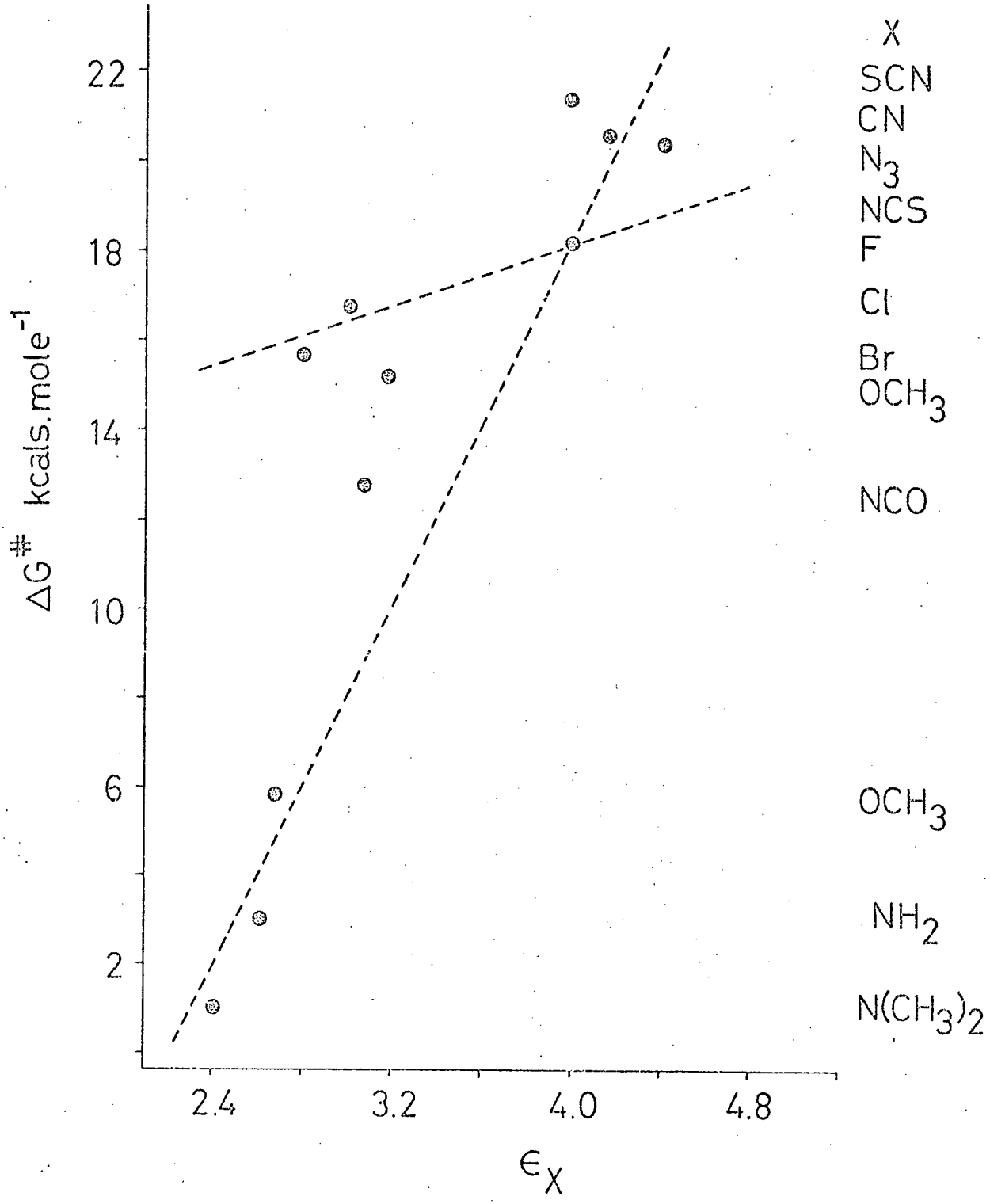

Fig. 4.16 Correlation of free energy of activation for hindered rotation with group electro-negativity, ϵ_X , of the X-substituent in N,N-dimethyl amides

Huckel calculation is illustrated by the trends in the π-bond orders and π-charge densities q_N listed in Table 4.9. As shown in Fig. 4.17, an excellent correlation is also obtained between $\Delta G^{\#}$ and the N-C π-bond order p_{N-C}. The calculated bond-orders p_{N-C} are consistently higher than those for the carbonyl bond in the amido ground state, $p^{G}_{C=O}$, but this is only a consequence of the particular parameterisation chosen for the N atom and does not affect any of the results presented for the relative effects of the X substituents.

As the simple Huckel π-MO model described above gives a consistent estimate of the differential energy ΔE_{π} for the ground and hindered rotation transition states for substituted N,N-dimethyl amides, such a model may be useful in a more general description of π-bonding within a conjugated amide system. In general terms, the details of an electronic charge distribution for any given molecule are contained in the expansion coefficients for the LCAO molecular orbitals, cf. Eq. (4.2.1). The probability density[191], D, at a point in space associated with an electron in a molecular orbital ψ_j is $\psi^*_j\psi_j$, and hence in accordance with Eq. (4.2.1):

$$D = \sum_{\mu} p_{\mu\mu} \phi^*_{\mu}\phi_{\mu} + \sum_{\mu}\sum_{\nu} p_{\mu\nu}\phi^*_{\mu}\phi_{\mu} \quad , \quad (4.2.13)$$

where $p_{\mu\nu}$ and $p_{\mu\mu}$ are defined for doubly occupied orbitals in Eqs. (4.2.8) and (4.2.9), respectively. Thus the bond order $p_{\mu\nu}$ is the predominant factor determining the distribution of π-electron charge in the space between the bonded atoms with $2P_Z$-AO's ϕ_{μ} and ϕ_{ν}. Although an approximate analysis is possible using bond orders, an electronic

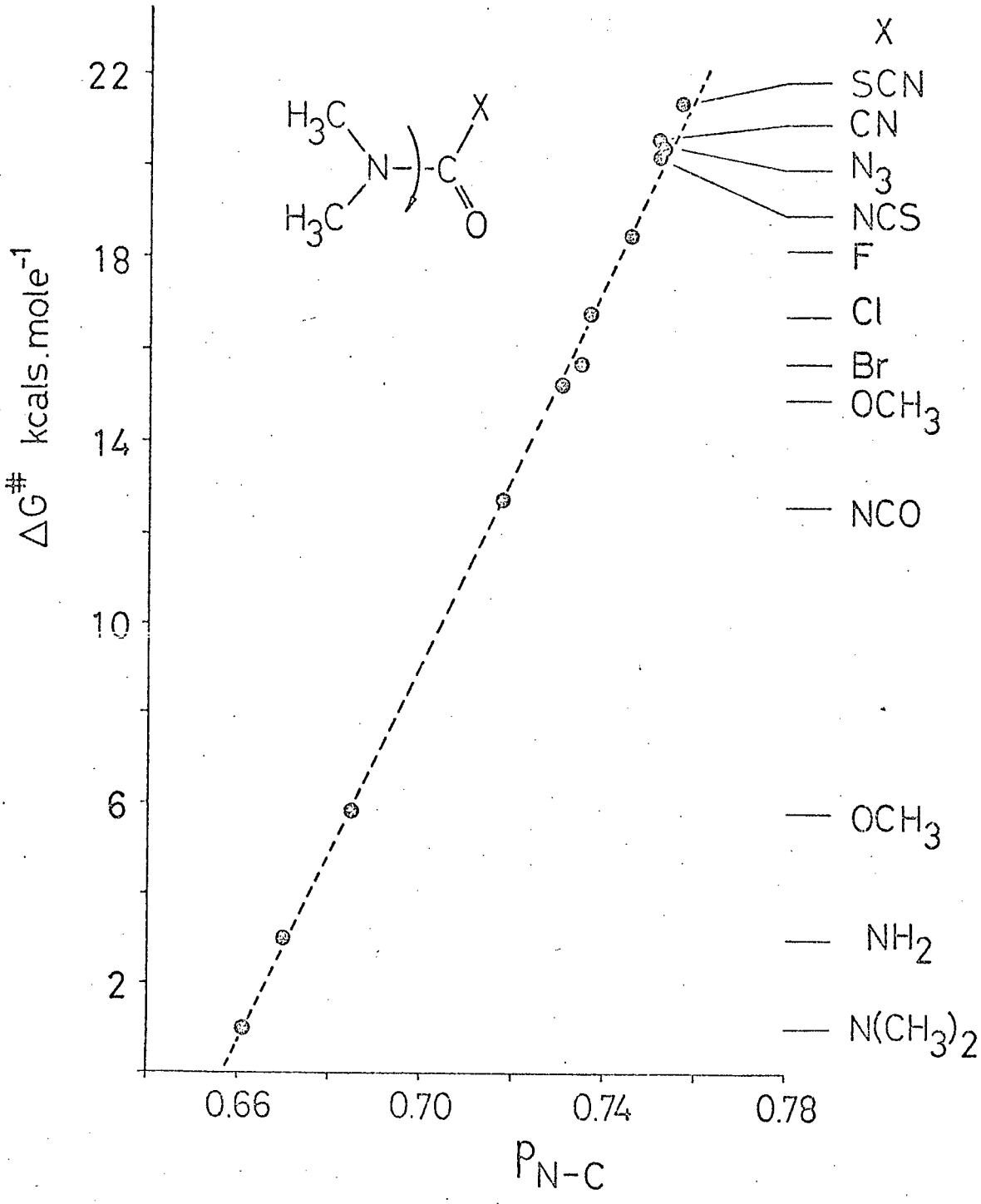

Fig. 4.17 Correlation of free energy of activation for hindered rotation with N-C π-bond order, p_{N-C}, obtained from Huckel MO calculations

charge density map[192,193] is the most explicit and complete means of showing the form of the π-charge distribution in a conjugated amide system. A FORTRAN-IV computer program CNTR has been developed to automatically plot contours for constant π-charge densities by direct numerical calculation of the probability density D using Slater type[194] atomic orbitals. A total charge density is obtained as a normalised sum of contributions from all of the occupied molecular orbitals. The Huckel π-MO electronic charge density maps obtained for (a) an unconjugated state and (b) the conjugated ground state of formamide (or N,N-dimethyl formamide) as defined by the molecular orbitals generated using the parameters listed in Table 4.9 are shown in Fig. 4.18, for the geometry given in Fig. 4.20 and in a plane parallel to the molecular plane and displaced by 0.6 Å. Comparison of these density maps shows the redistribution of charge in both the N-C and C=O bonding regions in the conjugated ground state, the formal lone pair electron density for the N atom being illustrated in Fig. 4.18 (a). The change in the π-bond order $p^{G}_{C=O}$ on forming the un-conjugated hindered rotation transition state, as given by $p^{T}_{C=O}$, is reflected in the charge density maps as the double bond character increases in the transition state and this is shown to correspond to an additional delocalisation of charge from the carbonyl oxygen atom. This is also consistent with a decreased contribution from the resonance form II given in (4.2.10). Similar density maps for carbamyl fluoride are shown in Fig. 4.19 for the geometry given in Fig. 4.22. In the conjugated ground state for this particular molecule the π-charge density is close to being symmetrical

(a)

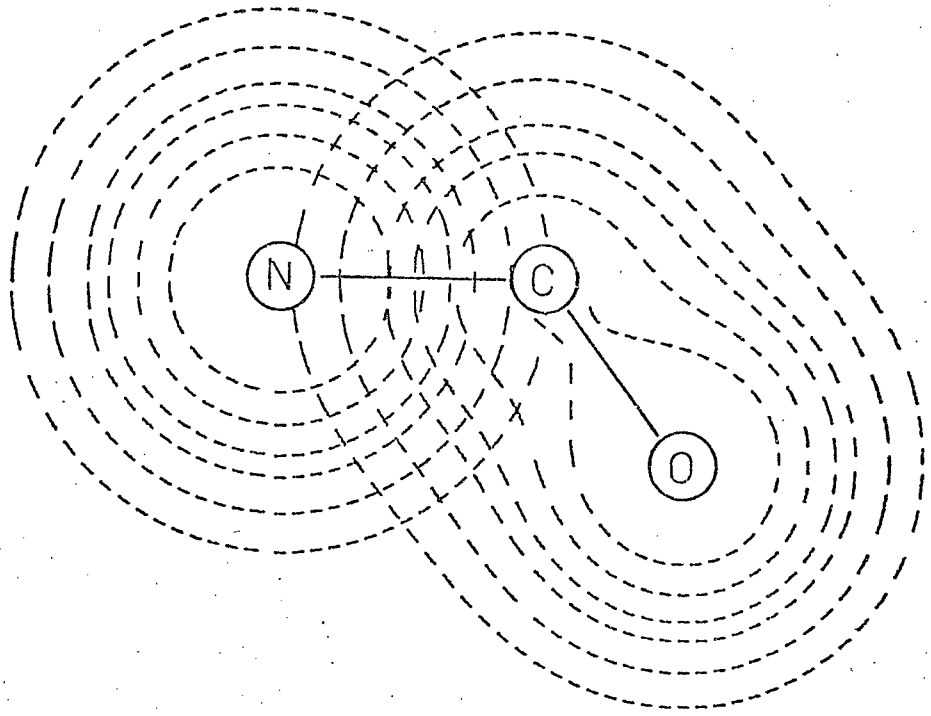

(b)

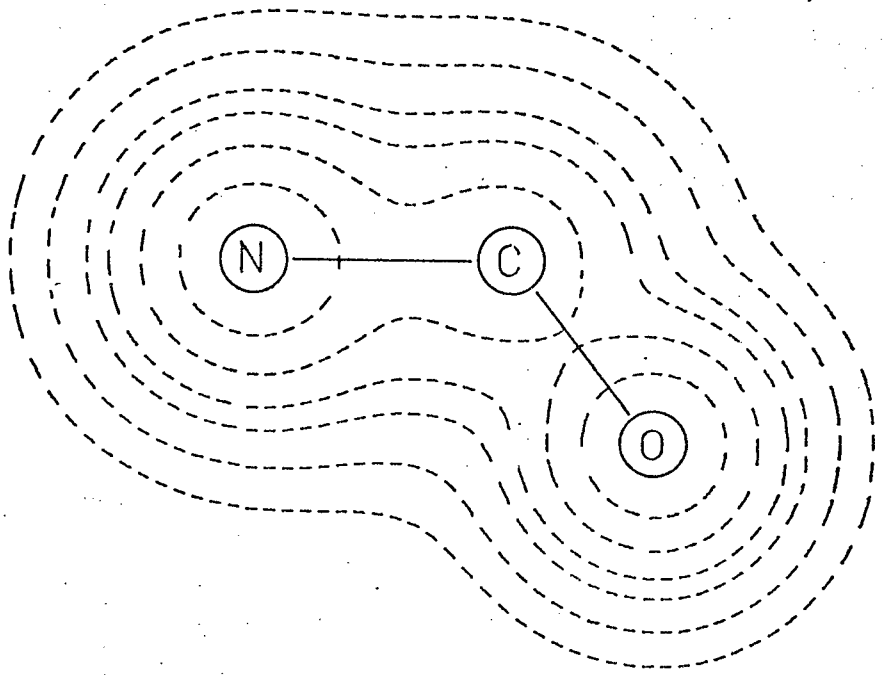

Fig. 4.18 Huckel MO electronic charge density maps for the (a) un-conjugated and (b) conjugated states of formamide

(a)

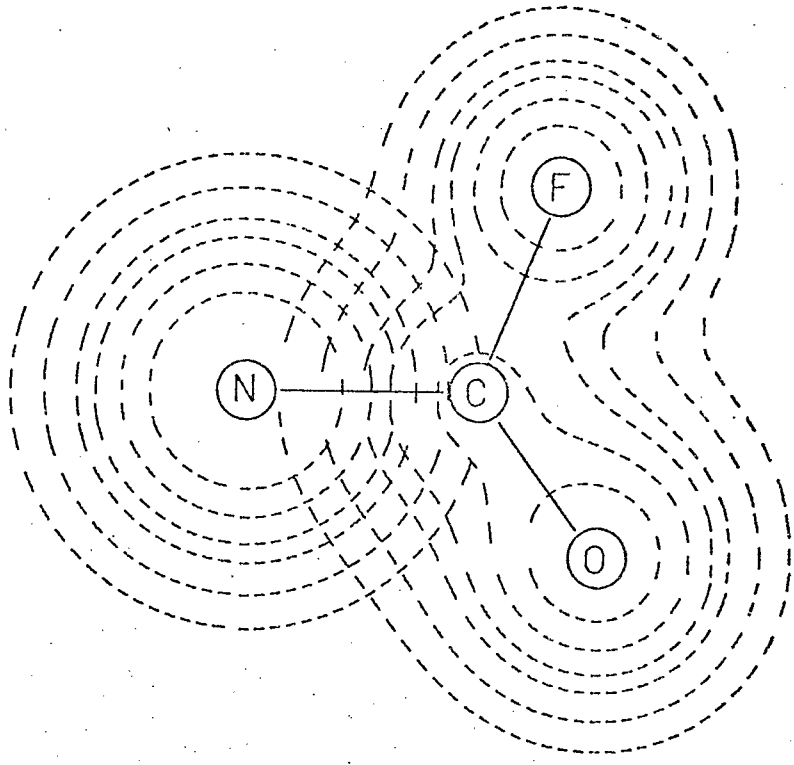

(b)

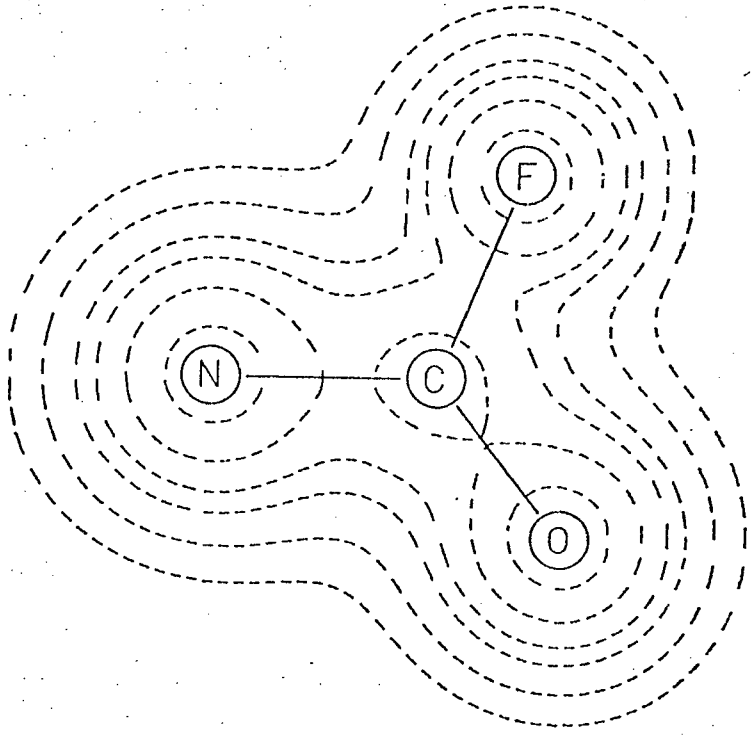

Fig. 4.19 Huckel MO electronic charge density maps for the (a) un-conjugated and (b) conjugated states of carbamyl fluoride

with respect to the N-C bond and this feature may be the dominant factor leading to very similar NMR shielding regions, due to the diamagnetic anisotropies of the C-F and C=O groups, for the methyl groups in N,N-dimethyl carbamyl fluoride, cf. section 4.1.4. Comparison of the contours for the same charge density in Figs. 4.18(b) and 4.19(b) shows the significantly different charge distributions in the N-C bond region for formamide and carbamyl fluoride, respectively. These density maps are consistent with an increased bond order p_{N-C} and a correspondingly higher barrier for hindered rotation in formamide, cf, Table 4.9.

4.3 Semi-empirical SCF-LCAO-MO calculations

The electronic structure of formamide, the simplest molecule containing the amide group N-C=O, is of basic importance in any spectroscopic study of a series of substituted amides. The amide linkage is also characteristic of the polypeptides and hence a detailed molecular orbital calculation for formamide gives a basis for the development of a configurational model for these more complicated systems of biological interest. The hindered rotation about the N-C bond in ^{15}N-formamide has been studied experimentally in section 4.1.5, and similar rotations in substituted amides have been extensively studied by NMR methods as discussed in sections 4.1.1 to 4.1.4 and as summarised in a recent review[195]. However, very little attention has been paid to a theoretical determination of the form of the transition states or to a semi-quantitative correlation of the measured free energies of activation with data available from a molecular orbital description of substituted

amides. Empirical estimates of the barrier to rotation have been made for formamide[164,168] and simple Huckel π-MO calculations for a series of substituted amides have been outlined in the preceding section of this thesis; but very recently, Christensen et al. have published a full ab initio molecular orbital study of formamide[196] in the ground and hindered rotation transition states. Thus it is of particular interest to supplement these results with a detailed semi-empirical SCF-LCAO-MO calculation for the hindered rotation in formamide, in the CNDO/2 approximation[75,76].

As preliminary CNDO/2 calculations showed that the ground-state geometry proposed by Costain[197] was less stable than a corresponding planar configuration, the basic structure determined by Kurland[198], and shown in Fig. 4.20, is used in the following calculations. By including d-functions in a Gaussian type orbital basis set, the ab initio calculation[196] indicates that the non-planar structure may be more stable, but the very small energy difference precludes a conclusive result. The geometry of the N-C(=O)-H group is fixed in the molecular xy-plane in Fig. 4.20, while a variable geometry for the amino group may be defined by the HNH angle 2α, the dihedral angle θ and the angle ϕ determining the rotation about the N-C bond. All bond lengths in Fig. 4.20 are given in Å, and the N-H-bond length is fixed at 0.995 Å[198].

To date, the most reliable MO calculations are based upon a full Hartree-Fock self-consistent field (SCF) theory[199], involving all electrons in a given molecular system, an unlimited basis set of atomic wavefunctions and an explicit formulation of all electron interactions. Roothaan[200] considered a finite basis set of orthonormal atomic orbitals,

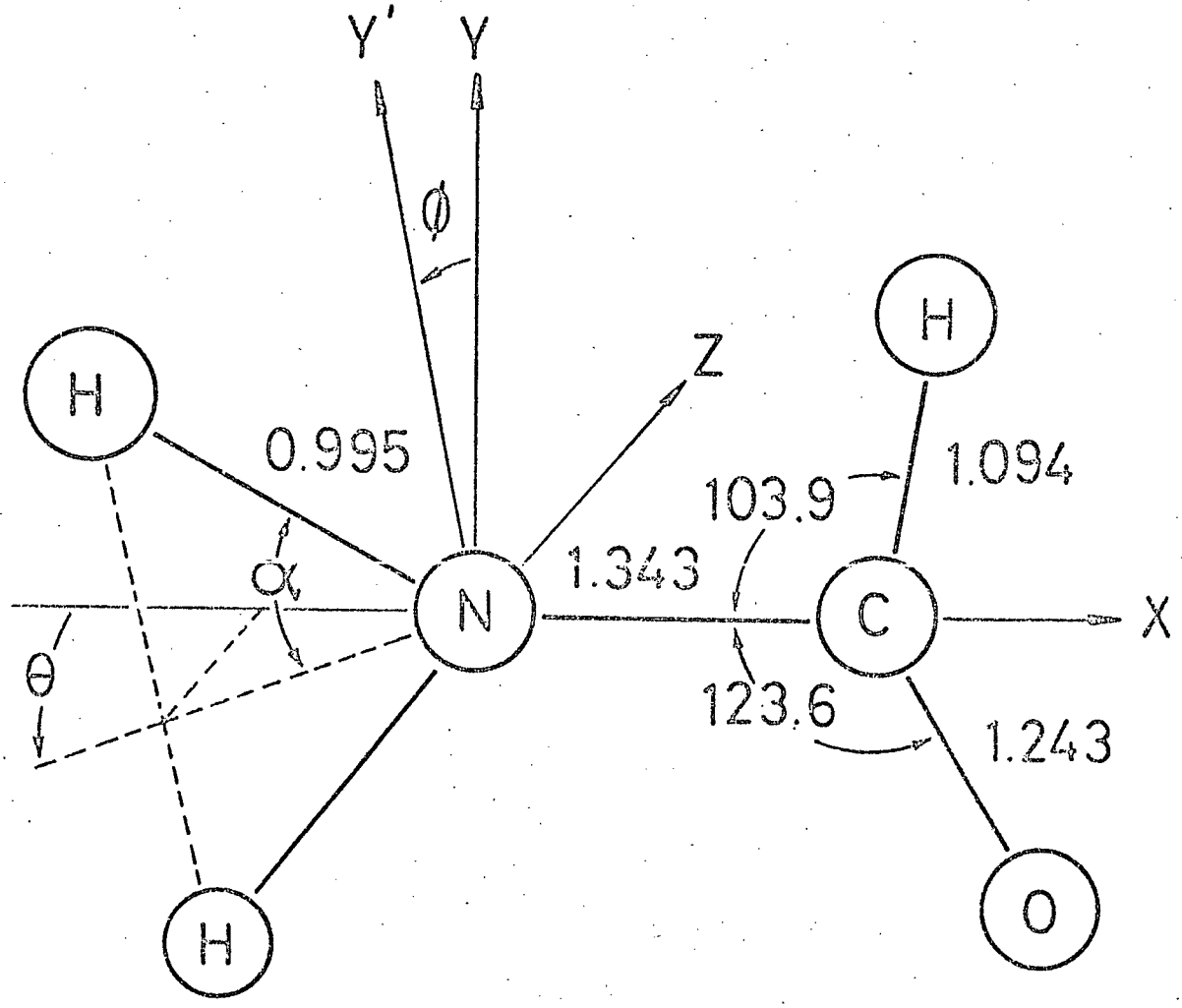

Fig. 4.20 Structure of formamide used in CNDO/2 SCF-LCAO-MO calculations

ϕ_μ, and modified the full SCF theory to give a more tractable formulation based upon a linear combination of atomic orbitals (LCAO) in an approximate description of molecular orbitals, cf. Eq. (4.2.1). The application of the Roothaan method, however, is still limited by computational complexity and hence, in general, it is necessary to consider further approximations within the context of the SCF theory. The CNDO method, as recently developed by Pople and coworkers, is a semi-empirical SCF-LCAO-MO theory which treats only valence electrons explicitly and simplifies the basic Roothaan equation by use of the complete neglect of differential overlap (CNDO) approximation. The Roothaan SCF equation then reduces to the form

$$\underline{\underline{F}}\,\underline{C}_j = E_j \underline{C}_j \quad , \qquad (4.3.1)$$

where $\underline{\underline{F}}$ is the Fock Hamiltonian matrix and $\underline{C}_j$ is the column vector of MO expansion coefficients $C_{j\mu}$ as given in Eq. (4.2.1). E_j is the energy eigen-value corresponding to the MO ψ_j. Overlap between atomic orbitals is only included in the evaluation of certain bonding integrals involved in this approximate SCF theory, but integrals describing two-electron repulsions are included in the Fock matrix elements $F_{\mu\nu}$. The fundamental assumptions used in the derivation of the Fock matrix elements have been described in detail by Pople[75], and in the CNDO/2 approximation[76] these matrix elements are given as

$$F_{\mu\mu} = -\tfrac{1}{2}(I_\mu + A_\mu) + [(P_{AA} - Z_A) - \tfrac{1}{2}(p_{\mu\mu} - 1)]\gamma_{AA} + \sum_{B\neq A} (P_{BB} - Z_B)\,\gamma_{AB}$$

and

$$F_{\mu\nu} = \tfrac{1}{2}(\beta^{\circ}_{A} + \beta^{\circ}_{B})\, S_{\mu\nu} - \tfrac{1}{2} p_{\mu\nu}\, \gamma_{AB}, \quad \mu \neq \nu \quad , \qquad (4.3.2)$$

for valence shell atomic (Slater) orbitals ϕ_{μ} and ϕ_{ν} on atoms A and B, respectively. In the above formulation, one- and two-centre electron repulsion integrals are retained while penetration integrals are excluded. The non-zero two electron integrals, γ_{AA} and γ_{AB}, are only dependent upon the atoms with which the orbitals ϕ_{μ} and ϕ_{ν} are associated and not upon the type of atomic orbital. Thus the atomic integrals γ_{AB} represent an average interaction between an electron in a valence AO on atom A and another electron in a valence orbital on atom B, and such integrals are readily evaluated using formulae derived by Roothaan[201]. The charge densities and bond-orders in Eq. (4.3.2), namely $p_{\mu\mu}$ and $p_{\mu\nu}$, are those previously defined in Eqs. (4.2.7) and (4.2.8); and P_{AA} is the total valence electron density for atom A:

$$P_{AA} = \sum_{\mu} p_{\mu\mu} \quad , \qquad (4.3.3)$$

where Z_A is the core charge for atom A. $S_{\mu\nu}$ is the overlap integral for atomic orbitals ϕ_{μ} and ϕ_{ν} and may be evaluated using the analytic expressions derived by Mulliken et al [188] for Slater orbitals. The semi-empirical bonding parameters, β°_{A}, and the parameters $\frac{1}{2}(I_{\mu} + A_{\mu})$[76] for 2s- and 2p- atomic orbitals determining the atomic core Hamiltonian matrix elements[75] as used in the following calculations are listed in Table 4.10 along with the Slater exponents ζ_{μ}. A FORTRAN-IV computer program similar to that available from the Quantum Chemistry Program

Table 4.10

Parameters for CNDO/2 calculations

	H	C	N	O	F	
ζ_μ	1.20	1.625	1.95	2.275	2.60	
$\frac{1}{2}(I_s + A_s)$	7.186	14.051	19.316	25.390	32.272	eV
$\frac{1}{2}(I_p + A_p)$	--	5.572	7.275	9.111	11.08	eV
$-\beta_A^\circ$	9.0	21.0	25.0	31.0	39.0	eV

Exchange has been developed for use on an IBM 360 system and all results reported here have been obtained using this program.

Initially, the hindered rotation was considered as a simple rotation of the planar NH_2 group with fixed N-H bond length and $2\alpha = 119°$[198] so that the transition state corresponds to $\theta = 0°$ and $\phi = 90°$ (structure II) in Fig. 4.20. The planar ground state is then defined by $\theta = 0°$ and $\phi = 0°$ (structure I), and the associated SCF-LCAO-MO data is summarised in Table 4.11. The net atomic electronic charge ($\sigma + \pi$) for the N atom, q_N, is shown to increase on forming the transition state; while the corresponding charge for the O atom, q_O, decreases. These variations are also reflected in the net atomic π-charges which are defined as $q_A^\pi = Z_A^\pi - 2 \sum_i^{occ} C_{i\mu}$, where ϕ_μ is a $2P_z$ atomic orbital on atom A with π-core charge Z_A^π (or a $2P_y$ orbital for N in the transition state) and $C_{i\mu}$ is the associated expansion coefficient for the ith occupied orthonormal LCAO molecular orbital. Table 4.11 shows that q_C^π is approximately constant while q_N^π and q_O^π differ widely in the ground and transition states. This is consistent with an increased contribution from the resonance form $\overset{+}{N} = C - \overset{-}{O}$ for the π-system in the planar ground state, in a simplified description of the amide group, cf. section 4.2. The N-C π-bond order, given as $p_{N-C}^\pi = 2 \sum_i^{occ} C_{i\mu} C_{i\nu}$ with ϕ_μ and ϕ_ν $2P_z$ atomic orbitals on the N and C atoms, is calculated as 0.482 in the ground-state and hence represents a significant delocalisation of the N π-electrons. For comparison, this bond-order is determined as 0.41 using the Kurland bond-length data in a formula given by Pauling[202], and as 0.63 using an alternative empirical equation proposed by Gordy[203]. In the transition state, conjugation between the N P_π-orbital and the

Table 4.1

CNDO/2 MO Data for Formamide

Structure	q_N	q_C	q_O	q_N^π	q_C^π	q_O^π	p_{N-C}^π	p_{C-O}^π	a) E_e	a) E_{total}	|μ|
I		$\theta = 0°$, $2\alpha = 119°$, $\phi = 0°$									
	-0.237 (-0.292)	+0.362 (+0.561)	-0.336 (-0.477)	+0.189	+0.229	-0.418	0.482	0.845	-79.5883	-39.3033	3.92 (4.13)
II		$\theta = 0°$, $2\alpha = 119°$, $\phi = 90°$									
	-0.313	+0.355	-0.262	+0.037	+0.206	-0.263	0.272	0.931	-79.5031	-39.2718	2.96
III		$\theta = 0°$, $2\alpha = 117.5°$, $\phi = 0°$									
	-0.236	+0.364	-0.335	+0.190	+0.229	-0.419	0.483	0.845	-79.5730	-39.3040	3.95
IV		$\theta = 55°$, $2\alpha = 110°$, $\phi = 90°$									
	-0.260	+0.335	-0.273	--	+0.212	-0.283	0.282	0.924	-79.9207	-39.2883	1.45
V		$\theta = 55°$, $2\alpha = 110°$, $\phi = -90°$									
	-0.249	+0.343	-0.261	--	+0.213	-0.284	0.284	0.923	-79.6962	-39.2879	4.24

a) Electronic only energy, E_e, and total energy, E_{total}, given in atomic units

b) Dipole moment components in Debyes

C = O π-system is not possible and p^{π}_{N-C} decreases to 0.272 (this bond-order representing an electronic charge overlap between the carbonyl π-system and the N hybrid σ-bonding system) with a corresponding increase in p^{π}_{C-O}, consistent with an increased contribution from the resonance form N - C = O in this state. In general, electronic charge distributions are successfully predicted in the CNDO/2 approximation[204] and thus it is of interest to compare the above ground-state data with that available from the ab initio calculation[196] without d-functions, as given in parentheses in Table 4.11. The relative net atomic charges are in good agreement, although the CNDO/2 values are consistently smaller in magnitude; but it is to be noted that, on inclusion of d-functions there are significant changes and the ab initio q_N value is given as -0.584 while q_C and q_O become + 0.498 and -0.479, respectively, illustrating the sensitivity to the chosen basis set of atomic orbitals. The net charges for the amino hydrogen atoms cis and trans to the carbonyl oxygen in structure I, q^{C}_{H} and q^{t}_{H}, are calculated as +0.131 and +0.124, respectively, which may be compared with those from the ab initio calculation: + 0.177 and +0.160. Thus these charge densities are signiicantly different in the ground state and both calculations indicate that q^{c}_{H} is more positive than q^{t}_{H}. Therefore, for an isolated formamide molecule, in the absence of through-space effects from the magnetically anisotropic C = O and C - H bonds the cis proton is less shielded and hence would resonate to low field of the trans proton in an NMR experiment, assuming the diamagnetic contribution to the proton chemical shift to be predominant. In view of the current interest in these chemical shifts[205] this is a particularly interesting result.

The complete CNDO/2 ground state dipole moment has a magnitude $|\mu| = 3.92$ D and is oriented at $\beta = 41°$ with respect to the N - C bond, in good agremement with the experimental data[198]: $|\mu| = 3.71 \pm 0.06$ D and $\beta = 39.6°$, whereas the ab initio calculation leads to a higher dipole magnitude and an increased orientation angle. In the CNDO/2 approximation, dipole integrals involving the product of two atomic orbitals on the same atom are retained in the calculation of a molecular electric dipole[204]. Thus the dipole associated with net charges at nuclear centres for the ground state of formamide is described by $\mu_x = 1.90$ and $\mu_y = 1.42$ D, and the contribution due to asymmetry of electronic charge about these centres gives $\mu_x = -1.06$ and $\mu_y = 1.15$ D. This shows the importance of including the asymmetry contribution, which is essentially a hybridisation term, in the dipole calculation for a polar molecule.

The barrier to hindered rotation in formamide is simply the difference in total energy (including nuclear repulsions) between the ground and transition states, $E_t - E_g$, and for structures I and II is calculated as 19.8 kcal. $mole^{-1}$. This energy may be compared directly with the free energy of activation for this rotation, $\Delta G^{\#}$, determined by a total lineshape analysis of NMR data for dilute solutions of N^{15}-formamide: $\Delta G^{\#} = 18.0 \pm 0.4$ kcal. $mole^{-1}$ (10 mole % in acetone) at 25°C, cf. section 4.1.5; and also with 19.9 kcal. $mole^{-1}$ from the ab initio calculation[196] and 20.1 kcal. $mole^{-1}$ obtained in an independent CNDO calculation by Scheraga and coworkers[206]. Of course, the total energies derived in the CNDO/2 approximation are far removed from the Hartree-Fock SCF limit and hence, in such a semi-empirical SCF

calculation, it must be assumed that the inherent errors involved in an energy calculation cancel out in the energy difference taken for any two configurations of a given molecule. Such an assumption appears to be vindicated in the close agreement of the theoretical $E_t - E_g$ values quoted above, in that a CNDO/2 total energy corresponds to only about 25% of that involved in an ab initio calculation.

In general, geometrical changes in a molecule may occur in the process of internal rotation; and in particular, a change in hybridisation at the N atom in formamide may be expected to have a significant effect upon the barrier to rotation about the N-C bond. Such a change in hybridisation would be associated with the breakdown of conjugation between the formal N lone-pair π-electrons and the carbonyl π-system in the transition state. Although detailed geometrical changes were considered by Christensen et al.[196], all calculations were restricted to a planar $\theta = 0°$ (in Fig. 4.20) configuration for the NH_2 group. A CNDO/2 energy minimisation, through a change in bond angle only, was checked by showing that the minimum energy configuration for a planar ground state corresponds to $2\alpha = 117.5°$ (structure III), which is in good agreement with the experimental value of 119° [198]. The SCF-LCAO-MO data for this structure is summarised in Table 4.11, and it is seen that the total energy, E_g, is lowered by only 0.44 kcal. $mole^{-1}$ from that for structure I. The transition state geometry about the nitrogen atom was then considered for $\phi = 90°$ (Fig. 4.20) in terms of variations of the dihedral angle θ in the range 25 - 75° and the HNH bond angle 2α in the range 100 - 120°. The calculated total energy differences, $E_t - E_g$, are plotted in Fig. 4.21, where it is shown that the minimum

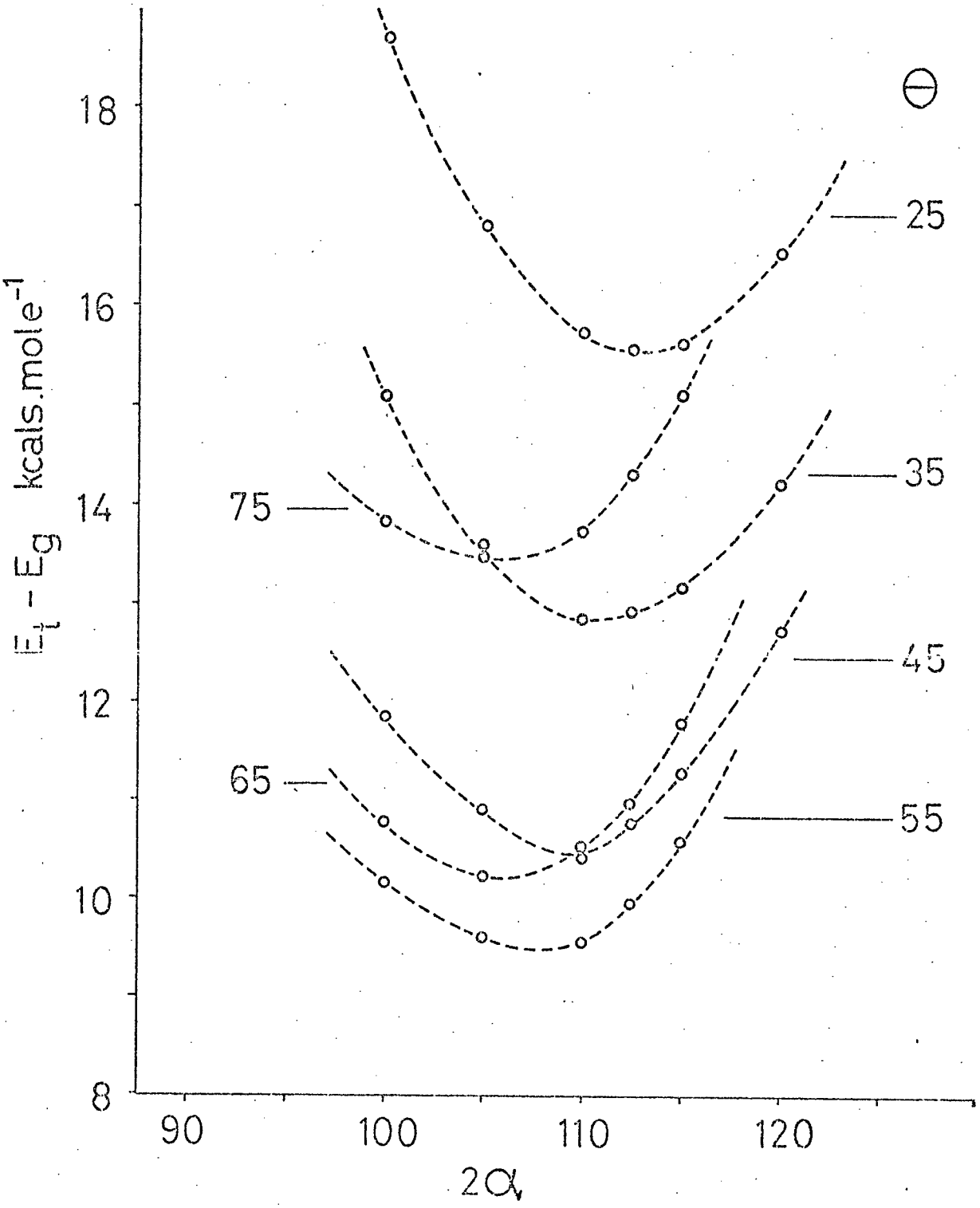

Fig. 4.21 Total energy differences for the formamide planar ground state and variable geometry transition state

energy configuration closely corresponds to $\theta = 55°$ and $2\alpha = 110°$ (structure IV). All calculated energies are seen to lie on well defined energy curves which are not, however, necessarily symmetric in α about the minimum energy point. The total energy for this structure is 10.4 kcal. $mole^{-1}$ lower than that for the initial transition state considered (structure II), and the barrier to rotation corresponding to the minimal energy molecular configurations, as determined in the CNDO/2 approximation, is now given as 9.86 kcal. $mole^{-1}$. This energy is approximately one half of the experimentally determined barrier, and the above calculation illustrates the necessity for careful geometrical optimisation before comparison with experimental data is attempted.

The above calculation of the barrier to hindered rotation in formamide, and the description of the associated ground and transition states, applies to an isolated molecule; indeed, the characteristics of the electric dipole moment for this molecule, as determined experimentally from measurements in the gas phase, have been satisfactorily reproduced by the approximate SCF-LCAO-MO model. The experimental data available for the internal rotation energy, however, are obtained from measurements in solution and it is expected that solute-solute and solute-solvent interactions for the polar formamide molecule will have a complex effect upon the hindered rotation. Thus, in general, it is only possible to compare theoretical and experimental energy data for a series of substituted amides at the same concentration (or through an extrapolation to infinite dilution) in a solvent that minimises

intermolecular interactions. Such a correlation of relative energies will be presented in detail elsewhere. At this point, it is of interest to consider further the calculated dipole moments for the parent amide--formamide. As shown in Table 4.11, the total dipole moment for structure IV has a magnitude of 1.45 D and is oriented at 6° to the N-C bond. A large contribution is due to the asymmetry of the N lone-pair electronic charge distribution (associated with an sp^3-type hybrid orbital) and is in opposition to that from the carbonyl system and thus leads to a decreased total moment as compared with that for the planar ground state, structure I (or III). Therefore, if the solute-solvent interaction is electrostatic in form and non-specific, the solvation stabilisation energy is decreased in the transition state and hence the enthalpy of activation $\Delta H^{\#}$ (or Arrhenius activation energy E_a) will be greater than $\Delta G^{\#}$ corresponding to a positive entropy of activation $\Delta S^{\#}$. That is, the activation parameters $\Delta H^{\#}$ and $\Delta S^{\#}$ are sensitive to intermolecular interactions, where $\Delta G^{\#}$ is predominantly determined by intramolecular interactions due to an effective compensation of $\Delta H^{\#}$ and $\Delta S^{\#}$ in the thermodynamic relationship $\Delta G^{\#} = \Delta H^{\#} - T\Delta S^{\#}$. So far, it has been assumed that the amino hydrogens are cis to the carbonyl oxygen in the transition state, $\phi = 90°$ in Fig. 4.20. A variational calculation, similar to that already described, for these hydrogen atoms trans to the carbonyl oxygen ($\phi = -90°$) shows that the minimum energy configuration again corresponds to $\theta = 55°$ and $2\alpha = 110°$ (structure V) and the total energy is only 0.25 kcal. $mole^{-1}$ higher than that for structure IV. As shown in Table 4.11, all net atomic charges and bond-orders are very similar to those for structure IV, but the calculated dipole

moment now has a magnitude of 4.24 D and is oriented at 70° to the N-C bond. In this configuration, the solvation stabilisation energy is increased in the transition state and if the differential solvation energy exceeds 0.25 kcal. $mole^{-1}$ this particular configuration becomes the preferred transition state for a solvated formamide molecule, and in this case $\Delta S^{\#}$ is negative. A description of stereo-specific solute-solvent interactions may require a more elaborate computational model, but the relative ease with which the CNDO/2 SCF approximation can be applied may allow a reliable and comprehensive description of the form of these intermolecular interactions and their effect upon the hindered rotation on formamide, which is of fundamental importance in the study of the more complex biological systems containing the amide linkage. However, it remains to be able to determine the activation parameters $\Delta H^{\#}$ and $\Delta S^{\#}$ with sufficient precision to warrant such detailed calculations for comparison with experimental data.

To allow a comparison with the experimental data available for the hindered rotations in N,N-dimethyl formamide and N,N-dimethyl carbamyl fluoride, calculations in the CNDO/2 approximation similar to those described above for formamide have also been carried out for the parent amide carbamyl fluoride. As this particular amide is unstable at room temperature a structure has not determined from the microwave spectrum[145], and hence the basic structure shown in Fig. 4.22 has been derived by comparison of the structural data available for acetaldehyde[207], acetyl fluoride[208] and formamide[198]. The NCF bond angle of 112.5° also corresponds to a minimum energy configuration as determined in the CNDO/2 approximation.

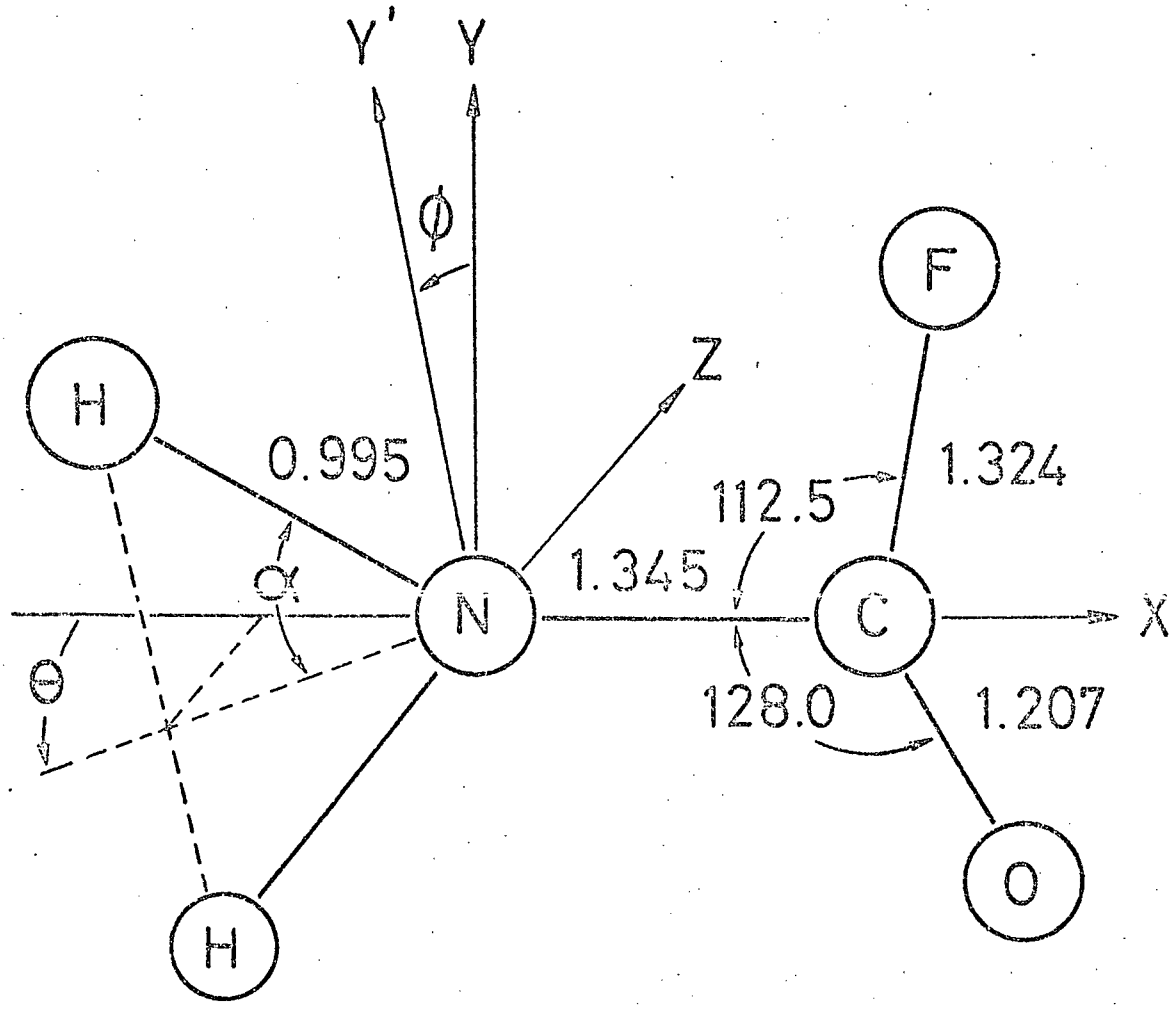

Fig. 4.22 Structure for carbamyl fluoride used in CNDO/2 SCF-LCAO-MO calculations

The minimum energy planar ground state configuration corresponds to $2\alpha = 118°$ and the total energy is given as -66.3134 a.u., Rotation of the planar NH_2 group to form a hindered rotation transition state ($\phi = 90°$) gives a total energy of -66.2922 a.u. and hence a barrier to rotation of 13.2 kcals. $mole^{-1}$, which is significantly lower than that calculated for a similar rotation in formamide, cf. structure II in Table 4.11. The total energies for the minimal energy configurations corresponding to $\phi = 90°$ and $\phi = -90°$ are then calculated as -66.3046 and -66.3062 a.u., respectively. Thus the transition state in which the amino hydrogen atoms eclipse the fluorine atom in carbamyl fluoride ($\phi = -90°$), for which $\theta = 57.5°$ and $2\alpha = 107.5°$, is more stable than the alternative transition state by 1.1 kcal. $mole^{-1}$ and is therefore the most probable transition state in solution. The stabilisation of this particular non-planar configuration is probably associated with the non-bonding interactions involving the fluorine atom. The alternative transition state structure ($\phi = 90°$) is defined by $\theta = 60°$ and $2\alpha = 107.5°$. The barrier to rotation, corresponding to the minimum energy transition state, is then calculated as $\Delta G^{\#} = 5.12$ kcals.$mole^{-1}$, which is to be compared with that given above for formamide: $\Delta G^{\#} = 9.86$ kcals.$mole^{-1}$. Assuming that the N,N-dimethyl and amino groups in substituted amides allow a direct comparison of the experimental data for hindered rotations about the N-C bond, the free energy of activation for carbamyl fluoride is estimated as 15.4 $\pm$ 0.8 kcals. $mole^{-1}$. The CNDO/2 calculations therefore predict the correct order for these activation energies, but the ratio of predicted energies is 1.9 while the experimental ratio is 1.2. Nevertheless it appears that

MO calculations at the CNDO/2 level of approximation may be very useful in detailed semi-quantitative descriptions of the overall bonding characteristics for substituted amides, and in correlations with experimentally determined differential energies. As all valence electrons are considered and both electron and nuclear repulsions are included in the calculation of molecular energies, allowing an estimation of non-bonding interaction energies, the CNDO/2 calculations have more physical significance than those using the simple Huckel π-MO model previously discussed.

CHAPTER 5

FOURIER TRANSFORM APPLICATIONS

5.1 Basic Formulation.

The duality of the pulsed and steady-state NMR methods is expressed by a Fourier transform relationship between the respective response functions describing the nuclear magnetic system under resonance conditions. Indeed, within the restriction that a nuclear spin system may be treated as a linear system, it can be shown that the free induction decay associated with the tranverse nuclear magnetization as observed in the pulse mode is also determined directly as the inverse Fourier transform of the unsaturated steady-state spectrum defined by the same component of nuclear magnetization. In 1954, Kubo and Tomita[94] derived an expression for the frequency dependent magnetic susceptibility of a general nuclear spin system in terms of quantum statistical mechanics. This theory provides a general physical basis for the Fourier transform calculation of resonance lineshapes from an autocorrelation function (or relaxation function) for nuclear magnetization, and may be considered as a generalization of the stochastic model developed by Anderson and Weiss[40]. Lowe and Norberg[67] demonstrated the above duality experimentally through an NMR study in the solid state, and in 1967, Ernst and Anderson[69] demonstrated the application of the general Fourier transform concept to high resolution NMR.

A simple model, based upon semi-classical concepts already discussed in this thesis, may be developed to allow a concise formulation of Fourier transform methods as applied to general first-order nuclear spin systems. Such a formulation forms an adequate basis for the numerical analysis of more complicated systems including second-order J-coupling. A first-order spectrum may be considered in terms of n spectral lines centred at resonance frequencies ω_i such that the overall lineshape function, $F(\omega)$, is expressed in the form

$$F(\omega) = \sum_{i=1}^{n} A_i f_i(\omega), \tag{5.1.1}$$

where A_i is an intensity normalization factor associated with the ith line defined by the Lorentzian function $f_i(\omega) = [1 + T_{2i}^2(\omega - \omega_i)^2]^{-1}$, cf. Eq. (2.1.12). T_{2i} is the total transverse relaxation time, and for the ith spectral line.

As the normal NMR detection schemes involve rf phase sensitive detection, it is convenient to again define an independent variable x by $x = \omega - \omega_o$ such that the function $f_i(x)$ is defined on the interval $-\infty < x < \infty$ in a rotating frame of reference as

$$f_i(x) = \frac{1}{1 + T_{2i}^2 (x - \Omega_i)^2} \tag{5.1.2}$$

In this way the ith line position relative to the reference frequency ω_o is given as $\Omega_i = \omega_i - \omega_o$, consistent with previous definitions, cf. Eq. (2.2.24).

In general, the inverse Fourier transform $\tilde{f}(t)$ is defined in the time domain by

$$\tilde{f}(t) = \frac{1}{2\pi} \int_{-\infty}^{+\infty} f(x) \exp(itx) dx \tag{5.1.3}$$

The transform pair may be considered in complex spaces and $\tilde{f}(t)$, in general complex, may then be readily evaluated using the contour integration in Appendix 1 as

$$\tilde{f}_i(t) = \frac{1}{2T_{2i}} \exp\left[-\left(\frac{1}{T_{2i}} - i\Omega_i\right)t\right]$$

$$= B_i \exp\left(-\frac{t}{T_{2i}}\right)[\cos\Omega_i t + i\sin\Omega_i t], \quad B_i = \frac{1}{2T_{2i}} \qquad (5.1.4)$$

for $0 \leq t < \infty$. The observable free induction decay described by the function $\tilde{f}(t)$ is necessarily defined by the real part only. Therefore, in accordance with Eq. (5.1.4), $\tilde{f}_i(t)$ corresponding to a single Lorentzian spectral line, $f_i(x)$, consists of an oscillatory decay with a fundamental frequency Ω_i and a characteristic time constant T_{2i}. As the Fourier transformation is linear[95], it follows from Eq. (5.1.4) that the overall real decay corresponding to F(x) (Eq. (5.1.1)) is described by

$$S(t) = \sum_i B_i \cos\Omega_i t \exp\left(\frac{-t}{T_{2i}}\right) \qquad (5.1.5)$$

That is, in general the function S(t) represents a modulated oscillatory decay with the modulations determined by all frequencies $|\Omega_i \pm \Omega_j|$. The detailed form of an observed free induction decay also depends upon the relative phases of the irradiating and reference rf magnetic fields involved in a given phase sensitive detection scheme. This aspect is considered further at a later point.

The normal absorption mode spectrum is defined by F(x). A dispersion mode spectrum is then defined by a corresponding function H(x) where

$$H(x) = \sum_{i=1}^{n} A_i \, h_i(x)$$

$$= \sum_i A_i \frac{T_{2i}(x-\omega_i)}{1 + T_{2i}^2(x-\omega_i)^2} \qquad (5.1.6)$$

cf. Eq. (5.1.1). As shown in Appendix 1, the inverse Fourier transform of $h_i(x)$ is given as

$$\tilde{h}_i(t) = i \, B_i \exp[-(\frac{1}{T_{2i}} - i\Omega_i)t] \qquad (5.1.7)$$

A complex lineshape function $g(x)$ may now be defined in the frequency domain as

$$g(x) = f(x) - ih(x), \qquad (5.1.8)$$

such that the corresponding complex inverse Fourier transform is given from Eqs. (5.1.4) and (5.1.7) as

$$\tilde{g}(t) = B \exp(-\frac{t}{T_2}) \, [\cos\Omega t + i \sin\Omega t] \, . \qquad (5.1.9)$$

Conversely, the Fourier transform of $\tilde{g}(t)$, $g(x)$, is given by

$$g(x) = \int_0^\infty \tilde{g}(t) \exp(-itx)dt = \frac{1}{1 + iT_2(x-\Omega)} \qquad (5.1.10)$$

for $\tilde{g}(t)$ defined on the interval $0 \leq t < \infty$. A complete spectral function $G(x)$ may now be considered in the form

$$G(x) = \sum A_i [f_i(x) - ih_i(x)] = \sum_{i=1}^{n} A_i \frac{1}{1 + iT_{2i}(x-\omega_i)} \qquad (5.1.11)$$

This function is equivalent to that previously defined in terms of a general complex transverse nuclear magnetization, $\underline{G}(x, \phi)$, in the normal rotating frame of reference Ouvz, cf. Eq. (2.4.3) and Fig. 2.2. In defining the nuclear isochromat component $\underline{G}(x, \phi)$, the u-axis corresponds

to the real axis of the complex plane and hence the phase angle ϕ is referred to this axis. Also, in a steady-state NMR experiment, the irradiating field vector $\underline{H}_1$ is assumed to be along the u-axis, cf. Eq. (2.1.9), and thus the absorption mode lineshape function V(x) describes the v-component magnetization. In pulsed mode NMR, however, the effective field vector $\underline{H}_1$ is considered to be along the v-axis of the normal rotating frame, such that at time t = 0 (following a $\pi/2$ pulse, $\beta = \pi/2$ in Fig. 2.1) all isochromats are aligned in the direction of the u-axis. This allows a consistent description of isochromat dephasing in terms of the phase angle ϕ for the free induction decay as determined by the u-component magnetization. Therefore, in the complex plane Ouv, the function G(x) in Eq. (5.1.11) is to be modified by a phase factor $\exp(i\pi/2)$, giving

$$G(x) = \Sigma A_i \left[h_i(x) + i f_i(x)\right], \qquad (5.1.12)$$

so that in accordance with Eq. (2.4.3) $u_i(x) = A_i h_i(x)$ and $V_i(x) = A_i f_i(x)$. Also, it is to be noted that the response s(t) corresponds to an irradiating rf field $\underline{H}(t)$ defined in a fixed frame of reference as $H(t) = 2H_1 \cos(\omega t + \pi/2)$, cf. Eq. (2.1.5). Thus it is seen that the absorption mode lineshape function f(x) describing the v-component nuclear magnetization, associated with the imaginary axis of a complex plane in the normal rotating frame is given as the real part of the complex Fourier transform of the free induction decay function s(t).

It is now necessary to consider the physical consequences of taking the real part only, s(t), of the causal function $\tilde{g}(t)$ in the time domain, cf. Eq. (5.1.9). In accordance with the general integral transformation given in Eq. (5.1.10), the Fourier transform of s(t) is

$$g'(x) = \frac{1}{2}\left\{\frac{2(1 + iT_2x)}{[1 + iT_2(x+\Omega)][1 + iT_2(x-\Omega)]}\right\}$$

$$= \frac{1}{2}\left\{ g_-(x) + g_+(x)\right\} \qquad (5.1.12)$$

with

$$s(t) = \frac{1}{T_2}\exp(-\frac{t}{T_2})\cos\Omega t$$

and (5.1.13)

$$g_\pm(x) = \frac{1}{1 + T_2^2(x\mp\Omega)^2} - i\,\frac{T_2(x\mp\Omega)}{1 + T_2^2(x\mp\Omega)^2}$$

Thus it is shown for s(t) defined by the single frequency Ω, that the Fourier transformation defines two lineshape functions centred symmetrically about the reference frequency ω_o (x = 0). That is, $f_+(x)$ and $f_-(x)$ (as defined in Eq. (5.1.8)) determine Lorentzian lines centred at $x = \Omega$ and $x = -\Omega$, respectively. This is an example of the Faltung property[95] of a Fourier transformation and is of importance in determining the frequency of the irradiating rf field, $\omega = \omega_o$, in a pulsed NMR experiment.

The Fourier transform of $\tilde{g}(t)$ is given in accordance with Eq. (5.1.10) as

$$g(x) = \int_o^\infty \tilde{g}(t)\cos tx - i\sin tx\, dt$$

and hence a cosine Fourier transform is defined by

$$g_c(x) = \int_o^\infty \tilde{g}(t)\cos tx\, dt \qquad (5.1.14)$$

The cosine transform of the real function $s(t) = \frac{1}{T_2}\exp(-t/T_2)\cos\Omega t$, cf. Eq. (5.1.9), is readily shown to be

$$g_c(x) = [1 + T_2^2(x+\Omega)^2]^{-1} + [1 + T_2^2(x-\Omega)^2]^{-1}$$

Comparison with Eq. (5.1.13) shows that this expression corresponds to $f_+(x) + f_-(x)$. That is, in general, the cosine Fourier transform of $s(t)$ determines the absorption mode lineshape function. Similarly, a sine transform determines the dispersion mode function, $h_+(x) + h_-(x)$.

The complex Fourier transform of $s(t)$ defines <u>both</u> the absorption and dispersion mode lineshape functions in the frequency domain as the real and imaginary parts of the function $g(x)$, respectively. For a general linear physical system, the Kramers-Kronig relations[96] relate the real and imaginary parts of the frequency response functions $g(x)$. These relations are equivalent to a Hilbert transform pair[97] in that the real and imaginary parts, $f(x)$ and $h(x)$, are related by

$$h(x) = \frac{1}{\pi}\int_{-\infty}^{+\infty} \frac{f(x')\,dx'}{x'-x} \quad , \quad f(x) = -\frac{1}{\pi}\int_{-\infty}^{+\infty} \frac{h(x')\,dx'}{x'-x} \qquad (5.1.15)$$

where the improper integrals are considered as principal values. These transforms may be compared with those discussed by Abragam[97]. To avoid the improper integrals in Eq. (5.1.15), the Hilbert transform $h(x)$ may be considered in the form[98]

$$h(x) = \frac{2}{\pi}\int_0^\infty \sin tx \int_0^\infty f(x')\cos tx'\,dx'\,dt \qquad (5.1.16)$$

For the Lorentzian lineshape function $f(x')$ given in Eq. (5.1.2), it follows that

$$h(x) = \frac{2}{\pi}\int_0^\infty \sin tx \left[\frac{\pi}{T_2}\exp(-t/T_2)\cos \omega t\right] dt$$

This integral represents a sine Fourier transform for a causal function,

and hence $h(x) = T_2(x-\omega)\left[1+T_2^2(x-\omega)^2\right]^{-1} + T_2(x+\omega)\left[1+T_2^2(x+\omega)^2\right]^{-1}$.
Thus the Hilbert transform of f(x) determines the dispersion mode lineshape functions $h_{\pm}(x)$ as given in Eq. (5.1.13).

Now by definition[96], h(x) in Eq. (5.1.15) is also given by the convolution

$$h(x) = -\varepsilon(x)*f(x) \qquad (5.1.17)$$

where $\varepsilon(x) = (\pi x)^{-1}$ and * denotes the principal value of a convolution integral. This convolution is readily evaluated indirectly by using Fourier transformations, in that it is well known that a convolution in the frequency domain corresponds to a simple multiplication in the time domain

$$\tilde{h}(t) = -\tilde{\varepsilon}(t)\,\tilde{f}(t).$$

The inverse Fourier transform $\tilde{\varepsilon}(t)$ is given by a contour integration as

$$\tilde{\varepsilon}(t) = -i, \; t > 0 \qquad (5.1.18)$$

and hence it follows that $\tilde{h}(t) = i\{\frac{1}{2T_2}\exp -(\frac{1}{T_2} - i\Omega)t\}$ which defines the dispersion mode function given in Eq. (5.1.6). It is similarly shown that $f(x) = \varepsilon(x)*h(x)$. With the advent of fast numerical Fourier transform algorithms, it is possible to extract accurate absorption and dispersion mode lineshapes from a steady-state spectrum[99] with arbitrary rf phase characteristics. This phasing feature is of course an inherent property of pulsed mode NMR data in the form of the free induction decay following a $\pi/2$ pulse.

5.2 Resonance Condition.

In pulsed mode NMR, the irradiating rf magnetic field, $\underline{H}_1$, is applied for a finite time only, in the form of a pulse of amplitude A and width t_w with a frequency $\omega = \omega_o$ rads sec.$^{-1}$. The free induction decay associated with a component transverse nuclear magnetization may then be observed in the absence of an rf magnetic field. Such a pulse may be considered as one of a sequence with a repetition period τ, and may be defined in a fixed frame of reference by

$$\begin{aligned} P(t) &= A\cos\omega_o t \qquad 0 \leq t < t_w \\ &= 0 \qquad\qquad t_w < t \leq \tau \,. \end{aligned} \tag{5.2.1}$$

P(t) may now be considered in terms of a complex Fourier series

$P(t) = \sum_{n=-\infty}^{+\infty} c_n(\omega) e^{i\omega t}$ with the Fourier coefficients $c_n(\omega) = \frac{1}{\tau}\int_o^{\tau} P(t) e^{-i\omega t} dt.$

For $\omega \sim \omega_o$, it is shown that for the fundamental frequency $\omega_f = 2\pi/\tau$

$$\begin{aligned} C_n(\omega) &= \frac{A}{\tau}\left\{\frac{\sin(\omega-\omega_o)t_w}{\omega-\omega_o}\right\} \\ &\quad \frac{A}{\tau}\left\{\frac{\sin(n\omega_f t_w)}{n\omega_f}\right\} \,, \end{aligned} \tag{5.2.2}$$

such that the frequency spectrum associated with the pulse consists of discrete frequencies ω_n defined in terms of ω_f as

$$\omega_n = \omega_o + n\omega_f, \quad n = \pm 1, \pm 2, \cdots \,. \tag{5.2.3}$$

The frequencies corresponding to n = 1, 2, $\cdots$ are conveniently referred to as the upper sideband spectrum, and those corresponding to n = -1, -2,

··· then form the lower sideband spectrum. The power corresponding to each component frequency is given by $c_n(\omega)^2$, maximum power at $\omega = \omega_o$ being $(At_w/2\tau)^2$. Thus rf power in pulsed mode NMR is distributed over a specific frequency range (symmetric about ω_o) which may include a large range of resonance frequencies ω_i. This frequency range is determined by the pulse width only, and from Eq. (5.2.2) it is seen that the first zero coefficient is defined by the condition $n\omega_f t_w = \pi$, that is, $\omega = 2\pi/t_w$. For a 5μsec. pulse, this corresponds to a frequency distribution about ω_o of ± 200 kHz and the rf power may be considered to be constant over a range ± 2 kHz. In general, if w (Hz) is the frequency width of a resonance spectrum to be irradiated, the pulse width is defined as $t_w \simeq 0.01\ w^{-1}$ sec. In addition, the overall resolution and reproducibility of the resonance spectrum obtained through a Fourier transformation of the response function s(t) for a nuclear spin system following an rf pulse are determined by the spacing of the discrete irradiating frequencies ω_n, that is, τ^{-1} Hz.

The form of the above pulse frequency distribution determines the centre frequency ω_o to be used in a given pulsed NMR experiment. As an rf phase sensitive detector is normally referenced to ω_o, the resonance spectrum defined in terms of the independent frequency variable x is considered for $0 \leqslant x < \infty$ only. For a spectral line with a resonance frequency $\omega_i > \omega_o$, the detected component free induction decay signal may be assumed to have the form $s(t) = B_i \exp(-t/T_{2i})\cos\Omega_i t$ with $\Omega_i = \omega_i - \omega_o$. In accordance with Eq. (5.1.13), the real part of the Fourier transform of s(t) defines Lorentzian lines described by lineshape functions given as

$$f_{i+}(x) = \frac{1}{1 + T_2^2 (x-\Omega_i)^2}$$

$$f_{i-}(x) = \frac{1}{1 + T_2^2 (x+\Omega_i)^2} \qquad (5.2.4)$$

On the interval $0 < x < \infty$, the contributions from $f_{i+}(x)$ and $f_{i-}(x)$ at $x = \Omega_i$ are 1 and $1 + 4T_2^2\Omega_i^2\ ^{-1}$, respectively. Thus a general condition for negligible distortion of the lineshape f_{i+} due to a contribution from f_{i-} is $T_2\Omega_i >> 1$. The distortional effects due to the transform function f_{i-} are shown in Fig. 5.1 for varying values of the parameter $\Omega_i T_2$. It is to be noted that a 0.25% contribution at $x = \Omega_i$ from f_{i-} corresponds to a frequency shift $\Omega_i = 10T_2^{-1}$ rad. sec.$^{-1}$. An additional lineshape distortion may arise through detector rf reference phase adjustment. This leads to the real part of the Fourier transform g(x) being a mixture of absorption and dispersion mode functions, and the effect of a dispersion function h_{i-} (analogous to f_{i-}) is more severe in that the contribution at $x = \Omega_i$ is $2T_2\Omega_i\ 1 + 4T_2^2\Omega_i^2\ ^{-1}$. In this case, a 0.25% contribution from h_{i-} corresponds to $\Omega_i = 200T_2^{-1}$. This form of distortion, however, is eliminated by a phase correction as described in the following section. The centre frequency ω_o may be decreased to increase the shift from resonance, Ω_i, and hence decrease the transform overlap distortion for a given spectral line; but in so doing, the frequency associated with the response s(t) is increased. Experimentally, the free induction decay signal is digitized using a sampling technique and the maximum frequency component that may be analyzed with

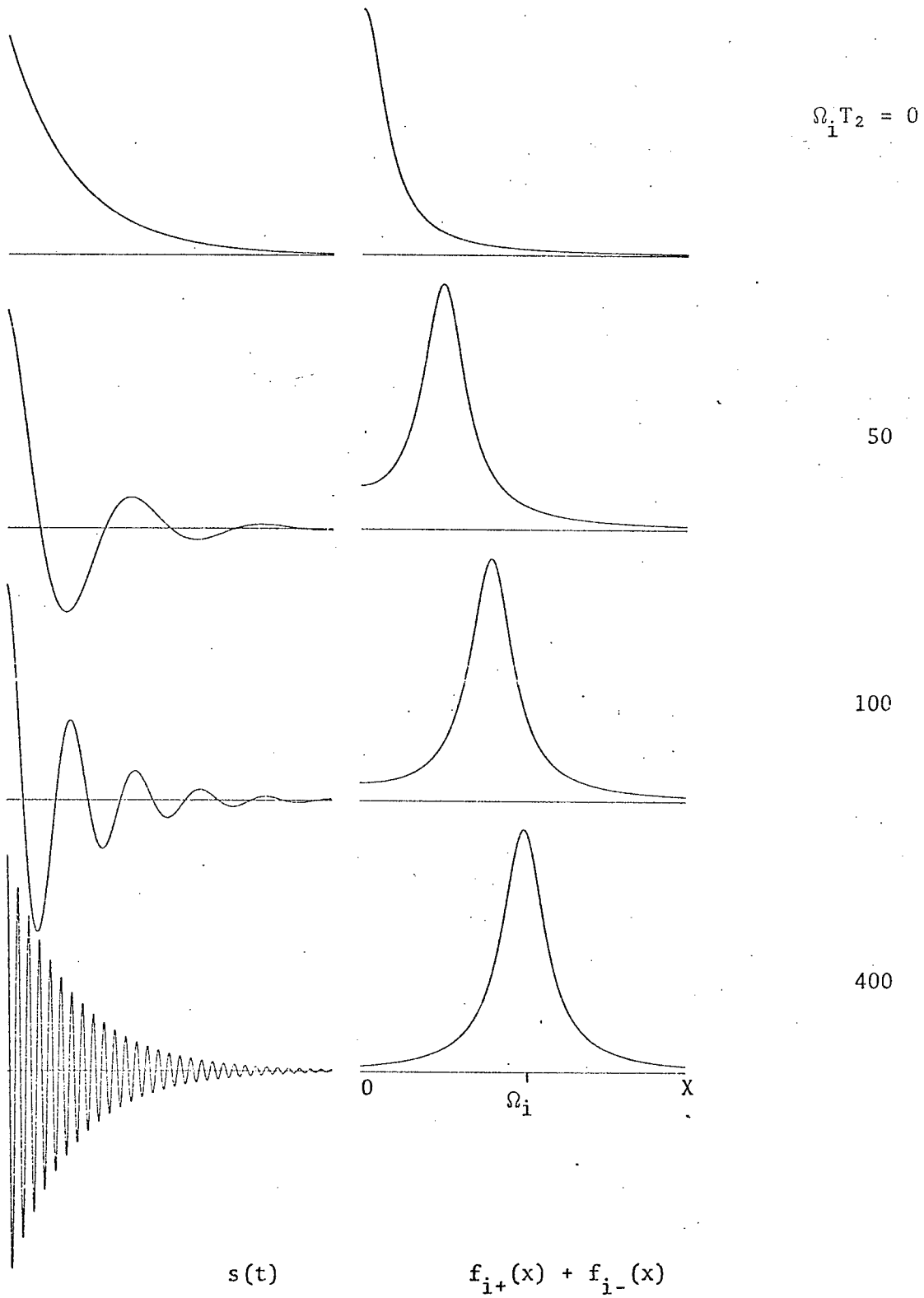

Figure 5.1 Pulsed mode NMR resonance conditions

N samples over the pulse interval τ is $N/2\tau$ [69,100]. If higher frequencies $x > N/2\tau$ are applied to the sampling device, they are down-converted into the frequency range $0 < x < N/2\tau$ and are then effective as the lower frequencies $x' = |x - nN/\tau|$,[101] with $n = 1, 2, \cdots$. Following a Fourier transformation of $s(t)$ these frequencies may give rise to spurious spectral lines on the interval $0 < x < N/2\tau$. In order to obtain a quantitative lineshape from the function $s(t)$, it is required in general that ω_o be set with respect to all resonance frequencies ω_i such that the frequencies Ω_i are minimized. Simultaneously, the transform function overlap distortion must be minimized according to the above conditions on the parameter Ω/T_2.

In a general pulsed mode NMR experiment, the total spectrum to be obtained as a Fourier transform of $S(t)$, cf. Eq. (5.1.5), must lie to one side of the centre frequency ω_o. That is, for $x > 0$ it is required that all resonance frequencies ω_i be such that $\omega_i > \omega_o$ $(\Omega_i > 0)$. In this manner only the upper sideband frequency spectrum associated with the rf pulse induces resonance effects in a given nuclear spin system. The reason for this general resonance condition is shown by considering two resonance frequencies ω_i and ω_j such that $\omega_j < \omega_o < \omega_i$. The actual separation of spectral lines is $\omega_i - \omega_j$, or $\Omega_i + |\Omega_j|$ where $\Omega_j = \omega_j - \omega_o < 0$. The response $S(t)$, however, is defined in terms of the frequencies Ω_i and $|\Omega_j|$ and hence the Fourier transform shows spectral lines centred at $x = \Omega_i$ and $x = |\Omega_j|$ with a false separation $|\Omega_i - |\Omega_j||$, and in the particular case for which $|\Omega_j| > \Omega_i$ an incorrect frequency ordering. The response $S(t)$ being defined in terms of the frequencies Ω_i and $|\Omega_j|$ may be considered to correspond to the

resonance effects induced by both the upper and lower sideband frequency spectra associated with the rf pulse.

In quantitative lineshape studies, once the general form of the NMR spectrum has been determined, it is often possible to set the centre frequency to minimize the off-resonance shift Ω_i for the particular spectral line of interest. In this way, the lowest frequency components in S(t) define the lineshape function $f_i(x)$ and these are the components most reliably analyzed for any given number of sampled data points, N.

5.3 Finite Complex Fourier Transform.

Experimentally, a function s(t) in the time domain may be determined for a finite number of data points only and hence the complex Fourier transform function g(x) is determined for an equivalent number of data points. Thus, at this point, it is necessary to discuss a basic finite complex Fourier transformation.

If the function s(t) is essentially finite only on the interval $0 \leq t \leq T$, it may be considered to be periodic with a period T and may be expressed in terms of a general finite Fourier series as

$$s(t) = \sum_{n=-N}^{N} A_n \exp(ix_n t) \tag{5.3.1}$$

where A_n is a complex coefficient corresponding to the harmonic component with frequency x_n. The fundamental frequency associated with the periodic function s(t) is x_f, defined as $x_f = 2\pi/T$ rad. $sec.^{-1}$. The finite number of harmonic frequencies x_n are then given by $x_n = n \cdot 2\pi/T$, and from Eq. (5.3.1) it follows that

$$s(t) = \sum_{n} A_n \exp(i\frac{2\pi n}{T}t). \tag{5.3.2}$$

Thus it is seen that the highest harmonic of the fundamental frequency x_f considered in the finite series approximation to a Fourier analysis is defined by N. It may now be assumed that s(t) is sampled by P data points on the interval 0 t T so that the time corresponding to the k^{th} data point is $t_k = kT/P$, where $k = 0, 1, \cdots, P-1$. The coefficients A_n are now given by a finite Fourier transform of the form

$$A_n = \frac{1}{P} \sum_{k=0}^{P-1} s_k \exp\left(-i \frac{2\pi k}{P} . n\right) \tag{5.3.3}$$

for P even, where s_k is the function s(t) value at t_k. This relationship is verified by considering an integral form of Eq. (5.3.1):

$$\int_0^T s(t)\exp\left(-\frac{i2\pi m}{T}t\right)dt = \sum_{n=-\infty}^{+\infty} A_n \left\{ \int_0^T \exp\left(\frac{-i2\pi m}{T}t\right)\exp\left(\frac{-i2\pi n}{T}t\right)dt \right\}$$

$$= \sum_n A_n T \delta_{mn}$$

$$= T A_m$$

The finite complex inverse Fourier transform of A_n defined in Eq. (5.3.3) is given in accordance with Eq. (5.3.2) as

$$s_k = \sum_{n=N}^{N} A_n \exp\left(i\frac{2\pi k}{P}n\right). \qquad (5.3.4)$$

It is to be noted that the coefficient A_{-n} is given as A_n^* and hence an explicit calculation for $n < 0$ is redundant and s_k is equivalently defined as

$$s_k = \sum_{n=0}^{N-1} A_n \exp\left(i\frac{2\pi k}{P}n\right) \qquad (5.3.5)$$

for N even. The coefficients A_n define the finite complex Fourier transform function corresponding to g(x) as previously considered, cf. Eq. (5.1.8), in terms of function values $g(x_n)$ at the discrete frequencies x_n separated by the fundamental frequency x_f. That is, the complex lineshape function g(x) is defined on the normal frequency interval $0 \leq x < \infty$ by $g(x_n) = A_n$.

The Fourier coefficient A_n as given in Eq. (5.3.3) may be expressed in the form

$$A_n = \frac{1}{p} \sum_{k=0}^{p-1} S_k \left[\cos\left(\frac{2\pi kn}{p}\right) - i \sin\left(\frac{2\pi kn}{p}\right)\right] \tag{5.3.6}$$

and hence the real part of this complex coefficient, a_n, is given as

$$a_n = \frac{1}{p} \sum_{k=0}^{p-1} S_k \cos\left(\frac{2\pi kn}{p}\right) \quad . \tag{5.3.7}$$

Thus it is seen that a_n is determined as the finite Fourier cosine transform of s_k, and this coefficient is equivalent to $g_c(x)$ where the general function $g_c(x)$ is defined in Eq. (5.1.4). A finite Fourier sine transform may also be considered to determine the coefficient b_n as the imaginary part of A_n. A simple correlation between the Fourier coefficients defining s_k in Eq. (5.3.5) and those in a standard finite trigonometric Fourier series is shown by considering s_k in the form

$$s_k = a_0 + \sum_{n=1}^{N-1} \left[a_n \cos\left(\frac{2\pi kn}{p} n\right) + b_n \sin\left(\frac{2\pi kn}{p} n\right)\right]$$

where $a_n = \frac{2}{p} \sum_{k=0}^{p-1} S_k \cos\left(\frac{2\pi kn}{p}\right)$ and $b_n = \frac{2}{p} \sum_{k=0}^{p-1} S_k \sin\left(\frac{2\pi kn}{p}\right)$. It then follows that $A_n = \frac{1}{2}(a_n - ib_n)$ and $A_o = \frac{1}{2}a_o$, showing that a_n and b_n are equivalent to the functions $f(x)$ and $h(x)$ defining the general complex lineshape function $g(x)$, in that $a_n = f(x_n)$ and $b_n = h(x_n)$.

In general terms, it is not possible to have a signal of finite time duration and strictly finite spectral bandwidth. However, a given signal $s(t)$ of duration T may be assumed to have an effective bandwidth W and then according to the sampling theorem in the time domain[106], this signal function is determined for all $0 \leq t \leq T$ to a good approximation by its values at $2TW >> 1$ sampling points separated by $2W^{-1}$ sec. This implies that the function $s(t)$ is well-defined if the

sampling frequency f_s is such that $2W \leq f_s$ Hz. The number of sampled data points, P, obtained over the time interval T is determined by the number of memory locations available for the digital data following an A-D conversion of the sampled analog signal data. The maximum sampling frequency usually corresponds to the minimum time, t_c, required in the A-D conversion process giving data to a specified accuracy (number of bits), as the sampling device may operate over a time interval of 1 μsec. or less. The sampling frequency may be effectively increased, however, by using a sample-and-hold device or "boxcar" integrator[107] to determine data points at a time separation $t_s < t_c$. The sampling theorem in the frequency domain[100] states that the frequency spectrum corresponding to a signal s(t) of duration T sec. is completely determined by amplitude values at a series of points separated by 1/T Hz. This separation frequency is just the fundamental frequency x_f, and hence the sampling theorem provides a basis for using the finite Fourier series given in Eq. (5.3.2) to define the function s(t), where the coefficients (amplitudes) A_n are determined only for the discrete frequencies $x_n = nx_f$. In addition, the sampling interval in the time domain has been determined as $2W^{-1}$ sec. and the maximum frequency $x > 0$ included in the finite Fourier series given in Eq. (5.3.2) is N/T Hz. Thus for $P >> 1$ it follows that N is determined as $N = P/2$. That is, the maximum frequency that may be analyzed for the sampled function s(t) as defined by P data points is the lowered frequency $f_m = P/2T$ Hz. The frequency range of interest becomes $0 \leq x \leq P/2T$ Hz, as in accordance with the sampling theorem it is invalid to calculate A_n for $n > P/2$ using Eq. (5.3.5). The highest frequency that may be analyzed

is therefore determined directly by the sampling frequency f_s, now defined as $f_s = 2f_m$.

In pulsed mode NMR using Fourier transform techniques, the signal function s(t) is the free induction decay following a $\pi/2$-pulse and T is equivalent to the pulse repetition period τ, as discussed in the preceding section. A Fourier transform frequency spectrum may be obtained by numerically evaluating the complex amplitudes A_n directly, as given in Eq. (5.3.3). This is a time-consuming process in that P operations, each of which may be considered as a complex multiplication followed by an addition, are required for each A_n. Cooley and Tukey[108], however, have developed an algorithm for a binary arithmetic calculation that allows a very significant reduction in computational time on a digital computer. The algorithm replaces an array of complex numbers of length $P = 2^r$, r an integer, by its complex Fourier transform. The total time involved corresponds to less than $2P\log_2 P$ operations[108], as defined above, without requiring more data storage than is required for the input data array. The largest array that may be transformed depends upon the computer memory: for a 32,768 word memory, the maximum is P = 8192. It is to be noted that for the finite Fourier transform pair as described by Eqs. (5.3.3) and (5.3.5), this algorithm generates a number of linearly independent spectral amplitudes equal to the number of input data points. However, it is readily shown that for real input data, the algorithm output data is symmetric about $n = P/2$ in that $A_n = A^*_{P-n}$. This is consistent with the data points defined by $n = 0, 1, \cdots, P/2$ determining the transform spectrum over the frequency range of interest.

A FORTRAN computer program LGTRN has been written and checked for general Fourier transform applications in NMR. This program uses the IBM SHARE library subroutine PK FORT to carry out the basic Fourier transformation using the Cooley-Tukey algorithm. The real input data is normalized, transformed and then separated into re-normalized absorption and dispersion mode spectral data sets. These data sets may be further processed using real arithmetic to obtain phase corrected spectra, enhanced resolution and filtered spectra[69] with improved signal-to-noise ratios, as discussed in the following section. Full plotting options are available for a CALCOMP plotter and spectral data may be presented over any specified frequency range, within the limits 0 and P/2T Hz. The basic output data point separation is defined as 1/T Hz, and hence a subroutine SBHARM has been developed to allow the calculation of sub-harmonic data points. This consists of extending the effective time interval for the input data and hence the number of data points P, rearranging the real input data as the two parts of a complex array, transforming this array and then assembling the spectral data over a specific frequency range. In this manner, accurate Fourier transform spectra may be obtained for sub-harmonic multiplicities of two, four and eight on a computer with a 32K memory. In high resolution NMR, the sampling interval T, as normally determined by the spin-spin relaxation time T_2, may be 2 - 5 secs. and hence the fundamental frequency is 0.5 - 0.2 Hz. Data points at this frequency separation are required to define accurately frequency positions and intensities for spectral lines with full-widths at half-maximum of the order of 0.5 Hz. This is not possible, in general, and significant distortions are

apparent in the resultant Fourier transform spectra. By using a sub-multiplicity of eight, however, the effective data point separation is reduced to 0.06 and 0.025 Hz for T = 2 and 5 sec., respectively, and an accurate reproduction of the unsaturated steady-state NMR spectrum is obtained. The program LGTRN has been developed for maximum efficiency and the computational (CPU) time for 1024 input data points and an 8192 point Fourier transformation, corresponding to a sub-harmonic multiplicity of eight, with phase corrections and the setting up of full plotting data arrays is typically less than 20 sec. on an IBM 360/67.

The overall accuracy of the numerical complex finite Fourier transformation is most clearly shown for a single spectral line with a given off-resonance shift Ω, cf. Eq. (5.2.4). The free induction decay as defined by s(t) in Eq. (5.1.13) may be considered on the interval $0 \leqslant t \leqslant 0.64$ sec. for a Lorentzian system with Ω = 100 Hz and T_2 = 0.1 sec. The numerical Fourier transform absorption and dispersion mode data are represented by crosses in Fig. 5.2a, and the full lineshapes as calculated in accordance with Eq. (5.1.13) are shown as full lines. The numerical data points are separated by 0.39 Hz, as defined by a sub-harmonic multiplicity of four, the full-line-width at half-maximum being 3.2 Hz. It is seen that the deviation from the exact absorption mode lineshape for this 4096 point transformation is minimal, the deviation being only 1% and 4% at frequencies of 103.1 and 105.47 Hz, respectively. An additional check on the overall accuracy of the Fourier transformation is afforded by Parseval's theorem[109], in that for an exact trans-

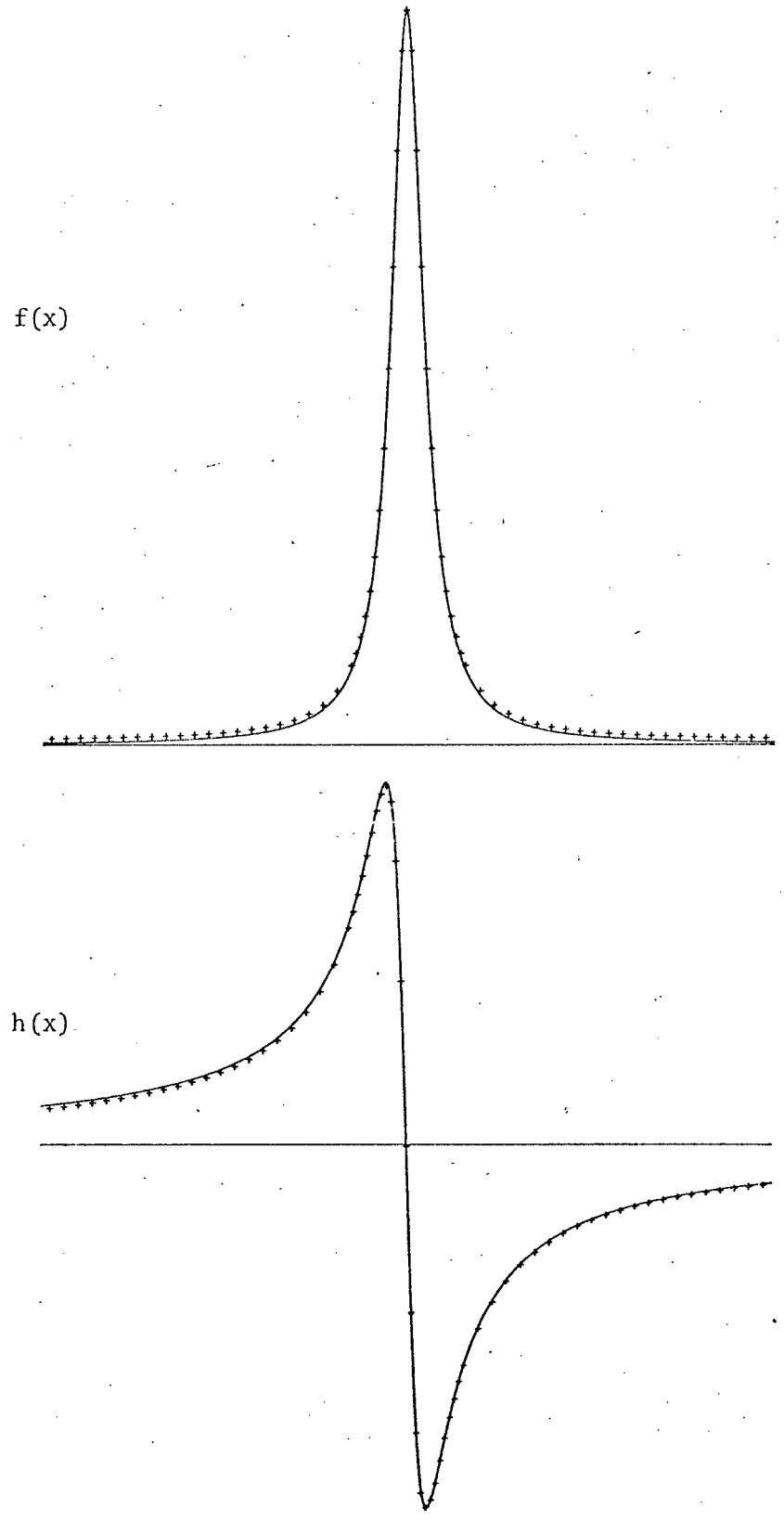

Figure 5.2(a) Finite Fourier transform characteristics for a Lorentzian lineshape system.

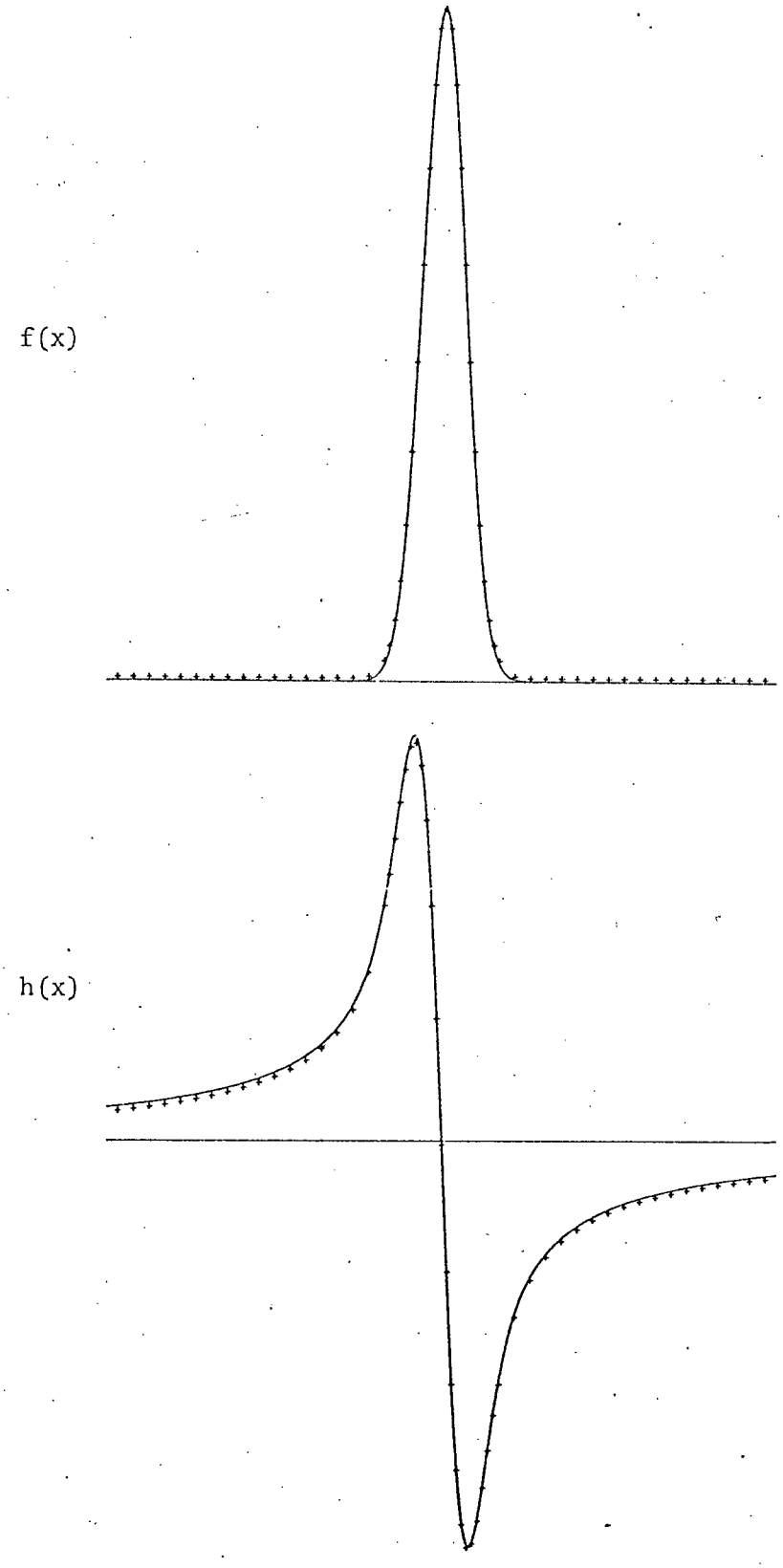

Figure 5.2(b) Finite Fourier transform characteristics for a Gaussian lineshape system.

formation $\Sigma\ |s_k|^2 = P\ \Sigma\ |A_n|^2$. The differency between these two factors was calculated to be less than 2% for the above lineshape function.

The corresponding lineshapes and numerical data points for a Gaussian system are shown in Fig. 5.2b. The absorption and dispersion mode Gaussian lineshapes, f(x) and h(x), are given in Eqs. (5.4.20) and (5.4.21), respectively. The associated response function, s(t), is taken as the real part of the function defined in Eq. (5.4.22) and is also shown in Fig. 5.2b. The Gaussian absorption mode lineshape function has characteristics distinct from those of the Lorentzian function, and again the deviation from the exact lineshape is shown to be minimal.

The response s(t) for a Lorentzian system may be considered in the form

$$s(t) = B\exp(-t/T_2)\cos\Omega t,$$

cf. Eq. (5.1.5), and has been assumed above to be finite only on the interval $0 \leq t \leq T$. It now remains to consider the effect of the truncation of this function as compared with the normal definition on the interval $0 \leq t < \infty$. The lineshape function f(x) is given as the Fourier cosine transform of s(t), cf. Eq. (5.1.14), and hence

$$f(x) = B \int_0^T \exp(-t/T_2)\cos\Omega t \cos xt\ dt. \qquad (5.3.8)$$

The function $f_+(x)$ centred at $x = \Omega$ is then defined by

$$f_+(x) = \frac{B}{2} \int_0^T \exp(-t/T_2)\cos[(\Omega - x)t]\ dt,$$

and hence

$$f_+(x) = \frac{\beta}{4}\left\{\frac{1}{\frac{1}{T_2}+i(x-\omega)}\left\{1-\exp\left[-\left(\frac{1}{T_2}-i(x-\omega)\right)T\right]\right\}\right.$$

$$\left. + \frac{1}{\frac{1}{T_2}+i(x-\omega)}\left\{1-\exp\left[-\left(\frac{1}{T_2}+i(x-\omega)\right)T\right]\right\}\right\}$$

$$= A\,\frac{1}{1+T_2^2(x-\omega)^2}\left\{1-\exp\left(-T/T_2\right)\left[\cos\left[(x-\omega)T\right]-T_2(x-\omega)\sin\left[(x-\omega)T\right]\right]\right\}$$

(5.3.9)

where A is a normalization constant. This equation shows that in the limit $T \to \infty$, the function $f_+(x)$ describes a normal Lorentzian absorption mode lineshape on the interval $0 \leq t < \infty$. For a finite value of T, however, this lineshape is modified by oscillatory terms with an overall amplitude factor $(\Omega - x)\exp(-T/T_2)$. For $x \simeq \Omega$, the exponential is dominant and defines an amplitude of < 1% of the normal Lorentzian function maximum for $T \geq 7T_2$. In addition, the cosine and sine terms in Eq. (5.3.9) tend to cancel for all x and hence the overall effect of truncation is expected to be negligible for the T limit defined above. This is shown to be the case for the Lorentzian absorption mode lineshape f(x) considered in Fig. 5.2a, for which $T = 6.4T_2$.

5.4 Phase Corrections.

In pulsed mode NMR the free induction decay signal is determined by the transverse nuclear magnetization and is described in terms of a complex function S(t), cf. Eq. (5.1.4), which is defined for a general first-order spin system by[†]

$$S(t) = \exp(-t/T_2) \sum_i B_i[\cos\Omega_i t + i \sin\Omega_i t] \qquad (5.4.1)$$

in the normal rotating frame of reference. B_i is an amplitude factor for the component decay with the characteristic frequency $\Omega_i = \omega_i - \omega_o$, cf. Eq. (5.1.2). The transverse magnetization may be considered in terms of isochromat components $\underline{G}(x, \phi)$ in the rotating frame, as shown in Fig. 2.2, with time-dependent phase angles ϕ defined with respect to the real u-axis of the complex transverse plane. All isochromat phase information is retained experimentally by using an rf phase sensitive detection scheme, in which the signal S(t) is mixed with a reference signal S_r and integrated over a time interval $t > 1/\Delta\omega$, where $\Delta\omega$ is the rf amplifier bandwidth. This mixing corresponds to a simple multiplication which may be represented in general as

$$S_o(t) = \text{Re}\, S(t) \cdot S_r \quad , \qquad (5.4.2)$$

where $S_o(t)$ is the real output signal and the reference signal is defined in complex form in a fixed frame of reference as

$$S_r = b \cdot \exp -i(\omega_o t + \phi_r) \quad . \qquad (5.4.3)$$

That is, this signal has a frequency equal to the rf pulse irradiating frequency and an associated phase angle ϕ_r which may be adjusted

arbitrarily and is defined with respect to the field $\underline{H}(t)$ defined by $|\underline{H}_1| \exp -i(\omega_o t + \pi/2)$, cf. Eq. (2.1.5), consistent with the assumption that the field vector $\underline{H}_1$ lies along the v-axis of the rotating frame, as previously discussed. The phase sensitive detector effectively references all output frequencies to $\omega = \omega_o$ $(x = 0)$. The time-independent reference field vector $\underline{H}_r$ may be represented in the rotating frame shown in Fig. 2.2 such that

$$S_r = b \exp(i\phi_r). \tag{5.4.4}$$

The output signal for a general complex response S(t) is given in accordance with Eqs. (5.1.4), (5.4.1) and (5.4.2) as†

$$\begin{aligned} S_o(t) &= \mathrm{Re}\{b\, e^{-t/T} \; B_i(\cos\Omega_i t + i \sin\Omega_i t) \;\; \cos\phi_r + i \sin\phi_r\} \\ &= b e^{-t/T} \; B_i \cos\Omega_i t \cos\phi_r - \sin\Omega_i t \sin\phi_r \; . \end{aligned} \tag{5.4.5}$$

For a component decay in Eq. (5.4.5), the Fourier transform of $s_o(t)$ takes the form

$$\begin{aligned} g'(x) \;=\; & \frac{1}{1 + iT_2(x+\Omega)} \;\; (\cos\phi_r - i \sin\phi_r) \\ & + \frac{1}{1 + iT_2(x-\Omega)} \;\; (\cos\phi_r + i \sin\phi_r) \end{aligned} \tag{5.4.6}$$

Therefore, on the frequency interval $0 \; x < \infty$, the complex lineshape function centred at $x = \Omega$ is given in accordance with Eq. (5.1.8) as

---

† For simplicity, it has been assumed that $T_{2i} = T_2$ for all spectral lines.

$$g'(x) = [f(x) - i\,h(x)][\cos\phi_r + i\sin\phi_r]$$

$$= [f(x)\cos\phi_r + h(x)\sin\phi_r] + i[f(x)\sin\phi_r - h(x)\cos\phi_r]$$

$$= f'(x) + i\,h'(x) \qquad (5.4.7)$$

Thus it is shown that the real part of the complex Fourier transform function, f'(x), in general corresponds to a linear combination of Lorentzian absorption and dispersion mode lineshape functions f(x) and h(x) as defined in Eqs. (5.1.2) and (5.1.6), respectively. For the particular case in which the reference field vector is in the direction of the u-axis of the rotating reference frame, $\phi_r = 0$ and from Eqs. (5.4.5) and (5.4.7) it follows that

$$S_o(t) = b\,\exp(-t/T_2)\sum_i B_i\cos\Omega_i t$$

and

$$G'(x) = b\sum_i A_i\left[f_i(x) - i\,h_i(x)\right] ,$$

consistent with the expression derived previously (Eq. (5.1.11)) under the assumption that the free induction decay was determined by u-component nuclear magnetization.

The absorption mode lineshape, f(x), is obtained from Eq. (5.4.7) as

$$f(x) = f'(x)\cos\phi_r + h'(x)\sin\phi_r . \qquad (5.4.8)$$

Both f'(x) and h'(x) are available from a numerical complex Fourier transformation of digitized data in the time domain and hence the phase

angle ϕ_r may be adjusted to define f(x) to an accuracy determined by the criterion used to define the correct absorption mode lineshape. Baseline equalization over specific frequency ranges has been shown to give particularly efficient numerical phase correction. Ernst and Anderson[69] have used an area ratio criterion for this rf phase adjustment.

It has been noted that the highest frequency contained in the response S(t) that can be analyzed using a sampling technique is $x = N/2\tau$ where N is the number of samples in the time domain and τ is the rf pulse repetition period. Higher signal frequencies are down-converted and give rise to spurious spectral lines as determined by a Fourier transformation, and high frequency noise similarly down-converted leads to a degradation of signal-to-noise ratio in the frequency range of interest, $0 < x < N/2\tau$. To minimize these effects, the output from the rf phase sensitive detector, $s_o(t)$, is followed by a low pass filter to attenuate the frequencies $x > N/2\tau$. The filter output signal $s_f(t)$ is then fed to a sampling device and an A-D converter to obtain the final data in digital form. This filter, however, introduces a frequency dependent phase shift which complicates the determination of a correct absorption mode lineshape. The effect of the filter in the time domain is described by a convolution relationship[102] and hence it is more convenient to define the Fourier transform functions $s_o(x)$ and $s_f(x)$ and to consider the effect of the filter in the frequency domain. In this manner

$$s_f(t) = \frac{1}{2\pi}\int_{-\infty}^{+\infty} T(x)\left[\int_{o}^{\infty} s_o(t)\exp(-itx)dt\right]dx,$$

where T(x) is the complex transfer function defining the filter characteristics, such that $s_f(x) = T(x)s_o(x)$. This transfer function may be considered in the form

$$T(x) = D(x)\exp i\theta(x) \tag{5.4.9}$$

so that D(x) determines an attenuation and $\theta(x)$ defines a characteristic frequency dependent phase shift. If it is assumed that the sampling device does not introduce a further frequency dependent attenuation or phase shift, the Fourier transform of the filtered signal may be considered equivalent to $g'_+(x)$. Therefore, in accordance with Eqs. (5.4.7) and Eq. (5.4.9), $s_f(x)$ is given by

$$\begin{aligned} s_f(x) &= f'(x) + i\, h'(x) \\ &= D(x)\left[f(x) - i\, h(x)\right]\left[\cos(\theta(x) + \phi_r) + i \sin(\theta(x) + \phi_r)\right] \end{aligned} \tag{5.4.10}$$

and the absorption mode function f(x) is now given in general form as

$$\begin{aligned} f(x) = D^{-1}(x)\{&\left[f'(x)\cos\theta(x) + h'(x)\sin\theta(x)\right]\cos\phi_r \\ &-\left[f'(x)\sin\theta(x) - h'(x)\cos\theta(x)\right]\sin\phi_r\}. \end{aligned} \tag{5.4.11}$$

The transfer function for a single section low-pass RC filter[102] is

$$T(x) = \frac{1}{1 + ix\,RC} \tag{5.4.12}$$

and hence $D(x) = \left[1 + (xRC)^2\right]^{-\frac{1}{2}}$, $\cos\theta(x) = D(x)$ and $\sin\theta(x) = -xRCD(x)$. For this particular filter, f(x) is independent of D(x) and from

Eq. (5.4.11) it follows that

$$f(x) = \left[f'(x)\cos\phi_r + h'(x)\sin\phi_r\right] + xRC\left[f'(x)\sin\phi_r - h'(x)\cos\phi_r\right]. \tag{5.4.13}$$

This expression allows a simple evaluation of the corrected absorption mode lineshape in terms of the complex Fourier transform functions f'(x) and h'(x), the reference rf phase angle ϕ_r and the filter parameter RC. This latter parameter may be empirically varied over a small range to obtain an improved lineshape from numerical Fourier transform data obtained experimentally using a standard sampling device incorporating a low-pass filter. The effect of filter and rf reference phasing is illustrated in Fig. 5.3 for a representative Lorentzian lineshape defined by Ω = 100 Hz and T_2 = 0.1 sec. (3.2 Hz full-width at half-maximum). The off-resonance shift of 100 Hz ensures that transform overlap distortion, as discussed in section 5.2 is minimal. The specific RC filter time constant is 0.001 sec., corresponding to a cut-off frequency of 160 Hz. The real and imaginary parts of the Fourier transform $s_f(x)$ are shown in Fig. 5.3a, the free induction decay function s(t) being defined by 1024 data points over a time interval of 0.64 sec. With a computational sub-harmonic multiplicity of four the data points shown in the frequency domain have a separation of 0.39 Hz, the corresponding fundamental frequency being 1.56 Hz. The filter frequency dependent phase correction determines the real function f'(x) shown in Fig. 5.3b, and an additional frequency independent rf reference phase correction of -20° determines the final Lorentzian absorption mode lineshape shown in Fig. 5.3c. The single section RC filter gives an attenuation of -3dB at the cutoff frequency $x_c = (2\pi RC)^{-1}$ Hz and

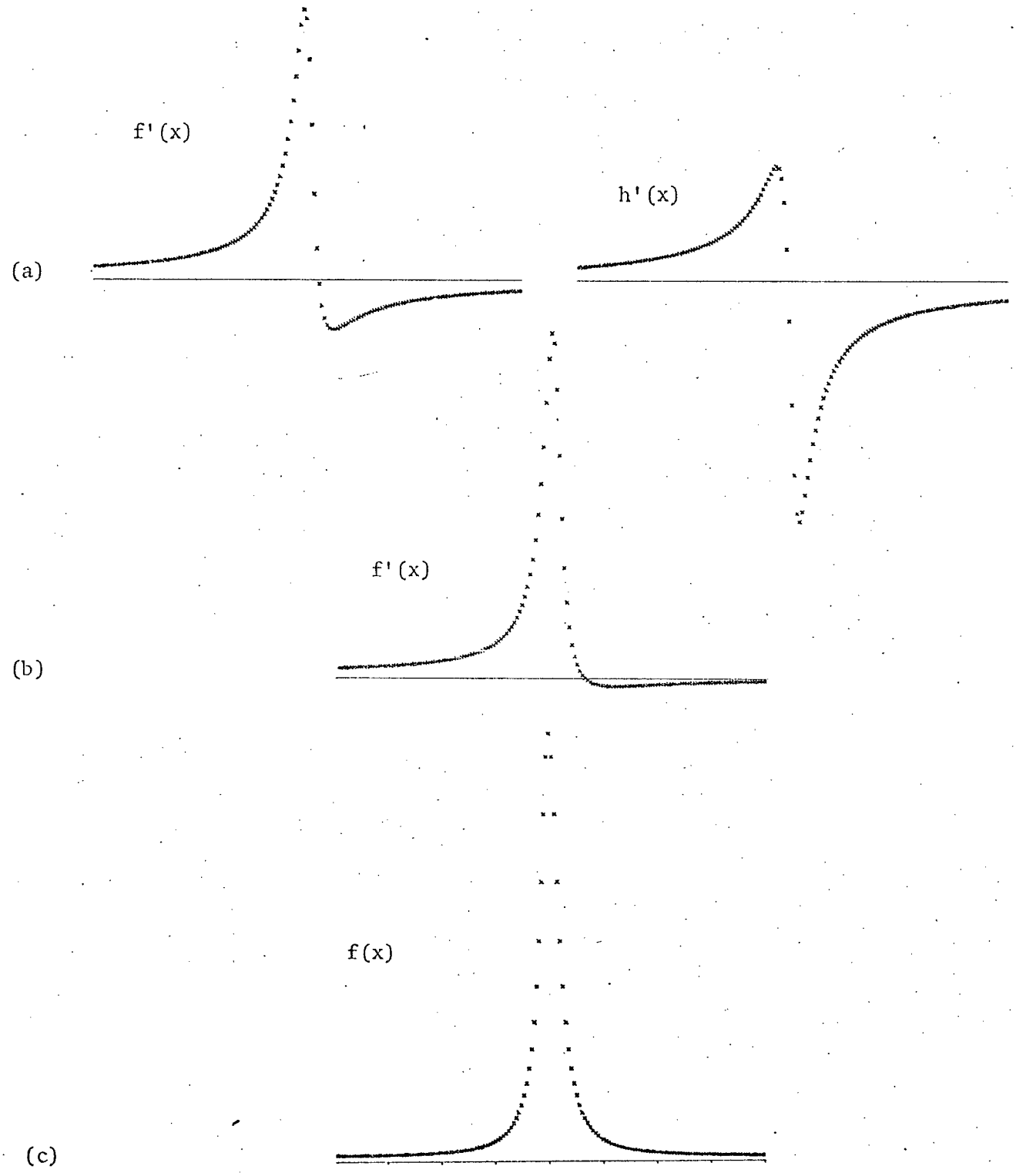

Figure 5.3 Filter and rf reference phase corrections for a Lorentzian lineshape system.

-40 dB at $x_\ell = 100x_c$. An increased attenuation of -80 dB at the frequency x_ℓ is obtained by using a two-section RC filter, each section being matched and isolated, with a transfer function

$$T(x) = \frac{(1-w^2) - i2w}{(1+w^2)^2} \tag{5.4.14}$$

where $w = xRC$ and $D(x) = (1 + w^2)^{-1}$, $\cos\theta(x) = (1 - w^2)D(x)$ and $\sin\theta(x) = -2wD(x)$. Again $f(x)$ is shown to be independent of $D(x)$ and in this case

$$f(x) = (1 - w^2)\left[f'(x)\cos\phi_r + h'(x)\sin\phi_r\right] + 2w\left[f'(x)\sin\phi_r - h'(x)\cos\phi_r\right]. \tag{5.4.15}$$

In general, experimentally, it is not possible to obtain the response $s(t)$ for $t \to 0$ because of the finite receiver recovery time following a $\pi/2$-pulse during which the free induction decay signal is not observable, and hence the function $s(t)$ is to be considered on the interval $t_o \leq t < \infty$. The time shift[103] $t_o > 0$ corresponds to a phase shift in the frequency domain which may be considered in terms of the Fourier transform of a modified response $p(t')$ defined, on the interval $0 \quad t' < \infty$, to be equivalent to $s(t)$ for $t_o \leq t < \infty$, that is,

$$\begin{aligned} s_m(x) &= \int_0^\infty p(t') \exp(-ixt')\, dt' \qquad , \quad t' = t - t_o \\ &= \exp(ixt_o) \int_{t_o}^\infty s(t) \exp(-ixt)\, dt \\ &\simeq \exp(ixt_o)\, s(x) \end{aligned} \tag{5.4.16}$$

where $s(x)$ is the Fourier transform of $s(t)$ as defined on the normal interval $0 \leq t < \infty$. By again considering the Fourier transform function

$s_m(x)$ as equivalent to $g'_+(x)$ in Eq. (5.4.7), it follows that $f(x)$ is given in terms of the frequency dependent phase shift xt_o by

$$f(x) = f'(x)\cos xt_o + h'(x)\sin xt_o. \qquad (5.4.17)$$

It is to be noted that all phase shifts involved in the evaluation of phase corrected lineshapes may now be combined as $\phi_t = \phi_r + \theta(x) + xt_o$, so that

$$g'(x) = f'(x) + i\,h'(x)$$

$$f(x) = f'(x)\cos\phi_t + h'(x)\sin\phi_t$$

and

$$h(x) = f'(x)\sin\phi_t - h'(x)\cos\phi_t. \qquad (5.4.18)$$

The definition of ϕ_t may be extended to include any additional phase factors.

In liquids under high resolution conditions the relaxation times T_1 and T_2 are of the order of seconds and the normal $\pi/2$-pulse widths used are 10 - 100 μsec. An average receiver recovery time is 10 μsec., and hence the phase factor xt_o over a frequency range of 1 kHz for ^{1}H NMR is negligible. For ^{13}C NMR involving chemical shifts (and hence spectral widths) of the order of 10 kHz, however, this factor may not be neglected. In solids with much shorter relaxation times, this phase factor becomes very significant as the spectral frequency width is extended by up to three orders of magnitude. Also, the above approximate linear phase correction may not be adequate when t_o becomes significant with respect to T_2 which defines the total signal sampling time. In the latter case it is possible to use

a $\pi/2$-πpulse sequence with a pulse separation $\tau < T_2$[104] and to sample the spin echo centred at $t = 2\tau$. The Fourier transform of $s(t')$ is obtained for $0 \leq t' < \infty$, as $t' = 0$ now corresponds to $t = 2\tau$, and it is well known that the spin echo signal on this interval is equivalent to the normal free induction decay.

The phase effect corresponding to the response $s(t)$ being undefined for $0 \leq t < t_o$ has been treated numerically, and is illustrated in Fig. 5.4 for the representative Lorentzian lineshape defined by $\Omega = 100$ Hz and $T_2 = 0.1$ sec., cf. Fig. 5.3. The free induction decay, $s(t)$, associated with a $\pi/2$-pulse width of $\simeq 1$ msec. was defined by 1024 data points over a time interval of 640 msec. with $t_o = 1$ msec. Fig. 5.4a shows the Fourier transform function $f'(x)$, cf. Eq. (5.4.17), with the frequency domain sub-harmonic data f points separated by 0.39 Hz. A linear frequency dependent phase correction as given by Eq. (5.4.17) determines the absorption mode lineshown in Fig. 5.4b, where the phase factor xt_o takes the value 36° at a frequency of 100 Hz. The small negative deviation, as compared with the correct lineshape shown in Fig. 5.4d, is presumably due to the integral approximation involved in Eq. (5.4.16). It is now interesting to compare the above absorption mode lineshape with that shown in Fig. 5.4c obtained by using a frequency independent phase correction, cf. Eq. (5.4.8). The correction angle, as defined by a baseline equalization in a determination of the correct lineshape, is $+36^\circ$. In general, however, for a series of spectral lines over an extended frequency range, the linear phase correction must be applied.

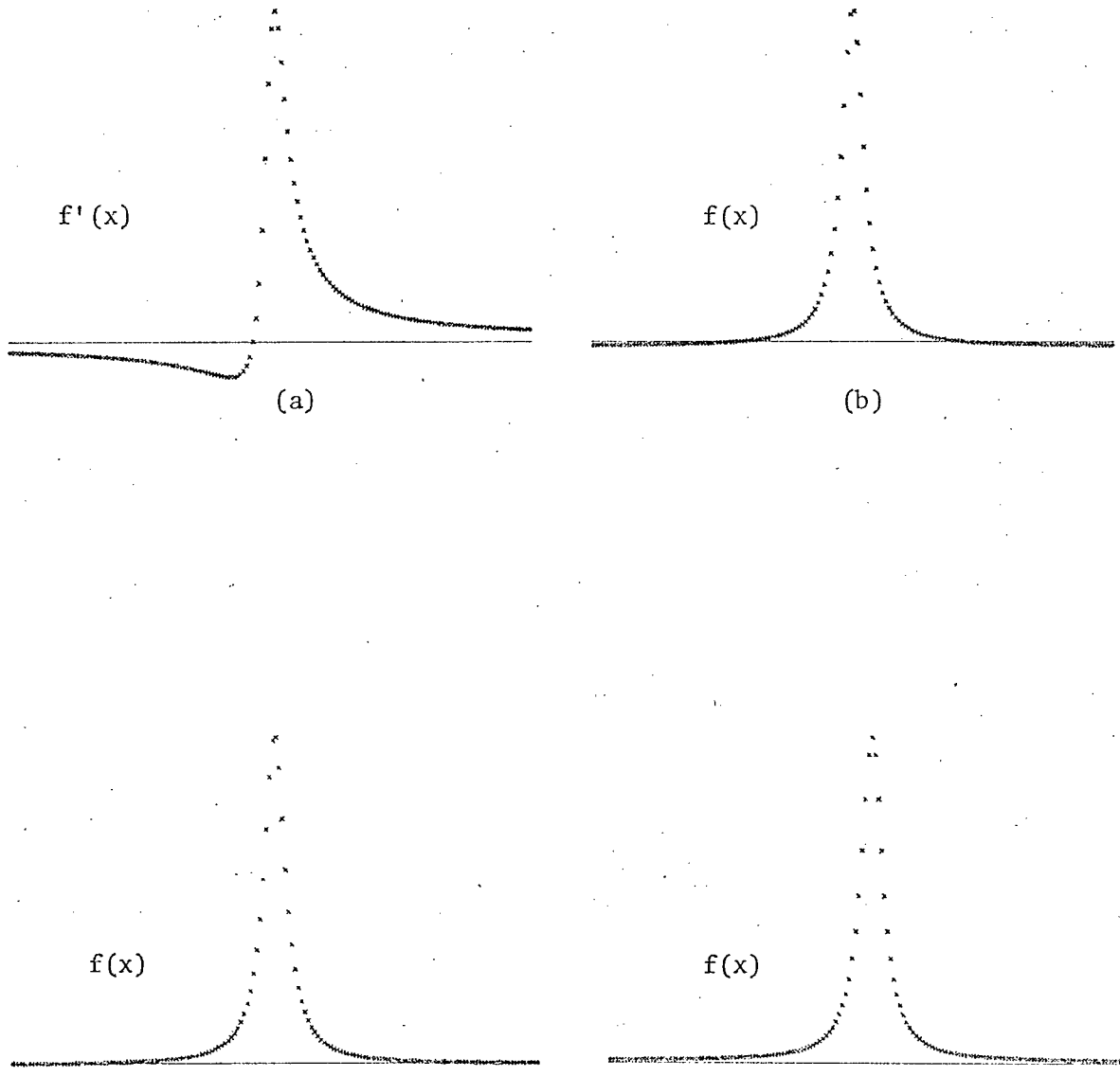

Figure 5.4 Linear frequency dependent phase correction for a Lorentzian lineshape system.

In general, a phase correction as given in terms of Eqs. (5.4.8) and (5.4.17) involves an iterative numerical fitting of the absorption mode lineshape to self-consistency as defined by a specific criterion for a correct lineshape. The phase independent part of the complex lineshape function g(x), cf. Eq. (5.1.8), may be considered to be defined by an amplitude function[106] A(x), where

$$g(x) = A(x)\exp(i\theta(x)) \qquad (5.4.18)$$

with $A(x) = [f^2(x) + h^2(x)]^{\frac{1}{2}}$ and $\theta(x) = \tan^{-1}[-h(x)/f(x)]$. Now, for a general Fourier transform lineshape function g'(x) with an arbitrary phase factor, cf. Eq. (5.4.18), it is shown that $f^2(x) + h^2(x) \equiv f'^2(x) + h'^2(x)$; that is, the amplitude function is simply derived from the numerical Fourier transform functions f'(x) and h'(x). Furthermore, for a Lorentzian lineshape as defined in Eqs. (5.1.2) and (5.1.6), it is seen that the absorption mode function is given directly as $f(x) = A^2(x)$. In this particular case, a very simple effective phasing correction is obtained by evaluating f(x) directly, as illustrated in Fig. 5.5 for the standard Lorentzian lineshape previously described with an associated phase angle of 20^o at a frequency of 100 Hz. Numerical Fourier transform functions are shown in Fig. 5.5a, illustrating the phasing error involved. As usual, the frequency domain data point separation is 0.39 Hz. Figs. 5.5b and 5.5c show the amplitude functions A(x) and $A^2(x)$, respectively, where the latter has been re-normalized to the maximum value defined by A(x). It is seen that A(x) takes the form of a modified Lorentzian lineshape with an increased full-width at half-maximum of $2\sqrt{3}\ T_2^{-1}$ rad. $sec.^{-1}$. The numerically derived function $A^2(x)$ is a very good

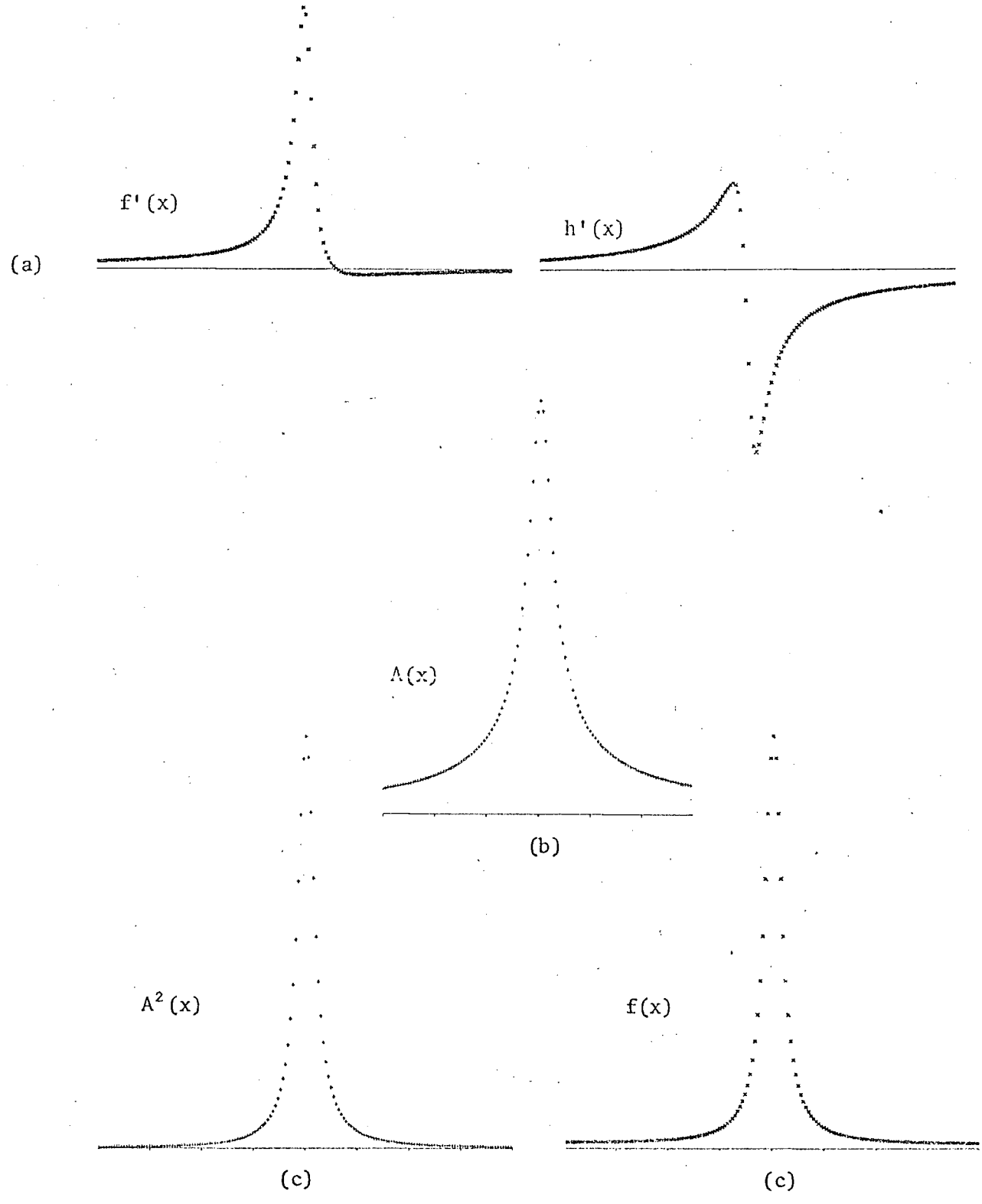

Figure 5.5. Amplitude function and phase correction for a Lorentzian line-shape system.

approximation to an exact Lorentzian absorption mode lineshape in that the deviation at x = 93.6 Hz (two linewidths from the centre frequency) is less than 2% and this frequency corresponds to an intensity approximately 4% of the maximum. This lineshape may be compared with that shown in Fig. 5.5d as obtained using the full phase corrections previously described.

With regard to effective line-width reduction and intensity enhancement leading to increased spectral resolution through numerical methods, modified Lorentzian absorption mode functions may be defined in general by

$$f_n(x) = A^{2n}(x) = A^n \left\{ \frac{1}{[1 + T_2^2(x-\Omega)^2]^n} \right\} \qquad (5.4.19)$$

with n = 1, 2, ··· and A a normalization constant for the normal lineshape function (n = 1). These modified functions have ideal spectral lineshape characteristics in that they are symmetric about x = Ω, they do not have zeros, the effective line-width decreases with increasing n and the signal-to-noise ratio is improved when this ratio is greater than unity. For n = 2 and 4, the full line-widths are given as $1.28T_2^{-1}$ and $0.84T_2^{-1}$, respectively, as compared with the normal Lorentzian width of $2T_2^{-1}$ rad. sec.$^{-1}$. The numerical resolution enhancement as determined by the functions $f_2(x)$ and $f_4(x)$ is illustrated in Fig. 5.6 for two Lorentzian lines centred at x = -Ω and x = Ω and for varying values of the parameter ΩT_2. Resolution in the above two-line spectrum may be defined in terms of the ratio of maximum intensity to the intensity at x = 0. For $\Omega T_2 = 0.16$, corresponding to a line separation of a full line-width, this ratio is 1.3 for n = 1 and 2.1 for n = 4, giving a fractional ratio increase of 1.6

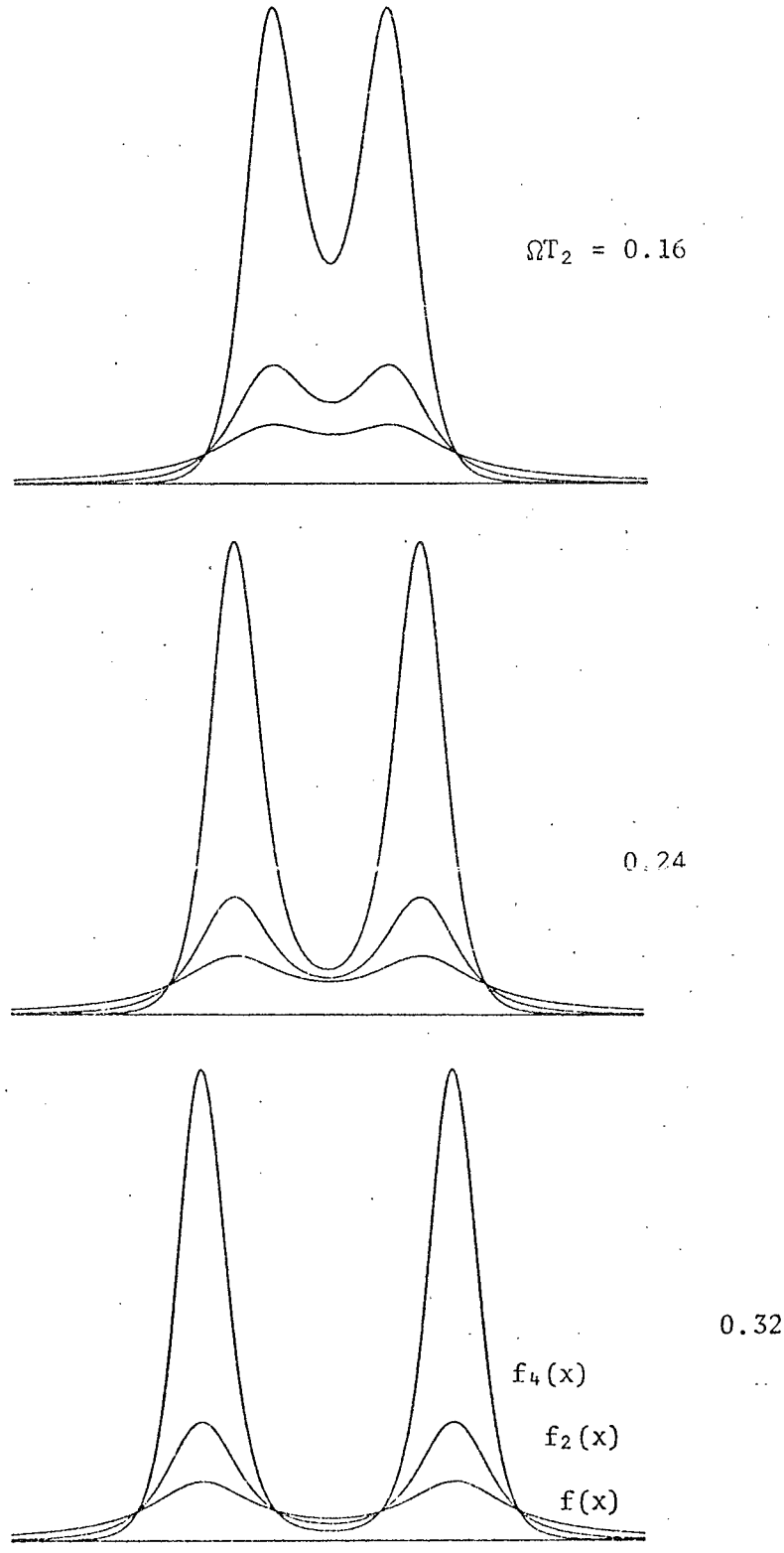

Figure 5.6 Resolution enhancement, modified Lorentzian lineshape system.

for the modified function $f_4(x)$. This fractional ratio increase is 6 for $\Omega T_2 = 0.24$ and 18 for $\Omega T_2 = 0.32$.

To determine the general validity of an effective phase correction through the evaluation of the amplitude function A(x), the Gaussian function may be considered as an example of a lineshape function with different characteristics as compared with the Lorentzian function. The absorption mode Gaussian lineshape function, cf. Eq. (2.1.13), may be considered in the form

$$f(x) = A \exp(-\tfrac{1}{2}T_2^2(x - \Omega)^2), \tag{5.4.20}$$

with all parameters defined as previously. The full-width at half-maximum is $2(2\ell n2)^{\frac{1}{2}}T_2^{-1}$ rad. sec.$^{-1}$. The corresponding dispersion mode function may be evaluated in terms of the inverse Fourier transform $\tilde{f}(t)$ by a contour integration, given in Appendix 2, as

$$\begin{aligned} h(x) &= A\frac{2}{\sqrt{\pi}} \exp(-\tfrac{1}{2}T_2^2(x-\Omega)^2) \int_0^{\frac{T_2(x-\Omega)}{\sqrt{2}}} \exp(\eta^2)\, d\eta \\ &= A\frac{2}{\sqrt{\pi}} \left\{ \int_0^{\frac{T_2(x-\Omega)}{\sqrt{2}}} \exp(\eta^2)\, d\eta \right\} f(x) \end{aligned} \tag{5.4.21}$$

in accordance with the general complex lineshape function defined in Eq. (5.1.8). These Gaussian functions are shown in Fig. 5.2b, as determined by a numerical Fourier transformation of the response s(t), where

$$s(t) = B \exp(-t^2/2T_2^2)[\cos\Omega t + i \sin\Omega t] \tag{5.4.22}$$

cf. Eq. (5.1.4). From Eqs. (5.4.20) and (5.4.21), it follows that

$$f(x) = A(x)\left\{1 + \frac{4}{\pi}\left[\int_0^{\frac{T_2(x-\Omega)}{\sqrt{2}}} \exp(\eta^2)\,d\eta\right]^2\right\}^{-\frac{1}{2}}$$

and hence the absorption mode function is not given simply in terms of A(x). As the integral term is symmetric in x about $x = \Omega$, A(x) defines a modified Gaussian lineshape with an increased line-width. This is shown numerically for $T_2 = 0.1$ sec. in that the normal full-width at half-maximum is 3.7 Hz (cf. 3.2 Hz for a Lorentzian function) and the full-width for the lineshape described by A(x) is 6.8 Hz. Thus, in general, it is possible to use the function $A^2(x)$ as an approximation to an absorption mode lineshape only for spectral lines closely described by a Lorentzian lineshape function, as is the case for high resolution NMR in liquids.

5.5 Signal Zero Correction.

In pulsed mode NMR, a signal voltage following phase-sensitive detection, filtering and dc amplification may be represented by

$$s'(t) = C + s(t), \qquad (5.5.1)$$

where s(t) is the free induction decay signal and C is a constant voltage, in general different from zero. A sufficient condition for the existence of a Fourier transform of s'(t) is absolute integrability, $\int_{-\infty}^{+\infty} |s'(t)|\,dt < \infty$, and the constant C does not satisfy this condition. It is readily shown, however, that the inverse Fourier transform of $2\pi C\delta(x)$ (with $\delta(x)$ the Dirac delta function) is simply the constant C. This implies that C is associated with an analytic approximation[105] to $\delta(x)$ in the frequency domain. That is, the Fourier transform of C,

c(x), may be considered in the form

$$c(x) = C\int_{-\infty}^{+\infty}\exp(-itx)dt$$

$$= C\lim_{t_m\to\infty}\left\{\frac{2}{t_m}\left[\frac{\sin t_m x}{t_m x}\right]\right\} \qquad (5.5.2)$$

The parameter t_m defines the limits of integration for a finite complex Fourier transformation as considered in section 5.3. The above equation defines an oscillatory function with a maximum value $2Ct_m$ at $x = 0$ and zeroes at $x_n = n\pi/t_m$ rad. sec.$^{-1}$ for $n = 1, 2, \cdots$ on the interval $0 \leq x \leq t_m$. As c(x) is real, the general Fourier transform of s'(t) may be expressed in the form

$$g'(x) = \left[c(x) + f'(x)\right] + i\,h'(x), \qquad (5.5.3)$$

cf. Eq. (5.4.18).

If the off-resonance shifts $\Omega_i > 0$ are minimized as described in section 5.2, the function c(x) may give rise to an oscillation with a frequency dependent amplitude superimposed on a spectral lineshape of interest. This effect is illustrated in Fig. 5.7 for a representative Lorentzian lineshape defined by $\Omega = 40$ Hz and $T_2 = 0.1$ sec. The signal s'(t) as determined by 1024 data points over an interval of 0.64 sec. is shown in Fig. 5.7a, where $s'(t) = 2.0 + 10.0\exp(-t/T_2)\cos\Omega t$. The absorption mode numerical Fourier transform function, c(x) + f'(x), is defined in Fig. 5.7b by data points separated by the sub-harmonic frequency 0.39 Hz. The superposition of c(x) is clearly shown over the frequency range 0 to 65 Hz, the constant C being 20% of the maximum value of the free induction decay signal.

The constant C is readily determined as the mean signal level

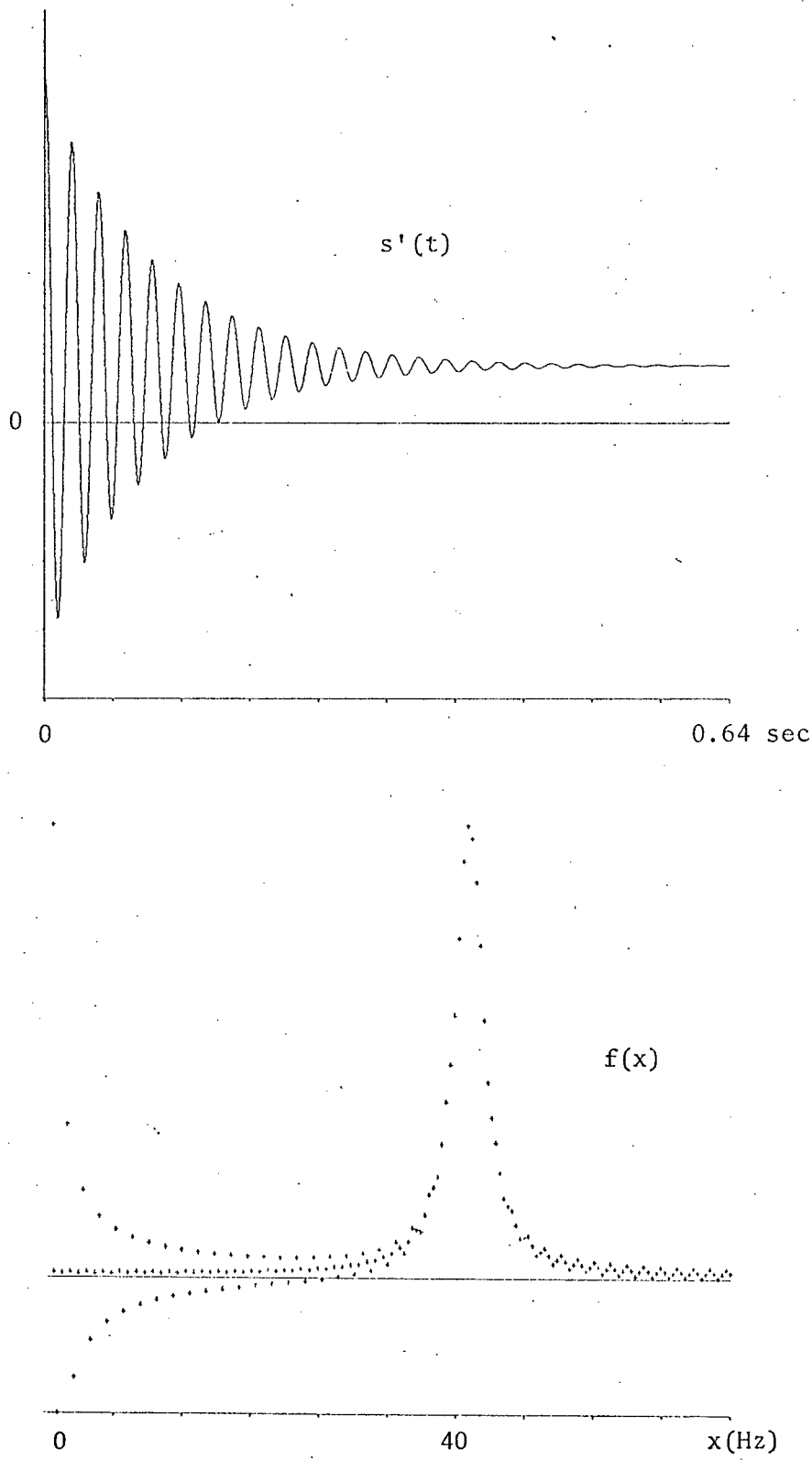

Figure 5.7 Numerical Fourier transform distortion due to non-zero average signal level.

for $t \rightarrow T$, T being the sampling time interval. A numerical correction of -C may then be applied to the sampled signal data to obtain a good approximation to the signal function s(t). A numerical Fourier transformation of s(t) then gives f'(x) and h'(x) as required for the general phase corrections discussed in the preceding section. This method for a signal zero correction has been shown to be both reliable and efficient by using a subroutine DIRCON in the FORTRAN program LGTRN previously outlined.

5.6 High Resolution Fourier Transform NMR

The basic concepts and computational methods involved in a Fourier transform NMR experiment have been considered in detail in the preceding sections of this thesis, with particular emphasis upon the possibility of using this technique for quantitative lineshape studies.

As an example high resolution application, the spectrum of dimethyl nitrosamine has been obtained at a relatively low H_0 field corresponding to an operating frequency of 10.0 MHz. This particular spin system was chosen because of the simplicity of the chemically shifted equal intensity doublet spectrum and the magnitude of the chemical shift,: 45 Hz at 60 MHz and 30°C. As the pulse spectrometer described in section 3.2 was designed specifically for ^{13}C studies in a field of 9.4 kgauss, it was also convenient to use the above operating frequency for ^{1}H NMR. The sample was prepared as an 8% CCl_4 solution, the solvent carbon tetrachloride being used to eliminate the large background l solvent ^{1}H signal as obtained in the non-selective pulsed NMR experiment. This sample in a 5mm od tube was degassed using the usual freeze-pump thaw cycles.

The free induction decay signal following phase sensitive detection was sampled using a FABRITEK FT-1064 A-D converter with a filtering time constant of 50 μsecs, the digital data corresponding to 12-bit amptitude resolution. The off-resonance shift, which is necessary to prevent the lineshape distortions described in section 5.2, was adjusted to be 27 Hz using a frequency synthesiser while the Ho field stability was maintained by a VARIAN flux super-stabiliser.

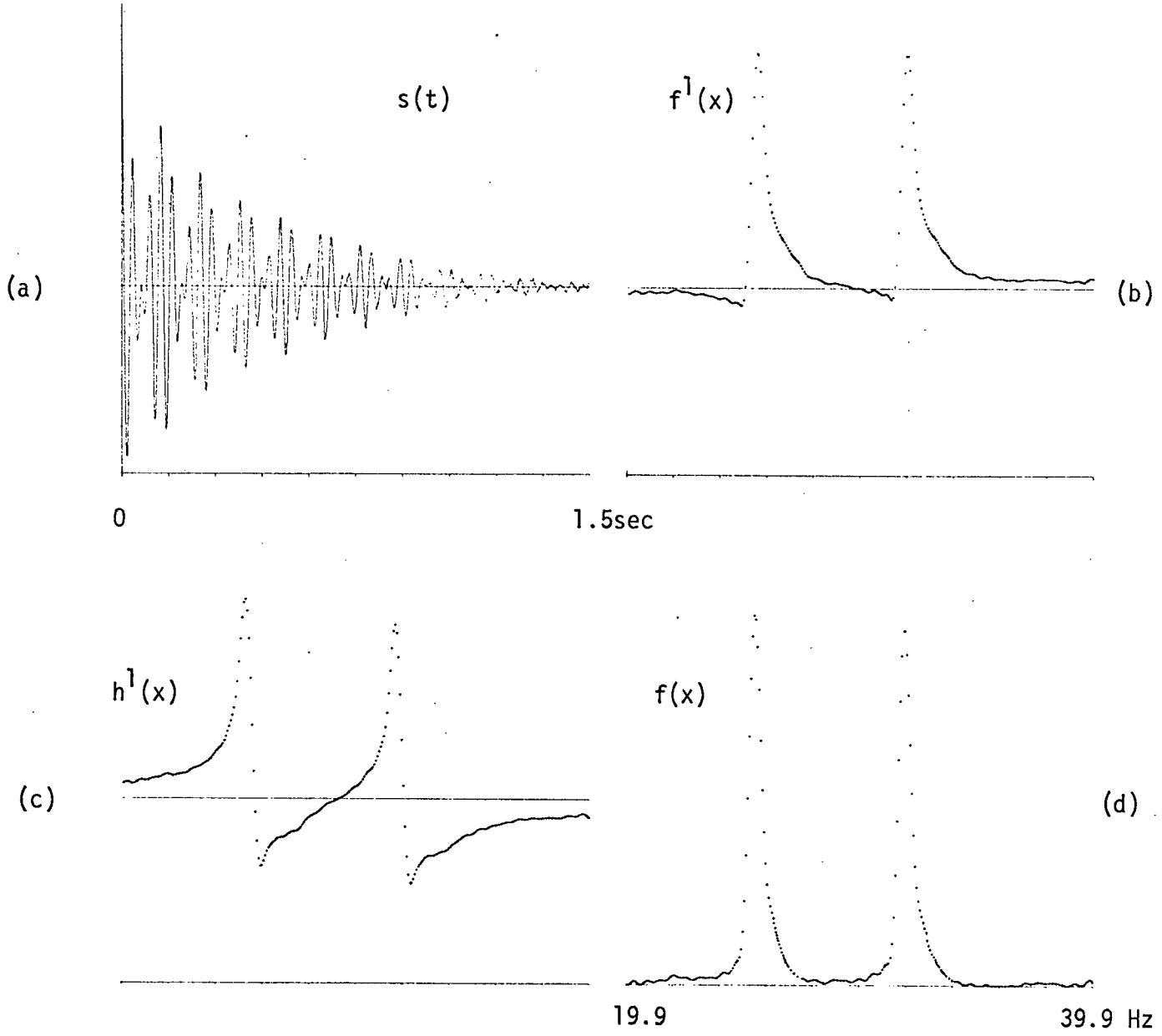

Fig. 5.8 Free induction decay and finite Fourier transform spectrum for dimethyl nitrosamine.

The resultant free induction decay signal slt, following a function zero correction as discussed in section 5.5, is plotted in Fig. 5.12(a) over a time interval of 1.5 secs.. Using the computer program hGTRN, the real and imaginary parts of the finite complex Fourier transform function are shown in Fig. 5.12(b) and (c), respectively. Through sub-harmonic analysis as described in section 5.3, the frequency spacing of the output data points is reduced to 0.08 Hz using a sub-multiplicity of 8 and 8192 transform data points. In this manner the relatively narrow lines are well defined by at least twenty data points. For the optimal filter time constant used a frequency dependent phase correction, of section 5.4, was not required. However, the reference of phase correction used to produce the final absorption mode spectrum shown in Fig. 5.12(d) was computed as $+20.5^{o}$. This spectrum consists of 288 data points on the frequency interval $19.9 < x < 39.9$ Hz, and the chemical shift is determined as 7.57 ± 0.08 Hz. The corresponding linewidth at half-maximum is 0.7 Hz, the small distortion of the line-shape being due to the form of the Ho field inhomogeneity which is very difficult to adjust by observing the free induction decay in the high resolution NMR limit.

Thus it has been shown that a spectrum of a quality which is at least comparable with that obtained from the tedious slow passage steady-state technique may be very readily obtained using the relatively rapid Fourier transform technique. Furthermore, all data is a convenient form for further processing on a digital computer.

APPENDIX 1

Lorentzian Fourier Transform Pair.

Consider the Lorentzian lineshape function f(x), defined on the interval $-\infty < x < \infty$ in terms of the real variable x, expressed in the form

$$f(x) = \frac{k^2}{k^2 + (x-\omega)^2} \quad , \; k > 0$$

where $k = 1/T_2$. The corresponding complex function, f(z), given in terms of the complex variable $z = x + iy$, has simple poles at $z = \Omega \pm ik$. These are shown, for $\Omega > 0$, in the z-plane as

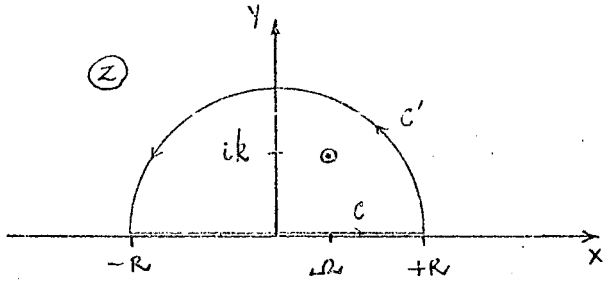

The inverse Fourier transform of f(z), $\tilde{f}(t)$, may be considered in terms of the real variable $t \geq 0$. The function $\tilde{f}(t)$ is then defined by a contour integration

$$\tilde{f}(t) = \frac{1}{2\pi} \int_C f(z) \exp(itz)\, dz$$

$$= \frac{k^2}{2\pi} \left\{ \int_{-R}^{+R} \frac{\exp(itx)\, dx}{k^2 + (x-\omega)^2} + \int_{C'} \frac{\exp(itz)\, dz}{k^2 + (z-\omega)^2} \right\}$$

where C' is the contour shown as part of the closed contour C in the upper-half-plane. In the limit $R \to \infty$, it can be shown that

$$\int_C f(z)\exp(itz)dz = k^2 \int_{-\infty}^{+\infty} \frac{\exp(itx)dx}{k^2 + (x-\Omega)^2}$$

The residue for $f(z)\exp(itz)$ at the simple pole $z = \Omega + ik$ is given as

$$R(\Omega+ik) = \lim_{z\to\Omega+ik} \left\{ \frac{[z-(\Omega+ik)]k^2 \exp itz)}{[(z-\Omega)+ik][(z-\Omega)-ik]} \right\}$$

$$= \frac{1}{2i} \; k \; \exp\,[-(k-i\Omega)t]$$

and in accordance with Cauchy's integral formula

$$\frac{1}{2\pi}\int_C f(z)\exp(itz)dz = 2iR(\Omega + ik)$$

$$= \frac{k}{2} \; \exp\left[-(k - i\Omega)t\right].$$

Thus it follows that the inverse Fourier transform is given as

$$\tilde{f}(t) = \frac{1}{2T_2} \; \exp\,[-(\frac{1}{T_2} - i\Omega)t] \quad ,$$

corresponding to

$$f(x) = \frac{1}{1 + T_2^2(x-\Omega)^2}$$

Now consider the Lorentzian lineshape function $h(x)$, defined on the interval $-\infty < x < \infty$, expressed in the form

$$h(x) = \frac{k(x-\Omega)}{k^2 + (x-\Omega)^2} \quad , k > 0.$$

The inverse Fourier transform $\tilde{h}(t)$ is defined by a contour integration similar to that described above, where the residue for $h(z)\exp(itz)$ at the simple pole $z = \Omega + ik$ is determined as

$$R(\alpha+ik) = \tfrac{1}{2}\, k \exp\,[-(k-i\Omega)t].$$

Thus it follows that the inverse Fourier transform is given as

$$\tilde{h}(t) = i\,\tfrac{1}{2}\sqrt{T_2}\,\exp\,[-(\frac{1}{T_2} - i\Omega)t]$$

corresponding to

$$h(x) = \frac{T_2(x-\Omega)}{1 + T_2^2(x-\Omega)^2}$$

APPENDIX 2

Gaussian Fourier Transform Pair.

Consider the function s(t), defined on the interval $0 \quad t < \infty$ in terms of the real variable t, in the form

$$s(t) = \exp\left[-\left(\frac{k^2t^2}{2} - i\omega t\right]\right.$$

where $k = 1/T_2$. The Fourier transform of s(t), g(x), is given in terms of the real variable x on the interval $-\infty < x < \infty$ by

$$g(x) = \int_0^\infty s(t)\, \exp(-itx)\, dt$$

$$= \int_0^\infty \exp\left[-\left\{\frac{k^2t^2}{2} + i(x-\omega)t\right]\right. dt$$

This integral may be evaluated through a contour integration $\int_C \exp(-z^2)dz$, where the complex variable may be defined as $z = \varepsilon + i\eta$ and the closed contour C in the z-plane is considered as shown below:

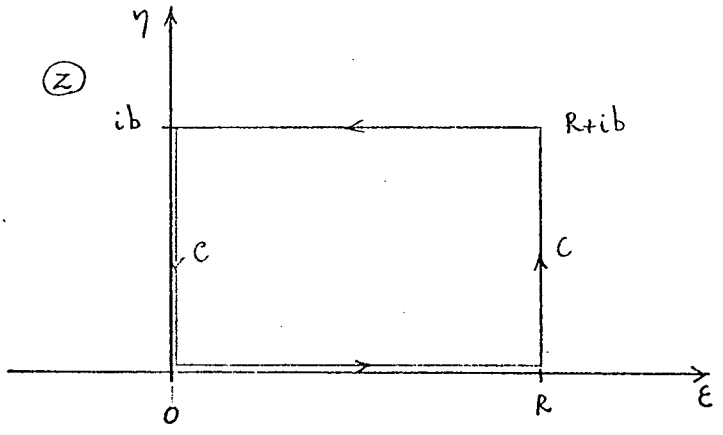

For the above contour, Cauchy's integral theorem gives

$$\int_C \exp(-z^2)\,dz = 0,$$

and hence

$$\int_0^R \exp(-\varepsilon^2)\,d\varepsilon + i\int_0^b \exp\left[-(R+i\eta)^2\right]d\eta + \int_R^0 \exp\left[-(\varepsilon+ib)^2\right]d\varepsilon + i\int_b^0 \exp(\eta^2)\,d\eta = 0$$

Thus in the limit $R \to \infty$, it is shown that

$$\exp(b^2)\int_0^\infty \exp\left[-(\varepsilon^2+2ib\varepsilon)\right]d\varepsilon = \int_0^\infty \exp(-\varepsilon^2)\,d\varepsilon - i\int_0^b \exp(\eta^2)\,d\eta$$

The first integral on the right hand side is a gamma function, and in the general case it follows that

$$\int_0^\infty \exp\left[-(\varepsilon^2+2ib\varepsilon)\right]d\varepsilon = \exp(-b^2)\left\{\frac{\sqrt{\pi}}{2} - i\int_0^b \exp(\eta^2)\,d\eta\right.$$

The required integrand is now given by the substitution

$$\varepsilon = \frac{1}{\sqrt{2}}\,kt, \quad b = \frac{(x-a)}{\sqrt{2}\,k}$$

and hence

$$g(x) = \frac{\sqrt{2}}{k}\exp\left[-\frac{(x-\omega)^2}{2k^2}\right]\left\{\frac{\sqrt{\pi}}{2} - i\int_0^{\frac{(x-\omega)}{\sqrt{2}k}} \exp(\eta^2)\,d\eta\right.$$

The Gaussian lineshape functions $f(x)$ and $h(x)$ are now given, in

accordance with the definition of the general complex lineshape function $g(x) = f(x) - ih(x)$, as

$$f(x) = A\exp\left[-\tfrac{1}{2}T_2^2(x - \Omega)^2\right]$$

and

$$h(x) = A\exp\left[-\tfrac{1}{2}T_2^2(x - \Omega)^2\right].\frac{2}{\sqrt{\pi}}\int_0^{\frac{T_2(x-\Omega)}{\sqrt{2}}}\exp(\eta^2)\,d\eta,$$

where A is a normalization constant. These functions define the inverse Fourier transform $s(t)$ in the form

$$s(t) = \exp\left[-t/(2T_2^2) - i\Omega t\right] \quad .$$

REFERENCES

1. N. Bloemburgen, E. M. Purcell and R. V. Pound, Phys. Rev., 73, 679, 1948.
2. F. Bloch, Phys. Rev., 70, 460, 1946.
3. H. S. Gutowsky, D. McCall and C. P. Slichter, J. Chem. Phys. 21, 279, 1953.
4. H. S. Gutowsky and A. Saika, J. Chem. Phys. 21, 1688, 1953.
5. E. L. Hahn and D. E. Maxwell, Phys. Rev., 88, 1070, 1952.
6. H. M. McConnell, J. Chem. Phys. 28, 430, 1958.
7. P. W. Anderson, J. Phys. Soc. Japan, 9, 316, 1954.
8. R. Kubo, J. Phys. Soc. Japan, 9, 935, 1954.
9. R. Kubo, "Fluctuation, Relaxation and Resonance in Magnetic Systems" D. ter Haar, ed., Oliver & Boyd, London, p. 23, 1962.
10. R. C. Tolman, "Principles of Statistical Mechanics", O.U.P., London, p. 424, 1930.
11. U. Fano, Rev. Mod. Phys., 29, 74, 1957.
12. C. P. Slichter, "Principles of Magnetic Resonance" Harper, N.Y., p. 127, 1964.
13. A. Abragam, "The Principles of Nuclear Magnetism" O.U.P., London, p. 276, 1962.
14. J. I. Kaplan, J. Chem. Phys. 28, 278, 1958.
15. J. I. Kaplan, J. Chem. Phys. 29, 462, 1958.
16. S. Alexander, J. Chem. Phys., 37, 967, 1962.
17. S. Alexander, J. Chem. Phys., 37, 974, 1962.
18. S. Alexander, J. Chem. Phys., 38, 1787, 1963.

20. R. K. Wangsness and F. Bloch, Phys. Rev., 87, 728, 1953.

21. F. Bloch, Phys. Rev., 102, 104, 1956.

22. F. Bloch, Phys. Rev., 105, 1206, 1957.

23. C. S. Johnson, J. Chem. Phys., 41, 3277, 1964.

24. C. S. Johnson and J. C. Tully, J. Chem. Phys., 40, 1744, 1964.

25. G. Binsch, J.A.C.S., 91, 1304, 1969.

26. R. P. Feynman, Phys. Rev., 84, 108, 1957.

27. D. W. Woessner, J. Chem. Phys., 35, 41, 1961.

28. L. W. Reeves and E. J. Wells, Disc. Far. Soc., 34, 177, 1962.

29. E. L. Hahn, Phys. Rev., 80, 580, 1950.

30. A. Y. Carr and E. M. Purcell, Phys. Rev., 94, 630, 1954.

31. S. Meiboom and D. Gill, Rev. Sci. Instr., 29, 688, 1958.

32. Z. Luz and S. Meiboom, J. Chem. Phys., 39, 366, 1963.

33. M. Bloom, L. W. Reeves and E. J. Wells, J. Chem. Phys., 42, 1615, 1965.

34. J. G. Powles and J. H. Strange, Mol. Phys., 8, 169, 1964.

35. A. Allerhand and H. S. Gutowsky, J. Chem. Phys., 41, 2115, 1964.

36. A. Allerhand and H. S. Gutowsky, J. Chem. Phys., 42, 1587, 1965.

37. A. Allerhand and H. S. Gutowsky, J. Chem. Phys., 42, 4203, 1965.

38. A. Allerhand, J. Chem. Phys. 44, 1, 1966.

39. H. S. Gutowsky, R. L. Vold and E. J. Wells, J. Chem. Phys. 43, 4107, 1965.

40. P. W. Anderson and P. R. Weiss, Rev. Mod. Phys., 25, 269, 1953.

41. C. N. Banwell and H. Primas, Mol. Phys., 6, 225, 1963.

42. S. Alexander, Rev. Sci. Instr., 32, 1066, 1961.

43. I. Solomon, Phys. Rev. Letters, 2, 301, 1959.

44. E. J. Wells and K. H. Abrahamson, J. Mag. Res., 1, 378, 1969.

45. R. Freeman and S. Wittekoek, J. Mag. Res., 1, 238, 1969.

46. S. Forsen and R. A. Hoffman, J. Chem. Phys., 39, 2892, 1963; 40, 1189, 1964.

47. F. A. L. Anet and A. J. R. Bourne, J.A.C.S., 89, 760, 1967.

48. H. M. McConnell and D. D. Thompson, J. Chem. Phys., 26, 958, 1957; 31, 85, 1959.

49. L. Pauling, "The Nature of the Chemical Bond", Cornell Univ. Press, Ithaca, p. 281, 498, 1960.

50. S. Mizushima, "The Structure of Molecules and Internal Rotation", Acad. Press, N.Y., p. 139, 1954.

51. S. Mizushima, T. Simanonti, S. Nagakura, K. Kuratani, M. Tsuboi, H. Baba and O. Fujioka, J.A.C.S., 72, 3490, 1950.

52. W. D. Phillips, J. Chem. Phys. 23, 1363, 1955.

53. J. A. Pople, W. G. Schneider and H. J. Bernstein, "High Resolution Nuclear Magnetic Resonance", McGraw-Hill, N.Y., 366 ff, 1959.

54. A. Loewenstein and T. M. Connor, Ber. Bunsenges. Physik Chem., 67, 280, 1963.

55. J. Delpuech, Bull. Soc. Chim. France, p. 2697, 1964.

56. L. W. Reeves, Adv. Phys. Org. Chem., Vol. III, p. 187, 1965.

57. C. S. Johnson, Adv. Mag. Res., Vol. I, p. 33, 1965.

58. K. J. Laidler, Reaction Kinetics, Vol. I, Pergamon Press, London, p. 85, 1963.

59. P. T. Inglefield, E. Krakower, L. W. Reeves and R. Stewart, Mol. Phys. 15, 65, 1968.

60. R. C. Neuman, D. N. Roark and V. Jonas, J.A.C.S., 89, 3412, 1967.

61. M. Rabinovitz and A. Pines, J.A.C.S., 91, 1585, 1969.

62. R. C. Neuman and V. Jonas, J.A.C.S., 90, 1970, 1968.

63. A. E. Lemire and J. C. Thompson, Can. J. Chem., 48, 824, 1970.

64. A. Allerhand, H. S. Gutowsky, J. Jonas and R. A. Meinzer, J.A.C.S., 88, 3185, 1966.

65. C. W. Fryer, F. Conti and C. Franconi, Ric. Sci. Rend., 8, 788, 1965.

66. ref. 13, p. 441, 1962.

67. I. J. Lowe and R. E. Norberg, Phys. Rev., 107, 46, 1957.

68. J. S. Waugh, L. M. Huber and V. Hacberlen, Phys. Rev. Letters, 20, 180, 1968.

69. R. R. Ernst and W. A. Anderson, Rev. Sci. Instr., 37, 93, 1966.

70. R. R . Ernst, Adv. Mag. Res., Vol. II, 1, 1966.

71. R. E. Lundin, R. H. Elsken, R. A. Flath and R. Teranishi, App. Spec. Rev., 1, 131, 1967.

72. A. Streitweiser, "Molecular Orbital Theory for Organic Chemists", Wiley, N.Y., p. 33, 1961.

73. R. A. Hoffman, J. Chem. Phys. 39, 1397, 1963.

74. L. C. Allen and J. D. Russell, J. Chem. Phys., 46, 1029, 1967.

75. J. A. Pople, D. Santry and G. A. Segal, J. Chem. Phys. 43, 3129, 1965.

76. J. A. Pople and G. A. Segal, J. Chem. Phys., 43, S136, 1965; 44, 3289, 1966.

77. J. Del Bene and H. H. Jaffé, J. Chem. Phys., 48, 4050, 1968.

78. ref. 12, p. 16, 1964.

79. F. Bloch and A. J. Seigert, Phys. Rev., 57, 552, 1940.

80. I. I. Rabi, N. F. Ramsey and J. Schwinger, Rev. Mod. Phys., 26, 167, 1954.

81. ref. 10, chap. 12, 1930.

82. H. S. Gutowsky and C. H. Holm, J. Chem. Phys., 25, 1228, 1956.

83. R. R. Ernst and W. Anderson, Rev. Sci. Instr., 36, 1696, 1965.

84. E. Grunwald, A. Loewenstein and S. Meiboom, J. Chem. Phys., 27, 630, 1957.

85. B. Muller and M. Bloom, Can. J. Phys., 38, 1318, 1960.

86. M. Takeda and E. O. Stejskal, J.A.C.S., 82, 25, 1960.

87. M. T. Rogers and J. C. Woodbrey, J. Chem. Phys. 66, 540, 1962.

88. ref. 53, p. 8, 104, 1959.

89. I. Solomon, Phys. Rev., 99, 559, 1955.

90. ref. 13, p. 272, 1961.

91. A. G. Redfield, IBM J. Res. Develop., 1, 19, 1957.

92. U. Fano, Phys. Rev., 131, 259, 1963.

93. G. Binsch, J.A.C.S., 91, 1304, 1969.

94. R. Kubo and K. Tomita, J. Phys. Soc. Japan, 9, 888, 1954.

95. R. Bracewell, "The Fourier Transform and Applications", McGraw-Hill, N.Y., p. 98, 1965.

96. E. A. Guillemin, "Theory of Linear Physical Systems", J. Wiley, N. Y., chap. 18, 1963.

97. ref. 13, p. 93, 1964.

98. Y. W. Lee, "Statistical Theory of Communications", J. Wiley and Sons, N.Y., p. 495, 1960.

99. R. R. Ernst, J. Mag. Res., 1, 7, 1969.

100. C. E. Shannon, Proc. I.R.E., 37, 10, 1949.

101. A. R. Billings, Elec. Radio Engr., 36, 70, 1959.

102. P. F. Panter, "Modulation, Noise and Spectral Analysis", McGraw-Hill, N.Y., p. 80, 1965.

103. ref. 95, p. 104, 1965.

104. J. G. Powles and J. H. Strange, Proc. Phys. Soc., 82, 6, 1963.

105. G. Arfken, "Mathematical Methods for Physicists", Acad. Press, N.Y., p. 323, 1966.

106. J. Reichert and J. Townsend, Rev. Sci. Instr., 35, 1692, 1964.

107. D. Ware and P. Mansfield, Rev. Sci. Instr., 37, 1167, 1966.

108. J. W. Cooley and J. W. Tukey, Math. Comp., 19, 297, 1965.

109. ref. 105, p. 520.

110. J. C. Buchta, H. S. Gutowsky and D. E. Woessner, Rev. Sci. Instr., 29, 55, 1958.

111. K. Luszczynski and J. G. Powles, J. Sci. Instr., 36, 57, 1959.

112. P. Mansfield and J. G. Powles, J. Sci. Instr., 40, 232, 1963.

113. S. Meiboom and D. Gill, Rev. Sci. Instr., 29, 688, 1958.

114. M. Sasson, A. Tzalmona and A. Loewenstein, J. Sci. Instr., 40, 133, 1963.

115. R. J. Blume, Rev. Sci. Instr., 32, 554, 1961.

116. W. G. Clark, Rev. Sci. Instr., 35, 316, 1965.

117. S. L. Gordon and J. D. Baldeschwieler, J. Chem. Phys., 43, 76, 1965.

118. I. J. Lowe and C. E. Tarr, J. Sci. Instr., 1, 604, 1968.

119. L. J. Burnett and J. F. Harmon, Rev. Sci. Instr., 89, 1226, 1968.

120. D. F. Holcomb and R. E. Norberg, Phys. Rev., 98, 1074, 1955.

121. J. J. Spokas and C. P. Slichter, Phys. Rev., 113, 1462, 1959.

122. M. Bloom, private communication, 1967.

123. J. Millman and H. Taub "Pulse and Digital Circuits" McGraw-Hill, N.Y. p. 246, 1956.

124. J.M. Doyle "Pulse Fundamentals" Prentice-Hall, N.Y., p. 1963.

125. K.H.Abramson, P.T. Inglefield, E. Krakower and L.W. Reeves, Can. Jnl. Chem. 44, 1685, 1966.

126. A.L. Van Geet, Anal. Chem. 40, 2227, 1968.

127. L.G. Parratt "Probability and Experimental Error", J. Wiley and Sons, Inc., N.Y., p. 126, 1961.

128. R.T. Birge, Rev. Mod. Phys. 19, 298, 1947.

129. K.J. Laidler, "Chemical Kinetics", McGraw-Hill, N.Y., p. 67, 1967.

130. W.F.K. Wynne-Jones and H. Eyring, J. Chem. Phys. 3, 492, 1935.

131. R.A. Fisher, "Statistical Methods for Research Workers", Oliver and Boyd, Ltd., Lond., p. 37, 1946.

132. P.T. Narasimhan and M.T. Rogers, J. Phys. Chem. 63, 1388, 1959.

133. L. Saunders and W.B. Whalley, Tetrahedron 26, 119, 1970.

134. K.J. Laidler, Trans. Far. Soc. 55, 1725, 1959.

135. (a) R.E. Powell and W.M. Latimer, J. Chem. Phys. 19, 1139, 1951.
(b) J.E. Leffler, J. Org. Chem. 20, 1202, 1955.

136. Z. Arnold, Collection Czechoslov. Chem. Communs. 24, 760, 1959.

137. W.T. Raynes and T.A. Sutherley, Mol. Phys. 18, 129, 1970.

138. R.L. Middaugh, R.S. Drago and R.J. Niedzielski, JACS 86, 388, 1964.

139. E. Lustig, W.R. Benson and N. Duy, J. Org. Chem. 32, 851, 1967.

140. A.E. Lemire and J.C. Thompson, Can. J. Chem. 48, 824, 1970.

141. W.W. Hartman and M.R. Brethen "Organic Synthesis", Vol. II, J. Wiley and Sons, N.Y., p. 278, 1943.

142. I.B. Wilson, J. Biol. Chem. 235, 2312, 1960; 236, 2292, 1961.

143. H.P. Metzer, J. Biol, Chem. 238, 3432, 1963.

144. H.A. Scheraga, Adv. Phys. Org. Chem. 6, 103, 1968.

145. J.S. Rigden and R.H. Jackson, J. Chem. Phys. 45, 3646, 1966.

146. G. Schrader, British Intelligence Objectives Subcommittee, Final Rept. No. 714, B.I.O.S., London, 1945.

147. E. Bock and D. Iwacha, Can. J. Chem. 46, 523, 1967.

148. D.L. Hooper and R. Kaiser, Can. J. Chem. 43, 2363, 1965.

149. S. Brownstein, JACS 91, 3034, 1969.

150. E.W. Randall and J.D. Baldeschweiler, J. Mol. Spec. 8, 365, 1962.

151. A.J.R. Bourn and E.W. Randall, J. Mol. Spec. 13, 29, 1964.

152. A.J.R. Bourn and E.W. Randall, Mol. Phys. 8, 567, 1964.

153. J.A. Pople, Mol. Phys. 1, 158, 1958; J.D. Baldeschwieler, J. Chem. Phys. 34, 718, 1961.

154. L.W. Reeves and K.N. Shaw, Can. J. Chem. 49,(in press) 1971.

155. R.C. Shaddick, L.W. Reeves and K.N. Shaw, Can. J. Chem.49, (in press) 1971.

156. J.H. Freed and G.K. Fraenkel, J. Chem. Phys. 39, 326, 1963.

157. H. Shimizu, J. Chem. Phys. 40, 754, 1964.

158. B. Sunners, L.H. Piette and W.G. Schneider, Can. J. Chem. 38, 681, 1960.

159. H. Kamei, Bull. Chem. Soc. Japan 38, 1212, 1965; ibid 41, 2269, 1968.

160. T. Drakenburg and S. Forsen, J. Phys. Chem. 74, 1, 1970.

161. L.H. Piette, J.D. Ray and R.A. Ogg, J. Mol. Spec. 2, 66, 1958.

162. S. Castellano and A.A. Bothner-By, J. Chem. Phys. 41, 3863, 1964.

163. K-I.Dahlquist, S. Forsen and T. Alm, Acta Chemica Scand. 24, 651, 1970.

164. S. Nagakura, Bull. Chem. Soc. Japan 25, 164, 1952.

165. E.L. Wagner, J. Phys. Chem. 63, 1403, 1959.

166. S. Nagakura, Mol. Phys. 3, 105, 1960.

167. F.E. Morris and W.J. Orville-Thoms, J. Mol. Spec. 6, 572, 1961.

168. R.L. Middaugh, R.S. Drago and R.J. Niedzielski, JACS. 86, 388, 1964.

169. J. Sandstrom, J. Phys. Chem. 71, 2318, 1967.

170. M.J. Janssen and J. Sandstrom, Tetrahedron 20, 2339, 1964.

171. A. Streitweiser, JACS. 82, 4123, 1960.

172. H. Eyring, J. Walter and G.E. Kimball "Quantum Chemistry" J. Wiley and Sons, Inc., N.Y., p. 99, 1965.

173. H.O. Pritchard and F.H. Sumner, Proc. Roy. Soc. A235, 136, 1956.

174. A. Streitweiser and P.M. Nair, Tetrahedron 19, Supp. 2, 88, 1963.

175. G.W. Wheland "Resonance in Organic Chemistry", J. Wiley and Sons, N.Y., p. 86, 1955.

176. L. Pauling and D.M. Yost, Proc. Natl. Acad. Sci. U.S. 14, 414, 1932.

177. R.S. Mulliken, J. Chem. Phys. 2, 782, 1934.

178. W. Gordy, Phys. Rev. 69, 604, 1946.

179. J. Hinze and H.H. Jaffe, JACS 84, 540, 1962.

180. J. Hinze, M.A. Whitehead and H.H. Jaffe, JACS 85, 148, 1963.

181. ref. 72, p. 97, 110, 1961.

182. F.A. Matsen, JACS 72, 5243, 1950.

183. ref. 72, p. 131, 1961.

184. R. Hoffmann, J. Chem. Phys. 39, 1397, 1963.

185. C. Sandorfy, Bull. soc. chim. France 615, 1949.

186. M.J.S. Dewar and H.N. Schmeising, Tetrahedron 5, 166, 1959.

187. R.S. Mulliken, C.A. Rieke and W.G. Brown, JACS 63, 41, 1941.

188. R.S. Mulliken, C.A. Rieke, D. Orloff and H. Orloff, J. Chem. Phys. 17, 1248, 1949.

189. L.E. Sutton, Chem. Soc. (Lond.) Spec. Publication No. 11, 1958.

190. C.A. Coulson and H.C. Longuet-Higgins, Proc. Roy. Soc. A191, 39, 1947; ibid A192, 16, 1947.

191. G. Herzberg "Atomic Spectra and Atomic Structure" Dover, N.Y., p. 40, 1944.

192. M. Roux, M. Cornille and L. Burnelle, J. Chim. Phys. 55, 754, 1958; J. Chem. Phys. 37, 933, 1962.

193. P.E. Cade, R.F.W. Bader, W.H. Hennecker and I. Keaveny, J. Chem. Phys. 46, 3341, 1967; ibid 50, 5313, 1969.

194. J.C. Slater, Phys. Rev. 36, 57, 1930.

195. H. Kessler, Angew. Chemie (Intern. Ed.) 9, 219, 1970.

196. D.H. Christensen, R.N. Kortzeborn, B. Bak and J.J. Led. J. Chem. Phys. 53, 3912, 1970.

197. C.C. Costain and J.M. Dowling, J. Chem. Phys. 32, 158, 1960.

198. R.J. Kurland and E. Bright-Wilson, Jr. J. Chem. Phys. 27, 585, 1957.

199. R.G. Parr "The Quantum Theory of Molecular Electronic Structure" W.A. Benjamin, N.Y., p. 21, 1963.

200. C.C.J. Roothaan, Rev. Mod. Phys. 23, 69, 1963.

201. C.C.J. Roothaan, J. Chem. Phys. 19, 1445, 1951.

202. ref. 49, p. 191, 1960.

203. W. Gordy, J. Chem. Phys. 15, 305, 1947.

204. J.A. Pople and M. Gordon, JACS 89, 4253, 1967.

205. W.T. Raynes and M.A. Raza, Mol. Phys. 20,339, 1971; and references therein.

206. F.A. Momany, R.F. McGuire, J.F. Yan and H.A. Scheraga, J. Phys. Chem. 74, 2424, 1970.

207. R.W. Kilb, C.C. Lin and E. Bright-Wilson, Jr. J. Chem. Phys. 27, 585, 1957.

208. L. Pierce and L.C. Krishner, J. Chem. Phys. 31, 875, 1959.

PUBLICATIONS

1. L.W. Reeves and K.N. Shaw, Can. J. Chem., 48, 3641, 1970.
   Nuclear Magnetic Resonance Studies of Multi-site Chemical Exchange. I. Matrix Formulation of the Bloch Equations.
2. L.W. Reeves and K.N. Shaw, Can. J. Chem., 49, 1971 (in press).
   NMR Studies of Multi-site Chemical Exchange. II. Hindered Rotation in N,N,-dimethyl carbamyl Fluoride.
3. L.W. Reeves, R.C. Shaddick and K.N. Shaw, Can. J. Chem., 49, 1971 (in press).
   NMR Studies of Multi-site Chemical Exchange. III. Hindered Rotation in Dimethyl Acetamide, Dimethyl Trifluoro-acetamide and Benzamide.
4. E.A. Allan, R.F. Hobson, L.W. Reeves and K.N. Shaw, J. Am. Chem. Soc., 1971 (in press).
   Hindered Rotation in N,N-dimethyl Amides with Halogen and Pseudo-halogen Substituents.
5. L.W. Reeves, R.C. Shaddick and K.N. Shaw, J. Phys. Chem., 1971 (in press).
   A Determination of the Hindered Rotation Barrier in Unsym-dimethyl Selenourea and Comparison with similar Compounds.
6. K.N. Shaw and L.W. Reeves, Chem. Phys. Letters, 1971.
   A. Semi-empirical SCF-LCAO-MO Study of the Hindered Internal Rotation in Formamide.
7. K.N. Shaw, Rev. Sci. Instr., 1971 (submitted for publication)
   A Simple Solid-state rf-pulse gate for NMR Spectrometers.